UNIVERSIDAD REY JUAN CARLOS

DEPARTAMENTO DE TECNOLOGÍA ELECTRÓNICA

PhD Thesis

Fabrication, Characterization and Modelling of Organic Electroluminescent Diodes with Blue Emission. Application to the Design and Manufacturing of Organic Displays.

Autora: Belén Arredondo Conchillo

Directores: Dr. Ángel Luis Álvarez del Castillo
Dra. Beatriz Romero Herrero

2008

Dr. D. Ángel Luis Álvarez Castillo y Dra. Dña Beatriz Romero Herrero, profesores Titulares de Universidad del Departamento de Tecnología Electrónica de la Universidad Rey Juan Carlos, directores de la Tesis Doctoral “Fabrication, characterization and modelling of organic electroluminescent diodes with blue emission. Application to the design and manufacturing of organic displays”, realizada por la doctoranda Dña. Belén Arredondo Conchillo.

HACEN CONSTAR

Que esta Tesis Doctoral reúne los requisitos necesarios para su defensa y aprobación,

En Móstoles, a 5 de Diciembre de 2007,

Dr. D. Ángel Luis Álvarez Castillo

Dra. Dña. Beatriz Romero Herrero

Tribunal

Presidente:	Dr. José Manuel Otón Sánchez
Secretario:	Dr. Juan Antonio Hernández Tamames
Vocales:	Dr. Fernando Calle Gómez
	Dr. Ricardo Mallavia Marín
	Dr. Robert Bellini
Suplentes:	Dr. Ignacio Esquivias Moscardó
	Dr. José Manuel Sánchez Pena
	Dr. Ricardo Vergaz Benito
	Dra. Julia Arias Rodríguez
	Dr. José Luis Segura Castedo

Agradecimientos

Esta tesis ha sido posible gracias al apoyo logístico, científico y personal de mucha gente, y en este sentido, es una prueba de que los avances se alcanzan mejor colaborando que compitiendo. En estas líneas intentaré expresar la gratitud acumulada en estos años, aunque en realidad, soy de la opinión de que la gratitud debe mostrarse en el día a día, y espero ser consecuente.

Gracias:

A mis directores de tesis, Ángel Luis y Bea, porque además de directores los considero co-autores. A él, por sus enseñanzas y buen entendimiento de los modelos teóricos. A ella, por su ayuda y predisposición para el trabajo tecnológico. A los dos, por todo el tiempo que han dedicado a esta tesis, por sus críticas constructivas y por todo lo que he aprendido con ellos. En definitiva, por formar un buen equipo.

A mis compañeros del Dpto. de Tecnología Electrónica (URJC) y afines, por ser geniales. A mi compañera de despacho, Susana, por aguantarme siempre de buen humor. A Norberto, por sus alegrías y soleás. A Roberto, por nuestras sesiones de terapia para doctorandos. A Araceli, por su colaboración en el trabajo experimental, y, junto con Cris, Juan Fran y Felipe, por ser unos estupendos compañeros de patinaje. A Juan Antonio, por apoyar y defender al grupo en todos los niveles. Y a todos los demás, Carmen, Emanuele, Manuel, José Luis y Joaquín, por los innumerables buenos ratos.

Al Grupo de Cristales Líquidos de la ETSIT (UPM). A José Manuel, por poner a nuestra disposición sus instalaciones y equipos para las tareas de fabricación, y por apoyar a los grupos pequeños. A Xabi, por su destreza e ingenio con las máquinas, su continua predisposición a ayudar y su buen humor. A Nour, por enseñarme el día a día en la sala limpia. A Bob, por presentarme los algoritmos genéticos y por muchas cosas más. A ellos y a los demás, Morten, Bea y David, por su generosidad y hospitalidad, y por acogerme en el grupo como una más.

A Ricardo Mallavia, del Instituto de Biología Molecular y Celular (UMH). Por la síntesis de los materiales electroluminiscentes orgánicos, por sus ganas y entusiasmo, y por ser nuestro químico de cabecera. A Paco Montilla, por las medidas de voltametría cíclica.

Al grupo de Displays y Aplicaciones Fotónicas de la (UC3M). A José Manuel, por prestarnos el analizador de impedancias para la caracterización en frecuencia. Y en especial a Ricardo, por su ayuda con las medidas.

Al grupo de Metrología del Instituto de Física Aplicada (CSIC), por permitirnos usar sus equipos para la caracterización óptica. En particular a Joaquín, por enseñarnos el manejo del espectrorradiómetro.

A Fernando Calle, del Instituto de Sistemas Optoelectrónicos y Microtecnología (UPM), por facilitarnos el acceso al perfilómetro para la caracterización de espesores. A Jimena y Marta, del Dpto. Tecnología Electrónica (ETSIT, UPM), por su ayuda con estas medidas.

Al grupo de Ingeniería Química y Ambiental (URJC), por cedernos su *glovebox* para las tareas de encapsulado.

A todos aquellos que con sus ideas y experiencia, nos han ido aconsejando. En especial a Ignacio Esquivias, Fernando González y Peter Stallinga.

A mis ex-compañeros y amigos de la Universidad Carlos III, porque las malas épocas nos hicieron mejores.

A mis amigos, por los grandes momentos que hicieron que la tesis pareciera insignificante.

A mis padres, por su apoyo y cariño incondicionales.

A mi hermana, por ser la mejor.

A Javi, por todo y siempre.

Contents

1 Introduction 3

1.1 Fundamentals of organic electronics 3

1.1.1 The dawn of organic electronics 4
1.1.2 Electroluminescent organic materials: molecules and polymers 7
1.1.3 Basic PLED/OLED operation principles 9
1.1.4 Advantages and disadvantages of PLED/OLEDs 12

1.2 Novel applications of organic electroluminescent devices 13

1.2.1 Electroluminescent organic diodes with different substrates: flexible OLEDs (FOLEDs) and transparent OLEDs (TOLEDs) 14
1.2.2 Displays based on organic materials 15
1.2.3 OLEDs in solid state lightning 19

1.3 Scientific and technological key issues currently under research 20

1.3.1 Study of conduction mechanisms in organic semiconductors. 21
1.3.2 Study of degradation mechanisms in organic materials. 21
1.3.3 Improving OLEDs efficiency. 22
1.3.4 Study of new electroluminescent materials: blue and white illumination. 22
1.3.5 Development of new technologies for display processing. 24
1.3.6 Driver design for integration in AMOLEDS. 24

1.4 Objectives of this thesis 25

1.5 Outline of this thesis 26

2 Fabrication and characterization techniques of PLED passive matrix 31

2.1 Experimental equipment 31

2.1.1 Fabrication equipment 31
2.1.1.1 Ultrasound cleaning bath 32
2.1.1.2 Spin coating system 33

2.1.1.3 UV lamp and alignment mask system 33
2.1.1.4 Thermal evaporator 34
2.1.1.5 Glove Box 35
2.1.2 Characterization equipment 36
2.1.2.1 Profilometer 36
2.1.2.2 Semiconductor parameter analyzer 37
2.1.2.3 Impedance analyzer 38
2.1.2.4 Spectroradiometer 38
2.2 PLED passive matrix fabrication procedure 39
2.2.1 General procedure of PLED passive matrix fabrication 40
2.2.2 Relevant steps in PLED fabrication procedure 42
2.2.2.1 Glass cutting and cleaning 42
2.2.2.2 Anode patterning 43
2.2.2.3 Diode geometry definition by photoresist wells 44
2.2.2.4 Polymer layers deposition 46
2.2.2.5 Cathode evaporation 48
2.2.2.6 Encapsulation and wire soldering 49
2.3 Thickness calibration 50
2.4 Electrical characterization techniques 51
2.4.1 Current-voltage 51
2.4.2 Admittance spectroscopy 52
2.5 Optical characterization techniques 53
3 PLED passive matrix based on polyfluorene derivatives 57
3.1 Overview of polyfluorene materials 57
3.1.1 Why polyfluorenes? 58
3.1.2 Poly(2,7-fluorene phenylidene) (PFP) 61
3.2 Thickness calibration of spin-coated active layers 63
3.2.1 P3HT and MDMO:PPV 63
3.2.2 Polyfluorene derivatives 65
3.3 Fabricated structures and electrical characterization results 67

3.3.1 Comparison of polyfluorene derivatives with commercial blue polymers.....67
3.3.2 Influence of the active layer thickness.....69
3.3.3 Improved performance of encapsulated devices.....72
3.3.4 Admittance spectroscopy (AS) characterization. Small signal equivalent circuit.....76

3.4 Results of the optical characterization.....79

3.4.1 Electroluminescence, luminance and CIE coordinates.....80
3.4.2 Degradation and colour shift in polyfluorenes.....87

3.5 Conclusions.....95

4 Modelling OLED electrical behaviour.....99

4.1 Literature review of DC conduction models.....99

4.1.1 Carrier injection into organic semiconductors.....100
4.1.1.1 Classical injection approaches.....101
4.1.1.2 Microscopic approach: Injection from a metal into a disordered hopping system.....104
4.1.2 Carrier transport in an organic semiconductor.....107
4.1.2.1 Concept of Space Charge Limited Current (SCLC).....107
4.1.2.2 Mobility formulation in semi-insulating systems.....108
4.1.2.2.1 Classical Poole-Frenkel mobility.....108
4.1.2.2.2 Gill's phenomenological mobility.....109
4.1.2.2.3 Gaussian Disorder Model (GDM).....110
4.1.2.3 Trap-controlled effective transport.....113

4.2 New proposal to model conduction in the presence of an injection barrier.....114

4.2.1 Charge transport in the presence of non-ohmic contacts.....115
4.2.2 Complete conduction model including hopping injection and transport mechanisms.....117

4.3 Simulation results and discussion.....118

4.3.1 Current dependence on device structure and material parameters.....119
4.3.2 Total electric field and carrier density.....122
4.3.3 Electric field at the interface versus bias.....123

4.3.4 Results obtained by fitting our model to experimental J-V of PLEDs based on two different polymers: MDMO:PPV and PFP:$(CN)_2$ 124

4.4 Admittance spectroscopy (AS) model 129

4.4.1 Review of small signal (AC) techniques applied to OLEDs 130

4.4.2 Reformulation of admittance spectroscopy model in the presence of non-ohmic contacts 133

4.4.3 Simulation results and discussion 136

4.4.3.1 Dependence of capacitance and conductance on mobility and disorder parameters 136

4.4.3.2 Comparison with other admittance spectroscopy models 139

4.4.3.3 Results obtained by fitting our model to experimental admittance measurements: Determination of the hole mobility of MDMO:PPV and PFP:$(CN)_2$ 141

4.5 Conclusions 144

5 New cathode patterning technique for PMOLED displays 147

5.1 Cathode patterning techniques 147

5.1.1 Shadow mask 148

5.1.2 Jet printing of polymers 149

5.1.3 Dry etching of the cathode 149

5.1.4 Cathode separators (“Pillars”) 150

5.2 Cathode patterning using mechanical ablation 151

5.2.1 Mechanical set up 152

5.2.2 Cathode patterning 154

5.3 Fabrication of a PMOLED display 156

5.3.1 Mask Fabrication 156

5.3.2 PMOLED display prototype 157

5.4 Conclusions 160

6 Conclusions and future work 163

References 167

Appendix I 183

Appendix II **185**

Resumen **191**

List of figures

Figure 1.1- Emission spectra of the most commonly used organic materials. 4

Figure 1.2 - Progression of luminous efficiency of monochrome OLEDs based on molecules or polymers, compared to some already known sources. 6

Figure 1.3 - Chemical structure of some organic small molecules used for OLEDs. 7

Figure 1.4 - Chemical structure of some conjugated polymers. 8

Figure 1.5 - p-orbital overlap to form LUMO and HOMO levels 9

Figure 1.6 - Basic PLED structure. 10

Figure 1.7 - Transmittance of different ITO coated glass substrates 10

Figure 1.8 - Light emission diagram for an OLED. 12

Figure 1.9 - FOLED (Universal Display Corporation) 14

Figure 1.10 - Ultra thin flexible OLED (Philips Research Laboratories) 15

Figure 1.11 - TOLED (Universal Display Corporation) 15

Figure 1.12 - AMOLED and PMOLED structures. 18

Figure 1.13 - PMOLED/AMOLED market evolution. 18

Figure 1.14 - 23.3 inch active matrix OLED display (Sony Japan) 19

Figure 1.15 - Increase in efficiency of SSL with respect to traditional lightning tech. 20

Figure 1.16 - Efficiency and lifetime for RGB based on OLEDs 23

Figure 2.1 - Clean Room. Liquid Crystal Group, ETSIT, UPM. 32

Figure 2.2 - Laminar flux cabin and ultrasound tanks 32

Figure 2.3 - Spinner 33

Figure 2.4 - Hybralign TM Series 400 Mask Alignment and Exposure system. 34

Figure 2.5 - Evaporator Vacudel 300 (Telstar). 35

Figure 2.6 - Mbraun Unilab Glove Box. 36

Figure 2.7 -Tencor Alphastep 200 Profilometer....37

Figure 2.8 - Semiconductor Parameter Analyzer Agilent and Pulse Generator Agilent....37

Figure 2.9 -Solartron 1260 Impedance Analyzer. 38

Figure 2.10 - Konica Minolta CS-1000 spectroradiometer....38

Figure 2.11 - Schematic of the complete fabrication process. 40

Figure 2.12 - Schematic of cutting and cleaning processes. 42

Figure 2.13 - ITO anode mask. 43

Figure 2.14 - Photolithography to define ITO anodes. 43

Figure 2.15 - Wet etching bath. 44

Figure 2.16 - Diode geometry mask. 45

Figure 2.17 - Schematic of diode geometry definition. 45

Figure 2.18 - Photograph of photoresist wells with two diameters. 46

Figure 2.19 - Deposition of PEDOT:PSS and active layer by spin-coating....47

Figure 2.20 - Cathode evaporation. 48

Figure 2.21 - Encapsulation. 49

Figure 2.22 - Final device cross section. 50

Figure 2.23 - Final device. 50

Figure 2.24 - Thickness measurement. 51

Figure 2.25 - Current vs voltage measurement set up. 52

Figure 2.26 - Impedance spectroscopy set up. 53

Figure 2.27 - Optical measurement set up. 54

Figure 3.1 - Monomer repeating units of PPP and PPV 58

Figure 3.2 - Molecular structure of fluorene and poly-(fluorine). 58

Figure 3.3 - PL spectra of polyfluorene films after annealing at different temperatures in nitrogen atmosphere and in air. 61

Figure 3.4 - Polyfluorene phenylidene structure with Br and CN as functional groups. 61

Figure 3.5 - Chemical structure of MDMO-PPV and P3HT 63

Figure 3.6 - Thickness calibration curves for P3HT and MDMO-PPV in toluene. Error bars indicate the profilometer resolution is 5 nm. 64

Figure 3.7 - Photographs of deposited films of P3HT and MDMO-PPV. 65

Figure 3.8 - Thickness calibration curves for PFP:Br_2 and PFP:$(CN)_2$ in toluene. Error bars indicate the profilometer resolution is 5 nm. 66

Figure 3.9 - Photographs of deposited films of PFP:Br_2 and PFP:$(CN)_2$ 66

Figure 3.10 - J-V characteristics of PLEDs with structure ITO/PEDOT:PSS/PF/Al based on PFC_6 , PFP:Br_2 and PFP:$(CN)_2$ 68

Figure 3.11 - J-V characteristics of PLEDs with structure ITO/PEDOT:PSS/Active Layer/Al based on P3HT and MDMO-PPV for different active layer thicknesses. 70

Figure 3.12 - J-V characteristics of PLEDs with structure ITO/PEDOT:PSS/PF/Al based on PFP:Br_2 and PFP:$(CN)_2$ for different active layer thicknesses 71

Figure 3.13 - J as function of time for the non-encapsulated MDMO-PPV diode 73

Figure 3.14 - Photograph of the non-encapsulated diode before and after 12 operating hours. 74

Figure 3.15 - Current density as function of time for the encapsulated MDMO-PPV diode. 74

Figure 3.16 - Photograph of the encapsulated diode before and after 18 operating hours. 75

Figure 3.17 - Evolution of the J-V characteristic after few days of continuous functioning for encapsulated and non-encapsulated diodes. 75

Figure 3.18 - Cole-Cole plots with frequency as the implicit variable for a PLED based on PFP:$(CN)_2$ and MDMO:PPV at different bias.. 76

Figure 3.19 - Small signal equivalent circuit of the AS response 77

Figure 3.20 - Derived mobility for a MDMO-PPV and a PFP:$(CN)_2$ based diode from the fit to the equivalent circuit of Figure 3.19. 78

Figure 3.21 - CIE phototopic luminous efficiency. 79

Figure 3.22 - Electroluminescence at different bias for a PLED based on MDMO:PPV. 81

Figure 3.23 - Luminance and efficiency of a PLED with based on MDMO:PPV. 82

Figure 3.24 - EL at different bias for a PLED based on PFP:$(CN)_2$. PL of PFP:$(CN)_2$ on top of a ITO coated glass. 84

Figure 3.25 - Luminance and efficiency of a PLED based on PFP:$(CN)_2$. 85

Figure 3.26 - Luminance as function of the duty cycle. 86

Figure 3.27 - CIE coordinates of two diodes based on PFP:$(CN)_2$ and MDMO:PPV. 86

Figure 3.28 - EL spectra for a diode with structure ITO/PEDOT:PSS/PFP:$(CN)_2$/Al after seven hours of continuous operation. Inset shows the normalized E.L. intensity. 89

Figure 3.29 - EL of an electrically degraded PLED based on PFP:$(CN)_2$ 90

Figure 3.30 - Luminance versus time for a ITO/PEDOT:PSS/PFP:$(CN)_2$/Al after seven hours of continuous operation. 91

Figure 3.31 - Colour shift of a ITO/PEDOT:PSS/PFP:$(CN)_2$/Al after seven hours of continuous operation. 91

Figure 3.32 - EL spectra of a degraded PLED with structure ITO/PEDOT:PSS/PFP:$(CN)_2$/Al. ..93

Figure 3.33 - EL of two PFP based diodes fabricated in different batches and subjected to different electrical treatments. 94

Figure 3.34 – Time evolution of CIE coordinates of a degraded PLED based on PFP:$(CN)_2$. 94

Figure 4.1 - Equivalent circuit for DC conduction. F_0 accounts for the electric field in the contact region. 100

Figure 4.2 -Injection barrier between a metal and an organic semiconductor. 100

Figure 4.3 - Band diagram of the metal-organic semiconductor interface for hole injection. 103

Figure 4.4 - Schematic of the two-stepped injection process proposed by Arkhipoc et al. 105

Figure 4.5 - Gaussian distribution of localized states 106

Figure 4.6 - Gaussian DOS showing the equilibrium and transport levels. 112

Figure 4.7 - Most probable jump of a carrier from a tail site to the E_t. 112

Figure 4.8 - Dependence of the current density on the barrier height and mobility..... 119

Figure 4.9 - Dependence of the analytical function β on the barrier height and mobility..... 120

Figure 4.10 - Dependence of the function β on sample thickness, for different injection barrier heights and mobilities..... 121

Figure 4.11 - Spatial distribution of electric field and carrier density for different mobilities.... 122

Figure 4.12 - Electric field at the interface, F_0, as function of applied bias..... 123

Figure 4.13 - Experimental J-V curve of PLEDs based on ITO/PEDOT:PSS/MDMO-PPV/Al and ITO/PEDOT:PSS/PFP:$(CN)_2$/Al, and theoretical fits..... 125

Figure 4.14 - Least square of the error J-V function vs parameter variation..... 127

Figure 4.15 - Least square of the error J-V function vs mobility..... 128

Figure 4.16 - Experimental J–V curves of devices with identical active layers but different thicknesses.. 129

Figure 4.17 - Frequency-dependent capacitance and conductance for an organic diode with area, A = 1.77×10^{-6} m^2, active layer thickness L = 200 nm and $\varepsilon_r = 4$ 136

Figure 4.18 - Simulated $-\Delta B = -\omega(C-C_{geo})$ obtained from Figure 4.17. 138

Figure 4.19 - Frequency-dependent capacitance and conductance for an organic diode with area, A = 1.77×10^{-6} m^2, active layer thickness L=200 nm and $\varepsilon_r = 4$. 139

Figure 4.20 - Frequency dependent capacitance and conductance using three admittance models: Martens et al., Tsang et al. at and that model presented in section 4.4.2..... 140

Figure 4.21 - Conductance and capacitance for ITO/PEDOT:PSS/MDMO:PPV/Al at different applied bias. The solid lines are fits to the experimental data 141

Figure 4.22 - Conductance and capacitance for ITO/PEDOT:PSS/PFP:$(CN)_2$/Al at different applied bias. The solid lines are fits to the experimental data 142

Figure 4.23 - Derived mobility for a MDMO-PPV and a PFP:$(CN)_2$ based diode from the fit to AS measurements. 143

Figure 5.1 - Cathode patterning using a shadow mask 148

Figure 5.2 - Depositing polymer solution using jet printing technique. 149

Figure 5.3 - Use of cathode separators to pattern the organic layer and the cathode. 150

Figure 5.4 - Epilog Mini / Helix 24 laser system 152

Figure 5.5 - Spring probe embedded in a methacrylate block and Mechanical piece mounted on a micropositioning system. 153

Figure 5.6 - Spring probe design 153

Figure 5.7 - Design of the cathode tracks 154

Figure 5.8 - Aluminium tracks performed with the mechanical ablation technique 155

Figure 5.9 - Mask design for the ITO photolithography and Pixel definition by overlapping the anode and cathode masks 156

Figure 5.10 - Mask employed in the ITO photolithography 157

Figure 5.11 - Sample after ITO photolithography showing anode columns. 157

Figure 5.12 - Pixel definition 158

Figure 5.13 - Final device mounted on a PCB 159

Figure 5.14 - MDMO-PPV based display prototype with different pixel configurations lighting. 159

Figure 5.15 - J-V curve of one pixel of a MDMO:PPV based display. 160

List of tables

Table 1.1 - Electrodes work function 11

Table 1.2 - Market and expectations for LCDs and OLEDs. 16

Table 1.3 - Efficiency and brightness data for several conventional light sources. 20

Table 2.1 - Summary of fabrication steps and their influence on the final device quality. 41

Table 2.2 - Aluminium evaporation parameters for thickness calculation 49

Table 3.1 - Electrochemical data obtained from the stabilized voltammograms. 62

Table 3.2 - PLED structures based on three different electroluminescent polyfluorenes: PFC_6, PFP:Br_2 and PFP:$(CN)_2$. 67

Table 3.3 - Summary of fabricated PLEDs using as active layer P3HT and MDMO-PPV for different thicknesses. Emission peak registered at room T. 69

Table 3.4 - Summary of fabricated PLEDs using as active layer PFP derivatives for different thicknesses. Emission peak registered at room T. 70

Table 3.5 -Two identical MDMO PLEDs: with and without encapsulation. 72

Table 3.6 - Resulting parameters obtained from the fits shown in Figure 3.18. 77

Table 3.7 - Summary of the optical performance for MDMO-PPV and PFP diodes. 87

Table 4.1 - Parameters obtained from the fit of Figure 4.13. 126

Acronyms

Alq3 – Tris(8-hydroxyquinoline) aluminum

AMOLED – Active Matrix Organic Light Emitting diode

AS – Admittance Spectroscopy

CIE – Commission Internationale de l'Eclairage

CDT – Cambridge Display Technology

DISCLC – Dark Injection Space Charge Limited Current

CRT – Cathode Ray Tube

DOS – Density of States

EA – Electron Affinity

EL – Electroluminiscence

EPLaR – Electronics on Plastic by Laser Release

EQE – External Quantum Efficiency

FL – Fluorene

FFT – Fast Fourier Transform

FOLED – Flexible Organic Light Emitting diode

FPD – Flat Panel Display

GDM – Gaussian Disorder Model

HIL – Hole Injection Layer

HOMO – Highest Occupied Molecular Orbital

IP – Ionization Potential

IR – Infrared Spectroscopy

ITO – Indium Tin Oxide

LCD – Liquid Crystal Display

LEC – Light Emitting Electrochemical Cell

LED – Light Emitting Diode

LUMO – Lowest Unoccupied Molecular Orbital

MEMS– MicroElectronic Mechanic System

OLED – Organic Light Emitting diode

PCB – Printed Circuit Board

PDP – Plasma Display Panel

PEDOT:PSS – Poly(3,4-ethylenedioxythiophene) poly(styrenesulfonate)

PF – Polyfluorene

PFC6 – Poly(9,9-dihexilfluoren-2,7-diyl)

PFP – Polyfluorene Phenylidene

PHOLED – Phosphorescent Organic Light Emitting Diode

PL – Photoluminiscence

PLED – Polymer Light Emitting diode

PMOLED – Passive Organic Light Emitting diode

PPV – Poly(phenilene vynilene)

PPP – poly(p-phenilene)

PVK – Poly(N-vinilcarbazol)

P3HT - Poly-(3-hexylthiophene)

SCLC – Space Charge Limited Current

SSL – Solid State Lightning

THF – Tetrahydrofuran

TFT – Thin Film Transistor

TPD – Tetraphenyl diamine

TOF – Time of Flight

TOLED – Transparent Organic Light Emitting diode

UPS – Ultraviolet Photoemission Spectroscopy

WOLED – White Organic Light Emitting diode

Summary

In the present work, electroluminescent organic diodes based on a new blue polyfluorene derivative have been fabricated, characterized and modelled. Passive matrix diodes have been fabricated adapting standard techniques such as photolithography, spin-coating and metal evaporation. Devices were fabricated for different active layer thicknesses and using different commercial organic materials for comparison. Electrical characterization was carried out in terms of current density – voltage and impedance spectroscopy. A simple but efficient encapsulation method serves to significantly improve the better electrical response and achieve longer lifetimes. Optical characterization was carried out in terms of photoluminescence, electroluminescence spectra, luminance and CIE coordinates. Moreover, these measurements were taken during prolonged operation times in order to identify the origin of different degradation mechanisms.

Furthermore, a new and original theoretical model has been developed for conduction in single carrier organic diodes with non-ohmic contacts, taking into account both, charge injection and bulk transport. The main contribution relies on the inclusion of a new term considering the electric field at the interface that accounts for the non-negligible injection barrier. This model has been validated by fitting it to experimental curves with different active layer thicknesses. Information of the active layer material and the device structure such as injection barrier height, mobility and other microscopic parameters have been extracted from the fits. Besides, a small signal model describing the frequency dependence of the admittance in organic diodes with non-ohmic contacts has been reformulated.

Finally, a new technique to pattern the cathode of an organic display based on mechanical ablation has been developed. The experimental set up is based on a computer-assisted commercial equipment that includes a micropositioner and a spring probe. The system is customized to define the display cathode columns by removing the unwanted metal following a previously designed pattern. This technique was successfully implemented to fabricate a 7x5 pixel display prototype.

CHAPTER 1

INTRODUCTION

Contents

1 Introduction 3

1.1 Fundamentals of organic electronics 3

1.1.1 The dawn of organic electronics 4
1.1.2 Electroluminescent organic materials: molecules and polymers 7
1.1.3 Basic PLED/OLED operation principles 9
1.1.4 Advantages and disadvantages of PLED/OLEDs 12

1.2 Novel applications of organic electroluminescent devices 13

1.2.1 Electroluminescent organic diodes with different substrates: flexible OLEDs (FOLEDs) and transparent OLEDs (TOLEDs) 14
1.2.2 Displays based on organic materials 15
1.2.3 OLEDs in solid state lightning 19

1.3 Scientific and technological key issues currently under research 20

1.3.1 Study of conduction mechanisms in organic semiconductors. 21
1.3.2 Study of degradation mechanisms in organic materials. 21
1.3.3 Improving OLEDs efficiency. 22

1.3.4 Study of new electroluminescent materials: blue and white illumination. 22
1.3.5 Development of new technologies for display processing. 24
1.3.6 Driver design for integration in AMOLEDS. 24
1.4 Objectives of this thesis 25
1.5 Outline of this thesis 26

Chapter 1

1 Introduction

The first chapter of this thesis serves as an introduction to organic electronics. It will include a general overview on the subject, the historical development of organic devices, and the main scientific and technological issues currently under discussion. The chapter is organized as follows. Section 1.1 describes the specific features of organic electronics that contribute to turn it into a new discipline within the field of traditional Electronics. Novel applications of organic light emitting diodes (OLEDs) in displays and solid state lighting (SSL) are highlighted in section 1.2. Section 1.3 reviews those technological challenges that are still under research in 2007. Section 1.4 summarizes the three general objectives of this thesis, and finally, a brief outline of this manuscript is offered in section 1.5.

1.1 Fundamentals of organic electronics

Until quite recently, optoelectronic technology has been dominated by inorganic semiconductor materials, specially III-V compounds, and II-VI to a lesser extent. These are covalent crystalline lattices with a residual ionic character, and in the 70s they created a high degree of expectation due to their high carrier mobility (i.e. capacity for a quick response under external fields). Nowadays, their main advantage when compared to Si lies in their direct gap, and they are present in most discrete light-emitting diodes (LEDs), lasers and photodetectors for optical communications and other IR applications, and certain high mobility transistors used for application in extreme conditions (e.g. satellites). Some of the main drawbacks of this technology are: high fabrication cost due to the large industrial complexes necessary for molecular epitaxy, need for specific substrates with similar lattice constants between adjacent layers, and the impossibility to generate flexible and transparent devices.

During the 90s, two new technologic disciplines have come to birth in this area: “Microsystems and Nanotechnology” and “Organic Electronics”. The former has resulted in the introduction of a concept: MEMS (MicroElectronic-Mechanic Systems), combining electronic systems with

micromachines, sometimes of nanometric dimensions. Although still not settled at a mass production scale, they are being increasingly used, mainly as sensors. The new discipline of "Organic Electronics" is the subject of the present thesis.

1.1.1 The dawn of organic electronics

Simultaneous use of electronics and organic compounds is taking place at two different levels:

On one hand, the high variety of geometries and chemical bonds between molecules implies the appearance of some interesting electrical features: anisotropic conductivities, symmetric electrical domains, charge storage and so on, all of which yield the possibility of designing electrical circuits with new properties. This line of research is currently referred to as "Molecular Electronics" and has derived towards the investigation of circuits and devices at a molecular scale (nanodevices) with new properties and applications, and their integration with current MOS Si devices. A review of different electronic applications of molecular size devices is given in [Heath03].

On the other hand, massive organic materials have properties that make them suitable for standard optoelectronic applications. Mainly, their intense luminescence, whose emission characteristics can be easily controlled during synthesis. Currently, there are several materials with emissions that cover the visible range almost continuously, and even some of the UV and IR spectra. This property can be very sensitive to reactivity with other substances, and this has taken polymers to a foremost position in the area of biological and chemical sensors.

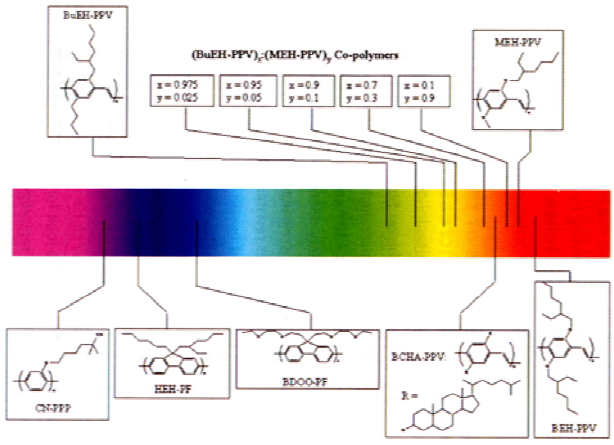

Figure 1.1- Emission spectra of the most commonly used organic materials.

A combination of luminescence and good semiconductor properties opens the possibility of obtaining electroluminescent devices. A new line of work appears: investigation of optoelectronic devices based on organic materials, with advantages such as ease of fabrication and processing thanks to simple and accessible technology, good efficiency and sensing capabilities. Figure 1.1 shows the most commonly used organic materials and their respective emission colour.

Therefore, Organic Optoelectronics is defined as the discipline in charge of studying how to use the properties of certain organic materials and their interaction with light via an electronic interface. It investigates those optoelectronic devices based on molecular materials or polymers: diodes, transistors, solar cells, photodetectors and lightning, as well as applications in the field of sensing and communications, among many others.

This technologic field presents a certain degree of horizontality, i.e., the electronic interface can serve as a necessary link between a number of chemical or biological sensors. It should be stressed that most electronic properties of semiconductor polymers are currently being studied over processed structures. Let us look at an example: traditional mobility measurement methods via Hall Effect are no longer valid since small mobilities and metal-semiconductor carrier injection barriers generate an undetectable Hall tension, so processed devices must be used for that purpose. This means that any collaboration in the field of organic electronics necessarily implies some experience in systematic electronic device processing.

The possibility of associating electronics and organic materials became real in the 1970s thanks to the discovery of some conjugated polymers that could conduct electricity (polyacetilene and others) by Hideki Shirakawa, Alan G. MacDiarmid and Alan J. Heeger, for which they were awarded the Chemistry Nobel Prize of 2000. A very convenient coincidence got Jack S. Kilby, H. Kroemer and Z. Alferov the same years's Physics Nobel Prize for inventing integrated circuits and semiconductor high-speed heterostructures for applications in optoelectronics and communications. In the last two decades, a combination of these two technologies has yielded great advances in the production of devices like those of traditional microelectronics and optoelectronics, but based on molecular materials and semiconductor solid-state polymers. Examples of this convergence can be found in the form of diodes [Tang87], [Tomozawa87], [Saricifti94], light emitting diodes [Burroughs90], [Friend99], photodiodes [Halls95], [Someya05], field effect transistors [Torsi96], [Katz02], [Muccini06], [Kitamura03], light-emitting electrochemical cells (LECs) [Pei95], biosensors [Zhu02],

[Crone02], photovoltaic cells [Yu95], first integrated optoelectronic devices [Sirringhaus98], [Huitema02], [Kitamura03], non-volatile memory cells [Scott07], etc.

The development of each organic device presents a different degree of difficulty. For instance, up to date no electric injection lasers have been achieved over amorphous polymers, although they do exist over certain molecular crystals based on tetracene [Schön00]. However, already in 1987, the first organic light emitting diodes (OLEDs) were made, based on thin molecular films (Alq3) with conducting and luminescent properties [Tang87] and reasonable operating voltages (<10 V), although with very small efficiencies (1%). Soon afterwards, in 1990, semiconductor fluorescent polymers (such as poly(phenilene vynilene) – PPV – and its derivatives, synthesized by a group in Cambridge) started being used as active layer, duplicating efficiency [Burroughs90].

Since then, organic LEDs have been developed, based on small molecules (OLED as such), or on polymers (PLEDs). In this thesis, LEDs based on molecules or polymers are equally named OLEDs, except for those cases where distinction becomes necessary. Molecule-based technology was initially developed by Eastman Kodak™. Generally, it relies on vacuum-deposition techniques (by sublimation), which grants an excellent width control. In contrast, polymers can be deposited by spin coating, an easy and more affordable technique.

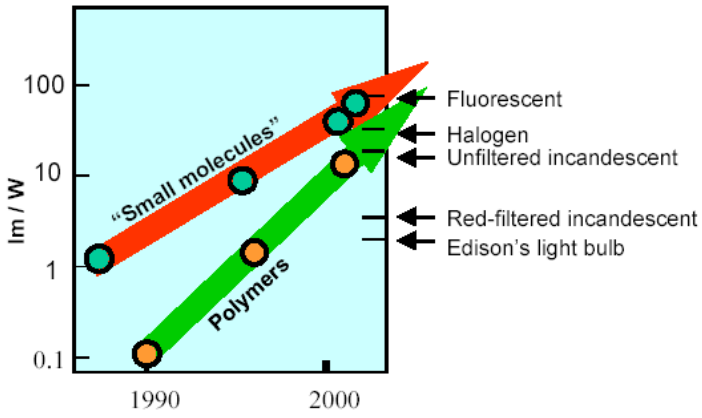

Figure 1.2 - Progression of luminous efficiency of monochrome OLEDs based on molecules or polymers, compared to some already known sources [OIDA02].

As Figure 1.2 shows, the efficiency of molecule-based LEDs is slightly higher than that of polymers, although this does not reflect the total amount of emitted light. It may be observed

that due to a faster evolution of PLED technology, convergence of both lines was expected by the middle of this decade. However, small molecule technology has undergone a greater development than expected due to its prior entrance into the display market. Currently, Asian leading companies such as Samsung and Pioneer are mainly working on molecule technology [isupply].

Technology based on polymers is cheaper, since it benefits from solution manufacturing (spin casting), which allows working in larger areas and using jet printing techniques. Moreover, they remain stable at higher temperatures, and are easier to tune in colour. It should be taken into account that the theoretical quantum efficiency limit is 25% for organic molecules, as derived from intrinsic recombination of doublet/triplet states, while in polymers it can go up to 50% [Wohlgenannt02], this being one of the hottest issues of discussion. Recently, the use of phosphorescent polymers has increased this limit to almost 100% [Tokito03]. Still, ulterior device development has decreased this value significantly. Current values reach 40 lm/W, higher than a bulb (typically 20 lm/W) and close to fluorescents (60 lm/W) [Friend99].

1.1.2 Electroluminescent organic materials: molecules and polymers

First observation of light emission from small organic molecules based LEDs was done by Tang et al, [Tang87], and from conjugated polymer LEDs by Burroughs et al. [Burroughs90]. Organic molecules can be doped to improve their electronic performance and their chemical structure can be modified to tune their optical emission. These materials are amorphous, with mobilities ranging in the order of 10^{-7} cm^2/Vs to 10^{-2} cm^2/Vs depending on their electron affinity and microscopic arrangement. Figure 1.3 shows the chemical structure of some widely used small organic molecules.

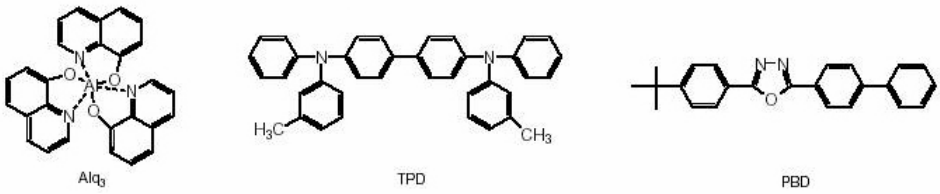

Figure 1.3 - Chemical structure of some organic small molecules used for OLEDs.

Polymers are macro-molecules consisting of a large number of repeating units (monomers), typically hundreds of them. Most polymers are saturated, meaning that all valence electrons of the carbon atoms contribute to single covalent (σ) bonds. This underlying orbital configuration

(sp^3) makes the material an insulator, so these plastics were considered uninteresting as active components for electronic devices. Conducting polymers possess a delocalised π-bonding system along the polymer backbone. It may be recognized by an alternating double-single bond along the main chain. Polymers exhibiting this feature are considered conjugated polymers. This π-bonding favours electron delocalization, conferring semiconducting properties to the polymer, and makes it able to support positive and negative charge carriers with high mobility along the polymer chain. Figure 1.4 shows several examples of conjugated polymers.

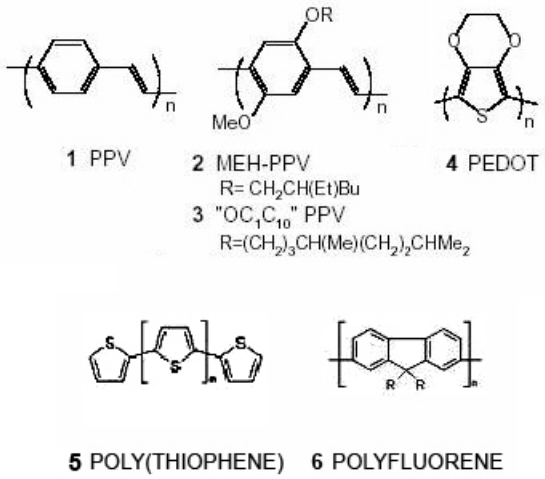

Figure 1.4 - Chemical structure of some conjugated polymers.

More precisely, semiconductor properties of these materials arise from the overlap of two p_z orbitals that originate from the double bonds. If the overlap is over several sites, the formation of well delocalised π (bonding) valence and π* (antibonding) conduction bands occurs, with an energy gap between them, see Figure 1.5. These “bands” are usually referred to as Lowest Unoccupied Molecular Orbital (LUMO) and Highest Occupied Molecular Orbital (HOMO).

Despite band formation, the mechanism for charge transport in these materials is not the same as in traditional inorganic semiconductors. The amorphous chain morphology results in an inhomogeneous broadening of the energies of the chain and in most of cases discrete hops are the dominant way of transport [Coropceanu07].

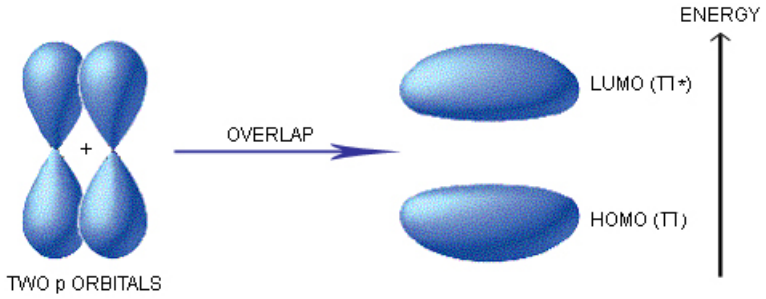

Figure 1.5 - p-orbital overlap to form LUMO and HOMO levels.

Throughout this thesis, especial emphasis will be given to blue emissive polymers. The big energy difference between the HOMO and the LUMO levels usually results in large injection barriers for carriers, and hence the need for significant high voltages to ensure conduction. This turns out in large energy consumption and easy device degradation. Polyfluorene derivatives are well known to be used as emissive layer in blue PLEDs. Chapter 3 of this thesis will explain blue polymers in more detail and electroluminescent devices based on a new polyfluorene derivative will be presented.

1.1.3 Basic PLED/OLED operation principles

Figure 1.6 shows the basic structure of a PLED/OLED. It consists of one or several layers of organic electroluminescent material placed between two metals with very different work functions that act as electrodes (anode / cathode). It should be noted that this is no longer the traditional P-N structure, since each carrier is injected from a different contact. The reason for this is the fact that doping of organic materials can easily degrade emission properties due to non-radiative recombination.

The choice of organic material and the layer structure determines the device's behaviour: colour of emission, lifetime, efficiency, etc.

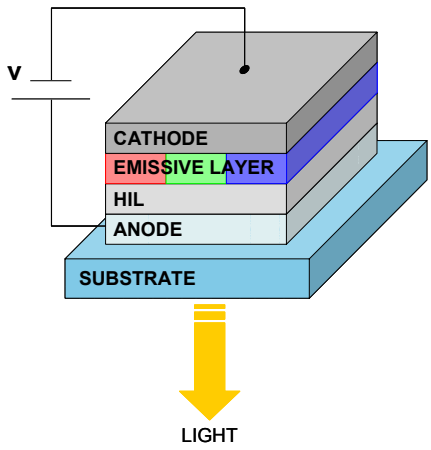

Figure 1.6 - Basic PLED structure.

Three different mechanisms need to be considered in PLED operation: injection, transport and recombination.

When a voltage is applied between the electrodes, electrons are injected from a low work function cathode, typically aluminium (Al) or calcium (Ca), and holes are facilitated from the anode, typically indium tin oxide (ITO). ITO is commonly used as anode due to its optimal combination of low resistivity (typically 10-40 Ω/sqr) and high transparency (> 80% at 560 nm) that allows light out of the device in the front direction.

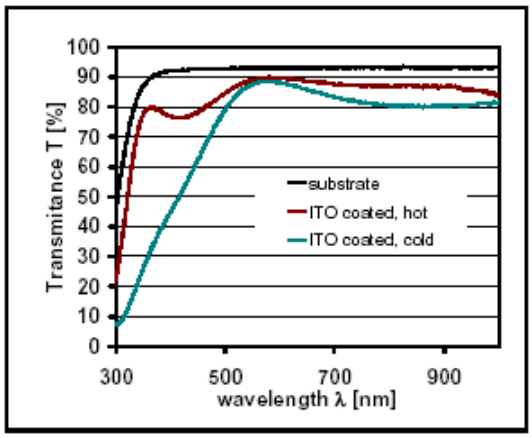

Figure 1.7 - Transmittance of different ITO coated glass substrates fabricated at Fraunhofer.

IPMS (Source: www.ipms.fhg.de/en/products/OMS/ito-coating-e.pdf)

Front emission instead of lateral is another main advantage of organic devices over inorganic ones. A hole injecting layer (HIL) is frequently employed [Crispin03], typically Poly(3,4-ethylenedioxythiophene) poly(styrenesulfonate) (PEDOT:PSS) since it helps conduction along the device and smoothes the ITO surface.

Misalignment between the metal work function (least energy required to remove an electron from the metal surface) and the LUMO/HOMO polymer level is responsible for the existence of an injection barrier at the metal/polymer interface. Generally, metals are carefully chosen to minimize this barrier and facilitate carrier injection. As an example, a commonly used polymer, MEH-PPV, has its HOMO and LUMO levels at 5.3 eV and 2.8 eV respectively. Using an ITO anode and an calcium cathode will result in barriers of the order of 0,5 eV for holes and 0.1 eV for electrons.

Table 1.1 shows work functions of the most frequently used electrodes.

	Au	**Al**	**Ca**	**PEDOT:PSS**	**ITO**
Work function (eV)	-5.1	-4.28	-2.87	≈ -5	≈ -4.8

Table 1.1 - Electrodes work function.

Recombination of carriers can occur via exciton formation that can radiatively decay resulting in light emission. If the amount of positive and negative charges injected in the active layer is not balanced, not all the carriers will combine to form excitons. This is a loss mechanism that produces a decrease of the OLED efficiency. In order to improve charge balance, multilayer structures can be used.

Besides, when recombination occurs, two types of excitons can be formed: singlets, that have a quick radiative decay, and triplets, whose decay mechanism is slow and non radiative. The maximum ratio of singlets to triplets in small molecules is determined by spin statistics to be 1:3. This ratio is a key issue still under research in polymeric materials [Wilson01], and is responsible for a loss in the OLED quantum efficiency.

Another important factor that decreases the efficiency is attributed to exciton quenching mechanisms. If mobilities of both carriers are very different, recombination takes place near one of the electrodes, where interface dipole fields and trapping effects may cause the quenching of radiative recombination.

Figure 1.8 shows a schematic of the OLED operation.

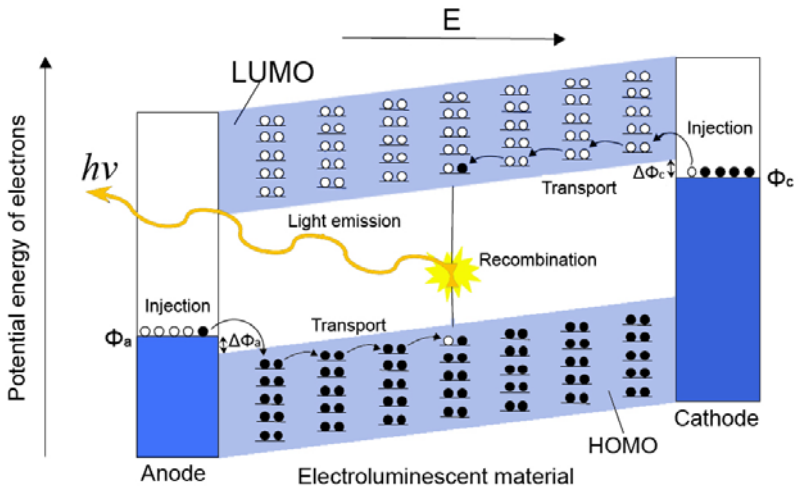

Figure 1.8 - Light emission diagram for an OLED.

At this point it is worth mentioning some aspects about carrier transport. Polymeric materials are amorphous. This means that the monomer chains bend, acquiring forms that differ from a straight shape and forming what could be referred to as disordered polymeric balls. This chain morphology results in an inhomogeneous broadening of the energies. Moreover, an injected charge causes a local configurational change in the chain structure. The ultimate consequence of this morphology is that conduction mechanisms can no longer be explained by traditional inorganic band theory. Instead, carrier transport across organic materials occurs via hopping between localized states. In this sense, works by Bassler et al [Bassler93], [Arkhipov98], [Arkhipov01APL], [Arkhipov03] have been of great importance to understand the electrical behaviour of these materials. Chapter 4 of this thesis takes a close look into the study of OLEDs' conduction mechanisms.

1.1.4 Advantages and disadvantages of PLED/OLEDs

The main advantages of OLEDs when compared to inorganic devices are:

- Frontal emission pattern, i.e. better pixel integration.
- Ultra thin, lighter, flexible, and in some cases semitransparent.
- Possible to make over any substrate, even large area and irregular ones.
- More readily accessible technology and lower production costs.
- RGB achievement with the same technology.

Also, OLED based displays present several advantages over their TFT-LCDs counterparts:

- Self-luminous active devices, i.e. no need for a back light source, resulting in smaller size, lighter, less energy consumption and more affordability.
- High brilliance and contrast (>1000:1), even in extreme illumination conditions.
- Wide vision angle, up to 165º.
- The spectra they can reproduce covers 75% of the visible range as opposed to typical values of 40-60% for TFT-LCD.
- Quick response, in the order of microseconds, much quicker that liquid crystals.
- High capacity of integration, therefore high resolution.

The main disadvantages of OLEDs are currently under investigation:

- Two-fold degradation: sensitivity to environment, and reaction with oxygen and moisture (especially with current going through).
- Moderate photostability: sensitive to UV.
- Low carrier mobility, in the order of 10^{-2} to 10^{-7} cm^2/Vs.
- Moderate thermal stability: vitreous temperatures of around 100º C, degradation temperatures of around 200-300 ºC.
- Tendency to autoquenching of photoluminescence, important drawback for lasers.

In relation to the low luminous efficiency, recent advances in new OLEDs based on phosphorescent materials (PHOLEDs) are reaching efficiencies close to 100% [Brown04], [Zhou05].

1.2 Novel applications of organic electroluminescent devices

As mentioned in section 1.1.1, along the past decades, optoelectronic devices based on organic materials, such as diodes, transistors, solar cells, photodetectors, lightning and sensors, have been under great research. This section will be focused on most recent achievements in the organic light emitting device market. These applications embrace organic displays over flexible and transparent substrates, large area panels and environmental lightning.

1.2.1 Electroluminescent organic diodes with different substrates: flexible OLEDs (FOLEDs) and transparent OLEDs (TOLEDs)

In the late 90's a leading company in OLED technology, Universal Display Corporation (Princeton, USA), introduced the concepts of FOLEDs (OLEDs over flexible substrate) and TOLEDs (OLEDs over transparent substrate) [universaldisplay].

Figure 1.9 - FOLED (Universal Display Corporation™)

FOLEDs allow the final device to change shape without losing its electroluminescent properties. Most commonly, metal and plastic laminated materials are used as substrates. Figure 1.9 shows a picture of a FOLED manufactured by Universal Display Corporation.

There is a great variety of flexible plastic substrates [Lewis04], although not all of them are totally impermeable to oxygen and humidity. In order to avoid this problem, barrier films are attached to the substrate. These barriers must be capable of enduring mechanical deformation. Several oxides are used, for example, SiON, which meets both requirements for impermeability and the necessary transparency not to compromise the OLED's light emission. Reference [Yoshida01] shows the development of a flexible, 3-inch colour display with 256 levels of greyscale, 0,2 mm thickness, weighing 3 g, and with a luminance of 70 cd/m^2. Regardless of the advantages mentioned earlier, several companies have already developed display prototypes based on FOLEDs. Lifetimes range between 3000 to 6000 h, and initial luminance between 425 and 1000 cd/m^2 [Yoshida01], [Weaver02], [Sugimoto04].

All degrees of flexibility are considered, from devices that can be slightly deformed to those that can be completely folded. This makes them especially suitable for portable devices due to their high impact resistance (laptops, etc.). The potential application market is huge: biosensors, electronic paper, identification tags, or any video screen adaptable to clothing or any type of instrumentation (aircraft cabins, car dashboards, etc.) or any irregular surface.

Figure 1.10 - Ultra thin flexible OLED (Philips Research Laboratories)

An example of a very recent technology is a new technique developed by Philips Research Laboratories to achieve ultra-thin flexible organic light emitting diodes. Through the use of the Electronics on Plastic by Laser Release (EPLaR) technology, they have developed and demonstrated 18 μm thick single-pixel OLEDs [Lifka07].

In this case, the OLED fabrication process is carried out on top of a polyamide attached to a thin glass using standard fabrication techniques. Once the OLED fabrication is completed, the device is released from the glass using a laser, leaving the polyamide as the only substrate. Figure 1.10 shows a fully operational 6 cm x 8 cm OLED of 18 μm thick fabricated with this technique.

As mentioned above, another possible OLED feature is semitransparency. TOLEDs can reach tranmittances of around 70-80% when they are off (close to the glass or plastics acting as substrates) with uses in virtual reality, medical or industrial applications.

Figure 1.11 - TOLED (Universal Display Corporation™)

Recently, researchers at Universal Display Corporation have set a record in TOLED resolution, reaching a value of 200 dpi [physorg]. Figure 1.11 shows a picture of a TOLED.

1.2.2 Displays based on organic materials

Most desirable applications for OLED technology are ultra-light TV screens, flexible displays (electronic paper), and ambient lightning panels. Television does not require a very high

resolution, but good colour definition, wide vision angle and high contrast, all of them typical OLED features.

Until the 90s, the TV market was largely dominated by CRT (Cathode Ray Tube) technology. This type of screens has attained a high degree of quality and excellence, thanks to technologies like Invar, Trinitron, etc, but they still suffer from an excessive weight, size and energy consumption. The great advances of Information Technology (IT) and Communications, together with the worldwide spread of Internet use, and a high demand for portable, light-weight and small size devices increased the interest on flat screens (FPDs, Flat Panel Displays). The first technology to answer this demand was LCDs (Liquid Crystal Displays), which covered all types of small portable equipment. Meanwhile, during the 80s, PDP (Plasma Display Panel) technology appeared on the TV market in competition with CRTs. PDPs work with small fluorescent valves with high brightness and contrast, but low resolution. Lately, LCDs are taking over PDPs also in the field of big displays, mainly due to the reduction in costs caused by the use of a single technology regardless of the size and type of monitor.

Therefore, liquid crystals have formed the basis for a range of technologies capable of fabricating a large number of screens, from small watch-size displays to large TV monitors, with a growing market quota (55000 mill $ in 2004). Table 1.2 shows that the evolution of LCD market is one order of magnitude higher than that of OLEDs.

OLED vs LCD	**2003**	**2004**	**2005**	**2006**	**2007**	**2008**	**2009**	**2010**
LCD (M$)	37399	54643	66497	73659	79124	84104	NA	NA
OLED (M$)	246	429	772	1369	1829	2255	2657	3273

Table 1.2 - Market and expectations for LCDs and OLEDs [issuply].

At present time TFT-LCD technology is much more advanced than OLED's and they dominate the flat panel display market. However, LCD's efficiency is by no means optimal. Liquid crystals are polarized light filters, and as such, they are passive devices and therefore need a back light source. In this sense, OLEDs are an effective alternative that overcomes all LCDs drawbacks. Their main current flaw is that they do not have an adequate mean lifetime / intensity ratio for certain commercial applications, especially white illumination. However, OLEDs displays are beginning to enter the market in portable applications such as mobile phones, mp3 players and other small devices that do not require long lifetime displays. The

future of OLED technology is promising. Predictions state that by mid 2010s organic displays might seriously compete with LCDs [Young05].

OLED based displays can, in turn, be divided in two types, depending on how the pixels are driven:

a) Passive matrix OLED (PMOLED). In order to create a passive-matrix display, the electrode material has to be deposited in a row-column matrix. An OLED is formed at each intersection point of the matrix, as Figure 1.12 right shows. Illumination of each OLED (i.e. every pixel) is obtained by driving the appropriate row and column. Therefore, to create a video image, all rows and columns have to be scanned so that all pixels necessary to form each frame are quickly turned on and off. Approximate refresh time of an entire screen is adapted to human vision and is around 1/60 seconds. Therefore, with increasing display size and thus pixel number, the scan rates are quicker and the time the pixel is in the ON state shortens. This leads to an inherent reduction of brightness that must be compensated with a higher pixel illumination. Furthermore, column and row lengths usually cause voltage drops, which make driver design more difficult. This trade-off between size and illumination limits PMOLEDs performance and restricts them to small displays.

b) Active matrix OLED (AMOLED). Active-matrix displays use thin film transistors (TFT) to drive each pixel, see Figure 1.12 left. Every OLED cell is controlled by at least two transistors, though more complex designs are currently under research [Ashtiani07], [You07]. All transistors in the array are individually addressable in a row/column format. Unlike the passive-matrix display, transistor circuits retain the state (on/off) and level (intensity) information programmed by the display driver. Therefore, the light output of every pixel is controlled continuously, rather than being "pulsed" with high currents just once per refresh cycle.

Active-matrix displays are considerably more expensive than passive displays, but they boast brighter, sharper images and use less power. Monochrome displays are generally of the passive type. Full-colour displays may be either active or passive. Similarly to other display technologies, the full colour spectrum is generated by modulating individual red, blue and green OLED cells that form subpixels, positioned side-by-side. AMOLEDs consume less energy and are adequate for larger areas.

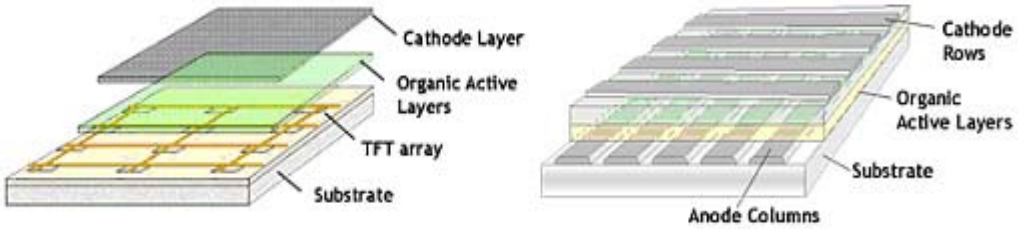

Figure 1.12 - AMOLED (Left) and PMOLED (Right) structures.

Figure 1.13 shows predictions of OLED display technology from 2003 to 2011. The graph shows a comparative between passive and active matrix technologies. By the beginning of next decade AMOLED would start dominating the organic display market.

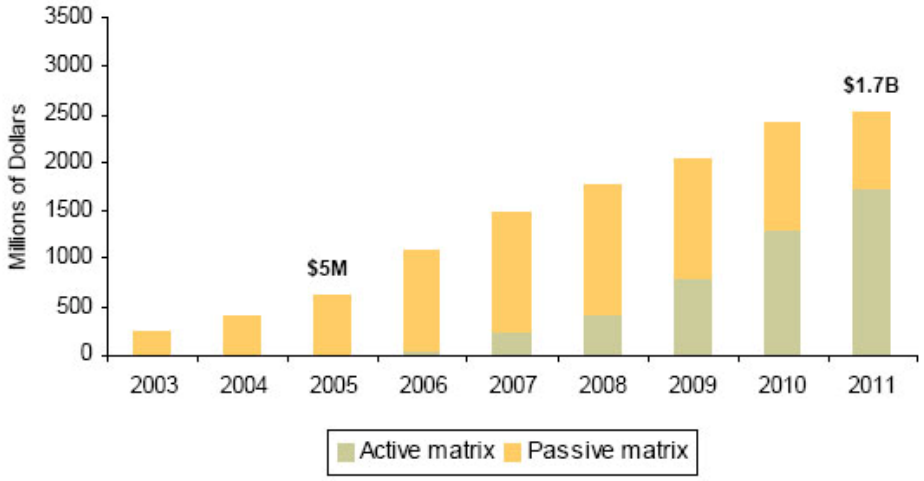

Figure 1.13 – PMOLED/AMOLED market evolution [isupply].

An example of the present state of the art is given by Sony Japan. They fabricated a 27.3-inch active matrix OLED display using a novel laser transfer technology for manufacturing large-sized organic OLED displays [Hirano07]. In this case, OLED materials are transferred from glass donors to a substrate by laser-induced pattern-wise sublimation (LIPS). This is a thermal transfer process. RGB pixels are precisely patterned by LIPS. Figure 1.14 shows the final display using LIPS technology.

Figure 1.14 - 23.3 inch active matrix OLED display (Sony Japan)

1.2.3 OLEDs in solid state lightning

At present time solid state lighting (SSL) is beginning to take over conventional lighting technologies, especially as far as flashing indicators are concerned. According to the US Department of Energy, by 2025 SSL efficiency would be one order of magnitude higher than incandescent lamps and double of fluorescent tubes [Brodrik07], see Figure 1.15.

OLEDs and LEDs are much more efficient than traditional incandescent light sources; in fact, they can reach similar values to those of fluorescent tubes. Brightness of a typical fluorescent tube is approximately 2000 cd/m^2, but for a 2-D source, the estimation is that 800 cd/m^2 would be enough for a good quality illumination [U.S. Department of Energy01]. The possibility of extending the light source to wider areas, and tune the colour brings in a new concept of ambient lightning [U.S. Department of Energy]. These panels are better for the environment, since they could save approximately 50% of all energy spent on illumination [US Department of Energy03].

In the context of solid state lightning, great effort is being made to develop efficient, long lifetime white OLEDs (WOLEDs). Due to their great interest, WOLEDs will be studied in section 1.3.4.

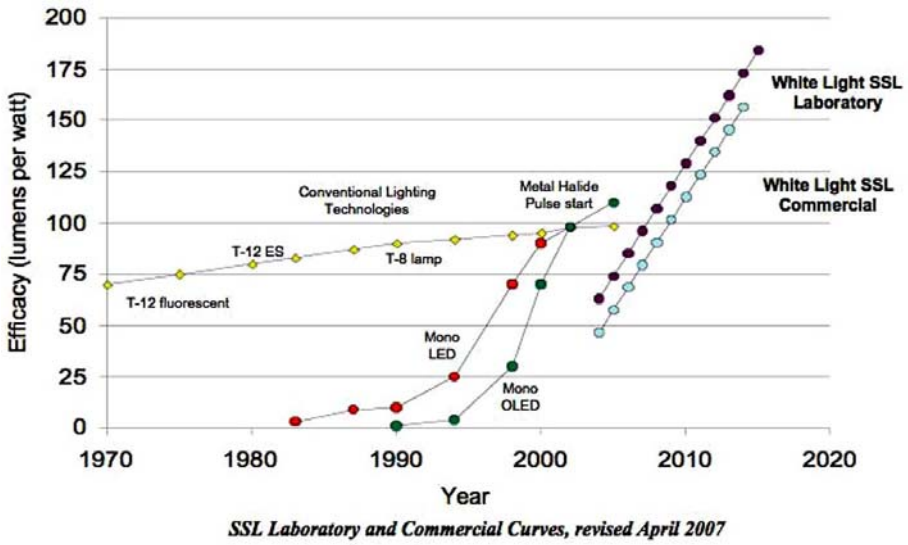

Figure 1.15 - Increase in efficiency of SSL with respect to traditional lightning tech. [Brodrik07]

Table 1.3 shows a comparison among several lightning devices performances.

	Efficiency (l/W)	Brightness (cd/m2)	Lifetime (h)
Bulb	<20	--	750-2500
Fluorescent tube	60	2500	>10000
Fluorescent Bulb	90	>2500	>10000
Green OLED	80	1000	10000
White OLED	≈10	300	300

Table 1.3 - Efficiency and brightness data for several conventional light sources [OIDA02]

1.3 Scientific and technological key issues currently under research

Though technology is progressing quickly due to the interest in commercial applications, numerous scientific questions remain unsolved. Their answers should feedback these technological advances and improve devices, opening paths for new ideas.

Nowadays, a great effort is being made by the scientific community to gain a deeper insight of a series of key points in relation with organic semiconductor based devices. Below, some of them are summarized.

1.3.1 Study of conduction mechanisms in organic semiconductors.

When studying conduction in organic materials, two regimes need to be defined: carrier injection from the electrodes into the organic layers and carrier transport along the bulk.

Injection mechanisms in organic materials have been so far based either on a classical approach, e.g. the thermionic effect, where a Richardson-like constant needs to be defined [Scott99], [Davids97], or on a microscopic approach of carrier hopping between discrete states. Within the latter approach, an analytical model for the injection current density including both structural and energetic disorder was proposed in [Arkhipov98].

Carrier transport in organic materials is not described using band theory as in inorganic semiconductors, but instead, is closer to the way a charge would behave in an insulating material. In insulators with ohmic contacts, charge is accumulated inside the bulk and current in the device is limited by this effect, referred to as SCLC (Space Charge Limited Current). In this situation, the current – voltage characteristic is given by the Mott-Gurney expression [Mott48]. Mobility in such materials is affected by a hopping barrier between adjacent sites, resulting in an effective dependence on the applied electric field (Poole-Frenkel formulation).

$$\mu \propto \mu_o \exp\left(\sqrt{E}\right)$$

Recent studies have also stated the intimate dependence of mobility with the non-neutral injected charge [Pasveer05]. Still, a great amount of work at microscopic level needs to be made.

1.3.2 Study of degradation mechanisms in organic materials.

It is well known that oxygen and moisture generate non-reversible changes in the chemical structure of organic electroluminescent materials. This type of degradation induces loss of luminance efficiency during operation and forces the use of packaging techniques in inert atmosphere for sample preservation [Lewis04].

Degradation is associated with the accumulation of non-radiative centres and luminescence quenchers in the radiative zone, but degradation mechanisms have not well identified yet.

Moreover, it is believed that the incidence of UV light when the device is under electrical operation tends to enhance these degradation processes. Many studies in the chemistry field are currently being carried out to get a better understanding of these mechanisms and to obtain new organic electroluminescent materials with better lifetimes [Kondakov07], [Klubek07], [Royster07].

1.3.3 Improving OLEDs efficiency.

There are various mechanisms responsible for the loss of efficiency:

First, the unbalanced injection of electrons and holes in the device prevents carriers from recombining (γ). New multilayered structures are currently under research to balance charge injection [Patel02]. Second, not at all excitons become singlets recombining in a radiative way, some become triplets that find non-radiative paths (r_{st}). Phosphorescent materials have been demonstrated to improve quantum efficiency from both singlet and triplet excitons [Gong03-a] and are successfully used for white emission. Third, not all singlet excitons decay radiatively. This loss in efficiency is related to the intrinsic photoluminescence efficiency of the organic material, as well as quenching mechanisms (q). Fourth, some of the light generated in the device is unable to escape, introducing another loss factor usually referred as to output coupling ($\eta_{coupling}$). In conclusion, external efficiency (EQE), $\eta_{ext,}$ may be formulated as

$$\eta_{ext} = \gamma \times r_{st} \times q \times \eta_{coupling}$$

These losses can be improved by using heterostructures with multiple function layers (injection/transport layers, blocking layers…). Besides, in order to improve output coupling, structures such as photonic crystals can be used [Fujita03].

As an example, scientists at Pacific Northwest National Laboratory have created an OLED with external quantum efficiency of 11% at 800 cd/m^2 [PNL]. This achievement is particularly notable since it was accomplished at a much lower operating voltage (6.2 V) than previous demonstrations using similar structures.

1.3.4 Study of new electroluminescent materials: blue and white illumination.

Chemist scientific community is employing a lot of effort to develop more efficient organic compounds (both small molecules and polymers). Special emphasis is given to develop blue

organic electroluminescence materials with high efficiency, deep blue colour and long operational lifetime [Ho07]. At present time, blue is the limiting colour to obtain white OLEDs (WOLED) with acceptable efficiency. Highly efficient deep blue emission is more difficult to achieve due to its intrinsic wide bandgap. This usually requires higher bias which in turn increases degradation and reduces lifetime. Figure 1.16 shows luminous efficiency and lifetime of the three fundamental colours.

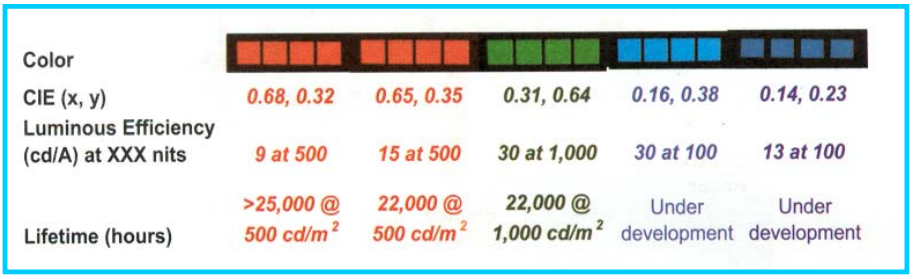

Figure 1.16 – Efficiency and lifetime for RGB based on OLEDs [Ghosh04].

On the other hand, WOLEDs are crucial to develop large area displays [Chu07] and to be used as backlight for other display technologies over rigid or flexible substrates [Forrest07]. Besides, they offer the opportunity to provide high-efficiency solid-state lightning at low cost. There are two main strategies to fabricate WOLEDS. The first one is based on the evaporation of several layers of small organic molecules, each one emitting one primary colour [Nakayama07]. This technology is more appropriate for small display applications. The second one uses monolayer devices with the active layer being a blend of several emissive organic compounds [Huang06]. Especial attention needs to be paid to the relative concentration of the materials forming the blend and the charge interactions among them. Recently WOLEDs using non conjugated polymers such as poly(N-vinilcarbazol) (PVK) doped with phosphorescent pigments have been reported [Kim06]. In these structures, both singlet and triplet excitons, contribute to light emission increasing the luminous efficiency, however they require high operating voltages due to charge capture phenomena. Mono-layer WOLEDs present several advantages as opposed to heterostructures: more stable, reproducible and easy fabrication. However, few single component materials are known to be white self-luminous [Liu06], [Fang-Iy07].

1.3.5 Development of new technologies for display processing.

The main techniques used to fabricate screens based on organic materials are photolithography, jet printing and recently laser ablation. Photolithography is widely used to design the display anode below the micron range. However, traditional photolithography is not suitable to pattern the cathode since the chemicals involved in the technique may degrade the organic layers. In this sense, new techniques based of photolithography to define the cathode using cathode separators ("pillars") are studied in chapter 5 [DeFranco06], [Huang 04]. However, these techniques require clean room environments, and include the use of accessories such as shadow masks and additional equipment, which increases dramatically the cost of production. Jet printing makes use of the fact that many organic compounds used in fabrication can be solution-processed and therefore can be deposited in the same way as ink [Bale06]. The main advantage of this technique is that it can be scaled to big area substrates. Using jet printing, the polymer is deposited over substrates that have been pre-patterned. In this way, fabrication steps and costs are reduced, and control via CAD on a PC platform enables easy implementation of different designs. The main drawback of this technique is that its resolution is limited to tenths of micron [DeFranco06], so it is oriented towards fabrication of medium to big size displays (PC monitors, TV, etc.). One of the companies leading jet printing processing is Cambridge Display Technology (CDT). Interesting information about advances in this field may be found at [cambridgedisplay].

1.3.6 Driver design for integration in AMOLEDS.

OLED displays are current-controlled display devices, in contrast to LCD displays which are voltage-controlled. In order to properly address all pixels of a display, multiplexing is necessary. Rows are scanned one by one, by the common drivers. Each pixel can be modelled as a capacitor in parallel with a diode. This parasitic capacitor requires a pre-charge (voltage drive) before current drive. Before the pixel voltage reaches the diode threshold voltage, there is no current flowing through the diode and the pixel is dark. If the capacitance is large, the pixel is off for a long time until the pixel voltage is above threshold. Resulting from this, the pixel becomes dim and its brightness is difficult to be controlled. By applying pre-charge, pixel voltage reaches the target level quickly, and the diode current flows at the desired level. One of the major circuit design challenges is to achieve highly uniform output currents. Both circuit design and layout topologies are critical to minimize the output current

variation. In this sense a lot of circuitry research is being carried out by the display industry [Lee07], [Chaji07].

1.4 Objectives of this thesis

a) The first objective of this thesis is to fabricate and study blue emitting PLEDs that use a derivative of polyfluorene as active layer.

This new blue material, synthesized in IBMC-UMH *(Instituto de Biología Molecular y Celular, Universidad Miguel Hernández)* [Mallavia05], has promising fluorescent properties. Firstly, single carrier structures will be fabricated in order to verify the diode electrical behaviour, i.e., current density-voltage (J-V) and impedance-frequency (Z-f) characteristics. Conventional fabrication techniques (e.g. spin coating, photolithography, metal evaporation, etc.) will be adapted to produce multilayer structures that help carrier injection (including hole injection layers). Besides, encapsulation techniques will be developed to isolate the device from external agents, oxygen and moisture, prolonging the operation lifetime. Secondly, emissive properties of blue emitting OLEDs will be characterized. In the case the case of blue emission, a difficulty arises from the big energy difference between the HOMO and the LUMO levels. This normally means large injection barriers for carriers, and hence the need for excessively high voltages to ensure conduction, which in turn increases both energy consumption and device degradation. In this sense, the evolution of the emission spectra under prolonged operation will be studied in order to track the origin of the degradation mechanism.

b) The second objective is to propose a complete conduction model including both injection and transport simultaneously and to verify it with experimental J-V curves and impedance spectroscopy.

In practice, current limitation of a device is rarely a consequence of only one of the limiting mechanisms (injection or transport) mentioned in section 1.3.1. Both are normally present and are responsible for current limitation. Existing models that simulate diode behaviour in this intermediate regime are complex and time consuming [Arkhipov03].

An objective of this thesis is to propose a new strategy to simulate diode J-V characteristic, by means of analytical expressions for the interface electric field that simplify the numerical computation. On this basis, an exhaustive study of the material's properties, as well as the conducting properties of the multilayer structure is to be performed. The main goal is to obtain a conduction model that takes into account a non negligible potential barrier at the interface.

This results in a new expression for the space charge current containing a new term accounting for the electric field at the interface. Combining this expression with the injection model from Arkhipov et al [Arkhipov98], a complete model will be fitted to experimental values with very small errors in the J-V curve. Also, an impedance study will be performed in these devices in the frequency domain, based on the models proposed by [Martens99] and [Tsang06]. Likewise, Z-f curves will be fitted. From those fits to experimental J-V and Z-f curves, the parameters that describe the material and the structure's behaviour will be obtained.

c) The third objective of this thesis is the fabrication and characterization of 7x5 passive matrix displays using a new method for cathode patterning.

When it comes to organic display processing, the most difficult step lies on cathode patterning, since it is the top layer above the most sensitive organic films. Jet printing is the most used technique to fabricate displays based on polymeric materials. This technique allows direct patterning of the active layers and manufacturing to be scaled to big area substrates. However, resolution is limited to tenths of microns and expensive equipment is required. On the other hand, photolithography is not suitable to pattern the cathode layer, since it involves the use of chemicals that may degrade the optical properties of the organic layers underneath.

In this thesis a 7x5 alphanumeric display is fabricated, using photolithography in the anode and a new technique based on mechanic ablation for the cathode patterning. The main advantage of the latter is the reduction in the number of intermediate steps and hence a reduction in fabrication time and costs.

1.5 Outline of this thesis

Chapter 2 presents the clean room and describes the experimental equipment employed in the fabrication process. PLED fabrication and characterization procedures are described in detail.

Chapter 3 starts with an introduction of polyfluorene (PF) materials with blue and their application to PLEDs emitting in the blue spectral range. Fabricated structures based on a new polyfluorene derivative are presented together with their electrical and optical characterization. JV curves are presented comparing diodes based on different emissive materials and with different active layer thickness. Degradation mechanisms in polyfluorene are their main drawback when using these materials as active layers in PLEDs. These mechanisms are also

identified in our diodes and analysed in terms of morphological changes occurring in the material when interacting with environmental agents.

Chapter 4 reviews all theoretical models proposed in literature to study both, charge injection and carrier transport, in organic devices. The model proposed by Arkhipov et al. [Arkhipov98] for carrier injection in an organic device is taken as basis to study our structures. A new approach to understand electrical conduction in the DC regime for organic devices in the presence of injection barrier, in which no previous assumptions related to injection or bulk limiting mechanisms, is proposed. By fitting this model to experimental J-V curves structure and materials parameters are obtained. Besides, small signal models proposed in literature are reformulated to include the presence of injection barrier, and it is used to extract mobility and material disorder parameters by fitting to impedance spectroscopy measurements.

Chapter 5 studies the different technologies to define the pixel in passive matrix organic displays. A new method is proposed to pattern the cathode using mechanical ablation. Advantages of this new method are reduction in fabrication steps and production costs.

In chapter 6 most relevant conclusions of this thesis are presented.

CHAPTER 2

FABRICATION AND CHARACTERIZATION TECHNIQUES OF PLED PASSIVE MATRIX

Contents

2 Fabrication and characterization techniques of PLED passive matrix 31

2.1 Experimental equipment 31

2.1.1 Fabrication equipment 31
2.1.1.1 Ultrasound cleaning bath 32
2.1.1.2 Spin coating system 33
2.1.1.3 UV lamp and alignment mask system 33
2.1.1.4 Thermal evaporator 34
2.1.1.5 Glove Box 35
2.1.2 Characterization equipment 36
2.1.2.1 Profilometer 36
2.1.2.2 Semiconductor parameter analyzer 37
2.1.2.3 Impedance analyzer 38
2.1.2.4 Spectroradiometer 38

2.2 PLED passive matrix fabrication procedure 39

2.2.1 General procedure of PLED passive matrix fabrication 40
2.2.2 Relevant steps in PLED fabrication procedure 42
2.2.2.1 Glass cutting and cleaning 42
2.2.2.2 Anode patterning 43
2.2.2.3 Diode geometry definition by photoresist wells 44
2.2.2.4 Polymer layers deposition 46
2.2.2.5 Cathode evaporation 48
2.2.2.6 Encapsulation and wire soldering 49
2.3 Thickness calibration 50
2.4 Electrical characterization techniques 51
2.4.1 Current-voltage 51
2.4.2 Admittance spectroscopy 52
2.5 Optical characterization techniques 53

Chapter 2

2 Fabrication and characterization techniques of PLED passive matrix

In this chapter, PLED fabrication and characterization techniques used in this thesis will be introduced. In section 2.1 the most relevant experimental equipment will be presented. In section 2.2, PLED matrix fabrication procedure will be described in detail, paying special attention to each individual step. Even though in some of the cases standard fabrication techniques are employed, they will be carefully described in the context of polymer based device fabrication. Thickness calibration procedure will be explained in section 2.3. Finally, both electrical (section 2.4) and optical (section 2.5) characterization techniques will be presented.

2.1 Experimental equipment

2.1.1 Fabrication equipment

All fabrication steps except for encapsulation were carried out in the clean room of the Liquid Crystal Group at the *Escuela Técnica Superior de Ingenieros de Telecomunicación, (Universidad Politécnica de Madrid)*. Thanks to this group, which kindly let us use their equipment, we fabricated our first PLED passive matrix in 2004. The clean room is composed of two different areas separated by plastic walls, both having nitrogen and distilled water supply systems. Figure 2.1 shows a schematic of the clean room.

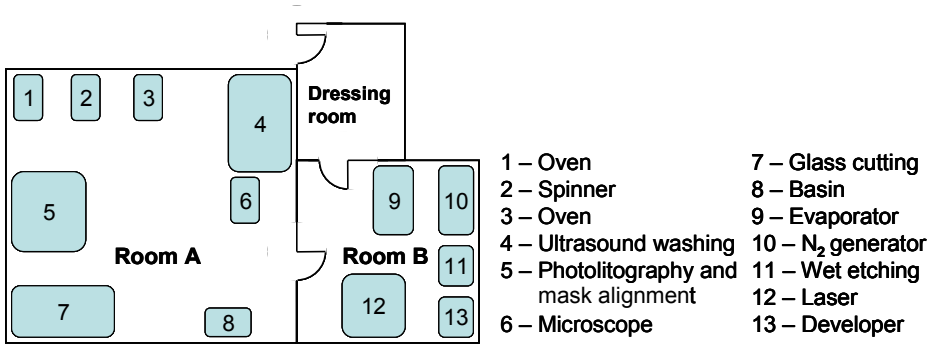

Figure 2.1 – Clean Room. Liquid Crystal Group, ETSIT, UPM.

Under optimal conditions room A is "class 100". The air is injected from the outside into room B through an ASHRAE pre-filter with efficacy 65%. Before entering room A, it goes through a second absolute filter, HEPA with efficacy 99.9%. The air is driven forward into the room by four fans that produce a laminar flux of 0.33 m/s. An overpressure is created in room A that produces an air flux from B to the outside.

The most relevant clean room equipment used in the fabrication process is listed below.

2.1.1.1 Ultrasound cleaning bath

The ultrasound cleaning equipment is embedded into a laminar flux area trademark TELSTAR, so that vapours of cleaning solutions can be easily absorbed. The laminar flux cabin is connected to a water purification system (ELIX) with a 60 litres storage capacity.

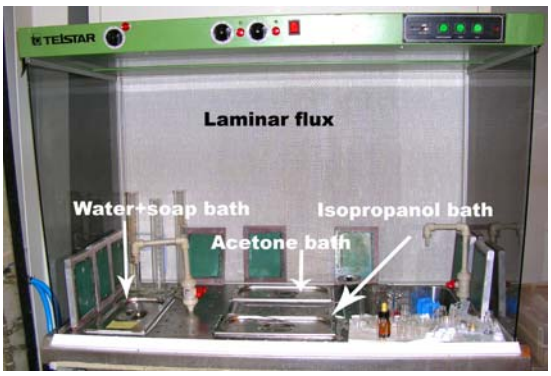

The cleaning system is composed of three ultrasound tanks with individual heaters and a capacity of 6 litres each (Ultrasons-H, J.P. SELECTA). The 40 kHz ultrasound waves mechanically spread along the tanks generating low pressure microscopic bubbles that clean the samples at molecular level.

Figure 2.2-Laminar flux cabin and ultrasound tanks

The system includes a switch-timer that controls the timings of the cleaning periods.

2.1.1.2 Spin coating system

Standard spinners present three relevant characteristics to control the spin coating process:

- Initial velocity slope. Time to reach the target velocity from the starting point.
- Spinning speed or angular velocity, usually measured in r.p.m.
- Spin-off interval. Time to hold a constant speed before stopping.

Current digital controls allow to program different speed profiles and slowing down processes, though these features are not generally relevant to obtain a good quality film. Our spinner can reach a maximum speed of 10700 rpm for up to 120 seconds. The initial ramp is fixed by the internal engine at 2000 rpm/s approximately. Lower slopes may be achieved manually.

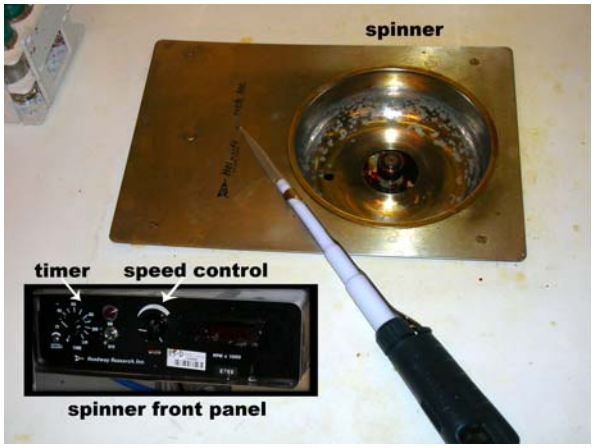

The start/stop is controlled by a pedal. A rubber washer on the peripheral edge of the spinner chuck holds the sample and avoids thermal contact with the metal rotor. Vacuum is applied to the space between sample and chuck to assure the sample is fixed while rotating.

Figure 2.3 – Spinner.

2.1.1.3 UV lamp and alignment mask system

Photolithography is carried out with a OAI Hybralign TM Series 400 Mask Alignment and Exposure system (see Figure 2.4).

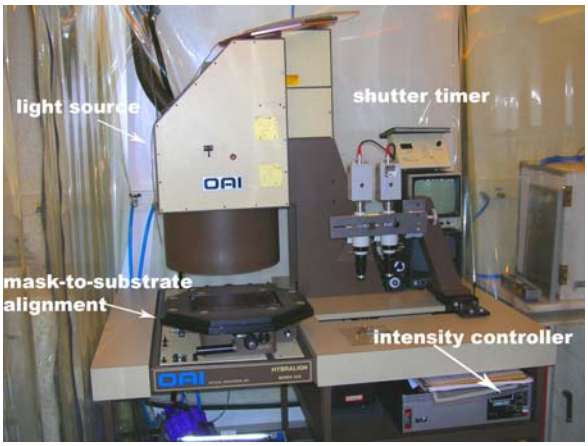

Figure 2.4 - Hybralign TM Series 400 Mask Alignment and Exposure system.

The equipment consists of a console that holds the Mask-to-Substrate alignment stage, viewing optics, transport assembly, light source, intensity controller and exposure monitor. The alignment stage posses a XYZ micrometer that can be adjusted via micrometric screws to align the mask and the sample with high accuracy.

The console that holds the alignment system is connected to a vacuum pump so that the sample is fixed while being aligned and transported from the alignment stage to the expose position. The mercury UV light source of 450 watts can illuminate an area of 16 inch diameter. The shutter timer enables to program the exposure time from 1 to 999 seconds

2.1.1.4 Thermal evaporator

Metals for the OLED cathode are evaporated with a Vacudel 300 (TELSTAR) Joule-effect evaporator, composed of a stainless steel chamber and connected to two vacuum pumps capable of generating a vacuum of 10^{-7} Torr. Crucibles (baskets) containing the material to be evaporated are fixed to electrodes inside the chamber. Target samples are placed on top of the chamber facing the baskets. These are most likely made of tungsten or molybdenum, whose melting point is considerably larger than that of the material to be evaporated. Crucibles support an electric current up to 150 A, and the desired material is evaporated by Joule effect. The evaporation can be controlled by a shutter that can be placed on top of the basket blocking the evaporation path. The evaporator incorporates a quartz crystal monitor system that measures the evaporated material thickness using the material density and a Z calibration factor. The evaporator is shown in Figure 2.5.

Figure 2.5 - Evaporator Vacudel 300 (Telstar).

2.1.1.5 Glove Box

Encapsulation is carried out in a MBRAUN UNILAB glovebox at the Chemistry Department of the Universidad Rey Juan Carlos. It includes a single H_2O/O_2 purifier unit to provide an inert atmosphere with less than 1 ppm H_2O/O_2 purity and a gas circulation capacity greater than 50 cubic feet per minute (cfm) at ΔP = 60 mbar. The glovebox is connected to a 10 c.f.m vacuum pump.

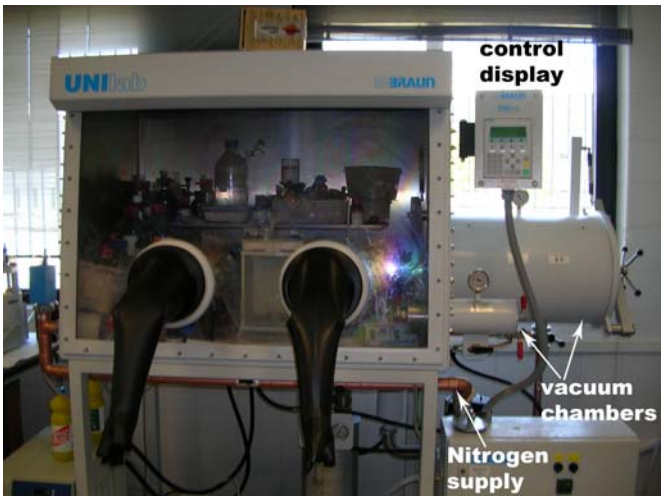

The glovebox dimensions are 1200x780 mm^2 with an antechamber size of 390x600 mm^2. It is made of stainless steel and is currently filled with nitrogen. It includes a digital Siemens control system with touch screen monitor.

Figure 2.6 - Mbraun Unilab Glove Box

2.1.2 Characterization equipment

Characterization tasks were carried out in different research facilities in Madrid. Profilometry was measured at the *Instituto de Sistemas Optoelectrónicos y Microtecnología (ISOM), Escuela Técnica Superior de Ingenieros de Telecomunicación, (Universidad Politécnica de Madrid)*. Optical characterization was performed at the *Instituto de Física Aplicada (IFA), CSIC*. Impedance spectroscopy measurements were carried out in the Electronic Department (*Grupo de Displays y Aplicaciones Fotónicas*) of the *Universidad Carlos III de Madrid*. Finally, current density-voltage characteristics were recorded at the *Laboratorio de Diseño de Circuitos Digitales y Tecnología Electrónica (LabTEL)* in the *Universidad Rey Juan Carlos*, headquarters of the Optoelectronic Organic Group.

2.1.2.1 Profilometer

Sample thicknesses were measured using an Alpha step 200 profilometer (Tenkor Instruments) as shown in Figure 2.7.

The equipment consists of a diamond-tipped stylus of 12.5 micron radius that scans across the sample surface, and is fixed onto a tray that can travel in the XY plane. The stylus tip is in contact with the sample exerting a controlled force on it (< 40 mN), and can register changes in the sample surface with vertical resolution of 5 nm.

Figure 2.7-Tencor Alphastep 200 Profilometer

2.1.2.2 Semiconductor parameter analyzer

Current-voltage characteristics are measured using a semiconductor parameter analyzer Agilent 4155C, and a pulse generator Agilent 41501B. The equipment can be controlled by a commercial Metric ICV software [Metricstech], specifically designed for semiconductor testing. This tool enables design of DC or pulse excitation signals that can be customized for every measurement.

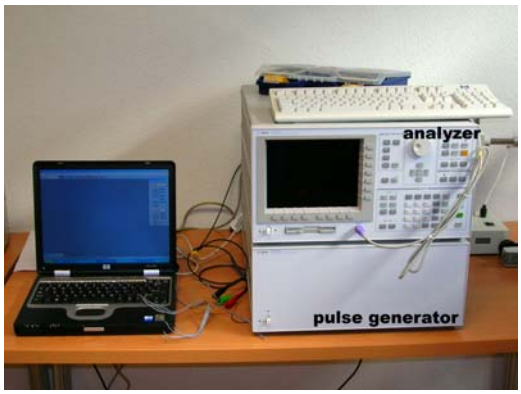

Figure 2.8 - Semiconductor Parameter Analyzer Agilent 4155C and Pulse Generator Agilent 41501B.

The Agilent 4155C can measure the voltage or current through a semiconductor device when an electric stimulus (current or voltage) is applied to the sample. It can perform dc or pulse measurements, and for dc type, voltage/current sweeps and sampling (time domain) measurements are available.

Output and input impedances are 0.3 Ω and 10^{13} Ω respectively.

The applied voltage range is ±40 V with a measurement resolution of 40 μV. Current resolution goes down to 10 fA for a current range of ± 10 nA. Single triaxial cables are used to connect the sample.

2.1.2.3 Impedance analyzer

Impedance spectroscopy and impedance versus voltage measurements are performed using a SOLARTRON 1260 Impedance Analyzer. It performs impedance measurements with a voltage or current stimulus over the frequency or time domain. The frequency scanning range goes from 10 μHz up to 32 MHz.

Figure 2.9-Solartron 1260 Impedance Analyzer

It is capable of measuring impedances up to 100 MΩ. The maximum polarization bias and small signal level are 40.95 V and 3 Vrms respectively. This equipment includes an equivalent circuit modelling software that helps the interpretation of results.

2.1.2.4 Spectroradiometer

Calibrated spectral radiance in w/(sr•m^2•nm), as well as chromaticity identification (CIE coordinates, etc) are measured using a Konica Minolta CS-1000 spectroradiometer. The system incorporates a high resolution photodiode capable of measuring over a spectral range from 380 to 780 nm in 1 nm intervals. The luminance can be measured within a range of 0.01 up to 80.000 cd/m^2.

Figure 2.10 – Konica Minolta CS-1000 spectroradiometer

The spectroradiometer is equipped with a 50 mm standard lens and a 50 mm macro lens for small objects measurements. This equipment can measure small emitting surfaces down to a diameter of 0.45 mm.

2.2 PLED passive matrix fabrication procedure

A major difference between polymer-based and molecular-based OLEDs lies in the methods used for device fabrication. Polymer active layers are deposited by spin-coating or jet printing from solution onto the substrate. Such wet deposition methods are potentially of lower cost, but a low work function metal cathode must still be deposited in vacuum, similarly to the case of molecular OLEDs. Current technology to fabricate molecular-based OLEDs is by means of vacuum sublimation. Such a technique grants good control of film uniformity, thickness and dimensions, as well as the ability to employ a complicated structure to optimize the device performance. On the other hand, the potential outcome for vacuum evaporated thin film devices is low, resulting in high production cost.

In this thesis, photolithography techniques are employed to define the PLED geometry. Using this technique, a high number of small scale diodes with suitable external connections may be obtained in one fabrication process, depending only on the quality of the previously designed masks. In any case, the use of photolithographic techniques with organic compounds must be performed carefully, since both photoresist and organic active layers are usually soluble in similar solvents. This implies the risk that an organic solution to be deposited on top of the photoresist may in turn dissolve it. Fortunately, a few active compounds have been deliberately designed to overcome this problem. An example is PEDOT:PSS, a conductive polymer used to enhance hole injection, that needs to be mixed up with water to be deposited by spin coating. The use of this water emulsion between the photoresist and the polymer active layer prevents organic solvents from affecting the photoresist layer.

The use of photolithography techniques in organic diodes fabrication is a major advantage compared to traditional manufacturing methods that use shadow masks, in which wire contacts must be applied directly onto the electrodes manually. Photolithography allows small scale fabrication and facilitates wire welding to the electrodes by arranging a set of tracks and pads at the periphery of the sample.

2.2.1 General procedure of PLED passive matrix fabrication

Figure 2.11 shows a general overview of the whole fabrication process. Most important fabrication stages are: glass cutting and washing, photolithography for ITO patterning, diode geometry definition by photoresist wells, spin coating of polymer layers, cathode evaporation, sample encapsulation and wire soldering.

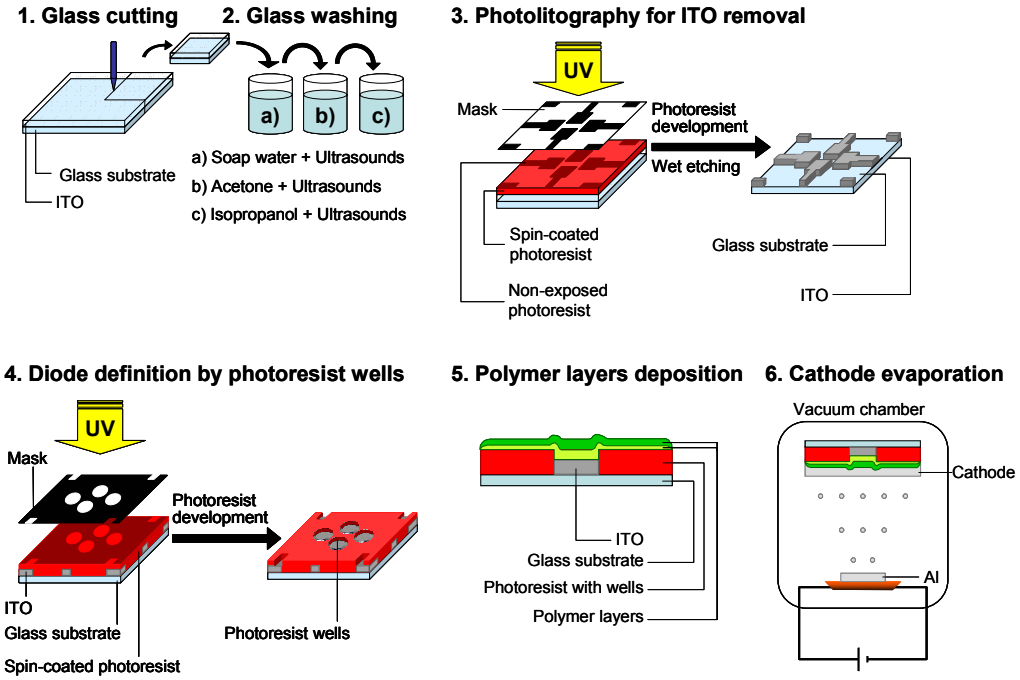

Figure 2.11 – Schematic of the complete fabrication process.

All fabrication steps are critical to obtain a good final device performance. The reliability of each process can be assessed with the use of relevant indicators before proceeding to the next stage. Table 2.1 summarizes each step with its corresponding quality parameter.

Fabrication Process	**Quality indicator**
Glass washing	Pristine and spotless glasses.
Anode definition	No short-circuits between adjacent diodes.

Fabrication Process	**Quality indicator**
Definition of diode wells	Good diode confinement. No leakage currents.
Spin coating of polymer layers	Smoothness, homogeneity and layer quality.
Cathode evaporation	Cathode thickness homogeneity. Good adherence when biasing.
Encapsulation	No oxygen or moisture inside the sample. Enlargement of device lifetime. Minimized degradation.

Table 2.1 - Summary of fabrication steps and their influence on the final device quality.

Commercial ITO coated glass is used as substrate. Glass cutting requires a great skill to obtain smooth and nice glass edges. Cutting is a high polluting process that needs to be carried out in a separate area of the clean room. Next, glasses need to undergo a cleaning process. This is of major importance since PLED layers are in the nanometre range and therefore any minor impurity can lead to malfunctions in the device. Once glasses are clean and spotless, samples go through a photolithographic process to define the diode anodes and tracks. This stage is critical since it will be responsible for the diode border definition.

Subsequently, a second photolithographic process will be in charge of isolating a diode from its neighbours by means of photoresist wells. Next, polymer layers: carrier injection/ transport layers and electroluminescent layers, are spin-coated. At this stage, good quality polymer solution needs to be prepared so that the resulting deposited layer is free from spots and other irregularities typical of spin-coating. Then, the aluminium cathode is evaporated at a pressure of 10^{-6} Torr, low enough to guarantee a good adherence between the polymer and the metal (metal films deposited below 10^{-4} Torr have been observed to detach during biasing). The aluminium acts as a common cathode for all diodes. Finally, encapsulation is crucial to avoid diode degradation by the effect of oxygen and moisture, enlarging lifetime significantly. The sample is sealed by means of an epoxy and a piece of glass. This process is performed in a glove box in a nitrogen atmosphere. Degradation mechanisms due to reaction with oxygen are associated to characteristic peaks in the electroluminescence spectra. This will be deeply study in chapter 3.

Next section will describe in detail most relevant fabrication steps.

2.2.2 Relevant steps in PLED fabrication procedure

2.2.2.1 Glass cutting and cleaning

Commercial wafers of ITO coated glass of dimensions 40x40 cm and thickness 0.7 mm will be cut in small pieces of the desired sample dimensions. ITO is 200 nm thick and has a sheet resistance of 20 Ω/sqr. The cutting is performed with a Silberschnitt cutter, a pencil ended in a rolling disc that acts as cutter. Wafers are placed on a plane surface with the ITO face on top. This is important to avoid scratches on the ITO surface. The cutter is then slipped on a vertical position over the wafer, leaving a mark on the glass that is easily cracked. Typical dimensions of our PLED matrix samples are 25x30 mm.

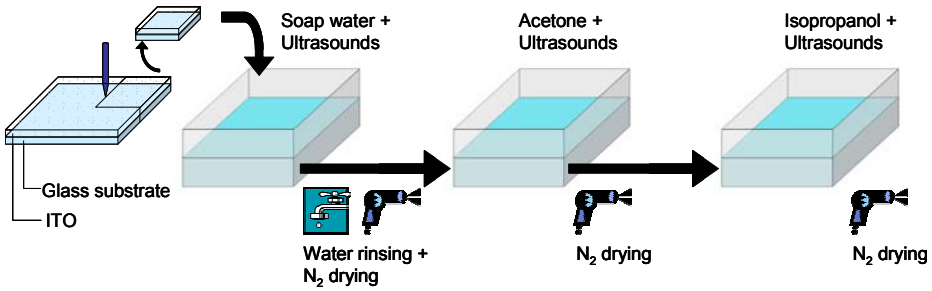

Figure 2.12 – Schematic of cutting and cleaning processes.

Next, samples are carefully placed on a basket to undergo a typical organic material cleaning process. They are positioned in an ultrasound bath of 40 kHz (Ultrasons-H, J.P. SELECTA), see Figure 2.2. At the same time, baskets are successively immersed in a soap based solution (Micro-filtered soap, Millipore) for 25 minutes and organic solvents, acetone and isopropyl alcohol baths, for 15 minutes each. After the soap bath, it is necessary to carefully rinse the samples with distilled water to remove any soap traces. Every bath is followed by a drying step with a nitrogen gun. The cleaning process is carried out twice during fabrication, first, after the glass cutting and second, after the photolithographic process to define the ITO anodes.

2.2.2.2 Anode patterning

The objective of this step is to define the ITO anode by means of a photolithographic process. Prior to this, a mask with the ITO anode, and tracks connecting to soldering pads need to be designed.

Figure 2.13 – ITO anode mask.

Figure 2.13 shows the mask employed in the photolithographic process. It can be observed that every passive matrix contains eight diodes, all of which have been placed in the centre to ensure thickness homogeneity. The dashed circle encloses diodes location.

Notice that the four rectangles at the corners of the mask will be used to solder the aluminium contacts.

Figure 2.14 summarizes the whole photolithographic process.

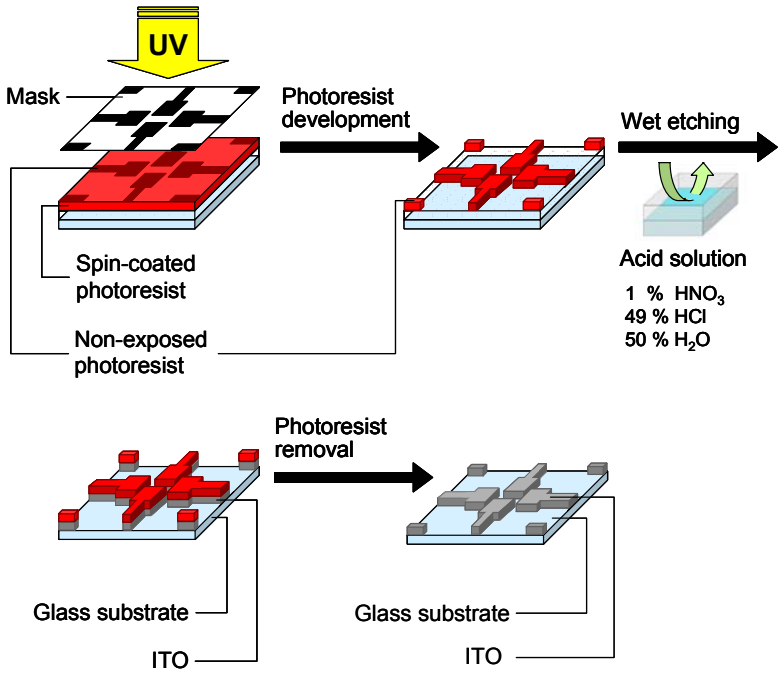

Figure 2.14 – Photolithography to define ITO anodes.

Clean samples are placed on the spinner and photoresist (Microposit S1818) is deposited at 4500 rpm for 30s. The spinner must increase up to 4500 rpm in the first 10 seconds and remain stable for the rest of the spin time. This slope-like velocity pattern has been observed to optimize the homogeneity and quality distribution of the layer [Calderón03]. Photoresist has been previously filtered with a 0.45 μm hydrophilic Millipore filter to remove all particles above that size. Samples are annealed at 90 ºC for 30 minutes to cure the photoresist. Then, the mask is aligned to the sample and they are exposed to a UV light source of 450 Watts for 30 seconds using the OAI Hybralign TM Series 400 system (see Figure 2.4).

To remove exposed photoresist, samples are developed using a Microposit Developer Concentrate for 15-20 seconds. Longer developing times may result in a low resolution of anode edges. Samples are cured for another 30 minutes at 100 ºC.

Next, non-protected ITO is removed by means of a wet etching process. Samples are immersed in an acid solution (50% H_20, 49%HCl and 1% HNO_3) at 65 ºC for 35 seconds and then rinsed with water.

Both temperature and time are carefully controlled by the wet etching equipment. Only ITO protected under the photoresist is left.

Figure 2.15 – Wet etching bath.

It is critical not to prolong the wet etching period longer than 35 seconds since the acid may begin to attack the ITO under the photoresist. Finally the remaining photoresist is eliminated using Microposit Remover 1165.

2.2.2.3 Diode geometry definition by photoresist wells

In order to define the diode geometry, a new mask must be designed. Contrary to the mask used in the previous step, this one will only let UV light fall on the areas of the photoresist that coincide with the ITO pads.

As Figure 2.16 shows, the mask design will define the circular shape of the wells that will be carved on the photoresist after development, thus determining the geometry of the actual OLED.

Figure 2.16 – Diode geometry mask.

Since these wells must coincide exactly with the eight ITO pads, a proper alignment of the mask is critical to obtain good OLED performance.

The thickness of the active layer is approximately 100 nm, and it is convenient that the photoresist well thickness is of a similar order of magnitude. With this purpose, previously to spin coating, the photoresist has been diluted in Microposit EC Solvent, in a one to one proportion. This enables obtaining wells with a thickness of 500 nm, instead of the 2 microns that would have resulted without dilution.

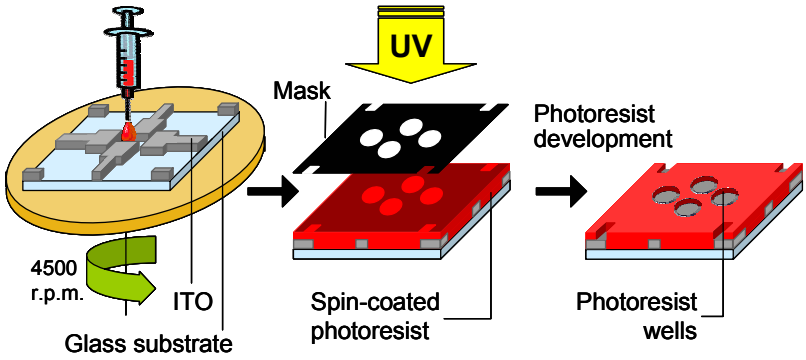

Figure 2.17 – Schematic of diode geometry definition.

Figure 2.17 shows the schematic of this photolithographic process. All intermediate steps are similar to those described in section 2.2.2.2. Since the photoresist is now diluted an exposure time of 10 seconds will be enough to ensure good results. Longer developing times may affect the unexposed photoresist area.

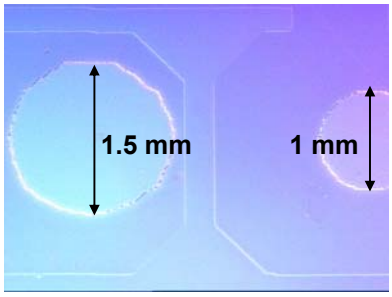

Figure 2.18 – Photograph of photoresist wells with two diameters.

After photolithography, the sample is annealed at 125ºC for 30 minutes to harden the photoresist. Notice that after development, all diodes remain isolated from their neighbours by the photoresist walls. Figure 2.18 shows a photograph of photoresist wells aligned with the ITO pads.

2.2.2.4 Polymer layers deposition

Prior to spin coating of the active layer, an intermediate film of a conductive polymer, PEDOT:PSS, is deposited. This layer offers three advantages: enhances hole injection due to a higher workfunction than that of ITO, helps conduction along the device and smoothes the ITO surface, reducing short-circuit risks. PEDOT:PSS is a mixture of two polymers: PEDOT (Poly(3,4-ethylenedioxythiophene)), an insoluble conjugated polymer that carries positive charges and is based on polytiophene, and PSS (poly(styrenesulfonate)), made up of sodium polystyrene sulfonate, a sulfonated polystyrene that helps carrying negative charges, and confers the water-soluble property when blended with PEDOT [Crispin03].

PEDOT:PSS usually comes in the form of an emulsion in water. This is of major importance when depositing it on top of photoresist layer. Since the photoresist is dissolved in organic solvents, it will not be affected by a water emulsion.

The term dispersion is used instead of solution, because PEDOT:PSS is not uniformly distributed in water, but forms pseudo-particles called “miceles”. The microscopic structure of micelas favours a particular arrangement when PEDOT:PSS is deposited as a solid state layer. As a result, it has been generally observed that horizontal conductance of PEDOT:PSS (parallel to the layer plane) is several orders of magnitude higher than the vertical conductance (along the multilayer axis, which is the relevant for OLED operation) [Mulfort03].

PEDOT:PSS must be filtered with a 0.45 μm filter before deposited, but due to its dispersive nature, prior to filtering, the emulsion should undergo a heating and ultrasound period to improve the mixture and thus facilitate the filtering. PEDOT:PSS is then spin casted at 6000

rpm for 30 seconds resulting in layer thicknesses of the order of 50 nm. Casting at 4000 rpm may increase the layer thickness by just a 10%, but a further slowing down may result in the appearance of vortices and other surface inhomogeneities. But, as explained above, very thick layers are not desirable since they may hinder conduction. On the other hand, increasing of the spinning velocity up to the maximum allowed by the spinner resulted in thickness reductions of about 10%. The PEDOT:PSS layer is then cured at 120ºC for 30 minutes. Recent investigations point out that blends of PEDOT:PSS with sorbitol (5% by weight) and curing at higher temperatures < 180 ºC, may enhance vertical conductance [Timpanaro04].

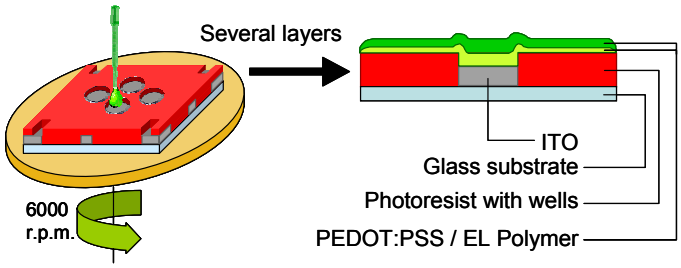

Figure 2.19 – Deposition of PEDOT:PSS and active layer by spin-coating.

Polymer solution is then prepared using an organic solvent, typically chloroform (polar solvent of low boiling point, $T_b \approx 62$ ºC) or toluene (non polar solvent of high boiling point $T_b \approx 110$ ºC) . To obtain a good quality solution, it is heated in an ultrasound field and stirred using magnetic shakers. This is crucial to achieve a good quality of the active layer morphology. The solution is then filtered and deposited on top of PEDOT:PSS at 6000 rpm for 30 seconds. Spinning velocities below 4000 rpm may not result in good quality and homogeneity of the polymer layer. Samples are annealed for 30 minutes at a temperature slightly higher than the solvent boiling point.

Three electroluminescent polymers are used as active layer in this thesis. Two commercial polymers, namely, poly(2-methoxy-5-{3',7'-dimethyloctyloxy}-p-phenylenevinylene) (MDMO:PPV) and poly(3-hexylthiophene) (P3HT), and a new polyfluorene derivative, poli(2,7-fluorene phenylidene) (PFP), synthesized at IBMC-UMH [Mallavia05]. This polymer, having its fluorescent emission in the blue spectral range, will be studied in detail in the next chapter.

It is worth mentioning here that at this step of the device fabrication, every time the active layer was deposited, another layer from the same solution batch was also spinned on top of a plane glass, and was used to check the thickness of the active layer. This parameter is very

important since it determines the electric performance of the diode. Final thickness of these layers will mainly depend on the solution concentration, on the solvent employed, and to a minor extent, on the spin-casting procedure. Special care must be taken when working with chloroform, since due to its low boiling point (62 ºC) solution concentration may increase very rapidly, and the deposited solution might start drying even before spinning takes place, which would have a very negative influence on the film quality.

2.2.2.5 Cathode evaporation

Aluminium is chosen as cathode due to its easy handling, low cost, and low reactivity against moisture. However, aluminium work function is 4.28 eV, relatively large, resulting in high electron injection barriers for typical polymer LUMO levels. Another metal commonly used as cathode is calcium. Due to its low work function (2.87 eV) it would result in an almost ohmic contact at the cathode. Nevertheless, it has the problem of being very reactive with moisture at relatively low percentages, so it is recommended to be handled in an inert atmosphere.

A Vacudel 300 (Telstar) evaporator (see Figure 2.5) is used to evaporate and deposit the cathode. Before introducing the samples in the chamber, a shadow steel mask is fixed to the sample perimeter to prevent aluminium from being deposited on the contacts. After evaporation the mask will be removed and the contacts will be cleaned before soldering the wires.

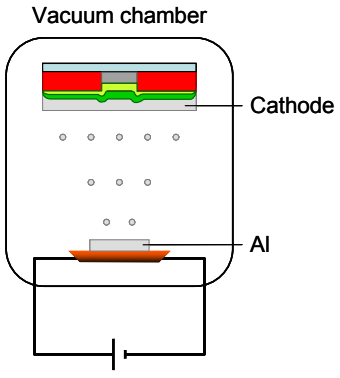

Samples are fixed to the top of the vacuum chamber facing the metal, and aluminium is placed on a tungsten crucible which in turn is connected to the evaporator electrodes. In order to obtain good adherence between the metal and the polymer the vacuum must reach at least 10^{-6} Torr before evaporation starts. This would take at least four hours. The current across the crucible is progressively increased up to 120 A in intervals of 20 A.

Figure 2.20 – Cathode evaporation.

After several tests it was established that this was the best current sequence to perform a controlled evaporation and to ensure the basket will not break [Calderón03]. The current flow

starts heating the tungsten basket by Joule effect which in turn heats the aluminium up to its sublimation point.

The evaporator includes a quartz crystal based system to display the thickness of the evaporated layer. The software makes use of the material density and a Z factor to calculate resulting thickness. In case of aluminium the following parameter were used:

	Density (g/cm^3)	Z factor
Aluminium	2.73	1.08

Table 2.2 – Aluminium evaporation parameters for thickness calculation.

Typical thicknesses for the aluminium cathode are of the order of 200-300 nm. Lower thicknesses may result in the cathode being torn off the device when bias is applied.

2.2.2.6 Encapsulation and wire soldering

As already mentioned in the first chapter, organic devices' main drawback is their short lifetime due to degradation mechanisms that are enhanced during operation in the presence of oxygen and moisture. Therefore, device encapsulation in an inert atmosphere is crucial to ensure a good performance and prolong diode lifetime.

Encapsulation is carried out in a Mbraun Unilab glove box filled with nitrogen, see Figure 2.6.

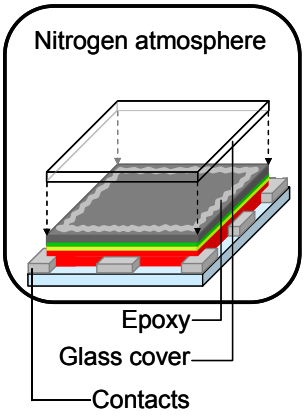

An optically transparent epoxy, EPO-TEK-302-3M, is deposited with a syringe along the sample perimeter, trying not to invade the contacts where the wires are to be soldered. At this point it is important to make sure the epoxy covers the entire sample border to ensure good sealing. A glass cover is then placed on top of the structure leaving the diode sandwiched between the glass substrate and the glass cover.

Figure 2.21 – Encapsulation.

The samples are then left inside the glove box at room temperature for 24 hours for the epoxy to be properly cured.

More sophisticated techniques also include a desiccant, usually BaO, between the sample and the glass cover. This absorbs moisture that may remain inside the sample. However, since the desiccant comes in the form of a hard powder, the deposition has to be done carefully along the sample perimeter in order not to scratch the cathode.

Finally, wires are welded to the contacts using indium. The soldering is done over the ITO contacts and using indium instead of tin was proved to be more suitable. In order to reinforce the soldering and fix the wires, a drop of insulating glue (Araldit) is deposited over the contacts.

The resulting matrix has a common aluminium cathode and each diode can be addressed individually biasing the appropriate ITO anode. Figure 2.22 and Figure 2.23 show the final device cross section and photograph respectively.

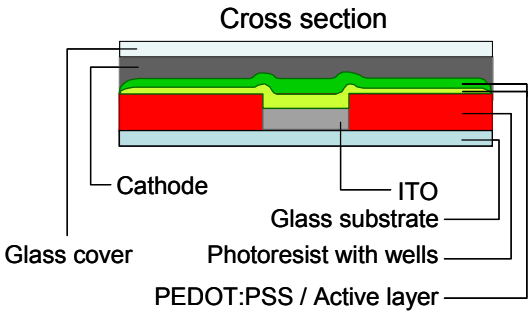

Figure 2.22 – Final device cross section.

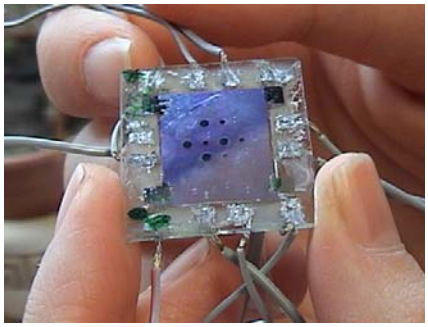

Figure 2.23 – Final device.

2.3 Thickness calibration

Active layer thickness is a critical parameter since it determines device electrical and optical features such as threshold voltage and electroluminescence onset.

Checking the thickness of conductive and active layers was done using a Tenkor Alphastep 200 profilometer (see Figure 2.7) on a layer deposited on a plane piece of glass in the same conditions of the device active layer.

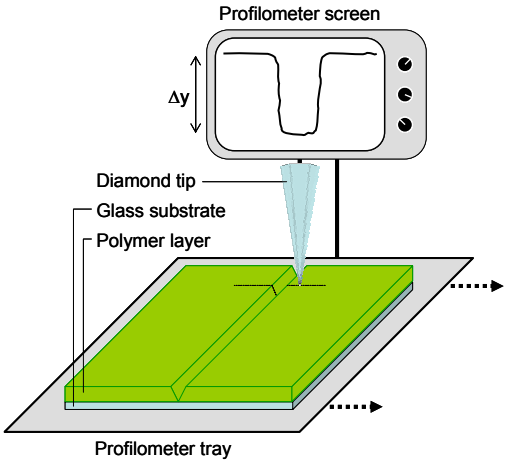

A straight line is scratched on the polymer layer using a punch and the sample is deposited on the profilometer tray. The stylus diamond tip scans across the sample surface and registers thickness changes with 5 nm vertical resolution. Thus, when it passes through the scratched line it detects the line depth and therefore measures the layer thickness. Besides, surface ripple is also registered.

Figure 2.24 – Thickness measurement

As it was already mentioned, thickness depends mostly on the concentration of the polymer solution. Concentration versus thickness calibration curves were performed for all polymers employed and they will be shown in next chapter.

2.4 Electrical characterization techniques

Standard electrical characterization techniques have been employed to measure the electrical behaviour of our organic diodes. When an electric field is applied to an organic diode, polymer layers can support positive and negative carriers, though in a different way as the inorganic semiconductors do. Organic semiconductors are amorphous materials and obey disorder conduction models. However, there are some conduction related issues still under research. In this thesis, electrical measurements are of major importance since they will provide the data that will serve as a basis for the theoretical conduction model presented in chapter 4.

2.4.1 Current-voltage

Current-voltage (I-V) characteristics were performed using a semiconductor parameter analyzer Agilent 4155C and pulse generator Agilent 41501B (see Figure 2.8). Measurements were performed using commercial Metric ICV software [Metricstech], specifically designed for semiconductor testing. This tool enables design of DC or pulse excitation signals that can be customized for every sample. Besides, DC/pulse voltage/current sweeps measurements are also available.

Samples were introduced in a Faraday box to avoid possible noise signals and were connected to the analyzer with triaxial cables. These types of cables are specially designed to measure small current signals (below 1 nA) since they do not suffer from triboelectric effect. The experimental set up is shown in Figure 2.25.

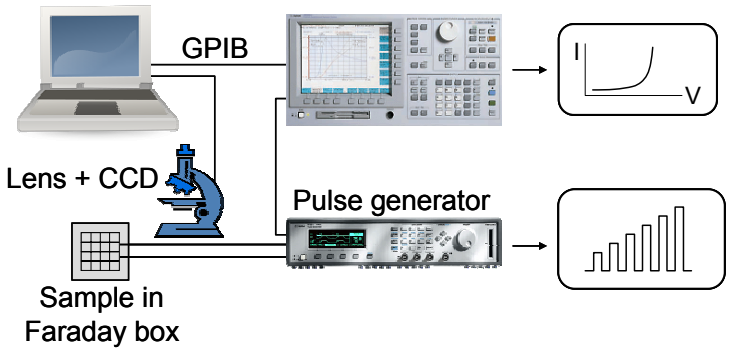

Figure 2.25 – Current vs voltage measurement set up.

Samples are excited with a voltage sweep pulsed signal that is previously designed changing the amplitude, period and duty cycle. For typical IV measurement the pulse train period was set to be 100 ms and the pulse width 0.1 ms. Refresh time between two consecutive pulses ensures long time operation without significant device degradation. Furthermore, the I-V curve stability was achieved by gradually increasing the pulse amplitude up to the point where reproducible measurements were observed. Curves were recorded using different resolutions in the low and high operation regimes. Train pulses with longer duty cycles and constant amplitudes where generated in order to measure the device electrical lifetime.

Sample images were recorded simultaneously to current-voltage curves to observe device degradation. Photographs were taken with a Motic microscope with a lens W10x/20 connected to a CCD Moticam 350 with an 8 mm CCD lens.

2.4.2 Admittance spectroscopy

Recently, admittance spectroscopy based on small signal was proposed to characterize the carrier dynamics in organic materials [Martens99]. This technique allows a study of dispersive transport in organic materials taking into account frequency dependence via transit time of individual carriers. Using this technique, material parameters such as mobility can be

determined as function of frequency and bias. Moreover, using equivalent RC-circuits, diode capacitance and conductance can be extracted. In chapter 4, these measurements will be used as experimental data to verify a proposed model describing the AC response of a biased PLED.

Measurements were carried out with a SOLARTRON 1260 Impedance Analyzer (see Figure 2.9). In order to minimize noise signal, samples are introduced in a Faraday box which is in turn grounded. The diode is connected to the analyzer that feeds the input signals, biasing the diode at different dc levels and superimposing an alternating voltage of 100 mV. The analyzer registers the induced alternating current in the OLED and provides the real and complex parts of the impedance. Two different approaches were taken to perform the measurements. First, impedance was measured as a function of frequency for different bias. Second, the measurement was repeated as function of bias at different frequencies.

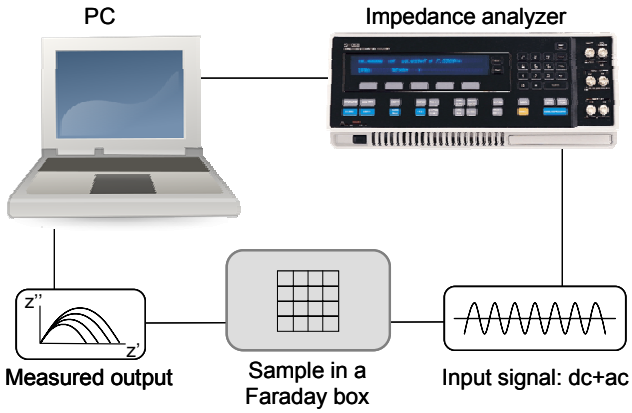

Figure 2.26 – Impedance spectroscopy set up.

The analyzer is controlled by the Zplotv2.8 software by Scribner Associates [Scribner] that allows programming the measurements. The equipment includes another commercial software, Zviewv2.8, that enables to represent the results graphically and fit the data to equivalent RCL-circuit models.

2.5 Optical characterization techniques

Optical measurements are crucial in all electroluminescent devices characterization. Radiance and chromaticity will determine whether a certain material would be suitable as active layer in

an organic display. In the case of OLEDs, where the lifetime is a critical issue, it is crucial to determine the operation time in hours without colour shift or significant loss in luminance.

The spectral radiance (electroluminescence, EL), luminance and emission chromaticity of our OLEDs are measured using a Konica Minolta CS-1000 spectroradiometer (see Figure 2.10).

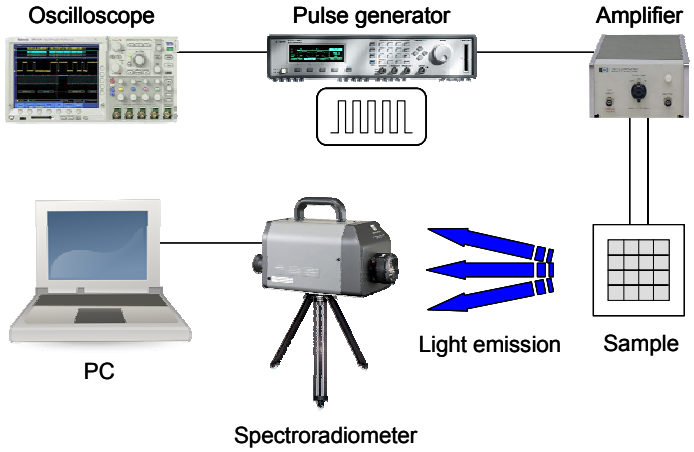

Figure 2.27 – Optical measurement set up

Samples were fed with a constant pulse train whose amplitude can be changed with an amplifier. The spectroradiometer is equipped with aperture mirrors to ensure proper alignment of the finder target and the exact measuring spot. The spectroradiometer is controlled via software (Minolta CS-S1RW) to schedule the measurements and display the data. EL spectra and chromaticity measurements were taken at different bias. Besides, in order to check how the device emission is influenced by degradation, measurements were repeated every 15 minutes for several hours.

CHAPTER 3

PLED PASSIVE MATRIX BASED ON POLYFLUORENE DERIVATIVES

Contents

3 PLED passive matrix based on polyfluorene derivatives 57

3.1 Overview of polyfluorene materials 57

3.1.1 Why polyfluorenes? 58
3.1.2 Poly(2,7-fluorene phenylidene) (PFP) 61

3.2 Thickness calibration of spin-coated active layers 63

3.2.1 P3HT and MDMO:PPV 63
3.2.2 Polyfluorene derivatives 65

3.3 Fabricated structures and electrical characterization results 67

3.3.1 Comparison of polyfluorene derivatives with commercial blue polymers 67
3.3.2 Influence of the active layer thickness 69
3.3.3 Improved performance of encapsulated devices 72
3.3.4 Admittance spectroscopy (AS) characterization. Small signal equivalent circuit. 76

3.4 Results of the optical characterization 79

3.4.1 Electroluminescence, luminance and CIE coordinates 80

3.4.2 Degradation and colour shift in polyfluorenes 87

3.5 Conclusions 95

Chapter 3

3 PLED passive matrix based on polyfluorene derivatives

This chapter presents different fabricated PLED passive matrices based on polyfluorene polymers, together with the most relevant results of the electrical and optical characterization. Although the main contribution lies in PLEDs based on polyfluorene derivatives, several other diode structures were fabricated using commercial electroluminescent polymers for the sake of comparison. Section 3.1 reviews the main features of polyfluorene materials paying special attention to those derivatives employed in this thesis. Section 3.2 presents the film thickness calibration curves for different materials. Section 3.3 summarizes the fabricated structures for different electroluminescent materials, studies the effect of encapsulation and presents the results of the electrical characterization for structures with different active layer thicknesses. Section 3.4 presents the results of the optical characterization and studies the different degradation mechanisms in polyfluorene based PLEDs. Most relevant conclusions are highlighted in section 3.5.

3.1 Overview of polyfluorene materials

In the latest years, polyfluorenes (PFs) have drawn great attention due to their interesting properties as blue emitters. Saturated blue emission is important due to its role as a primary colour for displays, as well as to serve as excitonic source for white emission, via energy transfer to other emitters. PFs are known for their high solid-state efficiencies, good carrier mobilities and exceptional thermal and chemical stability in inert environments [Lang04]. This section will review the basic operational principles of PFs together with their main characteristics. Particular consideration will be given to polyfluorene phenylidene derivatives, as they will serve as active layers for most devices presented in this work.

3.1.1 Why polyfluorenes?

Poly(p-phenylene-vinylene) (PPV) based materials are probably the most used active layer in PLED processing. PPVs are useful as red and green light emitters in PLEDs, but accessing blue light via electroluminescence (EL) has remained a challenge due to the large excitonic band gap required for blue emission.

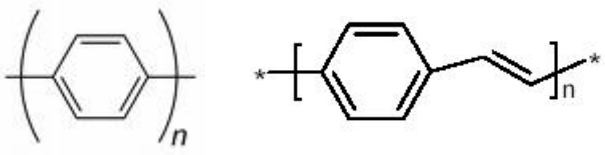

Figure 3.1 – Monomer repeating units of PPP (left) and PPV (right)

Initial research in blue emitting polymers was focused on PLEDs containing poly(p-phenylene) (PPP) as the emissive layer. Since PPP is insoluble in most solvents, derivatives containing solubilizing side groups were synthesized to improve processibility. However, introducing solubilizing groups causes an increase in the torsional angle between the phenyl rings [Bredas85]. This lowers the conjugation between rings and causes a blue shift in emission and a reduction in EL efficiency.

A promising alternative for violet-blue emission came up with polyfluorenes. Fluorene (Fl) is a polycyclic aromatic compound that received its name due to strong violet fluorescence which arises from highly conjugated planar π-electron system.

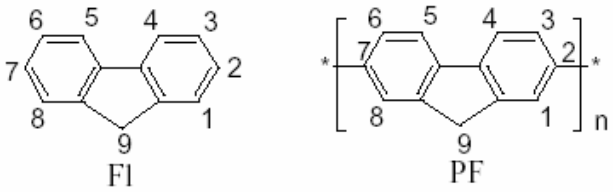

Figure 3.2 – Molecular structure of fluorene and poly-(fluorene).

The 2,7-positions in Fl are the most reactive sites towards electrophilic attack and allow construction of a fully conjugated rigid-rod polymer chain by substitution reactions. The methylene bridge (carbon 9 in Figure 3.2) serves to lock the ring pairs into a coplanar

arrangement and can be functionalized without distorting the torsional angle between the fluorene units.

The excellent optical and electronic properties together with a high chemical and thermal stability (glass transition temperature, Tg, typically around 100 ºC) make PFs attractive materials for PLEDs. In fact, PFs are the only type of conjugated polymers that can emit a whole range of visible colours with relatively high quantum efficiency [Bernius00]. Ohmori and co-workers first demonstrated blue EL from a PLED using poly(9,9-dihexylfluorene) as the emissive layer [Ohmori91].

Polyfluorenes are soluble in conventional organic solvents such as aromatic hydrocarbons (toluene, etc), tetrahydrofuran (THF) and chlorinated hydrocarbons (choloroform, etc), and result in high quality thin films when processed by spin coating.

Polyfluorenes can be classified according to the nature of the monomer unit that constitutes the conjugated backbone. Following this criterion, one may find two types of polyfluorenes: homopolymers and copolymers. Homopolymers consist of a conjugated backbone formed by linked fluorene units, while in copolymers other aromatic units are alternated with the fluorene rings. All polyflourene homopolymers are strong blue emitters when excited with UV light either in solution or in solid state. In contrast, copolymers based on polyflourene can emit in a wide spectral visible range depending on the aromatic ring that accompanies the flourene in the monomer unit. In this sense, copolymers are extremely versatile, since copolymerization enables to adjust the band gap to desired emission wavelength. All copolymers are of high molecular weight, and the incorporation of functional groups, such as acids, ammonium salts or sulphonates, to the lateral chains of the conjugated polymer is one the most common methodologies to improve their solubility.

One of the main challenges to be solved in PF synthesis is the dispersity of polymer molecular weights and the batch to batch variability. Among all the techniques employed for polyfluorene synthesis, prior importance should be given to that developed by Suzuki and co-workers [Miyaura81]. This is a general technique employed to synthesize conjugated polymers in the presence of palladium as catalyzer. Following this Pd-catalyzed polymerization process, it is possible to prepare alternating fluorene copolymer with various aromatic amines, exhibiting deep blue emission and solubility in conventional organic solvents. Hole mobilities of this amine copolymer are found to be quite high ($3x10^{-4}$ to 10^{-3} cm^2/Vs) [Redecker99], similar to hole mobilities of small molecules such as tetraphenyl diamine (TPD), a widely used hole

transport material. This high mobility value suggest that these copolymers are excellent candidates for photoconductors and hole transporters in PLEDs.

The choice of the alternated aromatic units in the fluorene based copolymer has served as an excellent synthetic tool for designing copolymers with well-balanced hole and electron transport properties and tuneable emission colour. Let us remember that solution processing such as spin-coating reduces the number of employed active layers. This means that materials with a maximum functionality are of major interest. A collection of fluorene copolymers prepared using the Suzuki route and emitting in the entire visible range can be found in [Bernius00].

Despite PFs being promising candidates as blue emitting materials in PLEDs due to their solution processability and high luminescence efficiencies, most of the polymers developed so far have suffered from unwanted lower-energy band emissions along with the desired blue one, due to a variety of degradation processes of chemical reactions. Particular interest has received the green emission band at 530 nm. This green band appears upon thermal annealing of the polymer film and/or during device operation. The initial hypothesis attributed this phenomenon to intermolecular excimer formation between polyfluorene chains [Bliznyuk99]. An excimer (short for “excited dimer”) is defined as a complex molecule resulting from the interaction of two identical monomers, one of which is in an electronic excited state, while the other one is in the ground state. Excimers act as charge traps that emit in the long-wavelength region. Indeed, the green emission increased during the thermal annealing and was not observed in the polymer solution. This hypothesis gave rise to a great amount of synthetic research activities, focused on the introduction of bulky substituents in the PF side chain or bulky fragments in the PF backbone, to prevent the excimers formation. In some cases, such modifications did result in a stabilization of blue emission, which was considered as a confirmation of the excimeric nature of the green band.

More recently, additional experimental evidence suggests that the origin of the green emission is related to the presence of fluorenone defects in the polymer chain, and not from the excimer emission [List02]-[Gaal03]-[Romaner03]. A fluorenone defect is created during synthesis or as consequence of a photo- (or electron) oxidative degradation processes, resulting in a C=O bond at the 9-position of the fluorene (see Figure 3.2). This was confirmed by comparing the photoluminescence of PF films in an inert atmosphere and in air. As shown in Figure 3.3, the intensity of the green band was progressively increasing when annealing in air [Gong03-b].

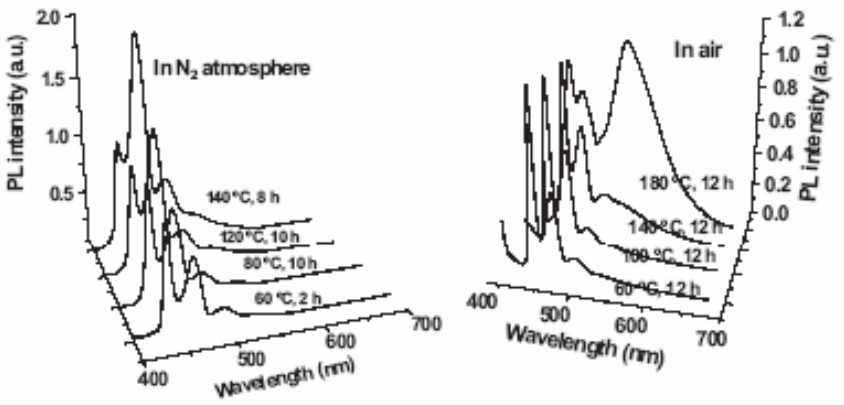

Figure 3.3 – PL spectra of polyfluorene films after annealing at different temperatures in nitrogen atmosphere and in air [Gong03-b].

Similar results were obtained when measuring the EL spectra during device operation, but in this case, the green band was even more pronounced.

In any case, the nature of this interaction remains a source of controversy in literature. Further attention will be given to this and other degradation mechanisms in PF in section 3.4.

3.1.2 Poly(2,7-fluorene phenylidene) (PFP)

As stated in section 1.4, the first objective of the present thesis is to fabricate and characterize PLEDs using two new derivatives of poly(2,7-fluorene-1,4- phenylidene) (PFP) as active layer. These two derivatives differ on the functional group at the C9-position of the polyfluorene, being a bromide species in one case (PFP:Br_2) and a cyanide type in the other case (PFP:$(CN)_2$). Figure 3.4 shows the structure of the polyfluorene phenylidene with Br and CN as functional groups in the side-chain.

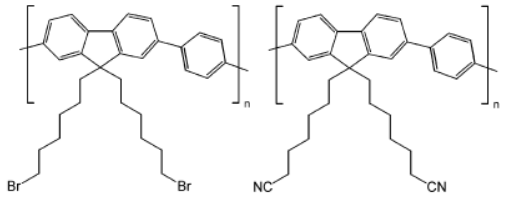

Figure 3.4 - Polyfluorene phenylidene structure with Br and CN as functional groups.

These conjugated polymers were synthesized at the *Instituto de Biología Molecular y Celular (IBMC, Universidad Miguel Hernández)*. The synthesis process starts from a previously designed precursor monomer, and follows a Suzuki polymerization route that yields the final PFP conjugated polymer. A detailed explanation of this synthesis procedure can be found in [Mallavia05]. By means of the interconversion of the functional group, different solubilities can be obtained in organic solvents. In fact, the resulting polymers are completely soluble in THF, toluene, chloroform and chlorobenzene.

Cyclic voltammetric analysis carried out at the *IBCM* was used to establish the HOMO and LUMO energy levels of the synthesized polymers [Montilla06]. In this technique, the polymer is deposited by spin-coating on top of the working electrode (ITO). Using a signal generator, a varying potential is applied between the working electrode and the reference electrode, typically Ag immersed into a solution of AgCl 3M. The potential is swept backward and forward, and the resulting current in the working electrode is registered. This current is the response of the electrochemical reactions occurring at the working electrode due to the potential variation, and thus, the oxidation and reduction processes occurring at the polymer can be inferred. The onset potentials at which the redox reactions are taking place indicate the HOMO and LUMO levels. Table 3.1 shows the obtained HOMO and LUMO levels for the two PFP derivatives and for the commercial polymer poly(9,9-dihexyl-2,7-fluorene) (PFC_6, from Aldrich).

Polymer	**HOMO (eV)**	**LUMO (eV)**	**E_{gap} (eV)**
PFC_6	-5.70	-2.49	3.21
PFP:Br_2	-5.53	-2.70	2.83
PFP:$(CN)_2$	-5.53	-2.63	2.90

Table 3.1 – Electrochemical data obtained from the stabilized voltammograms.

The voltammetric charge for both processes is similar and indicates a reversible reduction (doping n) and oxidation (doping p) process. The reversibility of both processes is evaluated according to the potential difference between the oxidation and reduction processes. In summary, PFP derivatives reveal electrochemical stability as a result of both electron and hole injection. However, more recent studies have revealed that a slight degradation is favoured during the reduction process [Molina07].

3.2 Thickness calibration of spin-coated active layers

As will be shown in the following sections, active layer thickness is a key parameter that determines the electrical and optical performance of the PLED. According to this, it is of great importance to achieve a good control of this parameter in order to process reproducible device structures. In order to calibrate the active layer thickness, several thin films were deposited by spin coating from solutions at different concentrations. It should be mentioned that thickness may slightly vary with the employed solvent for a fixed concentration. Thicknesses were measured using a profilometer as explained in the previous chapter. The calibration was performed for two commercial polymers poly(2-methoxy-5-{3',7'-dimethyloctyloxy}-p-phenylenevinylene) (MDMO-PPV, Aldrich) and poly-(3-hexylthiophene) (P3HT, Aldrich) and for the bromide and cyanide PFP derivatives.

3.2.1 P3HT and MDMO:PPV

P3HT is a regioregular polythiophene and MDMO-PPV is a phenylenevinylene derivative, both having main emission peaks centred at around 635 nm and 585 nm respectively. Figure 3.5 shows their chemical structure.

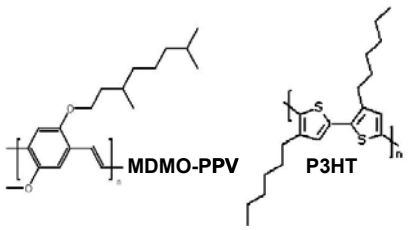

Figure 3.5 – Chemical structure of MDMO-PPV and P3HT

In general, PLED active layers thicker than 100 nm are not desirable since electrical conduction may be hindered due to the polymer low mobilities. In the opposite limit, very thin layers (below 40 nm) are usually discarded since short-circuits arising from imperfections such as surface roughness or impurities are favoured. In order to obtain the desired thickness using spin-coating, polymer solutions of a few percentages in weight are sufficient.

Figure 3.6 displays the thickness calibration curves for both polymers, using toluene as solvent. Concentrations of around 2.5% for P3HT and 1.75% for MDMO:PPV will be sufficient

to obtain adequate thicknesses (ranging from 80 to 120 nm), for spinning speeds of 4000-6000 rpm. In general, a square-law is observed, except for low concentrations < 1 %.

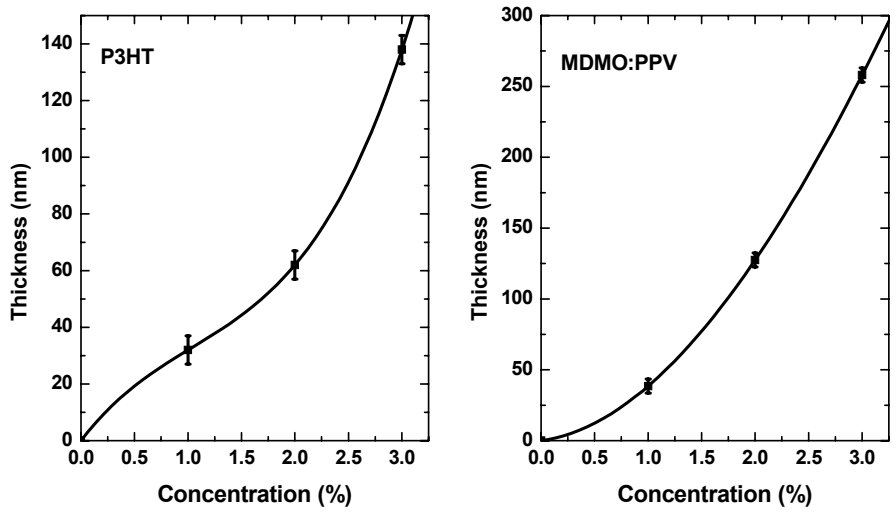

Figure 3.6 – Thickness calibration curves for P3HT and MDMO-PPV in toluene. Error bars indicate the profilometer resolution is 5 nm.

It should be noticed that these calibrations are valid as long as the same solvent and polymer molecular weight (same batch) are used.

Sample thicknesses were measured in a region of 1 cm diameter around the centre of the sample, since the film quality appears to be more homogeneous in this area than at the edges. Figure 3.7 shows photographs of the deposited films taken with a Nomarsky microscope of interferential contrast and a magnification of 1000. As can be observed, a significant amount of defects is present at the film edges while they do not appear at the centre. These defects are the consequence of non-dissolved particles that are spinned towards the sample boundaries. This indicates a better film quality in the central region.

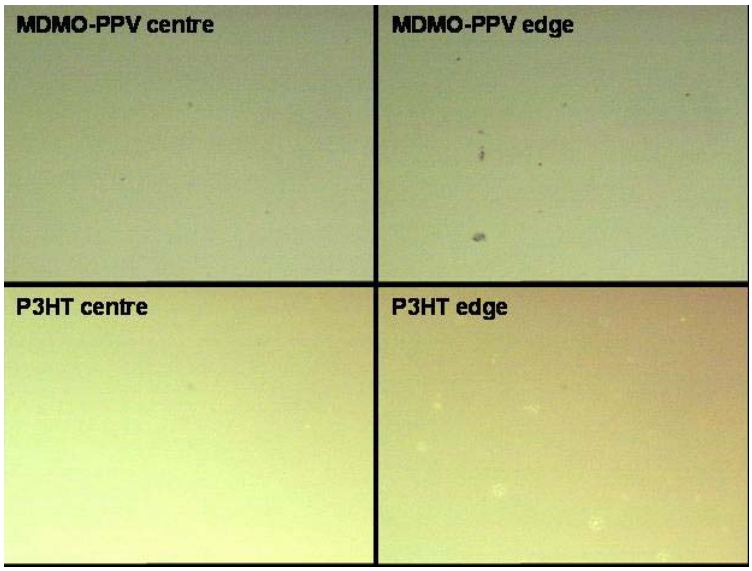

Figure 3.7 – Photographs of deposited films of P3HT and MDMO-PPV.

It is worth mentioning that solution concentrations corresponding to each data point in Figure 3.6 were obtained separately. This means that lower concentrations were not obtained by re-dissolving from a "mother" solution at a higher concentration. Resulting thicknesses from this latter method are not always reproducible, due to irreversible interactions between the solvent and the polymer. The nature of these interactions is not yet clear.

On the other hand, molecular weights above 200000 g/mol result in polymer films with a high degree of superficial roughness, though they dissolve easily at first glance.

3.2.2 Polyfluorene derivatives

Figure 3.8 illustrates the thickness calibration for the PFP derivatives in a toluene solution. The significant differences in thickness for similar concentrations between both derivatives could be attributed to the great variability of molecular weight from batch to batch of synthesized polymer. Within the same batch, fine control of layer thickness is achieved by tuning the spinning rate. In our case, a thickness reduction not higher than a 20% was observed as increasing spinning rate from 4000 r.p.m to 10000 r.p.m. At lower speeds, it was found that the probability of vortices and other features associated with an irregular solvent evaporation is increased. Although these curves may be useful as indicative guidelines to establish solution

concentration for a desired thickness, reproducibility is only achieved under a rigorous control of the solution preparation, including temperature [Álvarez03]. In OLED technology this is not a critical constraint. In any case, it is recommended to deposit a film sample to verify the active layer thickness at every fabrication.

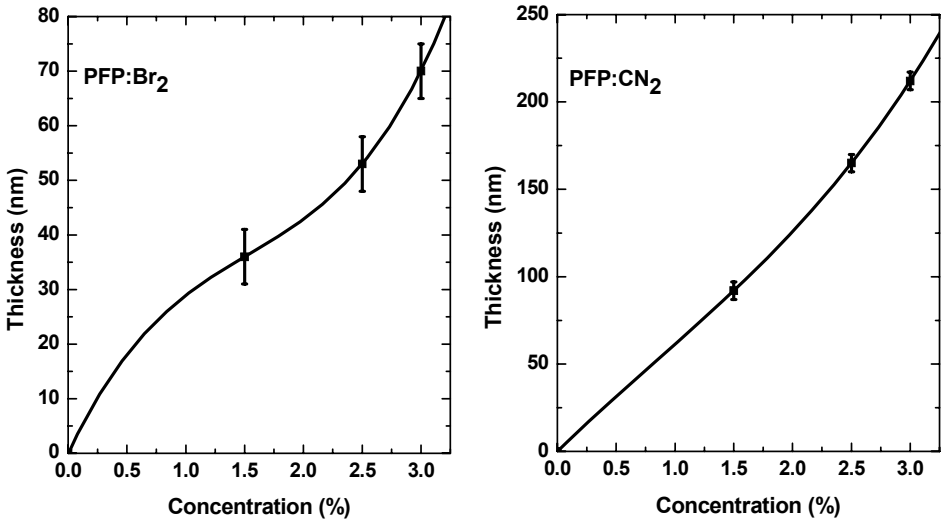

Figure 3.8 – Thickness calibration curves for PFP:Br_2 and PFP:$(CN)_2$ in toluene. Error bars indicate the profilometer resolution is 5 nm.

Figure 3.9 shows a photograph of the polyfluorene films. PFP derivatives exhibit a very good film quality, homogeneous and free of defects, indicating that they are well dissolved. The scratched line employed to measure the sample thickness by contact profilometry is also displayed for the cyano derivative.

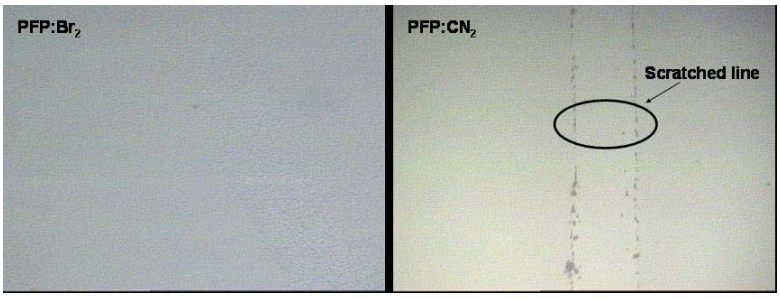

Figure 3.9 - Photographs of deposited films of PFP:Br_2 and PFP:$(CN)_2$.

3.3 Fabricated structures and electrical characterization results

This section presents the fabricated PLED passive matrix using PFP:Br_2 and PFP:CN_2. The PLED electrical behaviour is discussed by studying the J-V characteristics. In order to study the influence of the active layer thickness on the electrical performance, other structures using commercial polymers are fabricated and measured. The effect of encapsulation is analyzed in terms of electrical device degradation.

3.3.1 Comparison of polyfluorene derivatives with commercial blue polymers

Using the photolithographic techniques explained in chapter 2, three PLED passive matrices with structures ITO/PEDOT:PSS/PF/Al were fabricated having as active layers PFP:Br_2, PFP:$(CN)_2$ and PFC_6. The latter is a commercial polyfluorene from Aldrich that was used for comparison. Table 3.2 summarizes the characteristics of each PLED structure at room temperature.

Active Layer	Emission λ (nm)	Thickness (nm)	Areas (mm^2)
PFC_6	≈420	≈120	0.8 , 1.8
PFP:Br_2	≈420	≈120	0.8 , 1.8
PFP:$(CN)_2$	≈420	≈120	0.8 , 1.8

Table 3.2 – PLED structures based on three different polyfluorenes: PFC_6, PFP:Br_2, PFP:$(CN)_2$.

J-V characteristics were registered using a pulse train (pulse width of 0.5 % in a period of 100 ms) in order to minimize possible device degradation. Figure 3.10 shows that PFC_6 diodes exhibit the lowest threshold voltage (V_{th}), while those based on PFP derivatives show similar electrical performance. However, subsequent EL measurements revealed that PFP:$(CN)_2$ diodes are the most efficient (for a similar operating current), well above those based in PFC_6. As will be mentioned later, the emission of PFP:Br_2 based diodes was found to be very poor in most batches.

The threshold voltage depends directly on the carrier injection barrier at the interface (ϕ). In the case of a current dominated by holes, the injection barrier is, in a first approximation,

determined by the energy difference between the polymer HOMO level and the ITO/PEDOT:PSS work function. However, recent studies reveal that this initial approximated value for ϕ is modified when the two materials are put in contact, since the vacuum level may differ before and after the contact is made [Ishii02]. This is due to a narrow dipole layer formed at the metal-polymer interface as a result of local charge transfer. Thus, this dipole may be deliberately modified introducing very thin layers (< 1 nm) of appropriate materials in terms of electro-affinity, such as lithium salts (LiF) or metal oxides (Al_2O_3). Moreover, ITO work function may vary from 4.6 to 5 eV, depending on the previous ITO treatment [Li05]. In consequence, the difference in V_{th} between the PFC_6 and the PFP derivatives cannot only be attributed to a difference in the HOMO levels, but it can reflect a compendium of other variables such as interfacial mechanisms or mobility. In fact, as will be studied in chapter 4, conduction mechanisms in organic materials are extremely dependent on the energetic and microscopic positional disorder inside the polymer. On the other hand, similar values of V_{th} for both PFP derivatives confirmed that electrical properties of polymers are mainly determined by the polymer backbone, while functional groups in the lateral chains rather affect solubility and optical properties.

As expected, V_{th} did not show a clear dependenceon diode area within each sample.

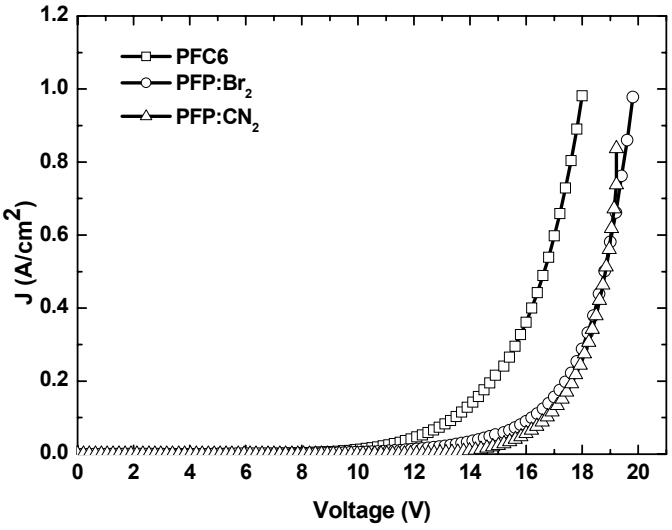

Figure 3.10 - J-V characteristics of PLEDs with structure ITO/PEDOT:PSS/PF/Al based on PFC_6 (squares), $PFP:Br_2$ (circles) and $PFP:(CN)_2$ (triangles). Thickness = 120 nm.

3.3.2 Influence of the active layer thickness

In order to study the influence of active layer thickness on the PLED electrical performance, several PLED passive matrix with structure ITO/PEDOT:PSS/Active Layer/Al were fabricated using different active layers and for different thicknesses.

Table 3.3 and 3.4 summarize the fabricated structures for P3HT, MDMO:PPV and PFP derivatives as emissive layers. Active layer films were deposited from a polymer solution in toluene. Every passive matrix contained eight diodes of two different areas. Emission peak wavelengths were determined at room temperature.

Active Layer	Emission λ (nm)	Thickness (nm)	Areas (mm^2)
P3HT	635	60	0.8 , 1.8
P3HT	635	100	0.8 , 1.8
P3HT	635	140	0.8 , 1.8
MDMO-PPV	585	60	0.8 , 1.8
MDMO-PPV	585	100	0.8 , 1.8
MDMO-PPV	585	140	0.8 , 1.8

Table 3.3 – Summary of fabricated PLEDs using as active layer P3HT and MDMO-PPV for different thicknesses. Emission peak registered at room temperature.

Active Layer	Emission λ (nm)	Thickness (nm)	Areas (mm^2)
PFP:Br_2	≈ 420	33	0.8 , 1.8
PFP:Br_2	≈ 420	45	0.8 , 1.8
PFP:Br_2	≈ 420	73	0.8 , 1.8
PFP:Br_2	≈ 420	115	0.8 , 1.8
PFP:$(CN)_2$	≈ 420	55	0.8 , 1.8
PFP:$(CN)_2$	≈ 420	95	0.8 , 1.8

Active Layer	Emission λ (nm)	Thickness (nm)	Areas (mm^2)
PFP:$(CN)_2$	≈ 420	140	0.8 , 1.8
PFP:$(CN)_2$	≈ 420	180	0.8 , 1.8

Table 3.4 - Summary of fabricated PLEDs using as active layer PFP derivatives for different thicknesses. Emission peak registered at room T.

Figure 3.11 shows the dependence of the J-V characteristic on the active layer thickness for PLEDs based on P3HT and MDMO-PPV. It can be observed that the threshold voltage increases considerably with the active layer thickness.

At first glance this could be interpreted as a current limitation due to the bulk mechanism. However, it should be remembered that all the injection mechanisms are electric-field dependent. Consequently, a field reduction caused by a thickness increase should also result in a decrease of injected carriers, followed by a V_{th} shift towards higher voltages. In chapter 4, a model to quantify both contributions to the V_{th} shift will be proposed.

Thus, for the diodes which are being investigated, both processes should be simultaneously analysed.

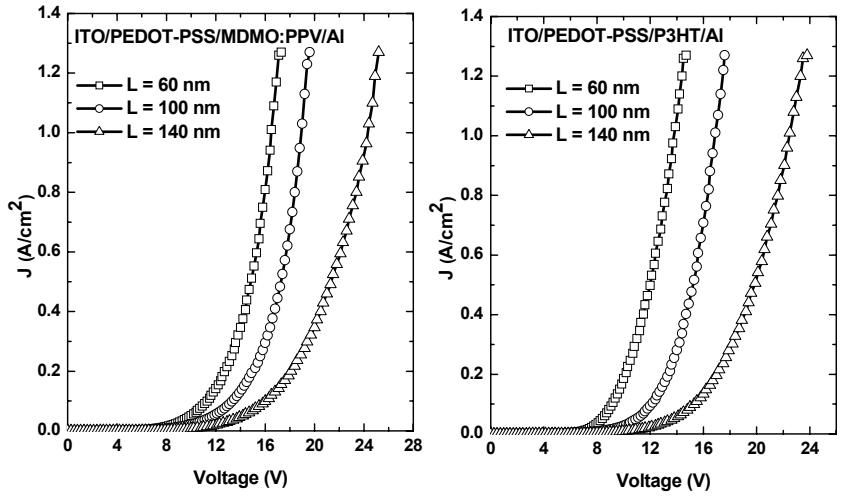

Figure 3.11 – J-V characteristics of PLEDs with structure ITO/PEDOT:PSS/Active Layer/Al based on P3HT and MDMO-PPV for different active layer thicknesses.

From Figure 3.11, it can also be inferred that for similar active layer thicknesses, V_{th} is higher for MDMO-PPV than for P3HT based diodes, concluding that V_{th} seems to be correlated to the LUMO and HOMO energy difference. As the excitonic "gap" of the active layer increases so does the threshold voltage of the device.

Figure 3.12 shows a similar electrical behaviour as increasing thickness for the PFP active layer.

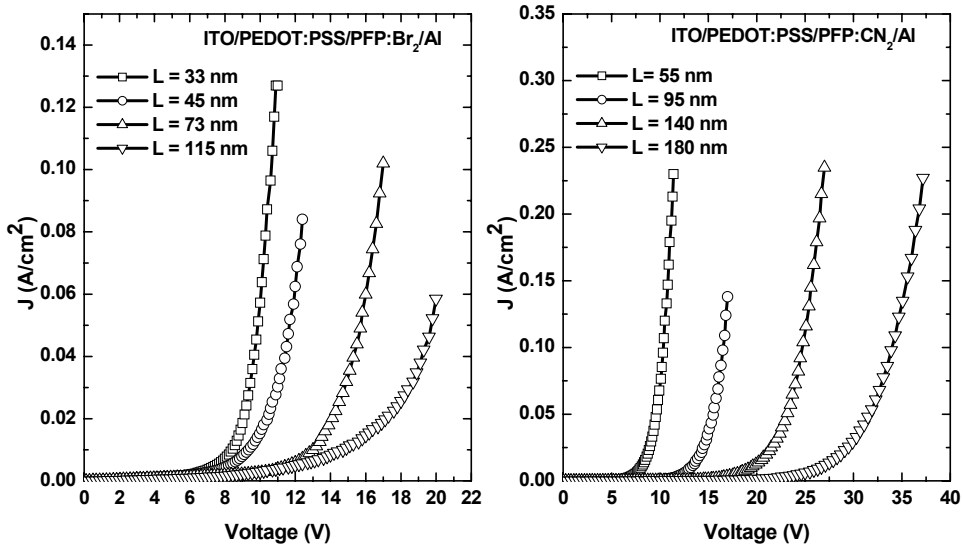

Figure 3.12 - J-V characteristics of PLEDs with structure ITO/PEDOT:PSS/PF/Al based on PFP:Br_2 and PFP:$(CN)_2$ for different active layer thicknesses.

Electrical transport in undoped conjugated polymers is similar to that of semi-insulating materials, meaning that the injected charge via the metal contact is significantly larger than the residual free charge. Then, charge transport along the bulk is dominated by space charge currents. In the case of a negligible injection barrier and a trap-free material, charge transport follows the well known Mott-Gurney law [Mott48],

$$J_{SCLC} = \frac{9}{8}\varepsilon_o \varepsilon_r \mu \frac{V^2}{L^3} \qquad [3.1]$$

where L is the active layer thickness and μ is the mobility. This expression will be given deeper consideration in section 4.1.2. According to this equation, current across the diode should scale with thickness as $1/L^3$. However, as mentioned before, this is a simplistic approximation for the case of ohmic contacts. For all structures listed in Table 3.3, an injection barrier is present due to the energy difference between the ITO work function and the HOMO level of the polymer. For the MDMO-PPV and P3HT diodes, injection barriers may be around 0.4-0.6 eV depending on ITO work function. In the case of PLEDs based on PFP derivatives, injection barriers are even higher. According to Table 3.1, these may go up to 0.7-0.8 eV. In order to study PLEDs conduction mechanisms, a complete theoretical model will be presented in chapter 4 in which both, injection and transport processes are considered.

3.3.3 Improved performance of encapsulated devices

A study of the effect of encapsulation on device lifetime was carried out in MDMO-PPV based PLEDs. Two identical diode passive matrices were fabricated, but one was encapsulated and the other one was left with the aluminium uncovered. The encapsulation process was done in an inert atmosphere as described in section 2.2.2.6.

Active Layer	Emission λ (nm)	Thickness (nm)	Encapsulation	Area (mm^2)
MDMO-PPV	585	73	No	0.8, 1.8
MDMO-PPV	585	73	Yes	0.8, 1.8

Table 3.5 –Two identical MDMO-PPV PLEDs: with and without encapsulation.

All electrical measurements were taken in an air atmosphere. Both diodes underwent an electrical conditioning process that lasted for two hours before the current density was beginning to be measured. During that time the duty cycle of the input signal was 0.5% in order to minimize device degradation. This electrical conditioning process is performed to ensure that the current reaches a stationary value. It is a well known process in PPV and PF based diodes that when using ITO/PEDOT:PSS as the anode contact, the current through the diode is enhanced after the first few voltage cycles [Woudenberg01]-[Woudenberg04]. This is attributed to the presence of electron traps near the anode interface, PEDOT:PSS/Polymer. These trap charges do not contribute to the current, but they contribute to build up an electric field that causes the enhancement of hole injection.

Figure 3.13 shows the evolution of the current density at a fixed voltage as a function of time for the non-encapsulated PLED. In order to accelerate the aging process, measurements conditions were hardened on the second day. Measurements were taken every 15 minutes for six hours during two consecutive days. For the first six hours the current increases as a consequence of the above mentioned process. During the second day, the current starts fluctuating and, at the end of the day, the current was 50% of the initial value. The diode appeared to be extremely degraded when observed using a microscope.

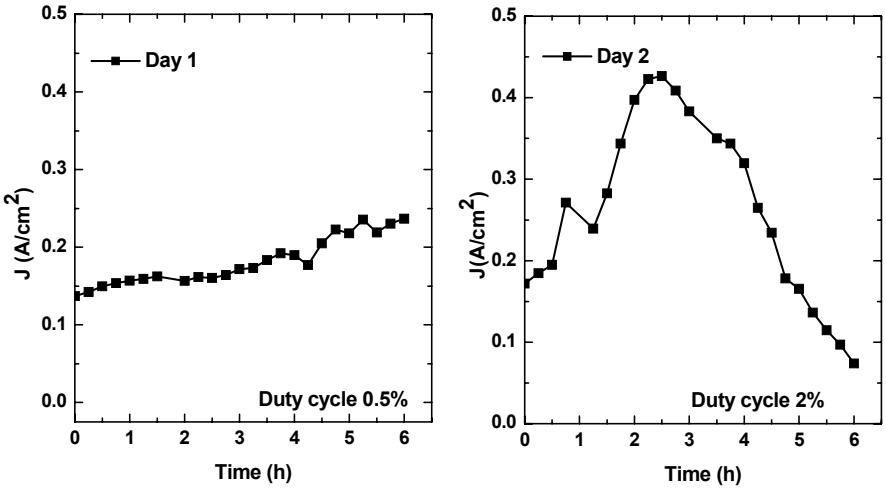

Figure 3.13 – Current density as function of time for the non- encapsulated MDMO-PPV diode.

The degradation of PLEDs occurs as a consequence of morphological changes in the polymer backbone due to the interaction with oxygen and moisture. These changes are enhanced in the presence of U.V. light. The degradation is accompanied by the appearance of strong fluctuations in the current and optical emission, together with a variation of the film resistance [Savvateev97]. These fluctuations are reflected in Figure 3.13. Moreover, the optical emission whitens as the degradation intensifies [Gammerith04]. Visible morphological changes due to the degradation can be observed in the microscope. First, the formation of “bubbles” at the aluminium/polymer interface due to the delamination of the polymer film from the metal surface. The bubble formation was enhanced at high current densities. Second, carbonized areas in the form of “black spots” are formed, see Figure 3.14. These black spots originate nonconductive regions at the cathode/organic interface and expand or grow as a result of

exposure to atmosphere. The dark spots are attributed to regions of poor electron injection formed by local oxidation [Kolosov01].

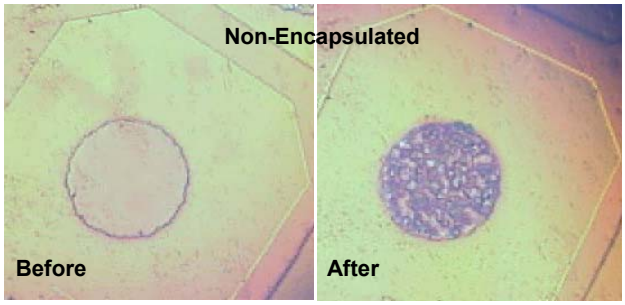

Figure 3.14 – Photograph of the non-encapsulated diode before and after 12 operating hours.

Figure 3.15 displays the evolution of the current for the encapsulated PLED. Again, measurements were taken every 15 minutes for six hours during three consecutive days. The current in the figure below is maintained almost constant along the three days, and it does not suffer from strong fluctuations, indicating that no significant morphological changes take place.

Figure 3.16 shows the encapsulated diode before and after the operating interval. Slight indications that degradation is beginning to occur can be observed. It should be noted that due to the glove box conditions, during the encapsulation process probably not all the oxygen is removed from the sample.

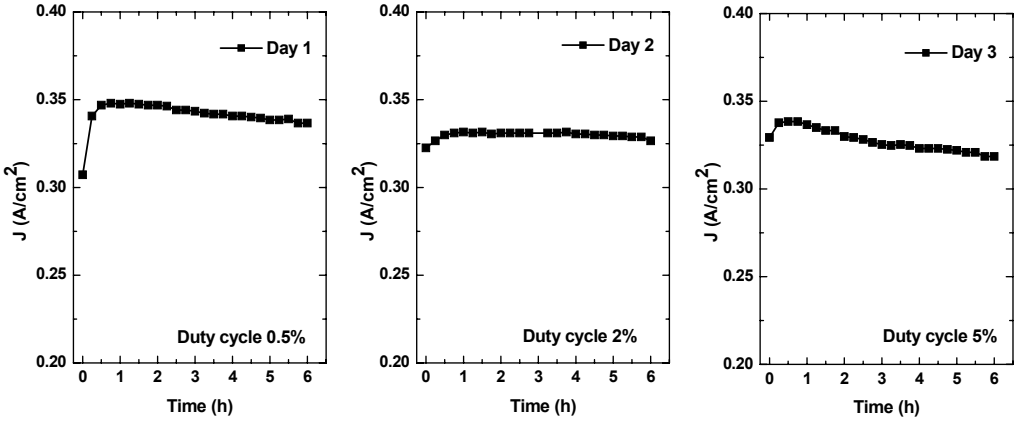

Figure 3.15 – Current density as function of time for the encapsulated MDMO-PPV diode.

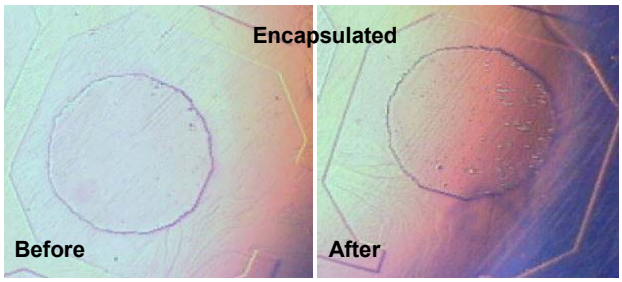

Figure 3.16 - Photograph of the encapsulated diode before and after 18 operating hours.

Figure 3.17 illustrates the evolution of the J-V characteristic after several days of continuous functioning. While the encapsulated device maintains a constant electrical response for three days, the non-encapsulated device decreases the current down to 17% of the initial value at the second day of operation. In summary, it is demonstrated that a simple encapsulation technique is essential to improve PLED electrical lifetime.

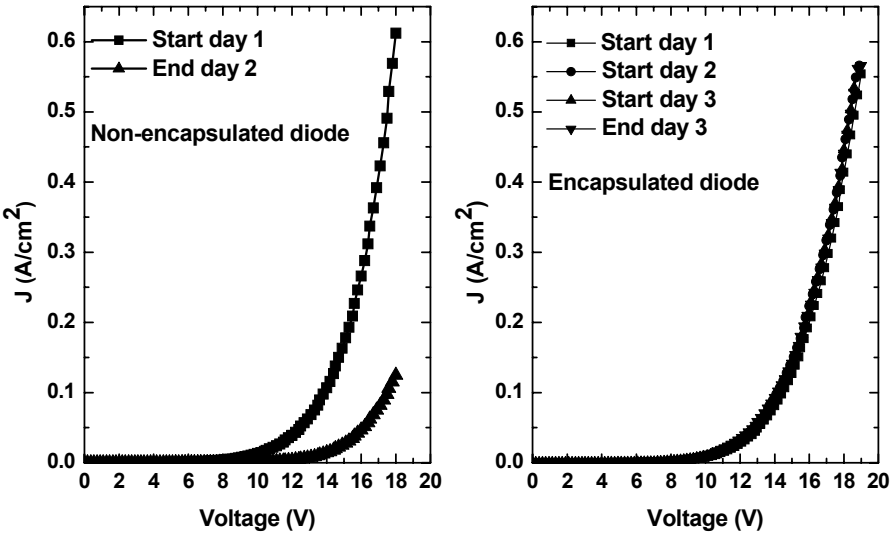

Figure 3.17 – Evolution of the J-V curve after few days of continuous functioning for encapsulated (right) and non-encapsulated (left) diodes.

3.3.4 Admittance spectroscopy (AS) characterization. Small signal equivalent circuit.

Measurements of admittance as a function of frequency in organic materials can be used to study carrier transport by means of charge-relaxation processes. Details on this technique are provided in chapter 2. In this section we present a simplified interpretation of the measurements in terms of an equivalent circuit. This procedure may be easily used to estimate the order of magnitude of the material mobility.

Figure 3.18 shows the experimental Cole-Cole plots, Im(Z) vs Re(Z) (symbols), for impedance measurements of PLEDs with MDMO:PPV (a) and PFP:$(CN)_2$ (b) as active layers. The frequency dependent, complex impedance reveals a Cole-Cole diagram consisting approximately of a semicircle, where the low frequency region is on the right side. The noise affecting the low frequency records (below 100 Hz) degrades in some cases the quality of the plot.

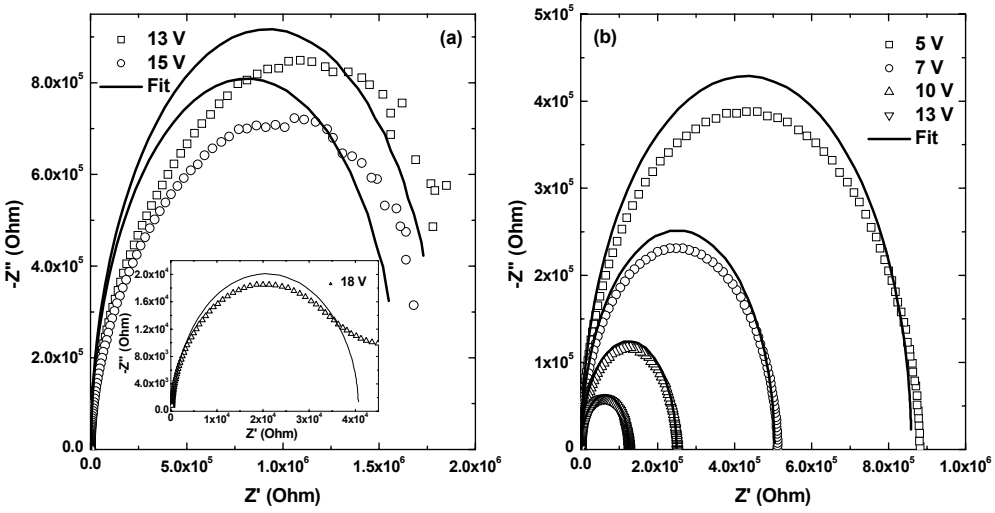

Figure 3.18 - Cole-Cole plots with frequency as the implicit variable for a PLED based on (a) PFP:$(CN)_2$ and (b) MDMO:PPV at different bias. Solid lines are the fit to an equivalent circuit shown in Figure 3.19.

Taking into account that the Cole-Cole plot of a capacitor in parallel to a resistor yields a perfect-semicircular plot, our experimental results indicate that the behaviour of our devices is not far from this circuital paradigm [Barsoukov05].

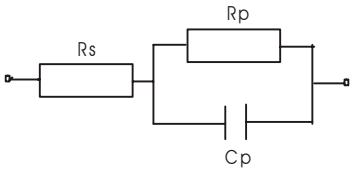

Figure 3.19 - Small signal equivalent circuit of the AS response.

This type of AS response is often measured in a wide variety of solids. Any structure of the type electrode-semi-inslulating-electrode exhibits a parallel capacitance C_p that represents the geometrical capacitance $C_{geo} = \frac{\varepsilon A}{L}$ and a bulk resistance in parallel with it, R_p (=R_∞). These elements lead to a time constant, $\tau_r = R_p C_p$, which is called the *dielectric relaxation time* of the basic material.

Series resistance takes into account soldering effects and sheet resistance (Ω/sqr) due to the ITO tracks. After correction for the contact and track resistance we can assume a parallel RC-circuit description in which the admittance can be expressed as $Y = G + j\omega C$ where G is the conductance and C the capacitance. This circuital assumption is generally accepted and will be adopted to obtain the capacitance and conductance from the admittance small signal model proposed in next chapter.

Solid lines in Figure 3.18 represent the fits to the equivalent circuit of Figure 3.19. The parameters obtained from the fit are summarized in Table 3.6:

	PFP:$(CN)_2$			**MDMO:PPV**			
	13 V	**15 V**	**18 V**	**5 V**	**7 V**	**10 V**	**13 V**
R_p (MΩ)	1.83	1.62	0.04	0.86	0.5	0.25	0.12
C_p (nF)	2.12	2.03	1.37	0.49	0.47	0.45	0.43

Table 3.6 – Resulting parameters obtained from the fits shown in Figure 3.18.

The series resistances were found to be around 500 Ω and 1kΩ for the MDMO and PFP:$(CN)_2$ based diodes respectively.

Considerable difference between modelled and experimental curves is attributed to the characteristic structural and energetic disorder of the organic materials. This disorder has a major influence on the material transport properties, and results in a dispersive transport with a frequency dependent mobility. Therefore, one should remark that this circuital representation is a simplistic approach to model small signal conduction in PLEDs. A full admittance model, taking into account the effect of the stationary space charge as well as disordered parameters (i.e. dispersive transport) will be developed in chapter 4. However, we can use this equivalent circuit to estimate, in a first approximation, the polymer mobility for every bias. The mobility is given by

$$\mu = \frac{L^2}{V\tau_t} \qquad [3.2]$$

where L is the active layer thickness and τ_t is the carrier transit time. As will be explained later, the relaxation time ($\tau_r = C_p R_p$) may be related to the average transit time by $\tau_t = 0.56\tau_r$ [Tsang06]. In the case of highly dispersive transport the scaling factor 0.56 varies ± 0.1.

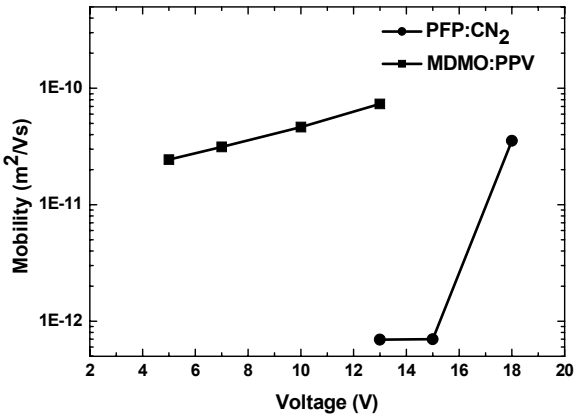

Figure 3.20 - Derived mobility for a MDMO-PPV and a PFP:$(CN)_2$ based diode from the fit to the equivalent circuit of Figure 3.19.

Figure 3.20 shows the derived mobility using the fitting parameters of Table 3.6 and equation [3.2]. This is a simple and useful method to obtain a good approximation of the dependence of mobility with bias. However, one should insist in the fact that this is not a rigorous procedure to model transport in organics since it does not take into account neither space charge nor disorder. In chapter 4, a complete model for the admittance will be used to calculate mobility and disorder parameters from admittance measurements. According to the mobilities that will be obtained using the admittance model, it can be said that circuital modelling can be used to predict mobilities within the same order of magnitude and with an error that can go up to 30%.

3.4 Results of the optical characterization

Optical characterization of any type of display requires bearing in mind certain aspects related to the emissive ability. The most relevant ones are: brightness, colour matching within the targeted specifications and longevity in operation. The term brightness describes the light intensity with respect to the wavelength sensitivity of the human eye. Actually brightness is an obsolete term that has been substituted by luminance (energy perceived by the eye, per solid angle through unit area). The eye response curve for the average observer follows an approximate Gaussian curve, with a maximum at the yellow-green wavelength and falling off rapidly towards both the red and blue, see Figure 3.21. This has significant implications when designing organic displays, since it means that for a green and red pixel to be perceived at the same brightness level, the red material must emit a greater number of photons than the green one.

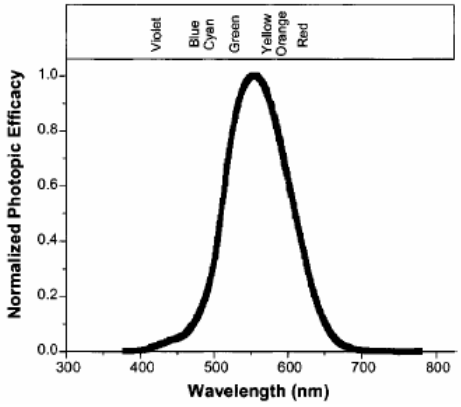

Figure 3.21 – CIE photopic luminous efficiency describing the spectral distribution of luminous energy and the efficacy factor upon the eye [CIE90].

Colour tuning is an important issue in organic devices. Due to the disorder of the polymer structure, emission peaks will be broad, with a full width at half maximum (FWHM) approaching 60-70 nm for monochromatic sources. Typical 40-50 nm are measured in bulk inorganic crystalline materials. Colour is calculated using the integral of spectral emission as a function of wavelength against the chromatic sensitivity of the eye. This results in a set of coordinates on a chromaticity graph defined by international standards given by the *Commission Internationale de l'Eclairage (CIE)*.

In this section, optical characterization was carried out for the MDMO and PFP based PLEDs using different measurements conditions. Electroluminescence, luminance and efficiency were determined for each material. In section 3.4.2, degradation mechanisms were studied for blue PLEDs, and device lifetime was estimated by measuring the spectra as a function of time.

3.4.1 Electroluminescence, luminance and CIE coordinates

Optical characterization requires long times of continuous operation in order to register the EL at different measurements conditions. This may imply the device degradation during the measurement process. In order to minimize this, small duty cycles, from 0.5% up to 10% with long refresh intervals, were employed to bias the sample during the optical measurements.

Figure 3.22 shows the normalized EL for the ITO/PEDOT:PSS/MDMO:PPV/Al diode at different bias. The emission peak is centred at 590 nm and the well known vibronic shoulder appears at around 630 nm. While the main peak is related to excitonic LUMO-HOMO transitions, the vibronic peak is associated to those exciton recombinations that are phonon-assisted, being very dependent on the material structure. The solid line represents the photoluminescence (PL) performed on a film deposited over a quartz substrate.

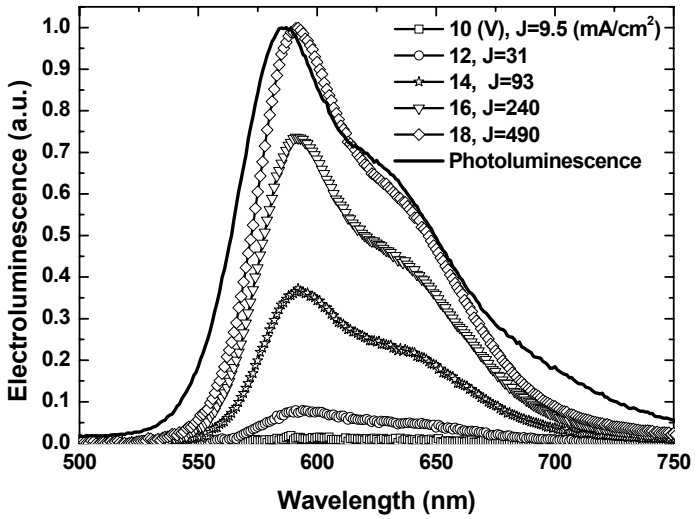

Figure 3.22 – Electroluminescence at different bias for a PLED based on ITO/PEDOT:PSS/MDMO:PPV/Al.

While specifications of point sources of filament bulb performance describe luminance intensity in candelas (cd), surface emitters are described in terms of luminance with units in cd/m^2. The material emission efficiency is obtained from the luminance and J-V curves, and is defined as the ratio of the output light intensity (cd) to the input current intensity (A).

Figure 3.23 shows both the luminance and the efficiency for a MDMO based diode. These structures were designed in order to guarantee single carrier operation for a long bias interval, so that they could be used to test the single carrier conduction model proposed in chapter 4. In this sense, PEDOT:PSS was used to enhance hole injection but no additional layers were introduced between the Al cathode and the organic layer to improve electron injection (typically LiF, or a few monolayers of group II metals, such as Ca or Ba). This unbalanced injection from both electrodes results in high hole currents but modest values for the luminance and consequently poor efficiencies. Moreover, the unbalanced amount of electrons and holes inside the device shifts the recombination zone towards the cathode, enhancing the probability of the singlet state quenching and consequently decreasing the internal efficiency.

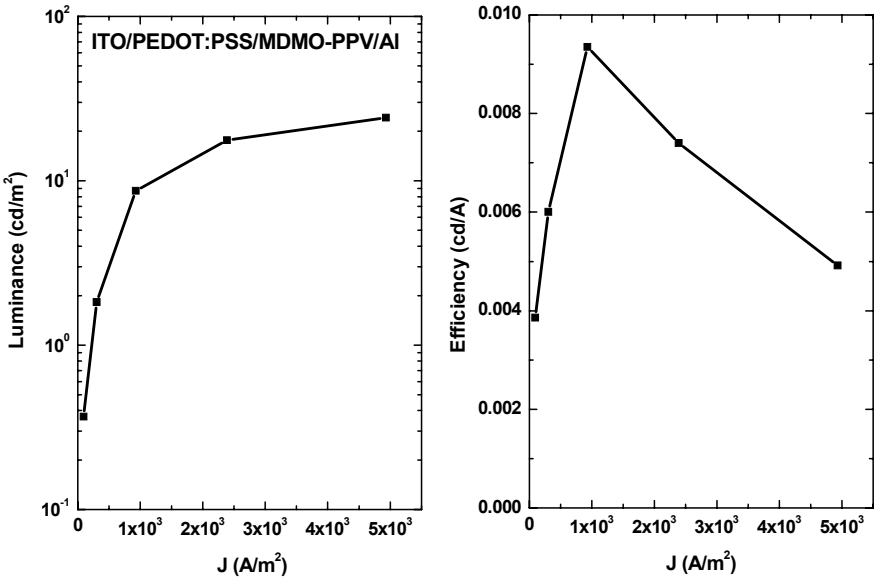

Figure 3.23 – Luminance and efficiency of a PLED with structure ITO/PEDOT:PSS/MDMO:PPV/Al.

Optimal efficiency is achieved if the two electrodes are dissimilar, specifically when the respective metals exhibit electronic work functions that closely match the HOMO and LUMO levels of the polymer. Using multilayer structures aids to balance the injected charge in the active layer as well as to locate the recombination far away from the electrodes, increasing the internal efficiency. The tandem ITO/PEDOT:PSS is the most widely used as anode, due to the reasonable vertical conductivity attributed to PEDOT:PSS (of the order of 10^2 S/cm for pure PEDOT in the layer plane), the high chemical stability (better than that of other materials such as polyaniline), its easily emulsion in water and the smoother effect that it produces on the ITO surface. However, recent studies have demonstrated that when electrons are injected into PEDOT over the PSS layer, an insoluble layer is created at the PEDOT/polymer interface resulting in a reduction of the photoluminescence and electroluminescence [Halls07]. Specifically, a loss of ohmic injection after prolonged electrical stressing was found at the interface PEDOT:PSS/polyfluorene [Papadimitratos07]. Recent investigations have demonstrated that trapped water in the organic layers (PEDOT:PSS is an emulsion in water) is likely to be the main source of electrical instability. This is attributed to the efficient traps for

charge carriers provided by the remained water in liquid phase [Gomes06]. Alternative materials to PEDOT:PSS are currently being investigated that eventually will improve the PLED efficiency [Halls07].

Figure 3.24 (a) shows the normalized EL spectra for the ITO/PEDOT:PSS/PFP:$(CN)_2$/Al diode at different bias. In order to distinguish the different emission intensity levels, the inset shows the EL normalizing each spectrum to its own maximum. As explained for the MDMO based diode, the absence of a layer to favour injection between Al and PFP indicates that this is not an optimal emissive structure, and explains the high voltage onset for EL.

The emission peak is centred at 425 nm and a well resolved vibronic shoulder appears at around 450 nm. Figure 3.24 (b) shows the PL of a PFP:$(CN)_2$ film over quartz substrate. EL and PL spectra are similar, implying that the excited states that lead to radiative recombination are the same. The vibronic peak exhibits similar or ever higher intensity values than that corresponding to the excitonic transition as bias is increased. This is a common feature in polyfluorene based diodes [Gong03-b]. It is straightforward that this indicates that phonon-assisted transitions are favoured in the same degree as excitonic band-to-band transitions, though further explanation to this behaviour is still under research.

On the other hand, a well defined peak appears at 480 nm. The appearance of this peak has been associated to the polymer degradation and it has appeared in many polyfluerene based PLEDs operating in vacuum atmosphere [Lu05]-[Gamerith04]-[Montilla07]. This feature exhibits a curious behaviour when increasing bias. The intensity of the degradation peak decreases when increasing the excitation level, in contrast to the excitonic and vibronic peaks. This can be explained in a similar way as emission from defects in inorganic materials. Defects possess a finite site density, so when bias (injected current) is increased, defect sites can be completely filled, followed by the corresponding peak reaching a saturation level. Thus, additional injected charge finds alternative ways to recombine, increasing the excitonic and vibronic peaks.

It is worth mentioning that this peak at 480 nm arises in addition to the usual green band at 530 nm, though both degradation mechanisms have different origins. Both degradation processes will be studied in detail in section 3.4.2.

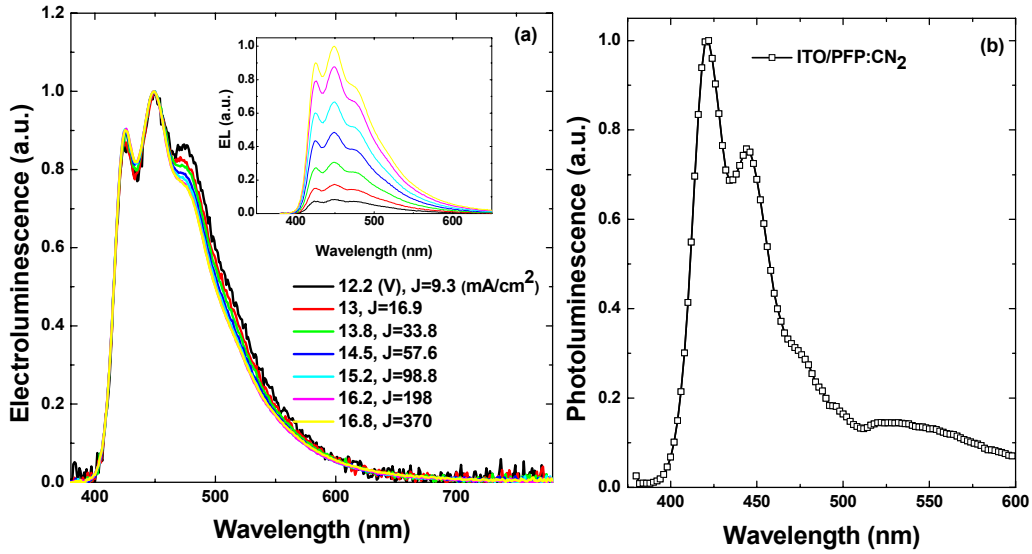

Figure 3.24 – (a) Electroluminescence at different bias for a PLED based on ITO/PEDOT:PSS/PFP:$(CN)_2$/Al. Inset shows the EL normalizing each spectrum to its own maximum. (b)Photoluminescence of PFP:$(CN)_2$ on top of a ITO coated glass.

Figure 3.25 shows the luminance and the efficiency for the PFP based diode versus current density. A luminance of 95 cd/m^2 was achieved for a threshold voltage of 14 V that corresponds to a current density of 600 A/m^2. A maximum luminance of 300 cd/m^2 at a current density of 3700 A/m^2 was accomplished. These values are in the same order of magnitude of those given in literature for similar types of polyfluorenes [Li04]-[Kanicki05]. Furthermore, the device luminance exhibits good stability when it works at several current densities.

The efficiency shown in Figure 3.25 for the PFP based diode is considerably higher than that of the MDMO-PPV device (Figure 3.23). This was expected since the PFP diode achieves higher luminance values at lower currents (as will be shown in chapter 4, hole injection barrier for the PFP diodes is about 0.1 eV higher than that of the MDMO:PPV). This result leads us to remark the excellent luminance characteristic exhibited by the polyfluorene, even in the case of unbalanced injection.

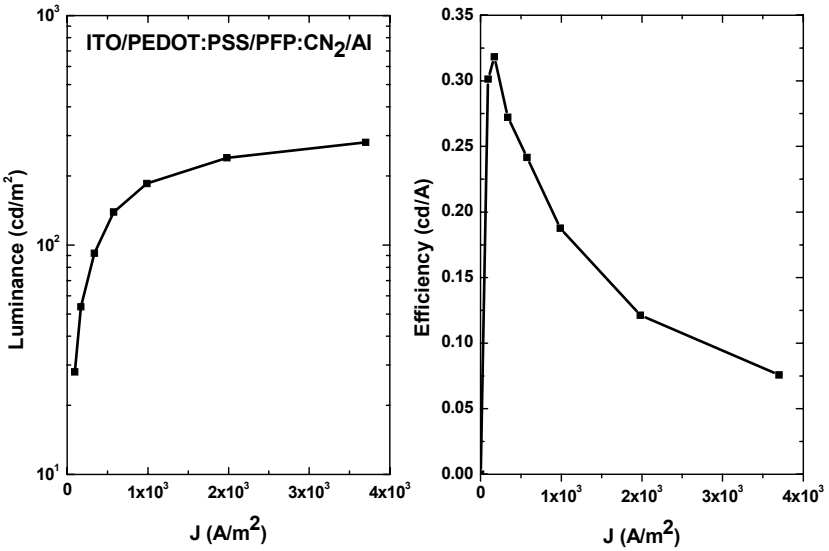

Figure 3.25 – Luminance and efficiency of a PLED with structure ITO/PEDOT:PSS/PFP:$(CN)_2$/Al.

In order to avoid device overheating, optical measurements were registered using a pulse train with a period of a 100 ms and a pulse width of 0.5 ms (duty cycle of 0.5%). Thus, to obtain the equivalent luminance in DC, the measured candelas should be multiplied by 200. This way of obtaining the DC luminance is consistent with the fact that in commercial PMOLEDs, pixels have refresh times in the order of milliseconds, i.e., they are also subjected to finite duty cycles.

Figure 3.26 shows the luminance measured with different duty cycles. It can be appreciated that the luminance has a sublineal behaviour with the duty cycle.

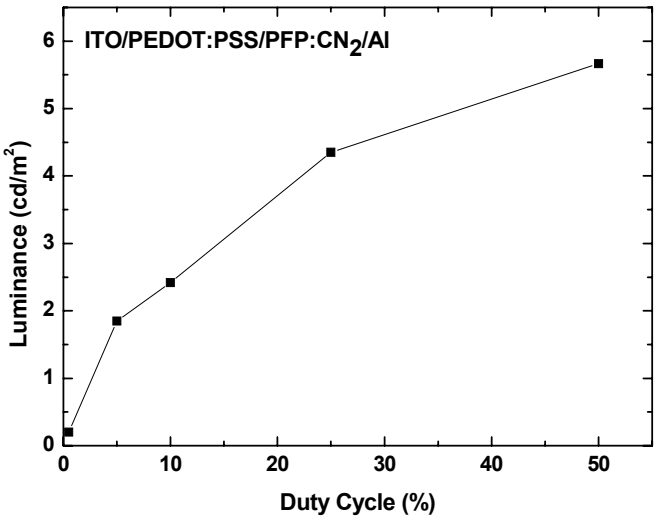

Figure 3.26 – Luminance as function of the duty cycle.

Figure 3.27 shows the colour emission on the CIE diagram for both diodes. These diagrams were provided by the "*CSS1RW*" software controlling the Minolta spectroradiometer. CIE coordinates were (0.16, 0.13) for the PFP corresponding to a deep blue colour, and (0.59, 0.4) for the MDMO corresponding to an orange-red saturated emission.

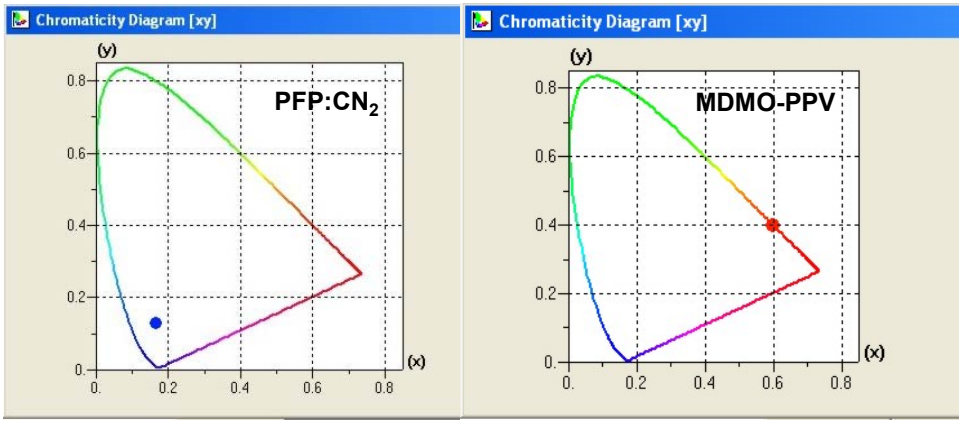

Figure 3.27 – CIE coordinates of two diodes based on PFP:$(CN)_2$ and MDMO:PPV.

The overall optical performance of MDMO:PPV and PFP:$(CN)_2$ devices are summarized in Table 3.7. These values are given for a current density of 2500 A/m^2 which is achieved at 16 and 16.5 volts for the MDMO and the PFP diodes respectively.

Active Layer	Main Emission Peak (nm)	Luminescence (cd/m^2) @2500A/m^2	Internal Efficiency (cd/A)	CIE	
				x	y
PFP:$(CN)_2$	425	250	0.110	0.16	0.13
MDMO-PPV	590	18	0.007	0.59	0.40

Table 3.7 – Summary of the optical performance for MDMO:PPV and PFP:$(CN)_2$ diodes.

3.4.2 Degradation and colour shift in polyfluorenes

The major problem of blue PLEDs made of PF is colour instability. PFs degradation mechanisms are currently the main drawback when using these materials as active layers in blue PLEDs, and consequently, this issue is the subject of numerous studies [Gaal03]-[Romaner03]-[Gamerith04]-[Montilla07]-[Gong03-b]. Two main features reveal degradation in PF materials. First, a green band centred at 530 nm is formed upon the reaction with oxygen either during device operation or under thermal annealing. A second degradation mechanism results in the appearance of a band at around 480 nm whose origin is still unclear. Both mechanisms will be discussed here.

Optical measurements were carried out on PFP:$(CN)_2$ based PLEDs as function of time, bias and pulse width. In order to identify degradation mechanisms, it is desirable that degradation occurs gradually, and this is achieved by employing small duty cycles of 0.5%. All devices employed in this study were encapsulated and all measurements were performed in air atmosphere.

Figure 3.28 shows several EL spectra registered at intervals of one hour. Together with the main blue emission and the vibronic peak at 425 nm and 450 nm respectively, a well resolved shoulder appears at around 480 nm. While the EL overall intensity level decreases after several hours of operation, it should be noticed that the relative intensity of the 480 nm peak increases with respect to that of the main emission whitening the colour emission. This is shown in the inset where the normalized intensities are plotted.

The appearance of these peaks at around 480 nm, in addition to the well known green band appearing at 535 nm, has been observed in many PLEDs even when operating in an inert atmosphere. The nature of these peaks is still unclear, though different studies seem to agree in the different origins responsible for these peaks. Several hypotheses have been proposed. Gamerith et al. suggest that the 480 nm peaks appear after the deposition of an easily oxidized metal (Ca or Al) onto fluorene-based polymer. These metals would react chemically with the polymer, forming a defect in the polymer structure, although the authors could not determine the exact nature of these interfacial defects [Gamerith04]. More recently, Montilla-Mallavia et al proposed that these peaks appear as a result of the electrochemical degradation of the polymer which would generate the formation of new C-C bonds and the modification of the aromatic rings [Montilla07]. Using an electrovoltammetry system and fluorescence spectroscopy simultaneously, they were able to characterize p- and n-doping processes in PFs. They found out that the peaks at 480 nm only appear when the polymer was degraded upon the reduction process (an excess of electrons in the material) and not during the oxidation one. Moreover, they characterized one thermally degraded sample and one electrochemically degraded sample using Infrared Spectroscopy (IR). They found out that while the IR spectra of the first one exhibits those characteristic peaks assigned to the vibrations of C=O (fluorenones), the second one does not exhibit those peaks, but instead, another peak at shorter wavelengths appears indicating the formation of new C=C bonds upon reduction.

The hypothesis of electrochemical degradation proposed to explain the peak at 480 nm would agree with the results shown in Figure 3.28.

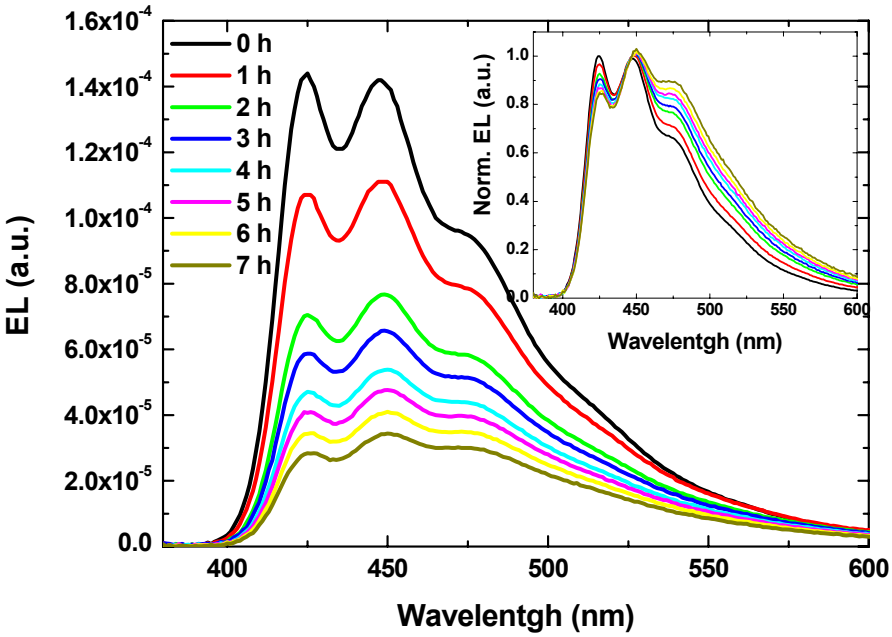

Figure 3.28 – EL spectra for a diode with structure ITO/PEDOT:PSS/PFP:$(CN)_2$/Al after seven hours of continuous operation. Inset shows the normalized EL intensity.

Indeed, when the device is operating for a prolonged time over the EL onset, an excess of electrons may be present in the material. This, in turn, would enhance the formation of new C=C bonds, and it will explain the increase of the relative intensity of the 480 nm peak with respect to that of the main emission.

Figure 3.29 shows the EL of a PFP:$(CN)_2$ based diode that has been biased at sufficiently high bias so that an excess of electrons in the device has induced electrochemical degradation. In this case, the intensity of peak at 480 nm has actually overcome that of the excitonic transition.

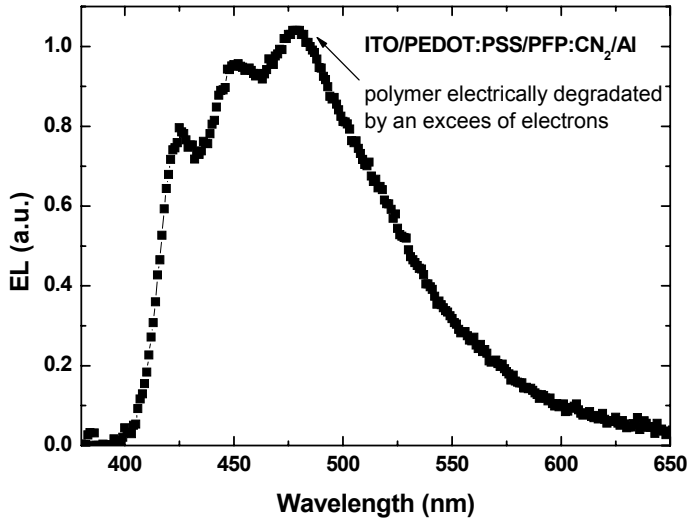

Figure 3.29 – EL of an electrically degraded PLED based on PFP:$(CN)_2$

Lifetime reliability is an important issue in PLEDs technology. Lifetime refers to that operating time corresponding to the decay of the device luminance to one-half of the initial value. Therefore, it is important to specify the initial luminance level from which measurements are taken, since lifetime may vary at different luminance starting values. In our case this value is the first time emission is observed in the pristine device.

Figure 3.30 shows the luminance versus time for the same PFP:$(CN)_2$ based diode of Figure 3.28. According to the above definition, and for a luminance starting value of 310 cd/m^2 (significantly high for a blue PLED), the lifetime of this diode was estimated to be 5.5 hours.

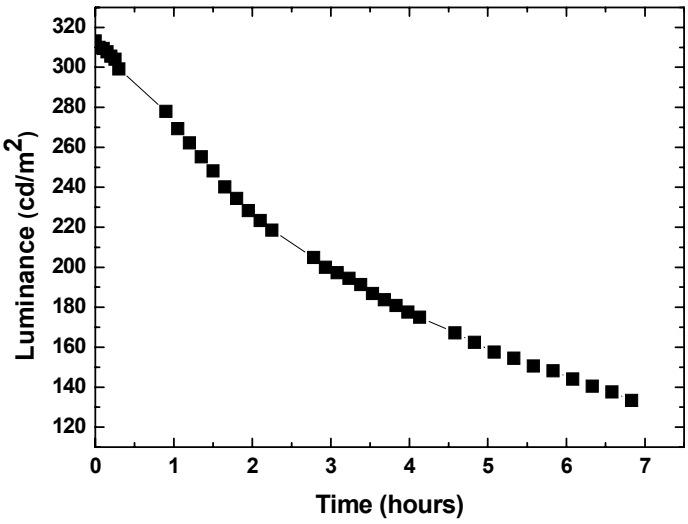

Figure 3.30 – Luminance versus time for a ITO/PEDOT:PSS/PFP:$(CN)_2$/Al after seven hours of continuous operation.

Figure 3.31 displays in a CIE diagram the colour shift of the PFP based diode after seven hours of continuous operation. A slight colour shift from the deep blue towards the centre of the diagram (white green spectral region) can be observed. The CIE coordinates of the fresh diode are (0.16, 0.13), and after seven hours of functioning they shift to (0.18, 0.2).

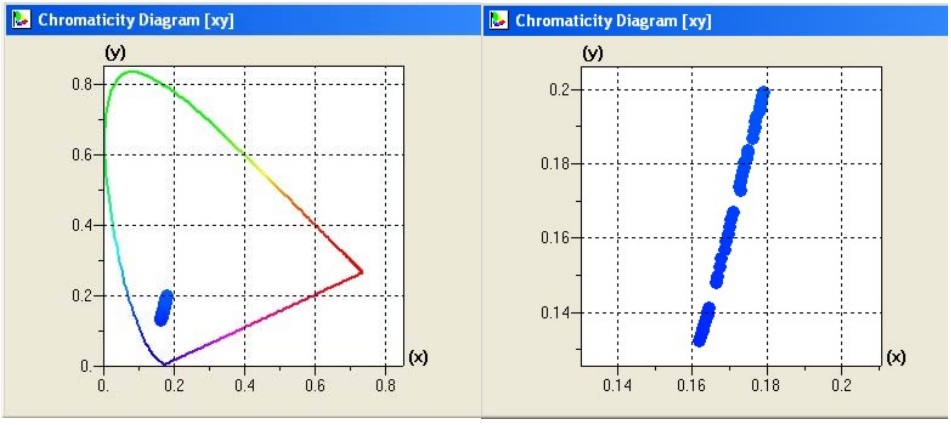

Figure 3.31 – Colour shift of a ITO/PEDOT:PSS/PFP:$(CN)_2$/Al after seven hours of continuous operation.

As it has been mentioned along this chapter, the pristine blue emission can be contaminated by an undesired low energy emission band (green band at 535 nm) during device operation or under thermal annealing. Figure 3.32 shows the EL at different bias levels of a PFP:$(CN)_2$ based diode in which degradation has occurred due to a prolonged device operation in air atmosphere. As a result of this degradation, the green band centred at around 540 nm appears, and its intensity is more pronounced as bias increases. Scherf and co-workers [List02]-[Gaal03]-[Romaner03] demonstrated that the green emission appears as a result of a defect introduced during synthesis or as a consequence of a photo- (or electron) oxidative degradation process resulting in a C=O bond at the 9-position of the fluorene. This defect is known as fluorenone defect or "keto" defect, this latter name comes from the formation of a ketone (C=O). Later on, Gong et al. corroborated this hypothesis by comparing the photoluminescence of PF films in an inert atmosphere and in air [Gong03-b]. The obtained results indicate that the intensity of the green band was progressively increasing when annealing in air, furthermore, similar results were obtained when measuring the EL spectra during device operation, but in this case, the green band was even more pronounced. This may evidence the presence of oxygen despite encapsulation, and that the formation of the keto defect is enhanced by the introduction of charge carriers into the material.

Four contributions of the emission spectra are indicated in Figure 3.32: the pristine blue emission due to the excitonic transition, the vibronic feature assigned to the phonon assisted emission, the 480 nm shoulder attributed to the formation of C=C bonds upon electrochemical degradation and the green band corresponding to the formation of fluorenone defects.

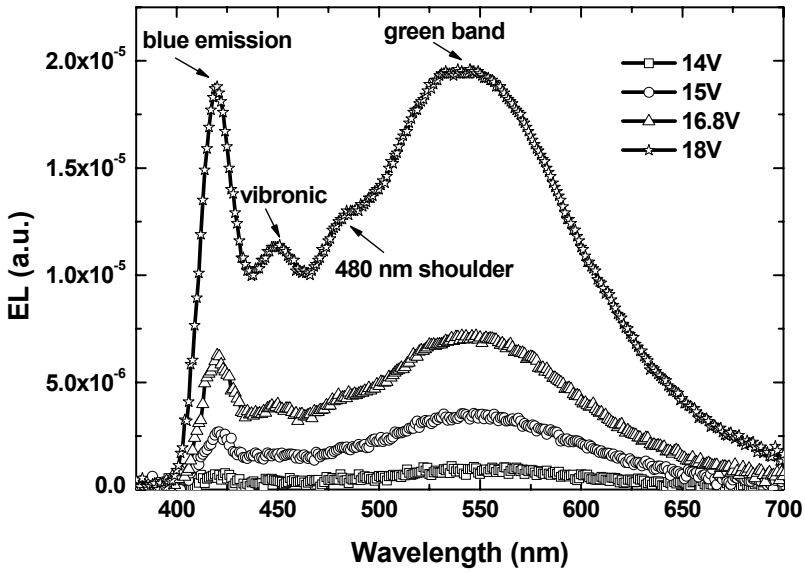

Figure 3.32 – EL spectra of a degraded PLED with structure ITO/PEDOT:PSS/PFP:$(CN)_2$/Al.

Due to the different origins of the degradation mechanisms, the EL of PLEDs based on the same PF compound can evolve in different patterns when subjected to long operation times, depending on the fabrication process and the electrical treatment employed in each one. It may occur that diodes in which no oxygen has remained inside the structure during fabrication, and that have been subjected to prolonged electrical excitement well above the EL onset, only exhibit in the first place a peak at 480 nm due to degradation caused by an excess of electrons. This is shown in Figure 3.33 (a). In contrast, if during fabrication some oxygen has entered the sample, but the diode has been subjected to an electrical conditioning at low bias, the first EL registered may exhibit a well pronounced green-white band centred a 530 nm with no traces of the 480 nm peak. Figure 3.33 (b) illustrates this latter situation.

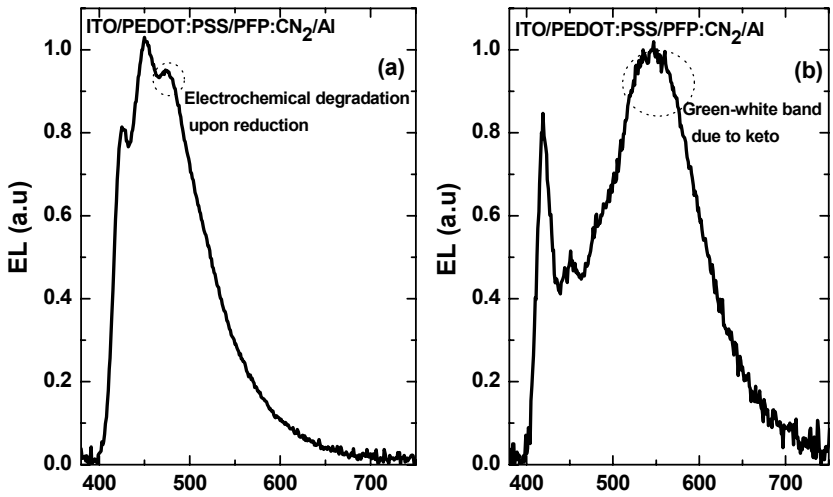

Figure 3.33 – EL spectra of two PFP based diodes fabricated in different batches and subjected to different electrical treatments.

Several attempts are being made to stabilize the blue colour of PF via chemical modifications, by introducing new chemical moieties into the PF main chain but, so far, the green band has not been completely eliminated [Setayesh01]-[Xiao03]. Further discussion on the chemical modifications of PF is beyond the scope of this thesis.

Figure 3.34 shows the CIE coordinates of the degraded PLED characterized in Figure 3.32. The emission colour is now well shifted towards the green spectral region, with CIE coordinates around (0.32, 0.41).

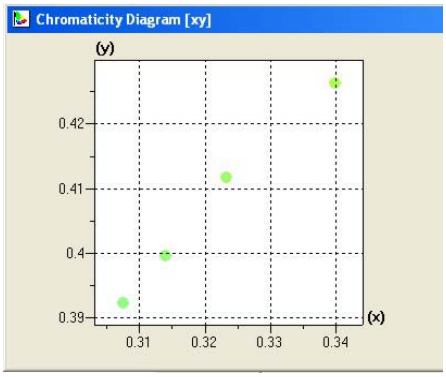

Figure 3.34 – Time evolution of CIE coordinates of a degraded PLED based on PFP:$(CN)_2$.

3.5 Conclusions

PLEDs passive matrices based on new polyflourene derivatives namely, poly(2,7-fluorene phenylidene) (PFP), have been fabricated and characterized. Comparison of PFPs with other commercial polyfluorenes like PFC_6 revealed similar electrical behaviour. Diodes using different materials and active layer thicknesses were fabricated. The diode electrical response was measured, confirming the fact that threshold voltages increase with thickness.

Besides, a study on the effect of encapsulation on the device electrical lifetime was carried out. For that purpose, two nominally equal MDMO-PPV diode passive matrices were fabricated, but while one was encapsulated in nitrogen atmosphere the other one was left in contact with air. Results show that the encapsulated diodes could operate during six hours along three consecutive days without significant electrical or morphological damage. However, a closer microscopic examination revealed that the non-encapsulated diode showed severe non-reversible morphological changes, namely, the formation of “bubbles” at the aluminium/polymer interface and the appearance of black spots that originate non-conductive regions at the cathode/organic interface. This degradation was attributed to modifications produced in the polymer chemical structure as a result of the interaction with oxygen and moisture.

A simplified small signal equivalent circuit was fitted to the diode admittance measurements. Using the circuit elements obtained from the fit, an approximated value for the mobility can be calculated. Subsequent more rigorous determinations reveal that this is a first order approximation since space charge effects and disorder parameters describing the dispersive character of transport are not taken into account.

Optical characterization of the PFP:$(CN)_2$ based diode showed a deep blue emission peak centred at 425 nm and a vibronic feature at 450 nm. Excellent luminance values are achieved for the polyfluorene structure even in the case of an unbalanced ratio of electrons and holes inside the device, as expected form the fact that the structure was not optimized for emission.

Typical degradation mechanisms traditionally attributed to polyfluorenes, were also identified in PFP based PLEDs. First, a low energy emission band centred at 530 nm appears, producing an overall colour shift towards green reflected in the CIE coordinates. This is the result of chemical changes in the polymer backbone, as a consequence of prolonged device operation or thermal annealing in air atmosphere. Oxygen reacts with the C-9 position of the

polymer main chain, creating what is called a flourenone or keto defect. A second peak at 480 nm is recognized, and although its nature is still unclear, the most reliable hypothesis suggests electrochemical degradation upon the introduction of electrons into the device. An excess of electrons inside the material would enhance the formation of new C=C bonds that eventually would result in an optical transition at around 2.5 eV.

CHAPTER 4

MODELLING OLED ELECTRICAL BEHAVIOUR

Contents

4 Modelling OLED electrical behaviour 99

4.1 Literature review of DC conduction models.....99

4.1.1 Carrier injection into organic semiconductors.....100

4.1.1.1 Classical injection approaches 101

4.1.1.2 Microscopic approach: Injection from a metal into a disordered hopping system 104

4.1.2 Carrier transport in an organic semiconductor.....107

4.1.2.1 Concept of Space Charge Limited Current (SCLC).....107

4.1.2.2 Mobility formulation in semi-insulating systems.....108

4.1.2.2.1 Classical Poole-Frenkel mobility 108

4.1.2.2.2 Gill's phenomenological mobility.....109

4.1.2.2.3 Gaussian Disorder Model (GDM).....110

4.1.2.3 Trap-controlled effective transport.....113

4.2 New proposal to model conduction in the presence of an injection barrier 114

4.2.1 Charge transport in the presence of non-ohmic contacts 115

4.2.2 Complete conduction model including hopping injection and transport mechanisms 117

4.3 Simulation results and discussion 118

4.3.1 Current dependence on device structure and material parameters 119
4.3.2 Total electric field and carrier density 122
4.3.3 Electric field at the interface versus bias 123
4.3.4 Results obtained by fitting our model to experimental J-V of PLEDs based on two different polymers: MDMO:PPV and PFP:$(CN)_2$ 124

4.4 Admittance spectroscopy (AS) model 129

4.4.1 Review of small signal (AC) techniques applied to OLEDs 130
4.4.2 Reformulation of admittance spectroscopy model in the presence of non-ohmic contacts 133
4.4.3 Simulation results and discussion 136
4.4.3.1 Dependence of capacitance and conductance on mobility and disorder parameters 136
4.4.3.2 Comparison with other admittance spectroscopy models 139
4.4.3.3 Results obtained by fitting our model to experimental admittance measurements: Determination of the hole mobility of MDMO:PPV and PFP:$(CN)_2$ 141

4.5 Conclusions 144

Chapter 4

4 Modelling OLED electrical behaviour

In this chapter a new macroscopic, analytical model of carrier transport in the presence of non-ohmic contacts is presented. This allows modelling the device's electrical performance for any injection mechanism under DC biasing, and eventually leads to a complete model for the OLED's electrical behaviour. Section 4.1 includes a detailed survey of conduction mechanisms in organic diodes. Section 4.2 presents a new contribution to the carrier transport model in the presence of injection barriers, and includes a complete model in which both, injection and transport along the bulk are taken into account. In section 4.3, simulation results are presented and the model is validated with experimental current density-voltage (J-V) characteristics. Section 4.4 takes a close look into impedance spectroscopy theory. It makes use of the previously formulated DC transport model to reformulate the small signal model in order to include the presence of injection barriers. The new AC model is used to extract mobility and other microscopic parameters by means of fitting the model to experimental curves. Finally, section 4.5 presents the most relevant conclusions.

4.1 Literature review of DC conduction models

Electrical behaviour of organic light emitting diodes has been generally interpreted by a paradigm consisting of two processes: carrier injection at the metal-organic interface and subsequent carrier transport along the bulk. In the case of large injections barriers, the conduction mechanism is limited by the amount of charge capable of overcoming such barrier and the total device current is hence called injection limited. Otherwise, if ohmic contacts are present, conduction will be limited by the maximum current an organic semiconductor can support which is determined by the electrostatic laws (Mott-Gurney formulation). This regime is called space charge limited current (SCLC) and will be thoroughly treated in section 4.1.2.1.

As follows from above, in general, I-V characteristics are modelled assuming simplifications such as injection limited or bulk limited conduction.

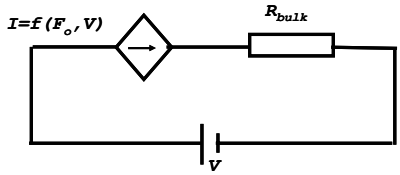

Figure 4.1 – Equivalent circuit for DC conduction. F_0 accounts for the electric field in the contact region.

In terms of an equivalent circuit, the OLED electrical behaviour under DC regime for single carrier conduction may be understood as an electric field controlled current source (injection), in series with a variable resistance, dependent on the injected space charge (bulk).

The continuity condition for the current derived from the above picture is one of the key principles of our model.

4.1.1 Carrier injection into organic semiconductors

The basic parameter that determines the injected charge from the contact to the semiconductor is the injection barrier. This injection barrier is given by the energy difference between the Fermi-level of the metal and the molecular orbital of the polymer (HOMO/LUMO) at the contact.

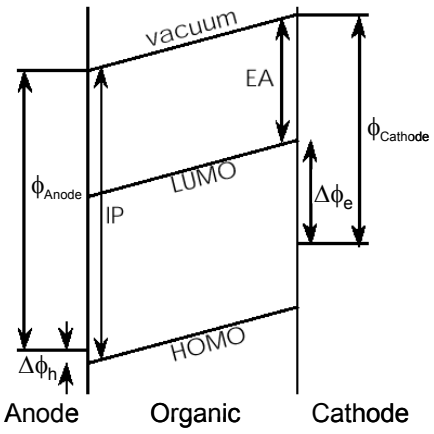

Figure 4.2 –Injection barrier between a metal and an organic semiconductor.

Figure 4.2 is a simplified energy diagram showing the barrier formed when a metal and an organic semiconductor are put in contact. The distance from the LUMO to the vacuum level is the so called electron affinity (EA) while the energy difference between HOMO and vacuum levels is the ionization potential (IP). $\Delta\Phi_h$ and $\Delta\Phi_e$ are the injection barriers for holes and electrons respectively.

This energy difference may not, in general, be calculated by a simple subtraction between EA and IP of the isolated materials, since when the metal and the polymer are put in contact, a very thin dipole layer is formed at the interface. This dipole layer shifts the energy barrier

significantly. In fact, manipulation of this value upwards or downwards may be done by introducing very thin layers (< 1 nm) of metallic-oxides or ionic salts. Lithium fluoride (LiF) is the most commonly used compound to reach alignment level due to its suitable electrical properties and its easy manipulation under standard evaporation techniques (low melting and boiling points at 848°C and 1676°C respectively), though Al_2O_3 has also been used [Wang00]. The resulting energy barrier can be measured by spectroscopic techniques such as ultraviolet photoemission spectroscopy (UPS) [Ishii02].

In general, the metal/polymer contact is assumed to be a Schottky contact. However, the Schottky formalism has been derived for crystalline inorganic semiconductors having a well defined energy band, and high carrier mobilities. On the contrary, energy levels in conjugated polymers are not well defined bands but their energy smears out and carrier mobilities are so low that the expected spatial regions are negligible. These features are the reason why the Schottky formalism can be questioned to hold in organic semiconductors. This will be given deeper consideration in the following sections.

4.1.1.1 Classical injection approaches

The classical approach to injection mechanisms in organic materials has been based on the thermionic effect which implies charge transfer via thermal activation from the metal Fermi level to the extended states in the semiconductor. This results in a carrier density given by [Sze81]

$$J = A^* T^2 \exp\left(-\frac{e\phi}{kT}\right) \qquad [4.1]$$

with k the Boltzman factor, A* the effective Richardson constant, T the temperature and ϕ the effective barrier due to the difference in energy levels at the interface. As can be inferred from equation [4.1], injection of a carrier from the metal into the organic layer strongly depends on temperature. In other words, the Boltzman factor $\exp\left(-\frac{e\phi}{kT}\right)$ reflects the fraction of the charges in the metal able to overcome the barrier by thermionic emission at a specific temperature. In this context, Scott et al. defined a Richardson-like constant for a metal-organic interface in analogy to the metal-inorganic semiconductor case [Scott99].

At this point it should be mentioned that a carrier leaving the metal into the organic material feels a barrier height lowering due to the image charge effect. An electron (hole) leaving the

metal induces a positive (negative) charge at the metal surface. This produces a screening effect that can be modelled by an image charge of the electron at the same distance in the metal. The force between the electron and its image charge is given by

$$Force = \frac{-e^2}{4\pi(2x)^2 \varepsilon_o \varepsilon_r} \quad [4.2]$$

with x the distance electron-metal interface, ε_o the vacuum permittivity and ε_r the relative permittivity of the semiconductor. The superposition of the external field, F, and the Coulomb field of the image charge results in a potential energy distribution for the electron (or hole in the case of hole injection), U(x),

$$U(x) = \phi - \frac{e^2}{16\pi\varepsilon_o \varepsilon_r x} - xeF \quad [4.3]$$

where ϕ is the zero-field barrier height. From equation [4.3] the maximum electrostatic potential height can be derived to be,

$$U_{\max} = \phi - \sqrt{\frac{e^3 F}{4\pi\varepsilon_o \varepsilon_r}} = \phi - \Delta\phi \quad [4.4]$$

which takes place at,

$$x_{\max} = \sqrt{\frac{e}{16\pi\varepsilon_o \varepsilon_r F}} \quad [4.5]$$

Equation [4.4] shows that in the presence of an electric field F, a charge carrier feels an injection barrier lower than the original ϕ. This is called the image charge lowering. Therefore, the original barrier in equation [4.1] should be replaced by $\phi - \Delta\phi$.

Figure 4.3 shows a potential energy diagram for the case of hole injection. The straight line depicts the triangular potential in the presence of an applied external field. The dashed line corresponds to the image potential and the solid line is the sum of the two contributions, and is the potential energy in the semiconductor. The effect of the barrier lowering due to the image force potential is also indicated.

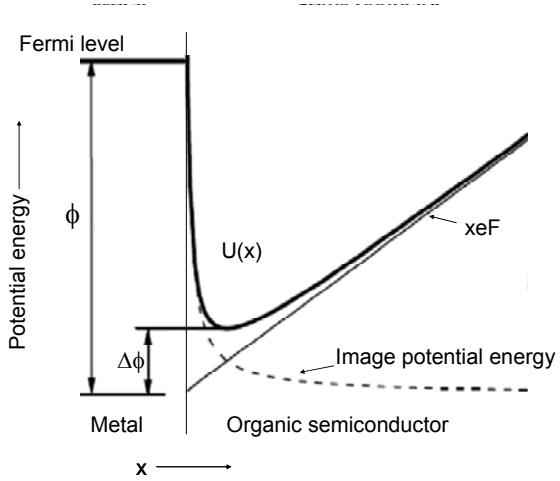

Figure 4.3 – Band diagram of the metal-organic semiconductor interface for hole injection.

Measurements of the dependence of the injected current on temperature in organic diodes have pointed out that predictions of the thermionic emission are not observed, so this model is not applicable to low mobility semiconductors [Simmons65] [Woudenberg01]. For semiconductors with $\mu \leq 10$ cm^2/Vs, charge carriers are stuck at the interface due to their low velocity. As a result, the injected current is rather predicted to be diffusion limited. For conjugated polymers, the hole mobility typically ranges from 10^{-8} cm^2/Vs to 10^{-4}cm^2/Vs, so the injection process is expected to be completely dominated by diffusion effects.

In this regime, a large accumulation of carriers at the boundary is expected, so a backflow current must also be taken into account. A recombination current due to a backflow of charge carriers using a classical formulation was already considered by Davids et al. [Davids97]. A similar approach for the injection model has been reformulated considering a field-enhanced surface recombination process [Scott99]. The backflow current is here considered to be drift-like, due to the negative component of the electric field for distances from the interface $x < x_{max}$ (as defined in eq. [4.5]).

Another classical injection mechanism has been traditionally adopted at sufficient high fields. In this situation, the band bending is assumed to favour carrier tunnelling from the electrode into the polymer. This mechanism obeys the Fowler-Nordheim formalism, which models carrier tunnelling from a metal through a triangular barrier into a continuum of energy states and ignores the image charge potential,

$$J = BF^2 \exp\left(-\frac{4\left(2m_{eff}\right)^{\frac{1}{2}}\phi^{\frac{3}{2}}}{3\hbar eF}\right) \quad [4.6]$$

with m_{eff} the effective mass of a carrier inside the organic and B a constant. Notice that this formulation is independent of temperature. However, currents given by equation [4.6] are actually several orders of magnitude greater than those measured experimentally [Davids96]. In fact, the Fowler-Nordheim formalism is derived for delocalised carriers within the band theory, which is not a good approximation for carriers in organic semiconductors.

In summary, low mobility values and energetic broadening due to disorder suggest that classical injection theories may not be suitable to model the electrical response of organic semiconductors.

4.1.1.2 Microscopic approach: Injection from a metal into a disordered hopping system

Carrier injection from a metal into a positionally disordered semiconductor, using a microscopic approach based on carrier hopping between discrete states was first proposed by Abkowitz et al [Abkowitz95]. However, this model did not take into account neither the image charge effect nor the energetic disorder of the system. These two issues were later included in a more refined injection model developed by Gartsein and Conwell and verified by Monte-Carlo simulations [Gartstein96], [Conwell97]. It was not until 1998 when Arkhipov et al proposed a microscopic-analytical model for the injection current from an electrode into a random hopping system as function of electric field, temperature and energetic width of the distribution of hopping states [Arkhipov98]. In this model, the injection mechanism is regarded as a two step process: a first jump from the metal Fermi level into the polymer state distribution, followed by either a diffusive escape from the interface or a back-flow to the electrode. This model assumes that the first jump is the rate limiting process and it was verified using Monte-Carlo simulations [Arkhipov99]. The latter injection approach will constitute the basis of our framework in section 4.2.2, and for this reason it will be given a deeper treatment in the paragraphs below.

The probability of a carrier to hop from the metal into the organic depends on the initial jump distance and on the target site energy. The energetic distribution of localized states in the polymer is given by the Bol (E) function,

$$Bol(E) = \begin{cases} 1, E < 0 \\ \exp\left(-\frac{E}{kT}\right), E > 0 \end{cases} \quad [4.7]$$

where E is defined with respect to the Fermi-level of the metal. After a carrier has made the first jump over a distance x_o, it can either contribute to the current escaping from the interface, or return to the electrode. The escape probability, w_{esc}, of a carrier that has made the initial jump is derived from the 1-D Onsager formula and is given by

$$w_{esc} = \frac{\int_a^{x_o} \exp\left[-\frac{e}{kT}\left(Fx + \frac{e}{16\pi\varepsilon_o\varepsilon_r x}\right)\right]dx}{\int_a^{\infty} \exp\left[-\frac{e}{kT}\left(Fx + \frac{e}{16\pi\varepsilon_o\varepsilon_r x}\right)\right]dx} \quad [4.8]$$

where T is the temperature, a is the distance from the electrode to the nearest hopping site and F the electric field. Figure 4.4 shows a schematic of the two-stepped injection process for the case of hole injection.

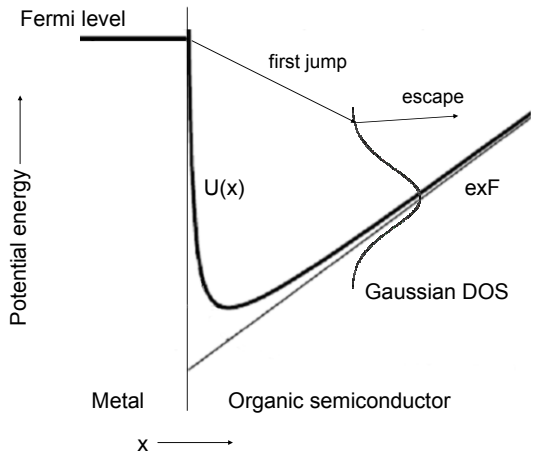

Figure 4.4 – Schematic of the two-stepped injection process proposed in [Arkhipov98].

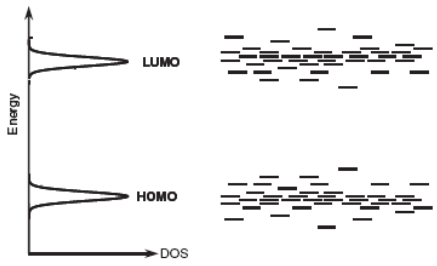

Figure 4.5 – Gaussian distribution of localized states.

If, after the first jump, the carrier chooses to enter the hopping system, the process is described as a continuous diffusive motion, and charge transport occurs among localized sites of a Gaussian distribution of states (DOS) with an energy width σ,

$$g(E) = \frac{N_t}{\sqrt{2\pi\sigma}} \exp\left(-\frac{E^2}{2\sigma^2}\right) \qquad [4.9]$$

where N_t is the total site density in m^{-3}. This is a physical parameter of difficult determination. In organics it may be estimated as the number of monomers or molecules per cubic meter.

In systems with large injection barriers, it is the first jump the rate limiting and contributes most to the field and temperature dependence of the entire injection process.

The total hopping injection current, J_{inj}, is eventually given in terms of an analytical expression [Arkhipov98],

$$J_{inj} = e\nu \int_a^{\infty} \exp(-2\gamma x_o) w_{esc}(x_o) dx_o \int_{-\infty}^{\infty} Bol(E) g[U(x_o) - E] dE \qquad [4.10]$$

where ν is the attempt-to-jump frequency, a is the distance from the electrode to the nearest hopping site (a <jump distance, x_o), and γ is the inverse localization radius of the electron (hole). The meaning of these parameters will be discussed in depth in section 4.3.

In summary, equation [4.10] states that the injection mechanism depends on two processes:

a) A first jump from the metal to the organic depending on the jump probability over a distance x_o, $\exp(-2\gamma x_o)$, and on the energy jump rate to the target site represented by the second integral of the equation (notice the Gaussian distribution is centred around the potential $U(x_o)$ given by Equation [4.3]).

b) A second jump into the hopping system described as a diffusive motion and whose probability w_{esc}, is given by Equation [4.8].

Experiments aimed to check the validity of classical thermionic and microscopic hopping injection approaches have been performed measuring the temperature dependence of the injected current [Woudenberg01]. According to these studies, the hopping nature of the charge injection from the contact into localized states of the polymer is currently well established.

4.1.2 Carrier transport in an organic semiconductor

The main parameter that determines carrier transport in either organic or inorganic materials is the mobility. Carrier transport in organic materials is considered to be similar to that of amorphous insulators, and consequently, mobility in such materials is several orders of magnitude lower than that of crystalline inorganic compounds of the IV or III-V groups. Moreover, mobility in organics has been shown to depend on the applied electric field, temperature and carrier density. In this section, mobility will be considered from several perspectives, a classical approach described by Poole-Frenkel formulation, and a microscopic view in which mobility is affected by a positionally and energetically disordered system of localized states.

4.1.2.1 Concept of Space Charge Limited Current (SCLC)

As pointed out in section 4.1, the injected (non neutral) charge may be significantly greater than the residual free charge (neutral) in insulators. As a result, the stationary charge density during conduction generates an additional electric field that must be considered. The resulting current in the device is referred to as Space Charge Limited Current (SCLC). This is the maximum current that an organic semiconductor can support for a given external voltage. Starting from the drift current expression and Gauss's Law and assuming an insulator contains no free carriers,

$$J = ep(x)\mu F \qquad [4.11]$$

$$\frac{dF}{dx} = \frac{ep(x)}{\varepsilon_o \varepsilon_r} \qquad [4.12]$$

with μ the mobility and $p(x)$ the carrier density. Eliminating the carrier density from the above equations and integrating from x = 0 to x (assuming the electric field to be zero at x = 0) we obtain

$$\frac{Jx}{\varepsilon_o \varepsilon_r \mu} = \frac{F^2}{2} \Rightarrow F(x) = \sqrt{\frac{2xJ}{\varepsilon_o \varepsilon_r \mu}} \qquad [4.13]$$

Integrating the field from x=0 to x=L (being L the distance between the electrodes), one finds the voltage,

$$V = \int_0^L F dx = \sqrt{\frac{2J}{\varepsilon_o \varepsilon_r \mu}} \frac{L^{3/2}}{3/2} \qquad [4.14]$$

From which the expression for the SCLC is determined to be,

$$J_{SCLC} = \frac{9}{8} \varepsilon_o \varepsilon_r \mu \frac{V^2}{L^3} \qquad [4.15]$$

This is known as the Mott-Gurney formalism [Mott48] and it holds for a field independent mobility and a trap-free semiconductor, i.e., when all the injected charge contributes to transport. In an organic diode, SCLC is achieved when the contact is ohmic. Based on simulation results, Arkhipov et al. established that ohmic contacts generally occur when the injection barrier is lower than 0.3 eV [Arkhipov03]. For larger barriers, the current will be injection limited and its value will be smaller than that given by equation [4.15]. However, this is only a rough guideline, because, as will be shown later, for intermediate barriers between 0.3 and 0.5 eV, the limiting mechanism is sensitive to factors such as active layer thickness or mobility.

4.1.2.2 Mobility formulation in semi-insulating systems

As mentioned before, since mobility in organic semiconductors is field-dependent, this dependence has to be included in the electrical equations to obtain a generalized Mott-Gurney expression. Different approaches to model mobility dependences are presented in this section.

Experimentally, mobility can be determined using techniques such as time-of-flight (TOF) or indirect techniques such as impedance spectroscopy. The latter will be carefully studied in section 4.4.

4.1.2.2.1 Classical Poole-Frenkel mobility

Generally speaking, one refers to Poole-Frenkel mobility when it is of the form $\mu \propto \exp\left(\gamma F^{1/2}\right)$. Originally, Poole-Frenkel model describes thermal-assisted transport of carrier through a media containing charge traps [Frenkel38]. These traps restrict the current flow due to a charge carrier “capture and release” process. The carrier is under the influence

of the Coulomb force that attracts it to the trap and the external applied field (F). The potential energy is:

$$U(x) = \Delta_{PF} - \frac{e^2}{4\pi\varepsilon_o\varepsilon_r x} - eFx \qquad [4.16]$$

where Δ_{PF} is the activation energy and x the coordinate along the field.

For a charge carrier to escape from the trap it should overcome the maximum of the potential at the point $x_{\max} = \sqrt{\frac{e}{4\pi\varepsilon_o\varepsilon_r F}}$ where the potential energy is given by

$$U(x_{\max}) = \Delta_{PF} - \sqrt{\frac{e^3}{\pi\varepsilon_o\varepsilon_r}}\sqrt{F} \qquad [4.17]$$

In this situation the thermally assisted rate should be proportional to $\exp\left(\frac{1}{kT}\sqrt{\frac{e^3}{\pi\varepsilon_o\varepsilon_r}}\sqrt{F}\right)$ and the Poole-Frenkel current will be of the form

$$J_{PF} \propto F\exp\left(-\frac{e\left(\Delta_{PF} - \sqrt{\frac{e^3}{\pi\varepsilon_o\varepsilon_r}}\sqrt{F}\right)}{kT}\right) \qquad [4.18]$$

However, the standard Poole Frenkel model reveals several inconsistencies when trying to explain experiments performed on doped polymers for different dopant concentrations [Preezant04]. Despite this, a similar field dependence of the classical Poole-Frenkel model for carrier transport is still used even in the absence of charge traps in the polymer.

4.1.2.2.2 Gill's phenomenological mobility

An empirical relation resembling "Poole-Frenkel-like" behaviour, describing the temperature and field dependence of the mobility in organic semiconductors exhibiting non-dispersive transport was proposed by Gill in 1972 [Gill72].

$$\mu = \mu^* \exp\left(-\frac{\Delta_G}{kT}\right)\exp\left(B\left(\frac{1}{kT}-\frac{1}{kT_o}\right)\sqrt{F}\right) \quad [4.19]$$

where Δ_G is the activation energy and μ^* is the mobility when T→∞, B a dimensional parameter and T_o an effective temperature also considered a parameter. Equation [4.19] shows a temperature-activated charge carrier mobility at low fields and temperature and field-dependent mobility at high fields.

This mobility behaviour was first observed by Gill in a well known fluorescent polymer poly(N-vinyl carbazole) (PVK), and at present time, numerous studies on molecularly doped polymers and amorphous molecular glasses have revealed a similar behaviour [Abkowitz92].

Notice that the zero-field mobility is given by $\mu_o = \mu^* \exp\left(-\frac{\Delta_G}{kT}\right)$. Besides, the pre-factor multiplying the square root of the electric field in [4.19], $B\left(\frac{1}{kT}-\frac{1}{kT_o}\right)$ is a material dependent parameter that typically decreases with increasing temperature. Gill's equation suggests that charge transport in organic semiconductors occurs by thermally assisted jumps from one localized site to another.

4.1.2.2.3 Gaussian Disorder Model (GDM)

Transport in disordered organic semiconductors occurs by means of hopping between localized sites and is believed to be governed by the energetically and positional disorder. In this sense, Bässler et al proposed a fundamental microscopic model (GDM) that serves now as a base for many other investigations [Bässler93]. Due to disorder effects, carriers are permanently localized in amorphous materials. A carrier will move inside the material by means of energetically upward/downwards jumps. The hopping rate between sites is described according to the Miller-Abrahams expression,

$$\begin{cases} \nu_{\downarrow} = \nu_o \exp(-2\gamma x), E_t < E_{st} \\ \nu_{\uparrow} = \nu_o \exp(-2\gamma x)\exp\left(-\frac{E_t - E_{st}}{kT}\right), E_t > E_{st} \end{cases} \quad [4.20]$$

where ν_o is the attempt-to-jump frequency, γ is the inverse of the localization radius, E_t is the energy of the target site and E_{st} the energy of the starting site.

The attempt-to-jump frequency is assumed to be enhanced by lattice vibrations and characterizes the intensity of electron-phonon interaction. In simple terms, it tells us how often a charge carrier hops due to an encounter with a phonon. Therefore, it can be estimated from the fluorescence spectra when vibronic scattering features are well resolved.

The inverse localization radius can be estimated by first principle calculations from the strength of the potential barrier, according to [Wolf85], nevertheless, no direct measurements for such a parameter are available.

The rate of upwards jumps is determined by the probability to jump over a certain distance x, $\exp(-2\gamma x)$ multiplied by the probability to obtain a certain amount of energy, $\exp\left(-\frac{E_t - E_{st}}{kT}\right)$. Equation [4.20] shows that the distance-dependent factor is completely symmetric, that is, the distance of hopping sites affects similarly forwards and backwards jumps meaning that it is equally difficult for a carrier to be trapped or released from an isolated state. However, it is not the case for an energy-disordered system. While upward jumps require thermal activation, downward jumps imply dissipation of energy via phonon emission. The former process is much slower and therefore rates of upward and downward jumps are very different. This strong asymmetry makes energy disorder much more important as far as transport is concerned.

Due to the presence of disorder it is assumed that energy levels are broadened into a Gaussian DOS with an energy width σ, as that given by equation [4.9].

In this Gaussian disorder model, the temperature and field dependence of the charge carrier mobility is given by an empirical equation [Bässler93],

$$\mu_{GDM} = \mu_\infty \exp\left[-\left(\frac{2\sigma}{3kT}\right)^2 + C\left(\left(\frac{\sigma}{kT}\right)^2 - 2.25\right)\sqrt{F}\right] \qquad [4.21]$$

whith μ_∞ the mobility in the limit T→∞ and C a constant. Notice that this expression resembles the classical one given by Poole-Frenkel.

The temperature dependence of activation energy in equation [4.21] is related to the energetic disorder $\Delta = \left(\frac{2\sigma}{3kT} \right)^2$. Monte-Carlo simulations showed that at low electric fields, carriers relax to an equilibrium level of energy $-\sigma^2/kT$ below the centre of the Gaussian distribution. Notice that this is situated in the tail of the Gaussian, where few sites are available for hopping. Thus, during the transport process, carriers will be activated to higher energy levels where the site density is higher.

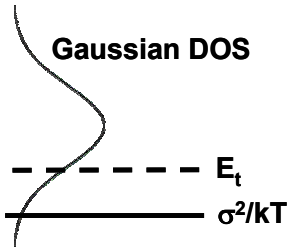

Figure 4.6 – Gaussian DOS showing the equilibrium and transport levels.

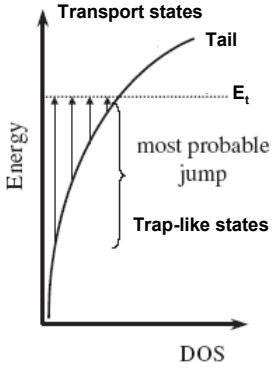

Figure 4.7 – Most probable jump of a carrier from a tail site to the E_t.

As already mentioned, the hopping rate probability depends on the energy difference between the starting and target sites, temperature, DOS distribution and localization radius. However, if the starting site is sufficiently deep in the DOS distribution, the energy level of the target site is independent of the origin site. This is therefore referred to transport energy level, E_t [Arkhipov01PRB].

In other words, E_t is a statistical tool that simplifies pure hopping transport in a positionally and energetically disordered medium, and approximates it to a trap-controlled effective transport. Each state below the transport energy level is a trap-like state while states above the transport energy level are regular transport states (as they were extended states despite all are localized). Only the latter ones contribute to transport. Carrier density contributing to transport is therefore a fraction of the total injected charge.

In the following section trap-controlled transport will be given deeper consideration.

Recent investigations have proposed that mobility not only depends on field and temperature but also on the carrier density [Pasveer05]. They suggest that at room temperature this dependence on carrier density is the most relevant factor while at low temperatures and high

fields, the electric field dependence becomes important. Considering an exponential DOS they proposed $\mu = a[p]^b$ and considering a Gaussian DOS $\mu = \mu_0 \exp\left(c\left[p\right]/[p_o]\right)^d$ (with a, b, c, d parameters and [p] carrier density) [Coehoorn05].

4.1.2.3 Trap-controlled effective transport

Trap controlled transport theory states that carrier motion is governed by the rate of carrier jumps between localized and extended states, disregarding direct jumps between localized states. This means that the jump rate is not affected by positional disorder of traps and the transport model is considered to be energy-controlled. This view may be translated to transport in organic diodes, where the transport level E_{tr} resembles the level of extended states. Thus, even in the case that no chemical traps are present in the organic, not all the injected charge contributes to transport, but just the fraction that reaches this level. In this framework, transport can be described on the basis of Miller-Abrahams expression (equation [4.20]), but only considering the probability of a carrier to obtain enough energy to be activated to the extended state.

$$\nu_{\uparrow} = \nu_o \exp\left(-\frac{E_{ex} - E_{st}}{kT}\right), E_{ex} > E_{st} \qquad [4.22]$$

with ν_o the attempt-to-jump frequency, E_{ex} the energy of the extended state and E_{st} the energy of the starting site. Downward jumps are independent of the energy of the target state, so

$$\nu_{\downarrow} = \tau_o^{-1}, E_{ex} < E_{st} \qquad [4.23]$$

where τ_o is the lifetime of a carrier in extended states.

Under thermal equilibrium, a relation between the total carrier density, p_{tot}, and the density of carriers in extended states, p_{ex}, has been obtained [Arkhipov01Philos],

$$p_{ex} = \frac{\nu_o \tau_o N_t}{\int_{-\infty}^{E_{ex}} dE g(E) \exp\left(\frac{E_{ex} - E}{kT}\right)} p_{tot} \qquad [4.24]$$

with N_t the total site density and g(E) the distribution of localized states. Actually, this linear relation is just a useful simplification. In fact $p_{ex} = (p_{tot})$ is a nonlinear function that has

been analytically formulated in [Arkhipov01APL]. It depends, among other factors, on a complex interplay between the energy density of states and the level of injected carriers. However, assuming that carrier densities are not excessively high in a range that may cover many of the typical currents in organic devices, a quasi-linear relation between p_{tot} and p_{ex} can be established in the form of equation [4.24].

Based on temperature measurements, some authors showed evidence that support a trap controlled effective transport, either based on real traps in a band framework [Stallinga05], [Stallinga06] or in a localized hopping system. In conclusion, trap-controlled effective transport will be used in this to model in an approximate way transport in amorphous media.

4.2 New proposal to model conduction in the presence of an injection barrier

As explained in the previous section, the OLED conduction is modelled by equating the injection and bulk currents at the interface with the mobility accounting for the material properties.

Nevertheless, if the contact is non-ohmic, equating both current contributions may present a problem. Injection mechanisms are verified in the region very close to the interface, and depend on the electric field at this boundary F(x =0), an internal value generally unknown. Meanwhile, the bulk current is formulated in terms of the integral of the electric field along the device thickness, i. e., the external applied voltage. Therefore, the solution of the continuity equation for the current requires knowing the relation between the electric field at the interface and the external voltage in a device. This is only known in two extreme cases that give rise to two well known approaches: injection limited and bulk limited conduction. So the question remains unsolved for intermediate injection barriers.

In this section, an easy formalism to determine the electric field at the interface, $F_0 = F(x = 0)$, of a single carrier OLED having a significant injection barrier is derived. This electric field is used to obtain the current density-voltage (J-V) characteristic without assuming previous approaches concerning injection or space-charge limited transport. Besides, a simple analytical expression to quantify the ratio between both limiting conduction regimes, injection and bulk, for any measured J-V characteristic is proposed. The resulting model may be readily used to model conduction in single-carrier OLEDs with a considerable reduction in computing time.

4.2.1 Charge transport in the presence of non-ohmic contacts

As it was mentioned is section 4.1.1, injection mechanisms are electric-field dependent, with $J_{inj} = J_{inj}(F_T)$, where F_T is the total electric field. Therefore, an accurate knowledge of the electric field at the interface is necessary for a reliable evaluation of the injected current. Let us consider the case of an OLED in which an external bias, V, is applied between the electrodes separated by a distance, L. If the injection barrier is high enough to consider the injected current negligible, as in the case of a capacitor, the internal electric field must be uniform, being $F_0 = V/L$ at the interface. However, if significant injected charge is present via ohmic contact, a dependence of F(x) on the square root of the position is predicted by Equation [4.13], giving $F_0 = 0$. Then, it may be considered that the effective field at the interface, F_0, falls within both limits (0 - V/L) when a moderate injection barrier from metal to organic is present.

Using the superposition principle the total electric field, $F_T(x)$ is split in two components, $F_T(x) = F_{sc}(x) + F_0$, where $F_{sc}(x)$ is due to the space charge effect, and F_0 is the remaining uniform field in the bulk, that must verify

$$F_o = \frac{V - \int_0^L F_{SC}(x)dx}{L} \qquad [4.25]$$

with L being the thickness of the active layer.

Since F_0 is deduced in terms of the voltage drop along the bulk, the contribution from the image charge effect, which is confined to the very thin region close to the interface, may be neglected in sufficiently thick diodes.

At this point it is important to make a remark concerning the carrier density inside the organic layers. Common conjugated polymers exhibit large band gaps and are not deliberately doped during synthesis. Thus, the existence of a neutralised free charge p_0 associated to shallow ionized impurities is generally discarded, and it is assumed that the total carrier density, p, arises from the injected charge. Despite p_0 being neglected, it was studied in section 4.1.2.3 that not all the injected current contributes to transport. Under the approximation of trap-controlled effective transport, it was established that only states above the transport energy level contribute to transport. According to this, it is necessary to review the fundamental equation [4.11]. This equation corresponds to the drift current, implying that the associated carrier density stands, only, for the charge contributing to transport, p_n.

$$J = ep_n\mu_{DC}F \quad [4.26]$$

Several notations for the mobility will be used along this chapter. For the sake of clarity, let us now refer to the mobility in the DC regime as $\mu_{DC.}$

On the other hand, Equation [4.12] represents the generation of an electric field due to the presence of space charge and accounts for the total carrier density, p.

Substituting $F_T(x)$ into [4.26] and combining with [4.12], the following first order, non-linear differential equation for $F_{sc}(x)$ is obtained:

$$\frac{J}{\mu_{DC}\varepsilon_r\varepsilon_o\Phi} = \frac{dF_{SC}(x)}{dx}(F_{SC}(x) + F_0) \quad [4.27]$$

where $\Phi = \frac{p_n}{p}$ is ratio between the carrier density contributing to transport and the total carrier density. This, under the approximation of trap-controlled effective transport, is given by the linear expression [4.24]. More sophisticated, non-linear approaches to this ratio are given in [Arkhipov 03].

Integrating [4.27] and applying the usual boundary conditions for the space charge field at the interface $F_{sc}(0) = 0$,

$$\frac{Jx}{\mu_{DC}\Phi\varepsilon_r\varepsilon_o} = \frac{F_{SC}^2}{2} + F_oF_{sc} \quad [4.28]$$

Equation [4.28] can be solved for F_{sc} to obtain,

$$F_{SC} = -F_0 + \sqrt{F_0^2 + \frac{2Jx}{\mu_{DC}\Phi\varepsilon_0\varepsilon_r}} \quad [4.29]$$

Integrating a second time between x = 0 and x = L, one finds the relation between the current and the applied bias,

$$(F_0^2 + \frac{2J}{\mu_{DC}\Phi\varepsilon_r\varepsilon_o}L)^{\frac{3}{2}} = \frac{3J}{\mu_{DC}\Phi\varepsilon_r\varepsilon_o}V + F_0^3 \quad [4.30]$$

From [4.30] a characteristic behaviour of J as a function of both the external bias, V, and the field at the interface F_0, is obtained:

$$J(F_0,V) = \mu_{DC}\Phi\varepsilon_r\varepsilon_o\frac{(9V^2 - 12F_0^2L^2) + \sqrt{(12F_0^2L^2 - 9V^2)^2 - 192\cdot F_0^3L^3(F_0L - V)}}{16L^3} \quad [4.31]$$

It is worth noting that when F_0 vanishes, equation [4.31] reproduces the Mott-Gurney expression in the presence of carrier trapping. If F_0 equals the other limit value, V/L, the situation is similar to a capacitor, where J = 0. In fact, it may be proven that F_0 approaches V/L asymptotically for injection barriers tending to infinity, and consequently also J_{inj} = 0. In any case, before reaching that limit, some of the approximations carried out, for instance neglecting p_0, likely fail.

On the other hand, either in the referred Mott-Gurney formalism or in other more sophisticated approaches for the space charge current [Mott48], [Arkhipov03], the dependence of mobility on the electric field and space charge is not usually considered in a first approximation. A similar simplification is assumed in our model, since otherwise, an analytical solution for the complete model including both injection and space charge contributions is not feasible.

4.2.2 Complete conduction model including hopping injection and transport mechanisms

In this section we use the continuity equation at the interface for the current density under steady regime (in the absence of carrier recombination) to obtain a complete system that allows to derive a function for the total current inside the diode.

Using this continuity equation at the interface we can combine any injection model, $J_{inj} = J_{inj}(F_0)$, with the bulk current J_b given by [4.31] to obtain,

$$J_{inj}(F_0) = J_b(V, F_0) \qquad [4.32]$$

In this framework we will use the microscopic approach for the injection model proposed by Arkhipov et al., with the J_{inj} given by equation [4.10].

Thus, providing that mobility and physical parameters of J_{inj} are known, Equation [4.32] may be numerically solved for any bias, V, to determine F_0, and hence the current density J_b.

In addition, one can readily derive with the aid of computational algebra, either from [4.30] or [4.31], an analytical expression for F_0 as a function of J_b and V, that may in turn be used to eliminate F_0 in [4.32], so obtaining an implicit function for the total diode current J_b. It is of major interest to have a J-V expression easily fitted to experimental data. In this sense, this method to determine F_0 overcomes the problem of using numerical recipes, leading to a significant reduction in computing time by one order of magnitude with respect to rigorous numerical procedures [Arkhipov03]. Using typical software for computational algebra, four analytical expressions are obtained for F_0,

$$F_{01,2} = \frac{V}{L}\left(\frac{1}{4} + \frac{1}{4\sqrt{3}}\sqrt{f_7} \pm \frac{1}{2}\sqrt{\frac{1}{2} - \frac{f_4}{3} - \frac{f_5}{3} - \frac{f_6}{3\cdot 2^{2/3}} + \frac{\sqrt{3}\cdot(1-f_4)}{2\sqrt{f_7}}}\right) \quad [4.33]$$

$$F_{03,4} = \frac{V}{L}\left(\frac{1}{4} - \frac{1}{4\sqrt{3}}\sqrt{f_7} \pm \frac{1}{2}\sqrt{\frac{1}{2} - \frac{f_4}{3} - \frac{f_5}{3} - \frac{f_6}{3\cdot 2^{2/3}} - \frac{\sqrt{3}\cdot(1-f_4)}{2\sqrt{f_7}}}\right) \quad [4.34]$$

where f_1, f_2, f_3, f_4, f_5, f_6 and f_7 are functions depending on bias, current density and active layer thickness. The complete expressions for the F_0 solutions are given in appendix I.

In conclusion, it is shown that the interface field not only depends on voltage but also on the particular injection model.

Moreover, one can define an efficacy factor, β, which represents the ratio of the real current across the OLED, J_b, and the maximum current, J_{SCLC} given by [4.15].

$$\beta = \frac{J_b}{J_{SCLC}} = \left(\frac{8L^3}{9\mu_{DC}\Phi\varepsilon_r\varepsilon_0}\right)\cdot\frac{J_b}{V^2} \quad [4.35]$$

Notice that β is a function varying in the range [0-1], and is useful to reveal the role played by each limiting conduction mechanism, either injection or bulk, in the diode. Thus, for a given bias, V, and any measured value of J_b, and assuming that material mobility is known, β provides a quantitative criterion to quickly check the validity of the injection limited ($\beta\cong 0$) or bulk-limited ($\beta\cong 1$) approximations.

The complete model was implemented in Fortran 90, using the compiler "*Microsoft FORTRAN Developer Studio*". This provides a friendly interface together with useful subroutines some of which were employed as part of the final program. The algorithm used for the complete model is explained in appendix II.

Complex computational algebra operations, such as obtaining expressions [4.33]-[4.34], were carried out with the software "*Mathematica*".

4.3 Simulation results and discussion

As it was explained in the above paragraphs, solving numerically equation [4.32] allows obtaining the electric field at the interface and concomitantly the total current across the device. In this section, theoretical simulations will be used to study the current dependence on material and structural parameters. According to these theoretical predictions it is possible to establish the OLED conduction regime. Moreover, using an appropriate non-deterministic

genetic fitting algorithm, the theoretical model will be fitted to experimental J-V of PFP:$(CN)_2$ and MDMO:PPV based diodes, obtaining structure and material microscopic parameters.

4.3.1 Current dependence on device structure and material parameters

Using the J-V complete model proposed in section 4.2.2, the dependence of J on the barrier height, ϕ, (a) and mobility, μ_{DC}, (b) for a typical active layer thickness of 100 nm and for several values of V has been calculated as shown in Figure 4.8.

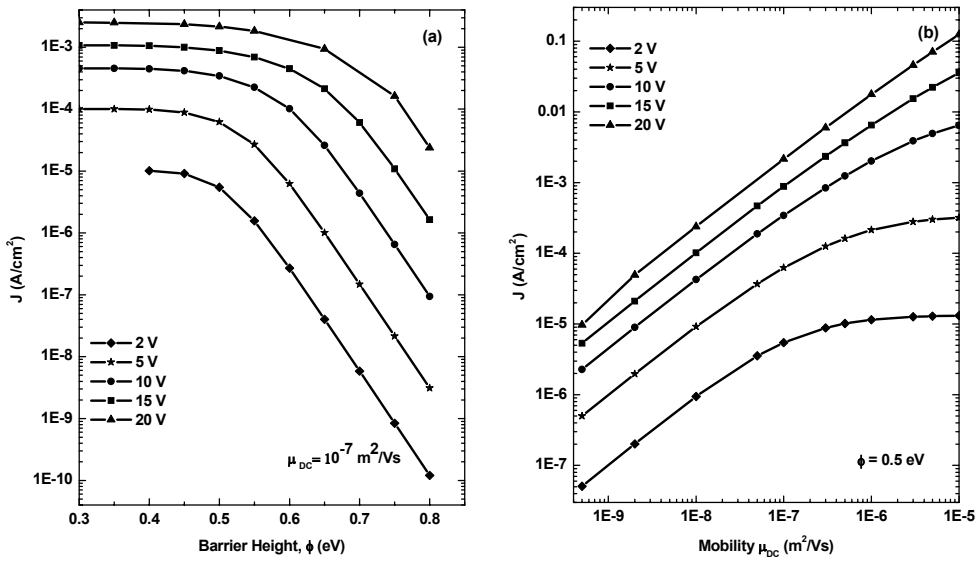

Figure 4.8 - Dependence of the current density on the barrier height (a) and mobility (b). The following material parameters are used: attempt-to-jump frequency ν_o = 4.75x10^{13} s^{-1}, inverse localization radius γ = 5x10^{9} m^{-1}, DOS width σ = 50 meV, site density N_t = 5x10^{20} cm^{-3}, intersite distance a=1 nm, and dielectric constant ε = 4.

As expected, the current increases with decreasing ϕ, and increasing μ_{DC}. Taking the extreme values of these two parameters it is easy to infer whether the current limiting factor is due to the charge injection process or transport along the bulk. However, for intermediate values of μ_{DC} and ϕ, establishing the conduction regime is not that straightforward.

In order to do that, it is necessary to compare the current predicted by [4.32] to the maximum current the diode can support, that given by Mott-Gurney (eq [4.15]). This is shown in Figure 4.9, where the efficacy factor, β, (given by Eq. [4.35]) has been plotted versus μ_{DC} and ϕ. When ϕ < 0.4 eV, Figure 4.9(a) shows that current across the diode equals the maximum current, so β = 1, and therefore conduction is bulk limited. As barrier height increases, the current gradually moves from a bulk limited to an injection limited regime. This regime transition occurs faster at lower bias. For intermediate barriers, 0.5 eV < ϕ < 0.6 eV, the conduction regime depends on the applied voltage. Further increasing ϕ, the injection limiting regime, β = 0, becomes dominant.

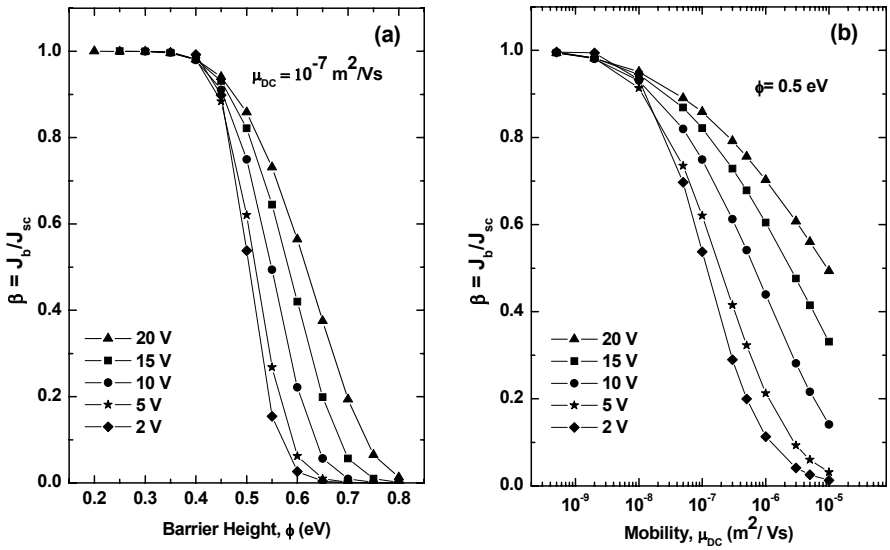

Figure 4.9 - Dependence of the analytical function β on the barrier height (a) and mobility (b). Material parameters are the same as in figure 4.8.

The transition from bulk to injection-limited conduction occurs at lower ϕ when dealing with higher mobilities. Figure 4.9(b) illustrates that mobility also plays an important role in determining the limiting conduction mechanism. As mobility increases, the accumulated space-charge is reduced, and the field at the interface approaches the total applied external field ($F_0 \approx$ V/L). In other words, the total current J is smaller than that predicted by a pure space-charge mechanism, so that the injection mechanism becomes dominant. As mobility decreases, the field at the interface is a smaller fraction of V/L, and the total current

approaches that given by the Mott-Gurney law. Figure 4.9 indicates to what extent reducing interface barrier and mobility favours bulk limiting conduction.

The dependence of the conduction regime (β) on thickness for different injection barriers and carrier mobilities is shown in Figure 4.10.

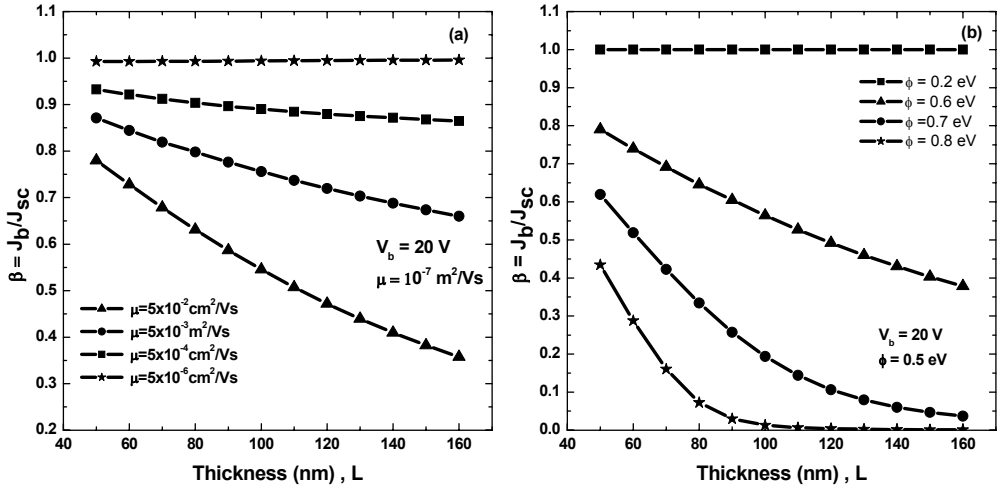

Figure 4.10 - Dependence of the analytical function β on sample thickness, for different injection barrier heights (a) and mobilities (b), for applied voltage V = 20 V. Material parameters are the same as in figure 4.8.

It can be observed in both plots that for a fixed thickness and bias 20 V, the conduction regime tends to be injection limited ($\beta \approx 0$) when either barrier or mobility are increased. This intuitively agrees with the fact that a high mobility does not favour carrier accumulation, thus lowering the space charge effect.

Both graphs show the general result that the injection limited regime, instead of the bulk limited one, is favoured by an active layer widening. At first glance this may be puzzling, since one would expect that the bulk mechanism should become dominant with increasing sample thickness. In order to understand this result it must be kept in mind that when varying mobility, bulk transport is affected independently of the injection process. Inversely, a barrier modification affects the injection process but not the bulk transport. However, both injection and bulk conduction are thickness-dependent, though they scale with thickness in a different manner. The injection process depends exponentially on the electric field, and thus on

thickness, whereas bulk current rather scales inversely with the cubic power of thickness. The exponential dependence eventually prevails over that of the bulk transport.

As a consequence, it is observed that, especially for intermediate barriers (0.3 - 0.5 eV) and mobilities (10^{-8} - 10^{-6} m^2/Vs), slight variations of sample thickness within the usual values in OLEDs may affect significantly the conduction regime.

4.3.2 Total electric field and carrier density

Spatial dependence of the total electric field ($F_T = Fo + F_{SC}$) and carrier density obtained with our model, for a 100 nm thick sample, 0.5 eV barrier for carrier injection, and biased at 20 V, are illustrated in Figure 4.11.

It may be noticed that the singularity predicted by the Mott-Gurney formalism in the space-charge density function at x = 0 is removed in our model (see Figure 4.11b).

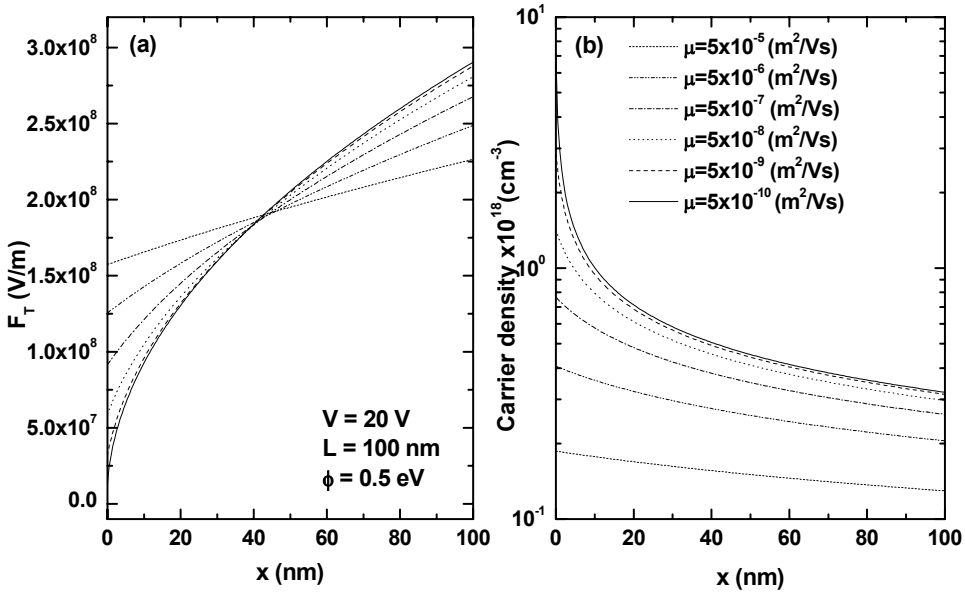

Figure 4.11 - Spatial distribution of (a) electric field and (b) carrier density for different mobilities. Material parameters are the same as in Figure 4.8.

For low mobility values, carriers are accumulated at the anode interface and slowly move towards the cathode. As a result, the electric field's spatial dependence is not linear and the injected current is predicted to be diffusion limited.

For high mobility values, space-charge effect is reduced and the electric field is quasi-uniform across the sample. In contrast, as mobility decreases the electric field resembles that of a bulk controlled mechanism. Notice that the electric field at the interface (x = 0) is never higher than V/L. The fact that the electric field may increase over V/L with increasing layer depth, is a common feature of the space-charge regime, here observed for x > 50 nm. These results are in perfect agreement with those shown by Arkhipov et al [Arkhipov01APL].

4.3.3 Electric field at the interface versus bias

Figure 4.12 shows the dependence of the interface electric field (F_0) on bias (V) with the injection barrier as the parametric variable. As expected, F_0 increases with increasing barrier height. If $\phi \leq 0.3$ eV, that is, in the bulk-limited regime, F_0 could be neglected when compared to V/L, and indeed, deriving Mott-Gurney's expression requires F(x=0) = 0 as a boundary condition for the integration. However, for intermediate injection barriers, F_0 increases considerably. Moreover, further increasing of ϕ up to values $\geq$ 0.7 eV, results in F_0 approaching the limit V/L. Therefore, it can be inferred that Mott-Gurney's equation does not hold in this latter situation. Instead, the model proposed in section 4.2.2 (equation [4.31]) can be used as far as F_0 is determined. Obtaining F_0 as function of J and V can be done either by numerically solving equation [4.32] or by applying the analytical equations [4.33]-[4.34].

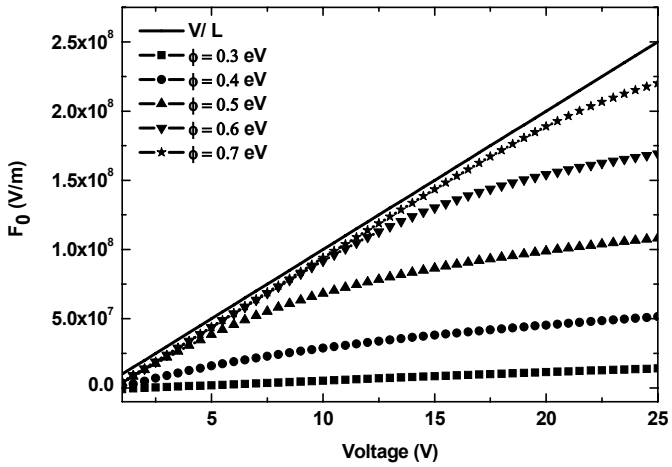

Figure 4.12 – Electric field at the interface, F_0, as function of applied bias. Solid line shows the total electric field F_T=V/L (L=100 nm). Material parameters are the same as in Figure 4.8.

4.3.4 Results obtained by fitting our model to experimental J-V of PLEDs based on two different polymers: MDMO:PPV and PFP:$(CN)_2$

The result of applying our model to the study of PLEDs electrical behaviour is presented in this section. The proposed model is fitted to experimental curves of MDMO:PPV and PFP:$(CN)_2$ based PLEDs using structure and material features as fitting parameters. The fitting procedure has been performed using a non-deterministic genetic algorithm proposed by Magnin et al. [Magnin]. This kind of algorithms is considered to be particularly suitable for systems with many parameters, achieving reliable results with significant reduction in computing time [Bäck97]. Genetic algorithms will be given deeper consideration in appendix II.

Figure 4.13 shows the experimental J_{exp}-V_{exp} of two diodes based on the structures: ITO/PEDOT:PSS/MDMO-PPV/Al and ITO/PEDOT:PSS/PFP:$(CN)_2$/Al. The EL onset for both PLEDS was detected above the maximum bias plotted, so single carrier conduction (holes) is ensured. The model proposed in section 4.2.2 has been fitted to the experimental data using as injection mechanism, $J_{inj}(F_0)$, the model proposed by Arkhipov et al. [Arkhipov98]. A number of physical parameters are involved in this model: barrier height for carrier injection (ϕ), energy width (σ) of the density of states for the energy level under Gaussian approximation, carrier inverse localization radius (γ), shortest intermolecular distance or nearest neighbour site (a), and the attempt-to-jump frequency (ν_o). Most of them may be physically measured, although not with similar accuracy. Solid lines in Figure 4.13 illustrate the fit.

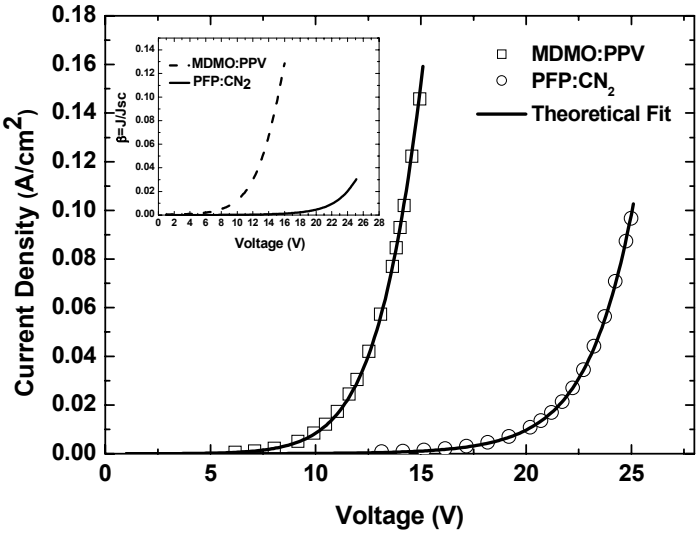

Figure 4.13 – Experimental J-V curve of PLEDs based on ITO/PEDOT:PSS/MDMO-PPV/Al (squares), and ITO/PEDOT:PSS/PFP:$(CN)_2$/Al (circles), and theoretical fits using the model proposed in this work (solid lines). Inset shows the variation of β with bias in both cases.

The attempt-to-jump frequency, ν_o, was previously obtained for each PLED from their EL spectra at high bias. Since it is assumed that ν_o is enhanced by lattice vibrations, spectrally resolved vibronic features allow a good estimation of this parameter, resulting ν_o (MDMO:PPV) = 3.55×10^{13} s^{-1} , and ν_o (PFP:$(CN)_2$) = 4.75×10^{13} s^{-1}.

Having derived an analytical expression for $F_0(J, V)$ from Eq. [4.33]-[4.34], the fitting process is considerably simplified. For that purpose, the following strategy has been used: the experimental data J_{exp}, V_{exp}, together with an initial mobility value are used to evaluate F_0. Within our model this is the exact value that should allow J_{inj} to verify the continuity equation [4.32], so that J_{inj} is calculated using that F_0 and the rest of fitting parameters. The error function between the theoretical current given by [4.32] (either J_{inj} of J_b) and J_{exp} is then evaluated, and subsequently minimized.

Parameters have been actually extracted from the fit of both the experimental J_{exp}-V_{exp}, and the dimensionless function $\frac{dJ_{\exp}}{dV_{\exp}} \frac{V_{\exp}}{J_{\exp}}$ which should be independent on multiplying factors

such as diode radius and attempt-to-jump frequency. The resulting fitting parameters for both PLEDs are shown in Table 4.1.

	ϕ (eV)	**a (nm)**	**γ (m^{-1})**	**σ (meV)**	**μ_{DC}* (m^2/Vs)**
MDMO:PPV	0.59	0.8	$4.3x10^{9}$	32	$8.3x10^{-10}$
PFP:$(CN)_2$	0.68	0.96	$3.26x10^{9}$	41	$6x10^{-9}$

Table 4.1 – Parameters obtained from the fit of Figure 4.13.

The resulting barrier heights are consistent with data for energy level alignment between ITO work function and the polymer HOMO levels [Mallavia05], [Frohne04]. The mobility, μ_{DC}*, is the average mobility corrected by the factor Φ given in [4.24], taking into account that not all injected charge contributes to transport, so that $\mu_{DC}^{*} = \mu_{DC}\Phi$. In other words, μ_{DC}* would resemble the mobility of carriers (holes) in the transport level.

Since carrier mobility is known to be dependent on both electric field and charge density [Pasveer05], [Tanasse03], these values must be considered as average within the range of applied voltages. In any case, we notice that, among all the fitting parameters, mobility is found to have the least influence on the error function. The error function (least square sum) increase is several orders of magnitude lower when it is caused by a change in mobility, as compared to when it is caused by a similar relative change in barrier or inverse localization radius. Therefore, this approximation is not considered critical for the other parameters. Mobility value for the MDMO:PPV is consistent with that given by [Pasveer05], [Tanasse03] for the fitted σ value. In turn, that obtained for PFP:$(CN)_2$ agrees with typical mobility values for polyfluorenes [Vijila07]. The shortest intermolecular distance, a, and the hole inverse localization radius, γ, and the DOS width,σ, are in the usual order for PLEDs [Arkhipov98], [Arkhipov01PRB].

Inset in Figure 4.13 shows the dependence of the efficacy factor, β, on bias for both PLEDs. In both cases, due to the high injection barrier, β remains close to 0, as expected for injection limited conduction. Moreover, a gradual increase of β for both diodes is observed for higher voltages, confirming that space charge effect becomes important with increasing bias. As one would also expect the MDMO:PPV based PLED will enter earlier in the bulk limited regime due to its lower barrier. This is reflected in a higher value for β. In this way, the factor β enables to quantify the amount of injection or space-charge effect.

In order to determine the influence of each parameter on the fitting process, several simulations of the current density error function versus the parameter variation were performed. For that purpose, a theoretical J-V curve was generated for a given set of physical conditions, typical of organic diodes (σ = 50 meV, γ = 5x10^9 m^{-1}, ϕ = 0.5 eV, a = 1 nm, μ = 10^{-7} m^2 /Vs). Each parameter was then varied a percentage around its current value and the error function (total least-squares sum) is evaluated. The results are plotted in Figure 4.14. As mentioned before, a small variation in the injection barrier, ϕ, generates great changes in the error function. However, it is remarkable that the major influence on the error function comes from the inverse of the localization radius, γ, which is the least known value and the most difficult to measure. On the contrary, great variations of intersite distance, α, and DOS width, σ, slightly affect the error function.

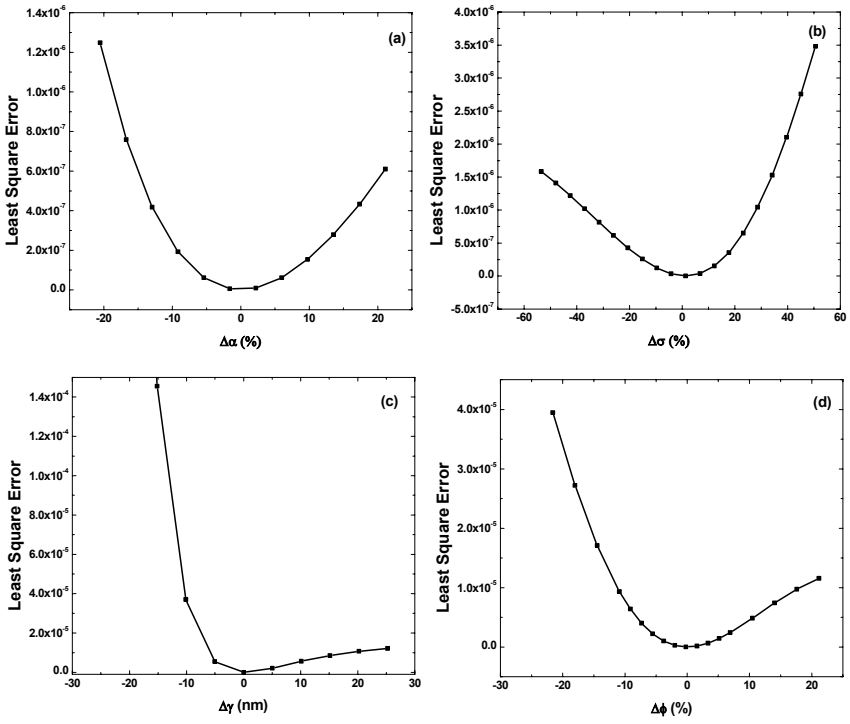

Figure 4.14 – Least square error of the J-V function vs parameter variation.

The variation of the current density error function with mobility deserves particular consideration, see Figure 4.15. For the usual mobility variation range, it can be seen that the

error function undergoes a smaller variation than that observed for the rest of the parameters. This may serve as a justification for considering the mobility constant in the bias working range. One must keep in mind that this result holds for structures with a non-negligible injection barrier, such as the ones we are dealing with in Figure 4.13. Nevertheless, this might not be the case for devices with ohmic contacts.

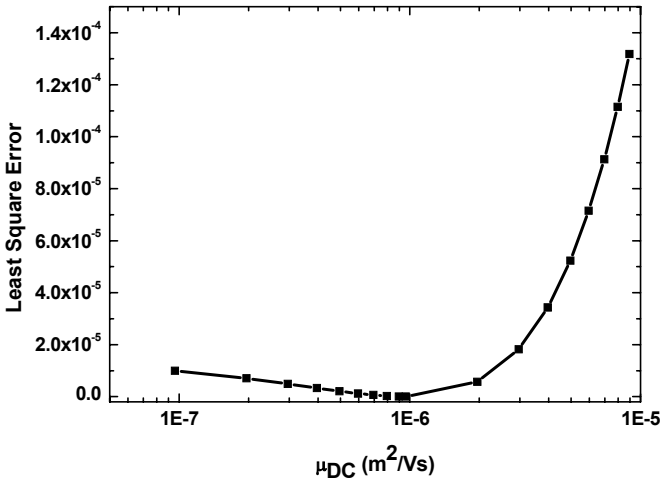

Figure 4.15 - Least square of the error J-V function vs mobility.

Finally, in order to demonstrate the validity of this model, diodes of the same material and thus with the same set of parameters, but with different thicknesses have been fabricated and their J-V characteristics have been compared to the model predictions. Experimental I-V curves (symbols) are plotted in Figure 4.16. Solid lines in these figures show theoretical simulations using the corresponding thicknesses and the subset of material parameters obtained from the fit of Figure 4.13. Assuming measurement uncertainties and disregarding non-ideal behaviour such as leakage currents, the agreement between theory and experiment is reasonably good [Alvarez08].

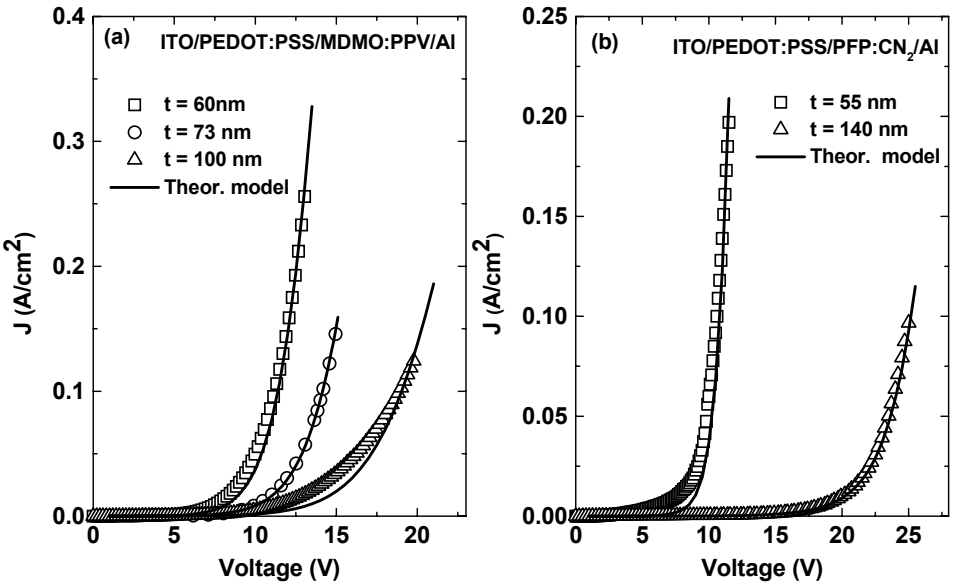

Figure 4.16 - Experimental J – V characteristics (symbols) of devices with identical active layers a) MDMO and b) PFP but different thicknesses. Theoretical curves determined with parameters from Table 4.1 and the corresponding thicknesses are plotted as solid lines.

4.4 Admittance spectroscopy (AS) model

Admittance spectroscopy (AS) has been traditionally used to characterize electrical properties of materials and their interfaces with conducting electrodes. It is a powerful technique to study the dynamics of mobile charge in the bulk and interfacial regions. The standard technique consists of applying a single-frequency small signal (tens of mV) superimposed to a dc signal (volts). The admittance is then computed by measuring the real and imaginary parts (amplitude and phase difference) of the resulting AC current using an analogue circuit or fast Fourier transform (FFT) analysis of the response.

In this section, AS is used to study the frequency-dependent electrical behaviour of a single carrier OLED. An analytical expression for the admittance is presented taking into account non-ohmics injecting contacts and a frequency-dependent hole mobility (so called dispersive). In this way, by fitting the new model to experimental data, dispersive parameters of hole mobility are obtained in polyfluorene derivatives (PFP:$(CN)_2$).

4.4.1 Review of small signal (AC) techniques applied to OLEDs

Traditionally, the study of the OLED AC electrical behaviour has been based on equivalent circuits [Campbell95], [Li98]. In these studies the bulk and contact region were modelled by circuit elements, so that the diode impedance was represented as an independent resistance in parallel with a capacitance, and both in series with another resistance. In most of the experimental set-ups, series resistance due to metal contacts or track lengths can be accurately estimated or alternatively neglected.

More sophisticated models for small signal response performance were used to study trapped interfacial charges and their influence on the current-voltage characteristic and electroluminescence delay times [Riess01].

It was in the late 90s when AS studies yielded relevant results concerning transport properties in organic solids. Martens et al used AS techniques to suggest that the OLED admittance exhibits a very specific frequency dependence that is governed by the transit times (τ_t) of the injected carriers [Martens99]. They argued that dispersive transport appears as a consequence of hopping conduction in a disordered material which results in a broad distribution of transit times and, consequently, a frequency dependent mobility. According to Böttger et al. [Böttger85], this dependence can be modelled as,

$$\tilde{\mu}(\Omega) = \mu(\Omega) \Big/ \mu_{DC} = 1 + M(i\Omega)^{1-\alpha} \qquad [4.36]$$

where Ω is the normalized frequency defined as $\Omega = 2\pi f \tau_t$, and M and α are dispersion parameters. This frequency-dependent function accounts for the dispersive transport influence on the admittance. For non-dispersive transport M=0 and α=1. Martens et al. derived a frequency dependent admittance given by [Martens99],

$$Y(\Omega) = \frac{\varepsilon A}{\tau_t L} \frac{\Omega^3}{2i\tilde{\mu}^2(\Omega)\left[1 - \exp\left(-i\Omega \Big/ \tilde{\mu}(\Omega)\right)\right] + 2\tilde{\mu}(\Omega)\Omega - i\Omega^2} \qquad [4.37]$$

where, ε is the dielectric constant and A and L are the device area and thickness respectively. Notice that $\mu(\omega)$ and $\varepsilon(\omega)$ are the only unknown functions.

Details concerning the derivation of the previous expression are explained in the following section 4.4.2.

The carrier transit time is defined as,

$$\tau_t = L^2 \Big/ \mu_{DC} V \qquad [4.38]$$

They fit expression [4.37] to the experimental measurements to obtain DC mobility, (μ_{DC}) and dispersion parameters, M and α. However, equation [4.37] is based on a trap-free Mott-Gurney formalism (eq. [4.15]) meaning that they work under the assumption of ohmic injecting contacts. Therefore, for diodes with non-negligible injection barriers the above expression is not applicable.

Following the above approach, subsequent studies on AS have derived a similar expression to [4.37] but using a τ_t that has been previously derived from other time constant, the relaxation time, τ_r. According to Martens et al. [Martens00], [Martens01], this relaxation time can be obtained by plotting the negative differential susceptance, $-\Delta B = -\omega\left(C - C_{geo}\right)$ versus frequency, with C_{geo} the geometrical capacitance. It was observed that this plot exhibits a maximum at a frequency, $f_r = \tau_r^{-1}$, and it was argued that this peak is related to the average transit time. Performed computer simulations by Tsang et al. suggested that for non-dispersive transport this relation is set to [Tsang06].

$$\tau_t = 0.56\tau_r \qquad [4.39]$$

When transport is dispersive, the scaling factor 0.56 varies ± 0.1.

Nevertheless, both studies performed by [Martens99] and [Tsang06] assume trap-free materials. In this sense, Gommans et al. developed an analytical model for the frequency-dependent space-charge-limited behaviour in the presence of single-trapping level [Gommans04]. In this latter work, the admittance spectra are interpreted in terms of a frequency dependent mobility in combination with a distribution of transit times. Moreover, they include in the model the trapping process in the SCL regime proposed by Dascalu [Dascalu66] and later by Kassing [Kassing75]. According to Kassing et al., the capture and emission of a charge carrier by a single trap is linearized and described by a steady-state and frequency dependent trapping parameter. Therefore, this model is applicable to determine mobilities in the SCL regime even in the presence of trap levels.

As far as double carrier transport (e- and h+) is concerned, Pitarch et al. developed an impedance model for pure SCL regime under the assumption of large recombination rate

[Pitarch06]. As a further simplification, electron and hole mobilities (μ_e, μ_h) are considered non-dispersive (i.e. constant with frequency) real magnitudes. In this framework, an analytical expression for the impedance including the sum of both mobility contributions ($\mu_e + \mu_h$) is obtained for OLEDs having double injecting contacts. However, by fitting this model to the experimental data, it is not possible to obtain mobilities of the different carrier species separately. In this sense, Martens et al. claimed to determine electron and hole mobilities independently in a PLED from admittance measurements [Martens00]. The technique employed is based on the fact that mobility can be obtained from the carrier transit time reflected in the frequency domain of the admittance measurement ($\omega \approx \tau^{-1}$). The transit time appears in the form of an inductive process consequence of a lag between the applied AC voltage and the carrier response. If both, electrons and holes, are present in the device, the charge distribution will be governed by two transit times. These are reflected individually in the admittance measurements as both inductive process, and therefore the mobility for each type of carrier can be deduced.

Alternatively to AS, several experimental techniques such as, time-of-flight (TOF), dark-injection space–charge-limited-current (DISCLC) and transient electroluminescence, have been employed to study charge transport properties in OLED.

So far, TOF is the most widely used experimental procedure to obtain carrier mobility [Campbell99]. A sufficient thick layer is sandwiched between two electrodes, one of which is transparent and non-injecting. Using light pulses of a short wavelength to guarantee high absorbance, charge pairs are photogenerated near the non-injecting contact and separated by an applied electric field. Carriers are pulled across the sample to the counter electrode generating a transient displacement current. The carrier transit time is then monitored. In a non-dispersive trap-free material, τ_t is directly related to the mobility by equation [4.38]. In the case of hopping transport, the transit time broadens, leading to what is called dispersive transport. However, thicknesses of at least 1 μm are required in order to have a well defined flight distance. This requirement becomes a drawback since electric fields decrease with increasing thickness. Besides, when it comes to characterizing new materials, they are usually synthesized in small quantities.

Dark-injection space-charge-limited-current is another experimental technique to extract mobility [Tuladhar05]. A step voltage is applied to a sample and the resulting current transient is registered. If the injecting contact is ohmic and the material is trap-free, then a characteristic

transient with a maximum is observed. The position of the maximum in time is related to the carrier transit time as $\tau_{\max} = 0.786\tau_t$ and the mobility is extracted from [4.38]. The latter relation was derived for a field-independent mobility and thus, applying this technique to organics, where mobility is field-dependent, results in average values. Nevertheless, when trying to characterize materials exhibiting dispersive transport, the transient shows a long decaying tail and in the case of high dispersion the maximum is not observed [Campbell01].

Transient electroluminescence measurements are also used to extract mobility. A voltage pulse is applied to an electroluminescent device and the transient EL is recorded. The appearance of light lags the voltage pulse and the delayed response time, t_d, is defined as the time between the rising edge of the voltage pulse and the occurrence of EL. This is the time taken for the radiative recombination of e–h pairs to occur. Then, the drift mobility, or the recombination mobility, is given by

$$\mu_{DC} = \frac{L^2}{t_d\left(V - V_{ON}\right)} \qquad [4.40]$$

where V_{ON} is the turn-on voltage, which is the work-function difference between both electrodes (built-in-potential).

4.4.2 Reformulation of admittance spectroscopy model in the presence of non-ohmic contacts

In this section we will derive an analytical expression for the frequency-dependent admittance following the same approach as [Martens99] and [Tsang06] described in 4.4.1. However, as it was mentioned in the previous section, these models are only applicable to OLEDs having ohmic contacts. The model proposed in the following paragraphs takes into account a non-negligible injection barrier by introducing the corresponding non-zero electric field at the interface. In this sense, the reasoning is similar to that explained in section 4.2.1 for the current-voltage behaviour. In fact, expressions derived in section 4.2 for the J-V characteristic and the electric field at the interface will be used here.

In order to describe the AC response of a biased OLED we make use of the basic equations for time-dependent injection of space-charge limited current. All the variables involved are described as the sum of two contributions: the continuous one (DC) and time dependent one (AC),

$$\begin{cases} F_T(x,t) = F_{DC}(x) + f(x,t) \\ \rho(x,t) = \rho_{DC}(x) + \upsilon(x,t) \\ J(t) = J_{DC} + j(t) \end{cases} \quad [4.41]$$

If time-dependent signals are small enough, equations can be linearized around the DC level. Moreover, in the presence of an injection barrier, the total DC electric field can be expressed as $F_{DC}(x)=F_0+F_{SC}(x)$, where $F_{SC}(x)$ is due to the space charge effect, and F_0 is the remaining uniform field in the bulk accounting for an injection barrier at the interface.

The time and position-dependent hole density, $\rho(x,t)$, is given by Poisson's equation,

$$\left(\frac{\varepsilon}{e}\right)\frac{\partial F_{SC}(x,t)}{\partial x} = \rho(x,t) \quad [4.42]$$

and the total current density, J(t), is given by is given by the drift and displacement components

$$J(t) = e\rho(x,t)\mu(t)F_T(x,t) + \varepsilon\frac{\partial F_T(x,t)}{\partial t} \quad [4.43]$$

In the absence of any perturbation the electric field is independent of time, so that $\frac{\partial F_T(x,t)}{\partial t} = 0$. Substituting [4.41] and [4.42] into [4.43] the following expression is obtained in a first approximation,

$$j(t) = e\mu(t)\rho_{DC}(x)f(x,t) + \varepsilon\mu(t)F_{DC}(x)\frac{\partial f(x,t)}{\partial x} + \varepsilon\frac{\partial f(x,t)}{\partial t} \quad [4.44]$$

Equation [4.44] exhibits $j(t)$ in terms of three contributions. The first term accounts for the response of the DC-charge carrier density. The second term represents the current due to the additional time-dependent injected charge-carrier density. The last term is responsible for the dielectric displacement current. Notice that in the above expression the term $\varepsilon\mu(t)f(x)\frac{\partial f(x,t)}{\partial x}$ has been neglected since $F_{DC} >> f$. Applying the Fourier transform to the above equation we may write,

$$j(\omega) = e\mu(\omega)\rho_{DC}(x)f(x,\omega) + \varepsilon\mu(\omega)F_{DC}(x)\frac{\partial f(x,\omega)}{\partial x} + i\omega\varepsilon f(x,\omega) \quad [4.45]$$

When an electric field is present at the interface, the total DC electric field, F_{DC}, is obtained from equation [4.29] as,

$$F_{DC}(x) = F_{SC}(x) + F_0 = \sqrt{F_0^2 + \frac{2Jx}{\mu_{DC}\Phi\varepsilon}} \qquad [4.46]$$

Differentiating $F_{SC}(x)$ and substituting into [4.42], the hole density can be expressed as,

$$\rho_{DC}(x) = \frac{J_{DC}}{2e\mu_{DC}^{*}\sqrt{F_0^2 + \frac{2J_{DC}x}{\mu_{DC}^{*}\varepsilon}}} \qquad [4.47]$$

Where $\mu_{DC}^{*} = \mu_{DC}\Phi$. Substituting equations [4.46] and [4.47] into [4.45], and using the frequency-dependent mobility given in [4.36], the differential equation can be solved to obtained the following expression for the complex admittance,

$$Y(\Omega) = \frac{A\varepsilon}{\tau L}\frac{\Omega^3}{-i\Omega^2 + \frac{\tilde{\mu}(\Omega)\mu_{DC}^{*}\Omega\varepsilon}{LJ_{DC}}\delta^2 + \frac{\left(\tilde{\mu}(\Omega)\mu_{DC}^{*}\right)^2\varepsilon^2}{2LJ_{DC}^{\ 2}}\delta^2\kappa\left[1-\exp\left(-i\Omega/\tilde{\mu}(\Omega)\right)\right]} \qquad [4.48]$$

with,

$$\delta = \sqrt{F_0^2 + \frac{2J_{DC}L}{\mu_{DC}^{*}\varepsilon}} - F_0\,,\quad \kappa = \left(\frac{2F_0\omega}{\tilde{\mu}(\Omega)\mu_{DC}^{*}} + i\frac{2J_{DC}}{\mu_{DC}^{*}\varepsilon}\right) \text{ and } \tau = \frac{\varepsilon}{J_{DC}}\delta$$

where τ is the new effective transit time.

The second term of the denominator of Equation [4.48] reflects the influence of dispersive transport on the admittance and in that sense this expression has a similar structure as that proposed by Martens et al. (equation [4.37]). However, the use of these functions implies two main differences. The first one is that, while [4.37] was derived under the assumption of injecting ohmic contacts, [4.48] is not subjected to that restriction as indicated by the F_0 dependence. The second one is that, in order to apply the latter expression, F_0 needs to be determined numerically from [4.33]-[4.34]. For that purpose, the corresponding J-V, either coming from the experiment or the model, must be used as input values. Therefore, the agreement with the experimental J-V characteristic is a previous condition in this model.

Thus, providing F_0 is known for each V, [4.48] may be fitted to the admittance measurements in order to determine $\mu(\Omega)$, with M, α and μ_{DC}* being simulation parameters.

4.4.3 Simulation results and discussion

In this section, theoretical simulations will be used to study the admittance dependence on mobility and disorder parameters. The theoretical model proposed in 4.4.2 will be fitted to experimental admittance-frequency curves of PFP:$(CN)_2$ and MDMO:PPV based diodes, obtaining the materials mobility versus bias. Moreover, the degree of disorder in transport can be estimated by extracting the disorder parameters.

4.4.3.1 Dependence of capacitance and conductance on mobility and disorder parameters

As stated by Martens et al., disordered materials exhibit dispersive transport, which results in a frequency dependent mobility given by Equation [4.36]. It then becomes essential to obtain a good knowledge of how DC mobility (μ_{DC}) and dispersive parameters (M and α) will affect the admittance model proposed in this thesis.

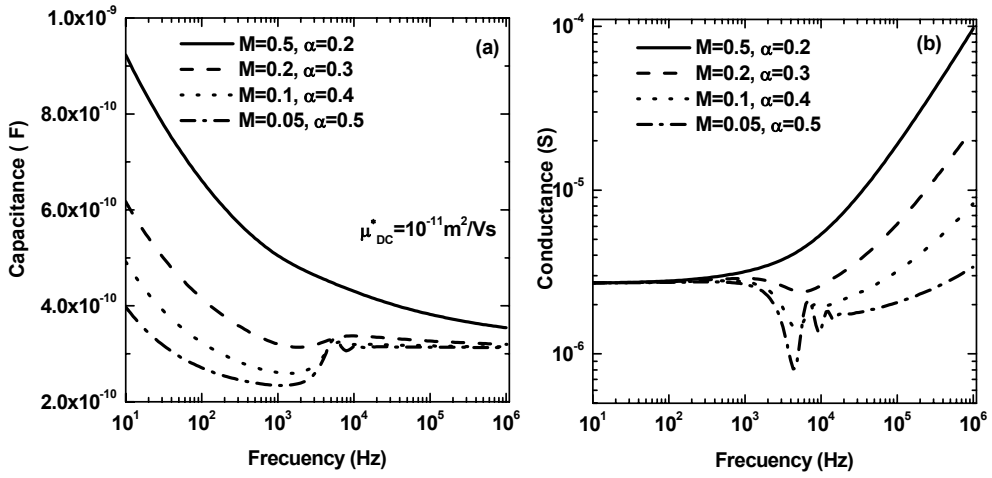

Figure 4.17 – Frequency-dependent capacitance (a) and conductance (b) for an organic diode with area, A=1.77x10^{-6} m^2, active layer thickness L=200 nm and ε_r = 4 under a DC bias of 10 V. Different degrees of dispersion are presented.

Figure 4.17 shows the frequency-dependent capacitance (a) and conductance (b) for different degrees of dispersion, using as a reference sample an organic diode with typical parameters (μ_{DC}* = 10^{-11} m^2/Vs and ϕ = 0.5 eV) and dimensions A=1.77x10^{-6} m^2 and L=200 nm. Ideally,

non-dispersive transport will occur when M=0 and α=1. Then, M=0.5 and α=0.2 represents the highly dispersive transport and M=0.05 and α=0.5 corresponds to the less dispersive transport.

At high frequencies, $\Omega = 2\pi f\tau_t > 1$, Figure 4.17(a) shows that the capacitance tends to the geometrical capacitance, $C_{geo} = \frac{\varepsilon A}{L} = 314\,pF$. However, when the frequency decreases below τ_t^{-1} (i.e., $\Omega < 1$), an inductive contribution appears and C displays a minimum. This inductive contribution is attributed to the redistribution of space charge when the electrical field is varied. When the bias is varied, the injected charge moves into the device to relax to the new equilibrium space charge distribution. Due to the finite τ_t, the injected current lags behind v_{ac} and therefore reduces the phase of Y. For times shorter than τ_t (or $\omega > \tau_t^{-1}$), the carriers do not relax and the inductive contribution tends to vanish. At very low frequencies there is a steep increase in the capacitance due to the dispersive transport behaviour. The same behaviour is exhibited in the model proposed by Tsang et al [Tsang06]. In conclusion, it is in the low-medium frequency range (< 1 kHz) of the capacitance where dispersion effects in the mobility are properly detected. On the contrary, these effects are better resolved in the high frequency range (> 10 kHz) of the conductance plot.

As stated by eq. [4.39] in section 4.4.1, the relaxation time can be obtained by plotting the negative susceptance, $-\Delta B = -\omega\left(C - C_{geo}\right)$ vs frequency. We can check the validity of this approach with our model.

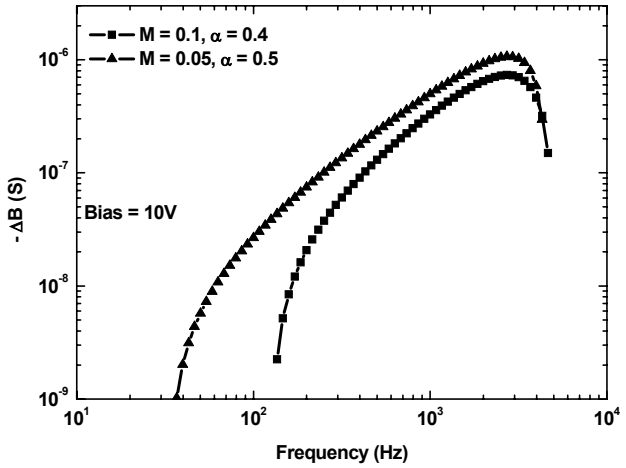

Figure 4.18 – Simulated -ΔB=-ω(C-C_{geo}) obtained from Figure 4.17.

Figure 4.18 displays -ΔB for two cases of low dispersion. This plot exhibits the mentioned maximum at a frequency $f_r = \tau_r^{-1}$, which should be related to the average transit time by the relation $\tau_t = 0.56\tau_r$ [Tsang06]. When transport is highly dispersive, the capacitance is larger than the geometrical capacitance at the measuring frequencies, and thus, τ_r cannot be resolved. For susceptances displayed in the above graph, the relaxation peak is situated at 3.7x10^{-4} s, yielding a $\tau_t = 2.1\times10^{-4} s$. Using this value of τ_t, equation [4.38] can be employed to extract mobility, obtaining a value of 1.9x10^{-11} m^2/Vs. This is in good agreement with the mobility used in the simulation, μ_{DC}* = 10^{-11} m^2/Vs, which confirms the validity of the approach proposed in [Tsang06].

Figure 4.19 shows the frequency-dependent capacitance (a) and conductance (b) obtained from equation [4.48] with μ_{DC} as the parametric variable. As expected, simulations show an increase of conductance with increasing mobility. The singularity in the capacitance plot due to the inductive contribution is shifted towards higher frequencies as mobility increases, indicating that the redistribution of space charge takes shorter times.

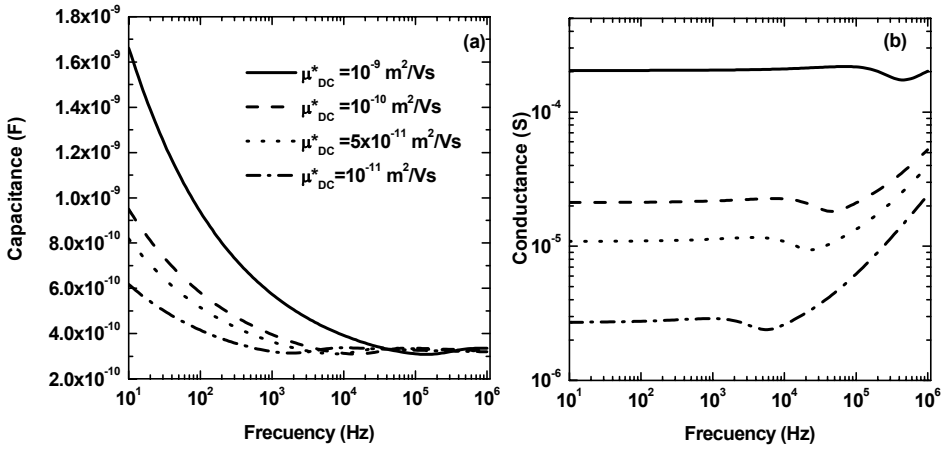

Figure 4.19 – Frequency-dependent capacitance (a) and conductance (b) for an organic diode with area, A=1.77x10^{-6} m^2, active layer thickness L=200 nm and ε_r = 4 under a dc bias of 10 V. Dispersive parameters are M=0.2 and α=0.3.

4.4.3.2 Comparison with other admittance spectroscopy models

Figure 4.20 shows a comparison of the admittance model proposed in this work and those proposed by Martens et al. [Martens99] and Tsang et al. [Tsang06]. The frequency-dependent conductance and capacitance are shown for two very different injection barriers: 0.3 eV and 0.7 eV. Since our expression of the frequency dependent admittance is derived for a non-negligible injection barrier, the comparison with other models has to be done using barriers representing both extreme situations, injection limited contacts and quasi-ohmic contacts. In all cases, a dispersive material is modelled with M = 0.2 and α = 0.3.

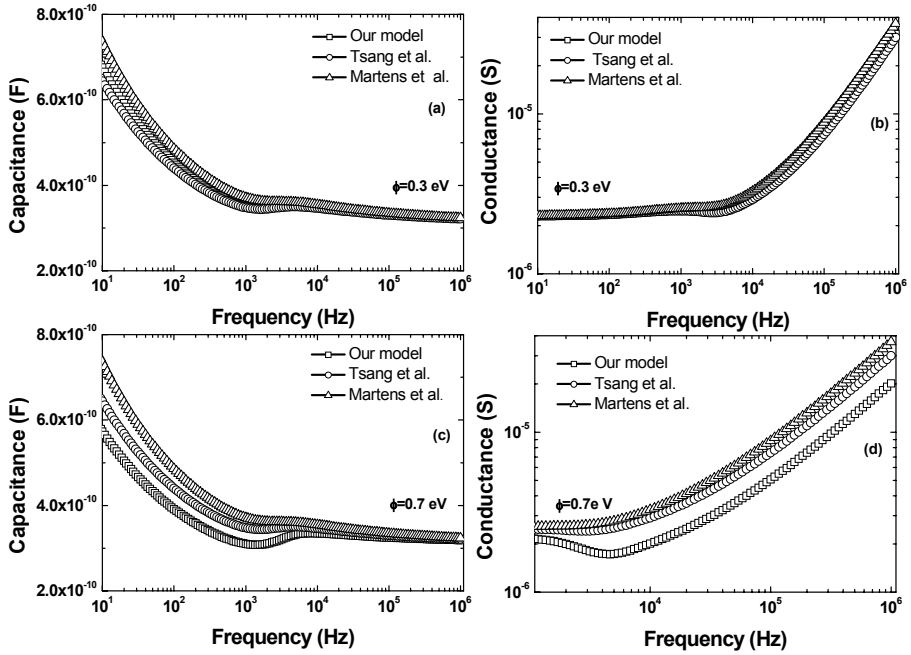

Figure 4.20 – Frequency dependent capacitance and conductance using three admittance models: Martens et al., Tsang et al. at and that model presented in section 4.4.2. Simulation was performed for $\mu^*_{DC}=10^{-11}m^2/Vs$, V_{bias}=10V and L=200 nm.

Simulations obtained from the three models are in good agreement for small values of the injection barrier. This result agrees with the fact that these authors assume ohmic contacts to derive the expression for Y(ω), or equivalently, they presume the electric field at the interface (F_0) is negligible when compared to V/L. However, for large injection barriers, the small signal model proposed in this work significantly differs from the other two. It is worth mentioning that dispersive materials soften this difference, which otherwise would be more noticeable.

If the injection barrier is increased, the charge present in the device is small and consequently the capacitance and conductance would decrease. This is predicted by equation [4.48] and is shown in Figure 4.20(c)-(d). Indeed, simulations for an external bias of 10 V and active layer thickness of 200 nm of devices with ϕ = 0.3 eV and ϕ = 0.7 eV yield electric fields at the interface of approximately F_0=1.56x10^7 V/m and F_0=4.99x10^7 V/m respectively. This means that for large barriers almost all the external field falls at the interface. Thus, taking into account F_0 when deriving an expression of Y(ω) is of crucial importance.

4.4.3.3 Results obtained by fitting our model to experimental admittance measurements: Determination of the hole mobility of MDMO:PPV and PFP:$(CN)_2$

Figure 4.21 and Figure 4.22 show the frequency dependence of the experimental capacitance and conductance deduced from impedance measurements at different biases for two different OLEDs based on MDMO:PPV and PFP:$(CN)_2$. When a positive bias is applied holes are injected from the ITO anode, and therefore it is clearly seen that conductance increases with bias.

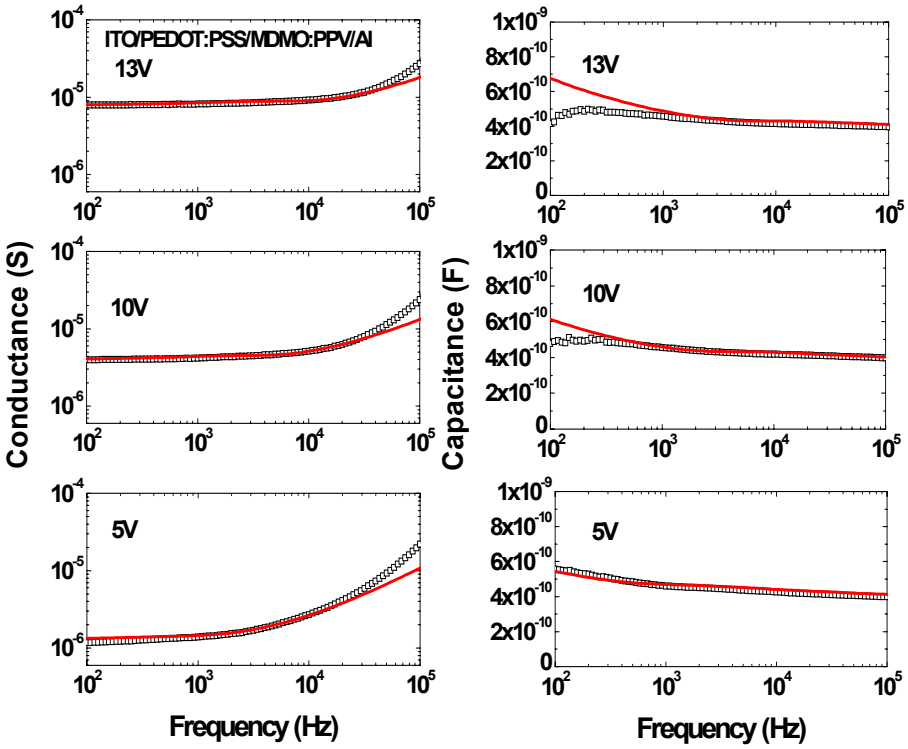

Figure 4.21 - Conductance (left) and capacitance (right) for ITO/PEDOT:PSS/MDMO:PPV/Al vs frequency at different bias. The solid lines are fits to the experimental data using Eq. [4.48].

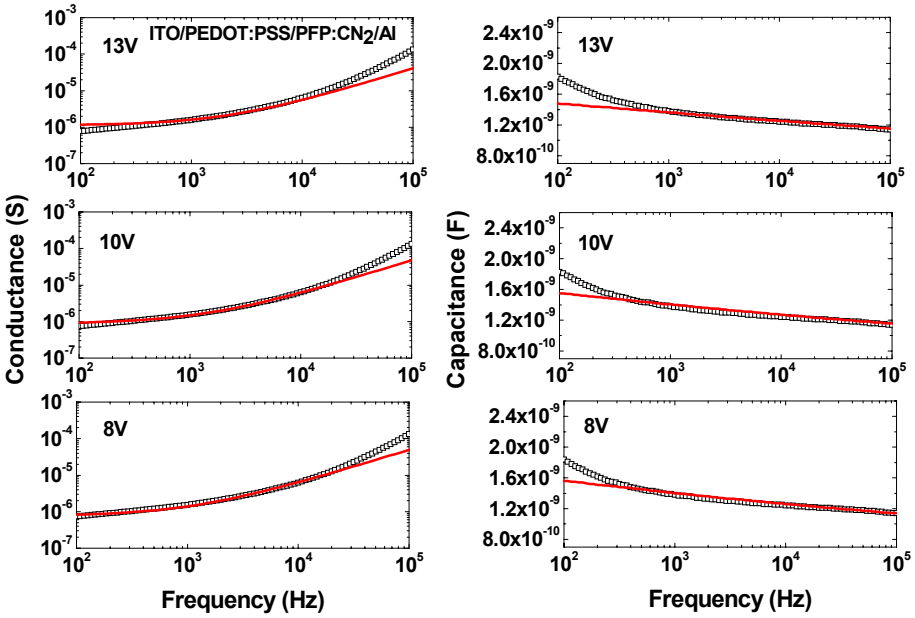

Figure 4.22 – Conductance (left) and capacitance (right) for ITO/PEDOT:PSS/PFP:$(CN)_2$/Al at different applied bias. The solid lines are fits to the experimental data using Eq. [4.48].

Figure 4.21 and Figure 4.22 show that capacitance has a weak dependence with frequency and bias and its value is approximately determined by the geometric capacitance. As bias increases, the capacitance for the MDMO:PPV based diode tends to decrease. At 13 V, just below the light emission threshold, electrons begin to be injected through the cathode, neutralizing the positive charge accumulated in the device and slightly decreasing the capacitance. Further increasing bias would induce a negative capacitance at low frequencies. According to [Castro05], if $\omega < \tau_t^{-1}$, the carrier does relax or, in other words, the carrier can transit between the electrodes. If recombination takes place, charges accumulated at the MDMO:PPV layer are consumed and therefore the capacitance decreases. This phenomenon is less pronounced for the PFP:$(CN)_2$ based diode, since the EL onset occurs at higher bias.

Fitted results to the experimental G and C using equation [4.48] are shown as solid red lines in Figure 4.21-4.22. Simulations are in good agreement with experimental values in most of the simulation frequency interval. According to what is explained in the above paragraph, a deviation of the theoretical capacitance from experimental values at low frequencies was expectable. Parameters obtained from the fit for the PFP:$(CN)_2$ are M=1 and α=0.08 and for

the MDMO:PPV, M=0.2 and α=0.3. These values reflect a high dispersive transport occurring in our devices.

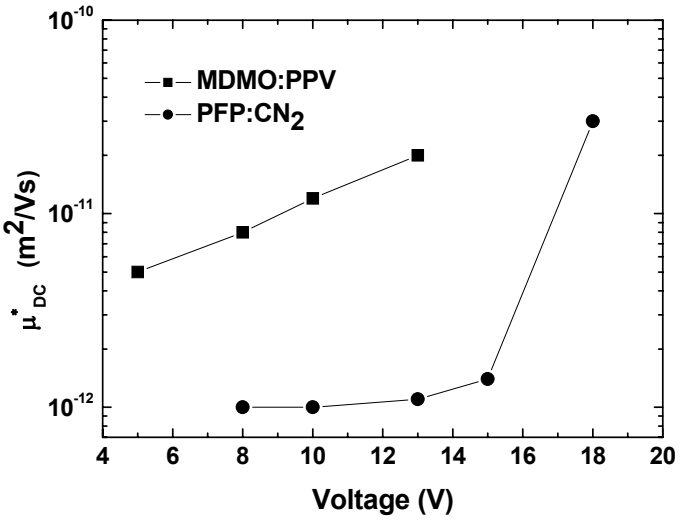

Figure 4.23 - Derived mobility for a MDMO-PPV and a PFP:$(CN)_2$ based diode from the fit to AS measurements.

Figure 4.23 shows the derived μ_{DC} as function of bias for both structures. The fitting process has been carried out for voltages below the light emission onset, to assure that only one type of carrier (holes) is present in the device. Mobility values for MDMO:PPV are in good agreement with measured mobilities for this polymer using time-of-flight techniques and dark injection techniques [Campbell99]. Mobilities obtained for PFP are approximately one order of magnitude lower than those of PPV, ranging from 10^{-12} to 10^{-10} m^2/Vs depending on bias. In the case of MDMO-PPV, the average mobility obtained for the fit of the DC current model in section 4.3.4 was μ_{DC}*=8.3x10^{-10} m^2/Vs. This is in excellent agreement with the values shown in Figure 4.23. The average mobility for the PFP:$(CN)_2$ obtained for the current fit was μ_{DC}*=6x10^{-9} m^2/Vs. However, this fit was performed over a voltage range up to 25 V. Experimental data for admittance are available only up to a DC bias of 18 V with a mobility of 3x10^{-11} m^2/Vs. Nevertheless, Figure 4.23 displays the exponential tendency of mobility with bias, predicting an increase of a few orders of magnitude at 25 V.

4.5 Conclusions

A new model for the SCL regime in the presence of non-ohmic contacts has been derived. In the case of an OLED with an intermediate-large injection barrier (>0.3 eV), the electric field at the interface cannot be neglected. Using this boundary condition, a general expression of the maximum space charge current was deduced in section 4.2.1. In the case of ohmic contacts, this equation reduces to the traditional Mott-Gurney expression.

Within the previous framework, this thesis proposes a complete model for conduction in single carrier organic diodes in which both injection and bulk currents are simultaneously considered. Traditionally, the bulk regime is considered to be predominant in those structures with quasi-ohmic contact. The model confirms the belief that space-charge current may also play an important role in structures with significant values of the barrier height (0.3-0.7 eV), depending on sample thickness, applied bias and carrier mobility.

An analytical function, β, defined as the ratio between the real current across the diode and the SCL current, has been used to quantify how close we are to the extreme simplifications, injection and bulk limited conduction, using measurable quantities such as current and bias.

Using the injection model proposed by Arkhipov et al., our model has been verified by fitting it to experimental curves of MDMO:PPV and PFP:$(CN)_2$ based OLEDs with different thickness. Device and material microscopic parameters extracted from the fit are in good agreement with those referred in literature. These parameters characterize the hopping type transport occurring in the diode. In order to demonstrate the strength of the model, diodes based on the same material, and thus having the same microscopic parameters, but with different active layer thicknesses have been characterised and compared with the model predictions. Despite measurement uncertainties, the agreement between theory and experiment is very good.

The general DC conduction model was successfully used to reformulate the small signal model in order to include the effect of injection barriers into the impedance measurements. A new expression for the admittance in organic diodes was derived using a frequency-dependent mobility as corresponds to dispersive transport. By means of fitting the model to experimental curves, the new AC model is used to extract mobility and parameters characterizing dispersive transport in OLEDs. Results indicate a highly dispersive transport in diodes based on MDMO:PPV and PFP:CN_2. Mobilities obtained from the fit of the DC model to the experimental J-V curves and those obtained from the fit the AC model to the C-f and G-f curves are in good agreement.

CHAPTER 5

NEW CATHODE PATTERNING TECHNIQUE FOR PMOLED DISPLAYS

Contents

5 New cathode patterning technique for PMOLED displays 147

5.1 Cathode patterning techniques 147

5.1.1 Shadow mask 148
5.1.2 Jet printing of polymers 149
5.1.3 Dry etching of the cathode 149
5.1.4 Cathode separators (“Pillars”) 150

5.2 Cathode patterning using mechanical ablation 151

5.2.1 Mechanical set up 152
5.2.2 Cathode patterning 154

5.3 Fabrication of a PMOLED display 156

5.3.1 Mask Fabrication 156
5.3.2 PMOLED display prototype 157

5.4 Conclusions 160

Chapter 5

5 New cathode patterning technique for PMOLED displays

A major issue in organic displays is the availability of a simple and affordable technique to pattern the metal cathode. Conventional photolithographic techniques used to define the anode with very good resolution cannot be used for cathode patterning simply because the chemicals involved in the lithography degrade the organic material. In this chapter, an innovative, easily implemented and cost-effective method for cathode patterning is presented. This technique is indicated to be used in displays for portable applications, though the extension to larger formats should not imply too much difficulty. Section 5.1 reviews the most widely employed techniques for cathode patterning. In section 5.2 a new method for cathode patterning based on mechanical ablation is described. Section 5.3 presents a small prototype of a PMOLED of 5x7 pixels fabricated using the new technique to define the cathode. Finally, conclusions are summarized in section 5.4.

5.1 Cathode patterning techniques

So far, this thesis has dealt with sets of organic diodes. Each sample contained eight diodes that shared a common cathode, and individual contacts through the anode were employed to bias each one separately. Ordinary displays manage thousands of pixels, and thus, a contact per pixel is not a feasible solution. Instead, electrodes are deposited in a row-column matrix, defining the pixel at each intersection point. Pixels are usually addressed by driving the appropriate row and column. When no additional devices are included within each pixel the display is considered as passive matrix.

An organic display of n x m pixels based on passive matrix consists of several organic layers sandwiched between two patterned metals. The width of the intersecting ITO and cathode metal lines define the size of the pixel. In displays with high information density the size of the

pixels has to be sufficiently small, i.e., the number of pixels per inch (ppi) indicates the display resolution. The n rows acting as anode in the matrix are defined using standard photolithographic techniques over an ITO coated glass (or plastic) substrate. The organic layers are then deposited using either evaporation in the case of small molecules or spin coating in the case of polymers. Finally the cathode is evaporated and the m columns defining the matrix are patterned. Cathode patterning requires techniques that do not damage the active layers underneath. Since organic materials are very sensitive to moisture, oxygen, UV radiation and organic solvents, standard photolithography and wet etching techniques are generally discarded. In this section, the most relevant techniques to define the cathode columns are outlined.

5.1.1 Shadow mask

The shadow mask technique is the simplest patterning method though it is difficulty used over large area displays. The metal acting as cathode is evaporated over the organic layer through a shadow mask [Tian97-Tian99]. In order to reproduce small size features accurately, shadow masks must be in contact with the organic layer, increasing the risk of damaging the organic materials. Moreover, high resolution shadow masks are expensive due to their stability requirements under certain pressure and thermal conditions. Besides, this method requires performing the mask alignment in vacuum conditions, and this is not, in general, an easy task. This technique is shown in Figure 5.1.

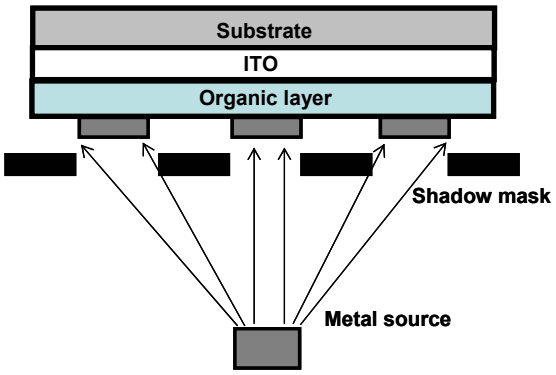

Figure 5.1 – Cathode patterning using a shadow mask.

This technique can also be employed to pattern the emissive layer of a RGB display. Incorporating a mechanical system that shifts the shadow mask into three different positions, it

is possible to evaporate the three emissive materials: red, green and blue. However, this is only applicable to small molecule materials, since the high molecular weight of polymers does not allow the deposition using thermal evaporation.

5.1.2 Jet printing of polymers

Jet printing technique was developed by Cambridge Display Technology (CDT) [cambridgedisplay] and is the most widely used method to manufacture polymer based colour displays. It allows to locally deposit the polymer material according to a previously designed pattern, in the same way as an ordinary ink-jet printer would do. In this case, a small drop of the polymer solution is deposited onto the substrate using a "printer". This, apparently simple technique, allows an easy fabrication of RGB displays since each colour is deposited following an independent pattern, and moreover, it is easily scalable to large panel displays. In addition, using jet printing saves the cathode patterning step since the organic layers have already been designed.

In order to confine the polymer solution, the substrate has to be previously pre-patterned with photoresist "banks" [Kobayashi00]. These banks help confining and homogenising the polymer layer. Figure 5.2 shows a schematic of the jet-printing technique.

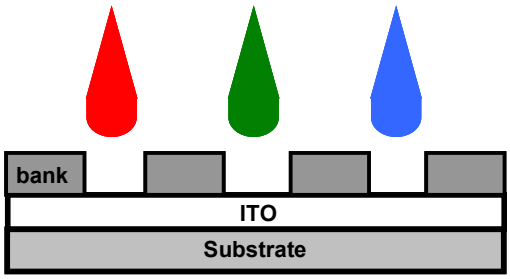

Figure 5.2 – Depositing polymer solution using jet printing technique.

5.1.3 Dry etching of the cathode

This method is similar to the standard photolithography technique but the etching step avoids any contact between the chemicals involved in the photolithography and the organic emissive layers. First, the cathode is evaporated on top of the emissive layer. Then the photoresist is spin coated on top of the cathode and patterned using conventional techniques. The metal cathode acts as a barrier and protects the organic layer underneath. Finally, the cathode is

etched using dry processes that do not affect the organic layer, such as plasmas or RIE (reactive ion etching). When using aluminium as cathode, the dry etching is easily performed using chlorine plasmas [Pschenitzka02].

5.1.4 Cathode separators ("Pillars")

One of the most extended techniques of cathode patterning in small molecules based displays is the construction of cathode separators (or "pillars") to isolate each pixel. These walls are built on the ITO coated substrate prior to the evaporation of the organic material and the cathode, and they are made of an insulating material, typically photoresist. The pillars are of several μm height in order to prevent short-circuits of the evaporated metal between two adjacent columns [Tian97]-[Py00]-[Huang04]. During fabrication, wet etching causes narrowing or undercuts at the bottom, resulting in overhanging top sides. This helps to keep an open circuit between top and bottom layers during metal deposition. Figure 5.3 shows the cross section of the resulting pixels separated by pillars.

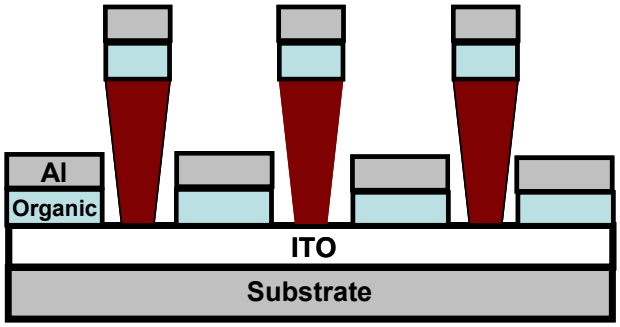

Figure 5.3 – Use of cathode separators to pattern the organic layer and the cathode.

However, this technique is not always applicable to polymer based displays. The fabrication of cathode separators results in a non-flat surface over which it is difficult to deposit the polymer by spin-coating. In the best case, spin casted materials act as a cover smoothing the pillars cross-section and causing the short-circuit protection to fail. Besides, an additional difficulty arises because the pillars are usually made of a photoresist-like material which is affected by solvents used in the spin coating process.

Nevertheless, this technique has been adapted to polymer processing by choosing specific materials and solvents [DeFranco06]. For example, the pillars are built with conventional photolithography on top of a separate backing layer. Then, the polymer is deposited by spin-

coating on top of the ITO layer. Next, the pillars are put in contact with the organic layer, and laminated at high temperature at the emissive polymer film. This method is called “Transferred photoresist” [Pschenitzka02]. The photoresist has to be carefully chosen so that it does not degrade the organic material. Finally, the metal cathode is evaporated.

5.2 Cathode patterning using mechanical ablation

Cathode patterning techniques mentioned in the above section present several disadvantages that prevent PLEDs based displays from being boosted in the display market. For example, standard photolithography requires chemical products that may degrade the organic layer. Jet printing uses specific printers for polymer deposition that must be specifically designed, increasing significantly production costs. Other techniques that rely on evaporation methods, such as the one based on cathode separators, are not scalable to large area displays and are only applicable to small molecules due to the high molecular weight of polymers.

In this section, a new method for cathode patterning based on mechanical ablation is proposed. The main advantages of this technique are:

- It avoids the contact between the organic layer and other chemicals that may deteriorate the device performance.
- Fabrication steps are minimized, which implies a reduction in the manufacturing costs.
- It does not require big and expensive equipment.
- It is applicable to both small molecules and polymer based displays.
- Once the fabrication set up has been calibrated, it is valid for any material used as cathode.
- It may benefit from computer assisted design (CAD) software.

Mechanical ablation for cathode patterning is based on the fact that organic materials are extremely soft in comparison with the anode material, typically ITO. The operational principle is very simple: a spring probe sweeps over the metal cathode following a previously designed pattern. The metal is lifted-off drawing the cathode column design without damaging the ITO anode. This method requires development of a mechanical set up in which the spring probe is adapted to an XY micropositioning system controlled by computer software.

5.2.1 Mechanical set up

This metal ablation patterning method required an experimental set up that had to be customized for this purpose. The whole set up relied on a commercial equipment, namely, a laser system Epilog Mini/Helix 24x12 model 8000, which includes an XY micropositioner and a tray to locate the sample [epiloglaser]. This equipment incorporates a 45 W CO_2 laser, originally meant to be used as an engraving, cutting and marking system. However, by setting the laser power to zero, it is possible to benefit exclusively from the micropositioner and the engraving tray. Figure 5.4 shows the Epilog system. The system motion control is carried out by two DC servomotors for precise positioning. The micropositioning system allows a resolution of 1200dpi. It also includes an external ventilation circuit to the outside. The original engraving area, which will now be used as the sample plate where the ablation will take place, has dimensions 610 x 305 mm^2. The XY micropositioner is controlled by software, so that the motion follows a previously designed pattern, in this case, the display cathode lines.

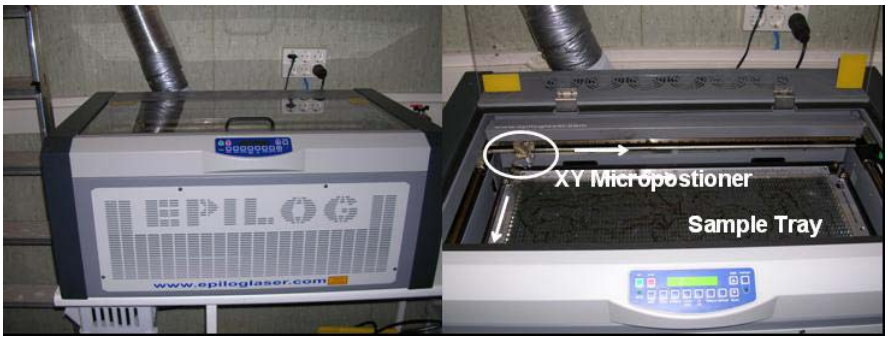

Figure 5.4 - Epilog Mini / Helix 24 laser system.

As already mentioned, to successfully carry out mechanical patterning, the laser has to be turned off. Instead, a home-made mechanical piece has been designed and adapted to the micropositioner. This piece includes a spring probe fixed in between two methacrylate blocks that enables upward and downward motion by means of a screw, see Figure 5.5(a). The whole piece is mounted on the micropositioner using a bolt as shown in Figure 5.5 (b).

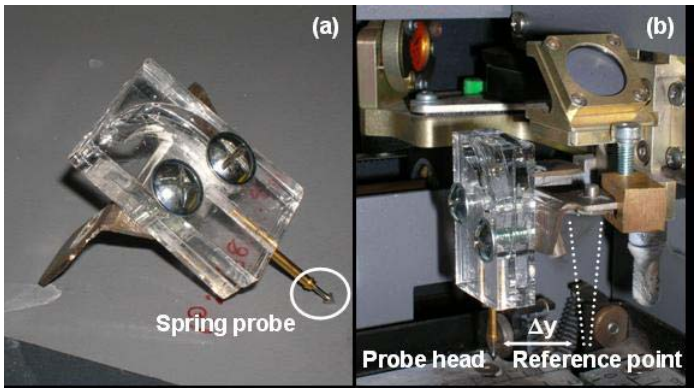

Figure 5.5 – (a) Spring probe embedded in a methacrylate block and (b) Mechanical piece mounted on a micropositioning system.

It is important to notice that the position of the new spring probe head that will be in contact with the sample is now shifted with respect to the reference point by a distance Δy. This distance is crucial since the micropositioner is calibrated according to that reference point, and consequently, the offset will have to be taken into account when configuring the software controlling the micropositioning system.

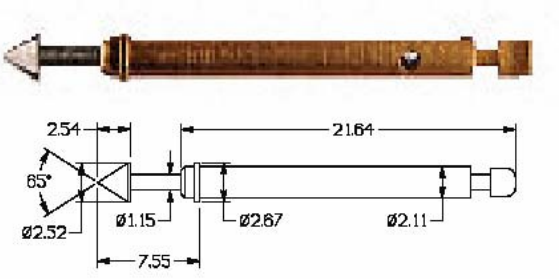

Figure 5.6 – Spring probe design.

The spring probe possesses a convex head with a 65º aperture angle which helps smoothing the initial contact between the probe and the sample. The spring included inside the probe shifts the head upwards and backwards allowing a trajectory of 2.4 mm.

Finally, the sample is fixed to the patterning plate by using a set of adjacent pieces of glass of the same thickness as the sample. The glasses surrounding the sample are fixed to the patterning tray, sticking the sample to a fixed position. The requirement of equal thickness for the sample and the contiguous glasses is a crucial issue since this will avoid surface discontinuities and thus it will prevent the probe from getting stuck or suffering undesired jumps.

5.2.2 Cathode patterning

The final display prototype will have 7x5 pixels, i.e., seven anode columns and five cathode rows. So, the first step is to design the pattern of the cathode tracks. The commercial equipment behaves as a printer, i.e., the pattern is designed with a vector graphic design application, namely Corel Draw, and the resulting file is sent to the commercial engraving system.

Figure 5.7 shows the designed cathode pattern. Tracks are 1 mm wide and the inter-pixel distance is not determined by the drawing but by the probe tip which is currently in the order of a hundred microns.

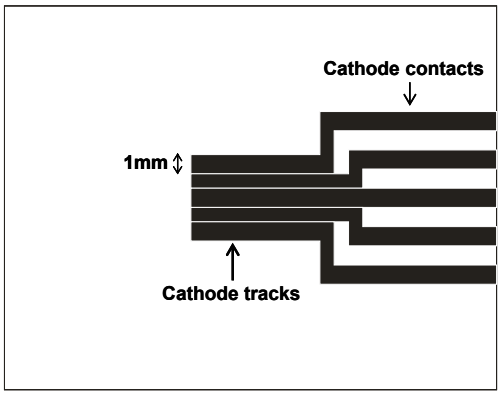

Figure 5.7 – Design of the cathode tracks.

Next, the commercial "printer" settings need to be configured before the file information is sent to the micropositioning system. The motion velocity was set to be between 0.5 -1 cm/s, this is around 5% of the maximum velocity achieved by the commercial micropositioner. On the other hand, the probe tip has to be focused with the exact pressure over the substrate. The pressure has to exceed the hardness of the metal layer so that it is properly lifted-off. At the same time, the pressure should not be as high as to affect the anode underneath. The exact value of the probe pressure depends on the nature of the set of layers organic-cathode, i.e., material hardness, thickness, etc. Though the ITO hardness is difficult to asses with high accuracy [Suzuki94], it is hard enough to enable a wide operation margin. After several attempts, the pressure was estimated to be at least 10^{11} N/m^2 to remove locally the metal without affecting

the ITO anode. This has been checked by adjusting the tip weight of a commercial contact profilometer.

For the PMOLED prototype presented in section 5.3, aluminium was used as cathode. Figure 5.8 shows a picture of the resulting Al tracks. It can be seen that the Al has been properly eliminated from the desired areas without metal shavings, and that the resulting track width is in the order a few hundreds microns. However, if the probe tip pressure on the sample is not adequate, it may happen that some portions of Al remain un-removed resulting in short-circuits between adjacent tracks. This could be sorted out by going over the sample as many times as necessary as long as the sample remains carefully fixed, i.e. it is not changed from the original position, otherwise the probe tip will not exactly trace the same path.

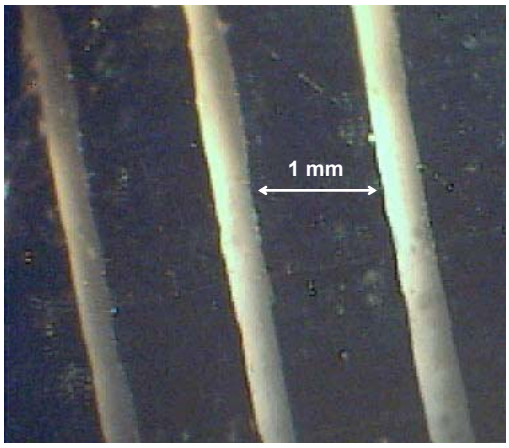

Figure 5.8 – Aluminium tracks performed with the mechanical ablation technique.

On the other hand, while the mechanical ablation is taking place, a ventilation system connected to the outside hoovers all possible aluminium shavings that also may cause short-circuits between tracks.

Finally, it is worth mentioning that the mechanical ablation technique to pattern metal surfaces came up as an alternative to laser ablation. The original idea was to pattern the aluminium surface using the CO_2 infrared laser incorporated in the Epilog engraving system. However, after several attempts, it was verified that the laser wavelength was not suitable since it not only removed the aluminium but also affected the ITO underneath. This caused open circuits in the anode rows, resulting in isolated pixels that could not be biased from the outside contacts.

5.3 Fabrication of a PMOLED display

In this section, a 7x5 pixels PMOLED display prototype based on MDMO:PPV is presented. The display fabrication process was done using conventional spin-coating, evaporation as well as photolithographic techniques for the anode patterning, as those described in chapter 2. The aluminium was column patterned using mechanical ablation.

5.3.1 Mask Fabrication

Firstly, the ITO anode columns needed to be designed. For this purpose, a new method was optimized to fabricate the mask employed in the photolithography. Instead of using a conventional acetate mask, the new mask was fabricated using laser ablation over a painted mirror. The Epilog engraving system was used for this purpose, but this time, the CO_2 laser was employed for the ablation. The mask was designed using Corel draw. The intersections of the anode rows with the Al columns (see Figure 5.7) would define the pixel matrix. This is shown in Figure 5.9(b).

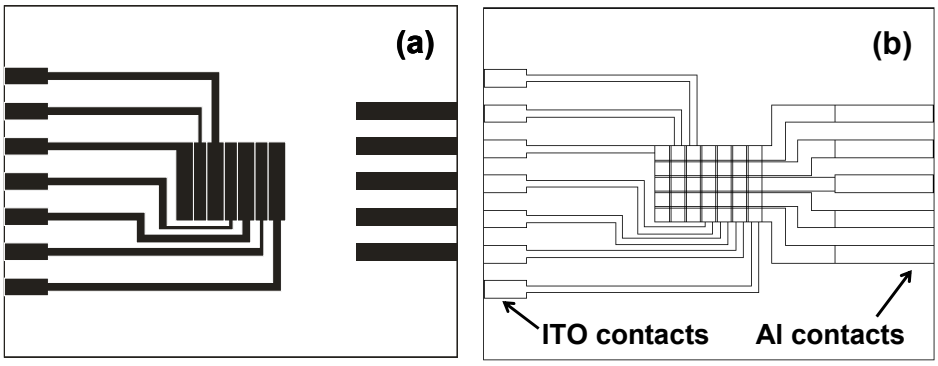

Figure 5.9 – (a) Mask design for the ITO photolithography and (b) Pixel definition by overlapping the anode and cathode masks.

The designed mask was implemented over the side of a piece of mirror coated with a reflective paint. This was fixed on the Epilog tray, and the designed mask was sent to the Epilog laser printer. The CO_2 laser removed the unwanted areas following the design in Figure 5.9(a). The final mask shown in Figure 5.10 was performed using both vectorial and raster configuration for the Epilog system. The vectorial mode was used to outline the ITO tracks while the raster

mode was use to eliminate the paint from the unwanted areas. The rastering was done with a laser power of 5% of the maximum (45 W) while for the vectorial job the power was set to 10%. The velocity of the micropositioning system never exceeded 10% of the maximum velocity achieved by this equipment.

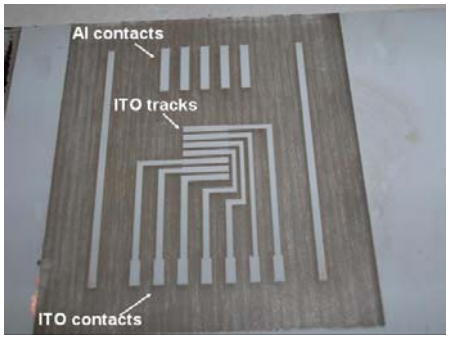

Figure 5.10 – Mask employed in the ITO photolithography.

5.3.2 PMOLED display prototype

The anode is column-patterned in a commercial ITO coated glass by means of conventional photolithographic techniques and using the previously designed mask (see Figure 5.10). Since this mirror caused the mask to absorb the UV light in a greater extent than a traditional acetate mask, the exposure time was increased up to 90 seconds. Figure 5.11 shows the sample with the defined ITO columns.

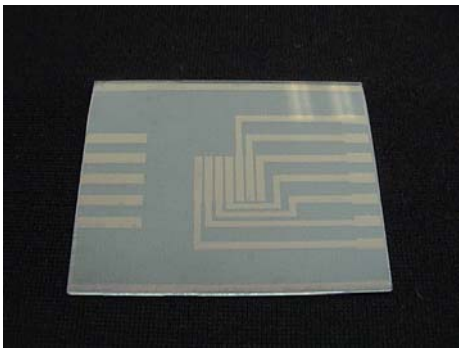

Figure 5.11 - Sample after ITO photolithography showing anode columns.

A conductive organic layer of PEDOT:PSS and the active layer were spin-coated on the anode patterned surface. The polymer used as active layer was MDMO-PPV having a thickness of 70 nm. The aluminium cathode was vacuum evaporated on top of the organic layer surface in an atmosphere of 10^{-6} Torr. Then, the cathode tracks were patterned using the mechanical ablation technique described in section 5.2. Figure 5.12 shows a picture of the defined pixels having approximately 1 mm side. It can be seen that the lines between adjacent tracks turn out to be half as wide when using mechanical ablation.

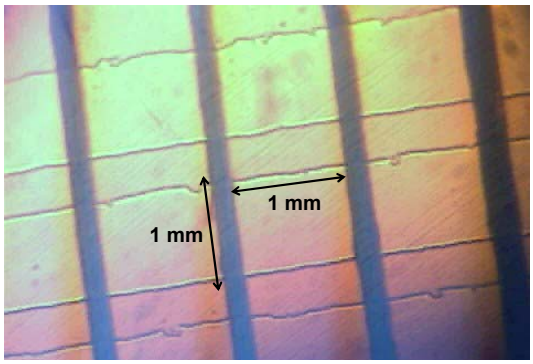

Figure 5.12 – Pixel definition.

Finally, displays were encapsulated in a glove-box under nitrogen atmosphere, and mounted on a Printed Circuit Board (PCB) in order to facilitate pixel driving. The soldering of the display to the board was done using a thermal bonding process. An anisotropic conductor film from Hitachi Chemical Co. was used as glue between the display and the board. The soldering was done at 300ºC, exerting a pressure on the sandwich structure of 30 N/m^2 during 1 minute.

Figure 5.13 shows the final PMOLED display prototype. Each track on the board is connected either to a cathode column or to an anode row. In order to address one pixel, the corresponding column and row need to be biased.

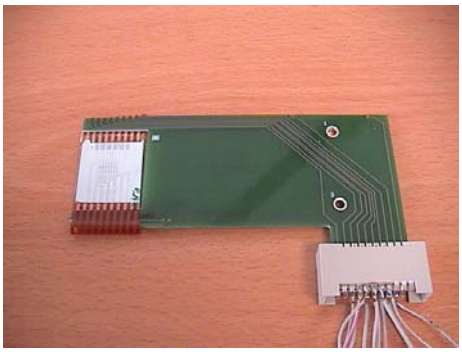

Figure 5.13 – Final device mounted on a PCB.

Figure 5.14 shows two photographs of a MDMO-PPV based display prototype, in which different pixel configurations have been biased (lighting squares). One of the major difficulties to overcome during the fabrication process was to avoid the appearance of shortcuts between adjacent aluminium tracks. This requires the mechanical set up for the aluminium ablation to be perfectly adapted to each individual sample.

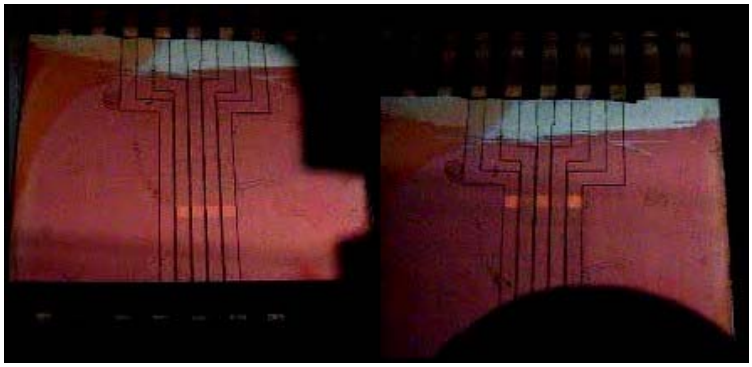

Figure 5.14 - MDMO-PPV based display prototype with different pixel configurations lighting.

Figure 5.15 shows a J-V characteristic of a pixel of a display based on ITO/PEDOT:PSS/MDMO:PPV/Al. The effect of a low parallel resistance at low voltages can be noticed. This is mainly attributed to leakage currents at the pixel corners, a main drawback regarding power consumption.

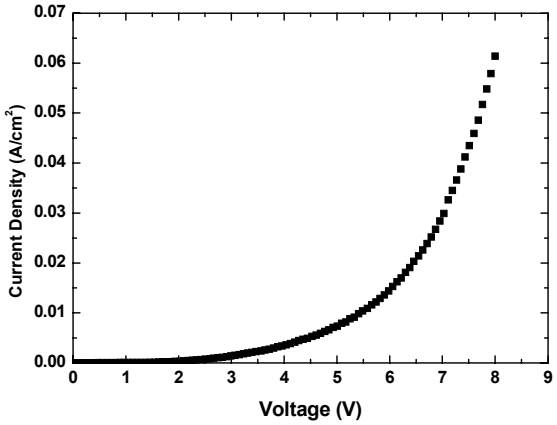

Figure 5.15 - J-V curve of one pixel of a MDMO:PPV based display.

As the display is current driven, the peak current requirement is dependent on the total number of pixels that need to be illuminated at one time.

5.4 Conclusions

In this chapter, a new method to pattern the cathode tracks of an organic display based on a new technique, so called mechanical ablation, has been developed and successfully tested by fabricating a small display. This is a cost-effective process that does not involve the use of chemical solvents that may degrade the organic materials. This new method for cathode patterning is based on the fact that organic materials are extremely soft in comparison with the anode material, typically ITO. The experimental set up of this technique is based on a commercial laser engraving system, Epilog Mini 24x12 Model 8000 that was customized for this purpose. Setting the laser power to zero and adapting the XY micropositioner to a spring probe by means of several home made pieces, it is possible to remove the metal from the unwanted areas following a previous designed pattern. Results show track width of the order a hundred microns. Resolution depends on many factors, the most relevant one being the size of the probe tip. In our case, it falls around 100 μm.

This method was successfully applied to the fabrication of a 7x5 pixel PMOLED display with structure ITO/PEDOT:PSS/MDMO:PPV/Al. The ITO columns were defined employing conventional photolithographic technology. The mask used in the photolithography was fabricated with the laser engraving system over a mirror having a surface coated with a

reflective paint. The final display was encapsulated and mounted on a PCB to facilitate biasing. It is shown that by properly addressing, different pixel configurations can be achieved. Results show a good pixel definition. Finally, the mechanical ablation was proven to be a clean and successful method to pattern the cathode in an organic display. Nevertheless, the key issue relies on a fine tuning of the experimental set up. This engineering task can still be improved by developing a customized system in which the micropositioner and the probe tip are integrated, and with an engraving tray adjustable to every sample dimension.

CHAPTER 6

6 Conclusions and future work

6.1 Conclusions and objectives accomplishment

The main contributions of this thesis can be placed at three different levels. Firstly, an exhaustive study within the framework of semiconductors and insulator physics theory serves as a solid base to develop a theoretical model to explain the electrical behaviour of organic light emitting devices. Secondly, a demanding job has been done in the context of device fabrication and characterization. In this sense, standard fabrication techniques such as photolithography, spin-coating, metal evaporation and encapsulation have been successfully applied to fabricate PLEDs based on a new polyfluorene derivative. Thirdly, at a system manufacturing level, a new technique to pattern the metal tracks in organic displays based on mechanical ablation has been developed. Most relevant conclusions of this work are summarized below, indicating whether the corresponding initial objective (as described in section 1.4) has been accomplished.

Theoretical Modelling: Objective (b)

- A new conduction model for the space charge limited regime in the presence of non-ohmic contacts has been developed. The new contribution of this approach is that it takes into account and determines a non-negligible electric field at the interface, in the range 0-V/L (with V the applied bias and L the active layer thickness).
- A complete theoretical model is proposed to simulate conduction in *single carrier* diodes taking into account both injection and transport contributions. The injection function is framed within a microscopic approach proposed by Arkhipov et al. in which the injection current depends upon the probability of a carrier to jump from the metal into an energetically and positionally disordered organic material.

- Hole mobility and several microscopic material and structure parameters were obtained by fitting the previous model to experimental J-V curves. In the case of PFP:$(CN)_2$ the mobility well above the threshold voltage was estimated to be in the order of 10^{-10} m^2/Vs.
- Theoretical predictions for devices in which active layer thickness is the only variable show a good agreement with experimental curves confirming the validity of the model. The model was checked using structures based on two different polymers: MDMO:PPV and PFP:$(CN)_2$.
- An analytical function, β, has been defined as the ratio between the bulk current that takes into account electric field at the interface and the pure space charge limited current (Mott-Gurney). This function is used to quantify the role played by each limiting conduction regime, either injection or bulk.
- The new J-V model serves to reformulate the small-signal admittance in order to include non-negligible injection barriers. This new model was successfully fitted to experimental C-f curves, obtaining the material mobility and dispersion parameters.

In view of the above results, it can be said that objective (b) has been fully accomplished. However, further improvements of the model can still be made and are left for future work.

Device fabrication and characterization: Objective (a)

- PLEDs passive matrixes based on a new polyfluorene derivative, PFP:$(CN)_2$, have been fabricated using standard fabrication techniques. Electrical characterization showed similar behaviour to commercial polyfluorenes, confirming the general trend that threshold voltage increases with thickness.
- The direct interaction between the device layer structure and environmental agents (mainly oxygen and moisture) triggers several chemical reactions between oxygen and the polymer backbone that result in morphological changes that degrade the organic material. A simple encapsulation technique in an inert atmosphere (N_2) has proven to overcome this problem and significantly increase the device operating lifetime.
- Encapsulation prevents “black spots”, that is, non-conductive regions at the cathode/organic interface. This results in a stabilization of the current along the diode.

- Optical performance of PFP:$(CN)_2$ devices shows luminance values of the order of 500 cd/m^2 with a deep blue emission displaying a main emission peak centred at 420 nm and a vibronic shoulder at 450 nm. This corresponds to CIE coordinates x = 0.16, y = 0.13.
- Optical characterization reveals two distinguished features centred at 480 nm and 535 nm. These are attributed to two characteristic degradation mechanisms in polyfluorenes. The first one is proposed to be a result of an excess of electrons that introduces new C=C bonds. The second one is due to the reaction of the oxygen with the C-9 position of the backbone creating a fluorenone or keto defect.

The above results cover most of the initial goals proposed in objective (a). Nevertheless, fabricated structures have not been optimized to obtain high optical efficiencies. This task requires the introduction of additional electron injecting layers between the cathode and the polymer, and it will be the subject of future work.

Display manufacturing: Objective (c)

- A commercial equipment that includes a micropositioner and a servomotor for a 2D motion, has been successfully adapted to develop a new method for cathode patterning.
- An innovative method for cathode patterning based on mechanical ablation has been proposed and proved. This technique reduces manufacturing costs since it does not involve expensive equipment. Moreover, it is a “dry” technique, meaning that it avoids contact with chemical solvents that may degrade the organic layers. Results show aluminium track widths of the order of hundreds of microns.
- A 7x5 pixel PMOLED display based on MDMO-PPV was manufactured using mechanical ablation for the cathode patterning. Results show a good pixel definition and device performance.

Prototypes of PMOLEDs displays using mechanical ablation for the cathode have been developed, accomplishing the main aims proposed in objective (c). However, the technological aspects of this technique require further improvement so that the fabrication process is customized for organic displays.

6.2 Future work

- A study of the mobility dependence on the electric field and injected charge, and including this dependence in the proposed space charge model.

- Fabrication of PLEDs improving the layer structure so that the electron injection from the cathode is increased. This can be done by adding a layer between the cathode and the organic layer (typically LiF or few monolayers of Ca or Ba). This will improve both threshold voltage and internal quantum efficiency.
- Electrical characterization of PLEDs at different temperatures. A study of the current temperature dependence may indicate the conduction mechanisms taking place in the sample.
- Further study of the degradation mechanisms in polyfluorenes that result in a broadening of the emission spectra.
- Fabrication of passive matrix PLEDs over flexible substrates. A study of the dependence of electrical and optical properties with the mechanical torsion of the sample.
- Developing a customized experimental system for mechanical ablation technique for the metal cathode.
- Driver design for a PMOLED display. The driver's electronic would be controlled with a FPGA.

REFERENCES

[Abkowitz92] M.A. Abkowitz, "*Electronic transport in polymers*", Philosophical Magazine B-Physics of Condensed Matter Statistical Mechanics Electronic Optical and Magnetic Properties, **65**, pp. 817, 1992.

[Abkowitz95] M.A. Abkowitz , H.A. Mizes and J.S. Facci , "*Emission limited injection by thermally assisted tunnelling into a trap-free transport polymer*", Appl. Phys. Lett., **66**, pp. 1288, 1995.

[Álvarez03] A.L. Alvarez, J. Tito, M.B. Vaello, P. Velasquez, R. Mallavia, M. M. Sanchez-Lopez and S. Fernandez de Ávila. "*Polymeric multilayers for integration into photonic devices*", Thin Solid Films, **433**, pp. 277, 2003.

[Álvarez08] A. L. Álvarez, B. Arredondo, B. Romero, X. Quintana, A. Gutiérrez-Llorente, R. Mallavia, J. M. Otón, *"Analytical evaluation of the ratio between injection and space-charge limited currents in single carrier organic diodes*", IEEE Transact. Elect. Dev., **55** (in press), 2008.

[Arkhipov98] V.I. Arkhipov, E.V. Emelianova, Y.H. Tak and H. Bässler, "*Charge injection into light-emitting diodes: Theory and experiment*", J. Appl. Phys., **84**, pp. 848, 1998.

[Arkhipov99] V.I. Arkhipov, U. Wolf, and H. Bässler, "*Current injection from a metal to a disordered hopping system II. Comparison between analytic theory and simulation*", Phys. Rev. B., **59**, pp. 7514, 1999.

[Arkhipov01APL] V.I. Arkhipov, P. Heremans, E.V. Emelianova and G.J. Adriaenssens, "*Space-charge-limited currents in materials with gaussian energy distributions of localized states*", Appl. Phys. Lett., **79**, pp. 4154, 2001.

[Arkhipov01Philos] V.I. Arkhipov, E.V. Emelianova and H. Bässler, "*Equilibrium carrier mobility in disordered hopping systems*", Philos. Mag., B, **81**, pp. 985, 2001.

[Arkhipov01PRB] V.I. Arkhipov, E.V. Emelianova and G.J. Adriaenssens, "*Effective transport energy versus the energy of most probable jumps in disordered hopping systems*", Phys. Rev. B, **64**, pp. 124124, 2001.

[Arkhipov03] V.I. Arkhipov, H. von Seggern, E.V. Emelianova, "*Charge injection versus space-charge-limited current in organic light emitting diodes*", Appl. Phys. Lett., **83** , pp. 5074, 2003.

[Ashtiani07] S.J. Ashtiani, G.R. Chaji, A. Nathan, "*AMOLED pixel circuit with electronic compensation of luminance degradation*", Journal of Display Technology, **3**, pp. 36, 2007.

[Bäck97] T. Bäck, U. Hammel, and H-P. Schwefel, "*Evolutionary Computation: Comments on the history and current state*", IEEE Trans. Evolutionary Computation, **1**, pp. 3, 1997.

[Bale06] M. Bale, J.C. Carter, C.J. Creighton, H.J. Gregory, P.H. Lyon, P. Ng, L. Webb, and A. Wehrum., "*Ink-jet printing: The route to production of full-color P-OLED displays*", J. SID, **14**, pp. 453, 2006.

[Barsoukov05] "*Impedance Spectroscopy. Theory, experiments and applications*" Edited by Evgenij Barsoukov, J. Ross Macdonald. John Wiley & Sons, 2005.

[Bässler93] H. Bässler, "*Charge transport in disordered organic photoconductors*", Phys. Stat. Sol. B, **175**, pp. 15, 1993.

[Bernius00] M. Bernius, M. Inbasekaran, E. Woo, W. Wu, L. Wujkowski, "*Fluorene-based polymers-preparation and applications*", J. Mater. Sci.:Mater. Eletron., **11**, pp. 111, 2000.

[Bliznyuk99] V.N. Bliznyuk, S.A. Carter, J.C. Scott, G. Klarner, R.D. Miller and D.C. Miller, "*Electrical and photoinduced degradation of polyfluorene based films and light-emitting devices*", Macromolecules, **32**, pp. 361, 1999.

[Böttger85] H. Böttger, V.V. Bryksin, "*Hopping conduction is solids*". Akademie-Verlag, Berlin, Chap. 6, pp. 224, 1985.

[Bredas85] J.L. Bredas, "*Springer Series of Solid State Science*", Kuzmany, H., Mehring, M., Roth, S., Eds.: Springer, Berlin, **63**, pp. 166, 1985.

[Brodrik07] J. Brodrik, "*Next-Generation Lighting Initiative at the U.S. Department of Energy: Catalyzing Science Into the Marketplace*", Journal of Display Technology, **3**, pp. 91, 2007.

[Brown04] J. Brown, R. Kwong, Y.J. Tung, V. Adamovich, M. Weaver, M. Hack, "*Recent progress in high-efficiency phosphorescent OLED technology*", J. SID, **12**, pp. 329, 2004.

[Burroughes90] J.H. Burroughes, D.D. Bradley, A.R. Brown, R.N. Marks, K. Mackay, R.H. Friend, P.L. Burns, A.B. Holmes. ''*Light-emitting diodes based on conjugated polymers*'', Nature, **347**, pp. 539, 1990.

[Calderón03] P. Calderón Badía, "*Ensayo de técnicas fotolitográficas compatibles con pantallas antiferroeléctricas*", Proyecto fin de carrera, Dpto. Tecnología Fotónica, ETSIT, UPM, 2003.

[cambridgedisplay] www.cdtltd.com

[Campbell95] I.H. Campbell, D.L. Smith, and J.P. Ferraris, "*Electrical-impedance measurements of polymer light-emitting-diodes*" Appl. Phys. Lett., **66**, pp. 3030, 1995.

[Campbell99] I.H. Campbell, D.L. Smith, C.J. Neef and J.P. Ferraris. *"Consistent time-of-flight mobility measurements and polymer light-emitting diode current–voltage characteristics*". Appl. Phys. Lett., **74**, pp. 2809, 1999.

[Campbell01] A.J. Campbell, D.D.C. Bradley and H, Antoniadis, "*Quantifying the efficiency of electrodes for positive carrier injection into poly(9,9-dioctylfluorene) and representative copolymers*", J. Appl. Phys., **89**, pp. 3343, 2001.

[Castro05] F.A. Castro, P.R. Bueno, C.F.O. Graeff, F. Nuesch, L. Zuppiroli, L. F. Santos and R.M. Faria. "*Crossover from capacitive to pseudoinductive charge-relaxation in organic/polymeric light-emitting diodes*". Appl. Phys. Lett., **87**, pp. 013505, 2005.

[Chaji07] G. Chaji, S. Alexander, A. Nathan and C. Church, "*A low-cost stable a-Si AMOLED display with full V_T shift and V_{OLED}-shift compensation*", J. SID, session 52.2, pp.1580, 2007.

[Chu07] C. Chu, J-k Ha, J-H Choi, S-S Lee, J-S Rhee, D-W Lee, J-K Chung, H-S Kim and K. Chung, "*Advances and issues in white OLEDs and color-filter arquitecture*" , J. SID, session 25.4, pp.1118, 2007.

[CIE90] CIE report 86, Commission Internationale de l'Eclairage, Vienna, Austria, 1990.

[Coehoorn05] R. Coehoorn, W.F Pasveer, P.A. Bobbert and C.J. Michels, "*Charge-carrier concentration dependence of the hopping mobility in organic materials with Gaussian disorder*", Phys. Rev. B, **72**, pp. 155206, 2005.

[Conwell97] E.M. Conwell and M.W. Wu, "*Contact injection into polymer light-emitting diodes*", Appl. Phys. Lett., **70**, pp. 1867, 1997.

[Coropcenau07] V. Coropceanu, J. Cornil, D.A. da Silva Filho, Y. Olivier, R. Silbey, and J.L. Brédas, "*Charge transport in organic semiconductors*", Chemical Reviews, **107**, pp. 926, 2007.

[Crispin03] X. Crispin, S. Marciniak, W. Osikowickz, G. Zotti, A.W. Denier van de Gon, F. Louwet, M. Fahlman, L. Groenendaal, F. de Schryver, W. Salaneck, "*Conductivity, morphology, interfacial chemistry, and stability of Poly(3,4-ethylene dioxythiophene)–Poly(styrene sulfonate): A photoelectron spectroscopy study*". J. of Polymer Science: PartB, Polymer Physics, **41**, pp. 2561, 2003.

[Crone02] B.K. Crone, A. Dodabalapur, R. Sarpeshkar, A. Gelperin, H.E. Katz and Z. Bao, "*Organic oscillator and adaptive amplifier circuits for chemical vapour sensing*". J. Appl. Phys., **91**, pp. 10140, 2002.

[Dascalu66] D. Dascalu, "*Small-signal theory of space charge limited diodes*" Int. J. Electron, **21**, pp. 183, 1966.

[Davids96] P.S. Davids, Sh.M.Kogan, I.D. Parker and D.L. Smith, "*Charge injection in organic light-emitting diodes: Tunnelling into low mobility materials*", Appl., Phys., Lett., **69**, pp. 2270, 1996.

[Davids97] P. S. Davids, I.H. Campbell and D.L. Smith, "*Device model for single carrier organic diodes*", J. Appl. Phys., **82**, pp. 6319, 1997.

[DeFranco06] J.A. DeFranco, B.S. Schmidt, M. Lipson and G.G. Malliaras, "*Photolithographic patterning of organic electronic materials*", Organic Electronics, **7**, pp. 22, 2006.

[epiloglaser] www.epiloglaser.com

[Fang-Iy07] W. Fang-Iy, Y. Xiao-Hui, N. Dieter, D. Rajasekhar, T. Ya-Hsien and S. Ching-fong, "*Efficient white-electrophosphorescent devices based on a single polyfluorene copolymer*" Adv. Funct. Mater., **17**, pp.1085, 2007.

[Forrest07] S. Forrest, "*Challenges of using organic light-emitting devices as white-light sources*" J. SID, session 25.1, pp.1109, 2007.

[Frenkel38] J. Frenkel, "*On pre-breakdown phenomena in insulators and electronic semi-conductors*", Phys. Rev., **54**, pp. 647, 1938.

[Friend99] R.H. Friend, R.W. Gymer, A.B. Holmes, J.H. Burroughes, R.N. Marks, C. Taliani, D.D.C. Bradley, D.A. Dos Santos, J.L. Bredas, M. Lögdlund and W.R. Salaneck. ''*Electroluminiscence in conjugated polymers*'', Nature, **397**, pp. 121, 1999.

[Frohne04] H. Frohne, C. R. McNeill, G. G. Wallace and P. C. Dastoor, "*Enhancement of polymer electronics via surface states on highly doped polymeric anodes*", J. Phys. D: Appl. Phys., **37**, pp. 165, 2004.

[Fujita03] M. Fujita, T. Ueno, T. Asano, S. Noda, H. Ohhata, T. Tsuji, H. Nakada and N. Shimoji, "*Organic light emitting diode with ITO/organic photonic crystal*", Electron. Letters, **39**, pp. 1750, 2003.

[Gaal03] M. Gaal, E. J. W. List and U. Scherf, "*Excimers or emissive on-chain defects?*", Macromolecules, **36**, pp. 4236, 2003.

[Gammerith04] S. Gammerith, H.G. Nothofer, U. Scherf, E.J.W. List, "*Identification of emissive interface-related defects in polyfluorene based light emitting devices"*, Jpn. J. Appl. Phys. Part 2, **42**, pp. 891, 2004.

[Gartstein96] Y.N. Gartstein and E.M. Conwell, "*Field-dependent thermal injection into a disordered molecular insulator*", Chem. Phys. Lett., **255**, pp. 93, 1996.

[Gill72] W.D. Gill, "*Drift Mobilities in Amorphous Charge-Transfer Complexes of Trinitrofluorenone and Poly-N-Vinylcarbazole*", J. of Appl. Phys., **43**, pp. 5033, 1972.

[Gomes06] H.L Gomes, P. Stallinga, M. Cölle, D.M. de Leeuw and F. Biscarini, "*Electrical instabilities in organic semiconductors caused by trapped supercooled water* ", Appl. Phys. Lett., **88**, pp. 082101, 2006.

[Gommans04] H.H.P. Gommans, M. Kemerink, G.G. Anderson and R.M.T. Pijper, "*Charge transport and trapping in Cs-doped poly(dialkoxy-p-phenylene vinylene) light-emitting diodes*", Phys. Rev. B., **69**, pp. 155216, 2004.

[Gong03-a] X. Gong, J.C. Ostrowski, D. Moses, G.C. Bazan and A.J. Heeger, "*Electrophosphorescence from a polymer guest-host system with an Iridium complex as guest: Förster energy transfer and charge trapping*", Adv. Funct. Mater., **13**, pp. 439, 2003.

[Gong03-b] X. Gong, P.K. Iyer, D. Moses, G.C. Bazan, A.J. Heeger and S.S. Xiao, "*Stabilized blue emission from Polyfluorene-based light-emitting diodes: elimination of fluorenone defects"*, Adv. Funct. Mater., **13**, pp. 325, 2003.

[Ghosh04] A. Ghosh and M. Hack, *"Fundamentals of OLEDs*", SID short course S-1, p. 31, Seattle, Washington, 2004.

[Halls95] J.J.M. Halls, C.A. Walsh, E.A. Marseglia, R.H. Friend, S.C. Moratti and A.B. Holmes. "*Efficient photodiodes from interpenetrating polymer networks*". Nature, **376**, pp. 498, 1995.

[Halls07] J. Halls. "*Recent advances in polymer OLED technology*", Seminar M-1, Society for the Information Display, Long Beach, California, 2007.

[Heath03] J.R. Heath, M.A. Ratner, *"Molecular electronics*", Physics Today, **56**, pp.43, 2003.

[Hirano07] T. Hirano, K. Matsuo, K. Kohinata, K. Hanawa, T. Matsumi, E. Matsuda, R. Matsuura, T. Ishibashi, A. Yoshida, T. Sasaoka, "*Novel laser transfer technology for manufacturing large-sized OLED displays*", J. SID, session 53.2, pp. 1592, 2007.

[Ho07] M-H. Ho, Y-S. Wu, S-W Wen, C. Chen, "*Highly efficient deep-blue EL devices*", J. SID, session 64.2, pp.1768, 2007.

[Hollands75] J. Holland, "*Adaptation in natural and artificial systems*", University of Michigan Press, 1975.

[Huang04] Z.H. Huang, W.M. Su, G.J. Qi, H.J. Lu, X.T. Zeng, and S. Wong, "*A novel method for fabrication of integrated shadow mask for patterning electrode in passive matrix OLED displays*", IEEE Proc. of the Electronics Packaging Technology Conference, pp. 169, 2004.

[Huang06] J. Huang, G. Li, E. Wu, Q. Xu and Y. Yang, "*Achieving high-efficiency polymer white-light-emitting devices*", Adv. Mater., **18**, pp. 114, 2006.

[Huitema02] H.E.A. Huitema, G.H. Gelinck, J.B.P.H van der Putten, K.E. Kuijk, K.M Hart, E. Cantatore and D.M. de Leeuw, "*Active-matrix displays driven by solution processed polymeric transistors*". Adv. Mater., **14**, pp. 1201, 2002.

[Ishii02] H. Ishii, K. Seki, "*Energy level alignment at organic-metal interfaces*", Conjugated polymer and molecular interfaces, Chap.10, pp. 293, 2002.

[isupply] www.isupply.com

[Kanicki05] J. Kanicki, S.J. Lee, Y. Hong, C.C. Su, *"Optoelectronic properties of poly(fuorene) co-polymer light-emitting devices on plastic substrate*", J. SID, pp. 993, 2005.

[Kassing75] R. Kassing, "*Calculation of the frequency dependence of the admittance of SCLC diodes*", Phys. Status Solidi A, **28**, pp.107, 1975.

[Katz02] H.E. Katz, X.M. Hong, A. Dodabalapur, Sarpeshkar. "*Organic field-effect transistors with polarizable gate insulators*", J. Appl. Phys., **91**, pp.1572, 2002.

[Kim06] T.H. Kim, H.K. Lee, O.O. Park, B.D. Chin, S.H. Lee, J.K. Kim, "*White-light-emitting diodes based on Iridium complexes via efficient energy transfer from a conjugated polymer*", Adv. Funct. Mater., **16**, pp. 611, 2006.

[Kitamura03] M. Kitamura, T. Imada, Y. Arakawa, "*Organic transistor circuits for application to organic light-emitting-diode displays*" Jpn. J. Appl. Phys, **42**, pp.2483, 2003.

[Klubek07] K. Klubek and D. Kondakov, "*Improving the operational lifetime of blue OLEDs with phenanthroline-based electron-transport materials*", J. SID, session 36.3, pp.1290, 2007.

[Kobayashi00] H. Kobayashi, S. Kanbe, S. Seki, H. Kigchi, M. Kimura, I. Yudasaka, S. Miyashita, T. Shimoda, C.R. Towns, J.H. Burroughes and R.H. Friend, "*A novel RGB multi-colour light-emitting polymer display*", Synth. Met., **111**, pp. 125, 2000.

[Kolosov01] D. Kolosov, D.S. English, V. Bulovic, P.F. Barbara, S.R. Forrest, M.E. Thomson, "*Direct observation of structural changes in organic light emitting devices during degradation*", J. Appl. Phys., **90**, pp. 3242, 2001.

[Kondakov07] D. Kondakov, W. Nichols, C. Lenhart, "*Structural identification of chemical products and mechanisms of operational degradation of OLEDs*" , J. SID, session 47.2, pp.1494, 2007.

[Lang04] D. V. Lang, X. Chi, T. Siegrist, A.M. Sergent, and A. P. Ramirez, "*Amorphouslike density of gap states in single-crystal Pentacene"*, Phys. Rev. Lett., **93**, pp. 086802, 2004.

[Lee07] J-H Lee, H-S Park, S-H Choi, M-K Han, "*Highly stable a-Si TFT pixel for large area AMOLEDs by employing both Vth storing and negative-bias annealing*", J. SID, session 13.2, pp.169, 2007.

[Lewis04] J.S. Lewis, M.S. Weaver, "*Thin-film permeation-barrier technology for flexible organic light- emitting devices*", IEEE J. Sel. Topics in Quantum Electron., **10**, pp. 45, 2004.

[Li98] Y. Li, J. Gao, G. Yu, Y. Cao, and A.J. Heeger, "*AC impedance of polymer light emitting diodes: A comparative study*" Chem. Phys. Lett., **83**, pp. 287, 1998.

[Li04] F. Li, Z. Chen, W. Wei, H. Cao, Q. Gong, F. Teng, L. Qian, Y. Wang, "*Blue-light-emitting organic electroluminescence via exciplex emission based a fluorene derivative*", J. Phys. D: Appl. Phys., **37**, pp. 1613, 2004.

[Li05] C.N. Li, C.Y. Kwong, A.B. Djurišić, P.T. Lai, P.C. Chui, W.K. Chan and S.Y. Liu, "*Improved performance of OLEDs with ITO surface treatments*", Thin Solid Films, **477**, pp. 57, 2005.

[Lifka07] H. Lifka, I. French, C. Tanase, D.J. McCulloch, P.van de Weijer, "*Ultra-thin flexible OLED device*", J. SID, session 53.4, pp.1599, 2007.

[List02] E.J. W. List, R. Guentner, P.S. de Freitas, U. Scherf, "*The effect of keto defect sites on the emission properties of Polyfluorene-type materials*", Adv. Mater., **14**, pp. 374, 2002.

[Liu06] Y. Liu, M. Nishiura, Y. Wang, H. Zhaomin *"π conjugated aromatic Enynes as a single-emitting component for white electroluminescence*", Chem. Soc, **128**, pp. 5592, 2006.

[Lu05] H.H. Lu, C.Y. Liu, T.H. Jen, J.L. Liao, H.E. Tseng. C.W. Huang, M.C. Chen, "*Excimer formation by electric field induction and side chain motion assistance in Polyfluorenes*", Macromolecules, **38**, pp. 10829, 2005.

[Magnin] http://magnin.plil.net/

[Mallavia05] R. Mallavia, F. Montilla, I. Pastor, P. Velasquez, B. Arredondo, A.L. Alvarez, C.R Mateo. "*Characterization and side chain manipulation in violet-blue Poly-[(9,9-dialkylfluoren-2,7-diyl)-alt-co-(benzen-1,4-diyl)backbones"*. Macromolecules, **38**, pp. 3185, 2005.

[Martens99] H.C.F. Martens, H.B. Brom and P.W. Blom. "*Frequency-dependendt electrical response of holes in poly(p-phenylene vinylene)*", Phys. Rev. B., **60**, pp. 8489, 1999.

[Martens00] H.C.F. Martens, J.N. Huiberts, P.W.M. Blom, "*Simulations measurements of electron and hole mobilities in polymer light-emitting diodes*", Appl. Phys. Lett., **77**, pp. 1852, 2000.

[Martens01] H.C.F. Martens, W.F. Pasveer, H.P.Brom, J.N. Huiberts, P.W.M. Blom. "*Crossover from space-charge-limited to recombination-limited transport in polymer light-emitting diodes*", Phys. Rev. B, **63**, pp. 125328-1, 2001.

[Mitchell99] M. Mitchell, "*An introduction to genetic algorithms*", The MIT Press, 1999.

[Miyaura89] Miyaura N., Yanagui T., Suzuki A., "*The Palladium-catalyzed cross-coupling reaction of Phenylboronic Acid With Haloarenes in the presence of bases*", Synth. Commun., **11**, pp. 513, 1981.

[Molina07] R. Molina, M. Ramos, F. Montilla, C. R. Mateo, and R. Mallavia "*A novel L–Tyrosine derivative of Poly [(fluoren-2,7-diyl-alt-co-(benzene-1,4–diyl)]: strategy of synthesis and chiroptical and electrochemical characterization*", Macromolecules, **40**, pp. 3042, 2007.

[Montilla06] F. Montilla, I. Pastor. C. R. Mateo, E. Morallon, R. Mallavia, "*Charge transport in luminescent polymers studied by in situ fluorescence spectroscopy*", J. Phys. Chem. B., **110,** pp. 5914, 2006.

[Montilla07] F. Montilla, and R. Mallavia, "*On the origin of green emission bands in fluorine based conjugated polymers*", Adv. Funct. Mater., **17**, pp. 71, 2007.

[Mott48] N.F. Mott and R.W. Gurney, "*Electronic Process in Ionic Crystals*", 2nd ed., Oxford University Press, 1948.

[Metricstech] www.metricstech.com

[Muccini06] M. Muccini, "*A bright future for organic field-effect transistors*", Nat. Mater., **5**, pp. 605, 2006.

[Mulfort03] K.L. Mulfort, J. Ryu and Q. Zhou, "*Preparation of surface initiated polystyrenesulfonate films and PEDOT doped by the films*", Polymer Science, **44**, pp. 3185, 2003.

[Nakayama07] T. Nakayama, K. Hiyama, K. Furukawa, and H. Ohtani, "*Development of phosphorescent white OLED with extremely high power efficiency and long lifetime*", J. SID, session 19.1, pp. 1018, 2007.

[Ohmori91] Y. Ohmori, M. Uchida, K. Muro, K. Yoshino, "*Blue electroluminescent diodes utilizing Poly(alkylfluorene)*", Jpn. J. Appl. Phys., **30**, pp. L1941, 1991.

[OIDA02] "*OLEDs for general illumination update 2002*", O.I.D.A Technology Roadmap, Milan Stolka, 2002.

[Pasveer05] W.F. Pasveer, J.Cottar, C. Tanase, R. Coehoorn, P.A.Bobbert, P.W.M. Blom, D.M. de Leeuw, M.A.J. Michels, "*Unified description of charge-carrier mobilities in disordered semiconducting polymers*", Phys. Rev. Lett., **94**, pp. 206601-1, 2005.

[Patel02] N.K. Patel, S. Cinà, and J.H. Burroughes, "*High-Efficiency Organic Light-Emitting Diodes*", IEEE, IEEE J. Sel. Topics in Quantum Electron., **8**, pp. 346, 2002.

[Papadimitratos07] A. Papadimitratos, H.H. Fong, G. Malliaras, A. Yakimov, A. Duggal, "*Degradation of hole injection at the contact between a conducting polymer and a fluorene copolymer"*, Appl. Phys. Lett., **91**, pp. 042116-1(-3), 2007.

[Pei95] Q. Pei, G. Yu, C. Zhang, Y. Yang, A.J. Heeger. ''*Polymer light-emitting electrochemical cells*'', Science, **269**, pp. 1086, 1995.

[Physorg] http://www.physorg.com/news4270.html

[Pitarch06] A. Pitarch, G. Garcia-Belmonte, J. Bisquert, H.J. Bolink, "*Impedance of space-charge-limited currents in organic light-emitting diodes with double injection and strong recombination*", **100**, pp. 084502-1, 2006.

[PNL] www.pnl.gov

[Preezant04] Y. Preezant, "*Electrical properties of contact region of polymeric semiconductor devices*", PhD Thesis, Technion-Israel Institute of Technology, 2004.

[Pschenitzka02] "*Patterning techniques for polymers light emitting devices*", PhD F. Pschenitzka, Princeton University, 2002.

[Py00] C. Py, M. D'Iorio, Y. Tao, J. Stapledon, and P. Marshall, "*A passive matrix addressed organic electroluminescent display using a stack of insulators as row separators*", Synth. Met., **113**, pp. 155, 2000.

[Redecker99] M. Redecker, D. Bradley, M. Inbasekaran, E. Woo., "*Mobility enhancement through homogeneous nematic alignment of a liquid-crystalline polyfluorene*", Appl. Phys. Lett., **74**, pp.1400, 1999.

[Riess01] W. Riess, H. Riel, T. Beierlein, W. Brutting, P. Muller, P.F. Seidler, "*Influence of trapped and interfacial charges in organic multilayer light-emitting devices*", J. Res. & Dev. IBM, pp 77, 2001.

[Romaner03] L. Romaner, A. Pogantsch, P.S. de Freitas, U. Scherf, M. Gaal, E. Zojer, E.J.W. List, "*The origin of green emission in Polyfluorene-based conjugated polymers: on-chain defect fluorescence*", Adv. Funct. Mater, **13**, pp. 597, 2003.

[Royster07] T. Royster, M. Ricks, M. Helber, "*Deep-blue OLEDs with exceptional device lifetime*", J. SID, session 30.4, pp.1197, 2007.

[Saricifti94] N.S. Saricifti and A. J. Heeger, "*Conjugated polymer-acceptor heterojunctions; diodes, photodiodes, and photovoltaics cells*". US patent, 5454880, 1994.

[Savvateev97] V. N. Savvateev, A,V. Yakimov, D. Davidov, R. Pogreb, M.R. Neuman, Y. Avny, "*Degradation of non-encapsulated polymer-based light-emitting diodes: noise and morphology*", Appl. Phys. Lett., **71**, pp. 3344, 1997.

[Setayesh01] S. Setayesh, A.C. Grimsdale, T. Weil, V. Enkelmann, K. Mullen, F. Megh-dadi, E. J.W List, G. Leising, "*Polyfluorenes with Polyphenylene Dendron side chains: toward non-aggregating, light-emitting polymers*", J. Am. Chem. Soc., **123**, pp. 946, 2001.

[Schön00] J.H. Schön, Ch. Kloc, A. Dodabalapur, B. Batlogg. ''*An organic solid state injection laser*'', Science, **289**, pp. 599, 2000.

[Scott99] J.C. Scott and G.G. Malliaras, "*Charge injection and recombination at the metal-organic interface*", Chem. Phys. Lett. **299**, pp. 115, 1999.

[Scott07] J. C. Scott , L. D. Bozano, "*Non-volatile Memory Elements Based on Organic Materials*", Adv. Mater., **19**, pp. 1452,2007

[Scribner] www.scribner.com

[Simmons65] J.G. Simmons, "*Richardson-Schottky effect in solids*", Phys. Rev. Lett., **15**, pp. 967, 1965.

[Sirringhaus98] H. Sirringhaus, N. Tessler, R.H. Friend. ''*Integrated optoelectronic devices based on conjugated polymers*'', Science, **280**, pp. 1741, 1998.

[Someya05] T. Someya, Y. Kato, S. Iba, Y. Noguchi, T. Sekitani, H. Kawaguchi, T. Sakurai. "*Integration of Organic FET with organic photodiodes for large area, flexible and lightweight sheet image scanners*". IEEE Trans. Electron. Devices, **52**, pp. 1502, 2005.

[Stallinga05] P. Stallinga, H.L Gomes, "*Traps states as an explanation for the Meyer-Neldel rule in organic semiconductors*", Org. Electr., **6**, pp. 137, 2005.

[Stallinga06] P. Stallinga, H.L Gomes, "*Thin-film field-effect transistors: the effects of traps on the bias and temperature dependence of field-effect mobility, including the Meyer-Neldel rule*", Org. Electr., **7**, pp. 5932, 2006.

[Sujimoto04] A. Sujimoto, H. Ochi, S. Fuimura, A. Yoshida, T. Miyadera, and M. Tsuchida, "*Flexible OLED displays using plastic substrates"*, IEEE J. Sel. Topics in Quantum Electron., **10**, pp. 107, 2004.

[Suzuki94] S. Suzuki, N. Hashimoto, T. Oyama and K. Suzuki. "*Effect of internal stress on adhesion and other mechanical properties of evaporated Indium Tin Oxide (ITO) Films*" J. Adh. Sci. Technol., **8**, pp. 261, 1994.

[Sze81] S.M. Sze, "*Physics of semiconductors devices*", Wiley-Interscience, 1981.

[Tanasse03] C. Tanasse, E.J. Meijer, P.W.M. Blom, and D.M. de Leeuw, "*Unification of the hole transport in polymeric field-effect-transistors and light-emitting diodes*", Phys. Rev. Lett., **91**, pp. 216601-1, 2003.

[Tang87] C.W. Tang, S.A. Van Sylke. "*Organic electroluminescent diodes*". Appl. Phys. Lett., **51**, pp. 913, 1987.

[Tian97] P. F. Tian, P.E. Burrows, and S.R. Forreset, "*Photolithographic patterning of vacuum-deposited organic light emitting devices*", Appl. Phys. Lett., **71**, pp. 3197, 1997.

[Tian99] P. F. Tian, V. Bulovic, P.E. Burrows, G. Gu,S. R. Forrest, and T. X. Zhou, "*Precise, scalable shadow mask patterning of vacuum-deposited organic light emitting devices*", J. Vac. Sci. Technol. A, **17**, pp. 2975, 1999.

[Timpanaro04] S. Timpanaro, M. Kemerink , F.J. Touwslager , M.M. De Kok , S. Schrader, "*Morphology and conductivity of PEDOT/PSS films studied by scanning–tunnelling microscopy*", Chem. Phys. Lett., **394**, pp. 339, 2004.

[Tokito03] S.Tokito , M. Suzukia, F. Satoa, M. Kamachib and K. Shiraneb. "*High-efficiency phosphorescent polymer light-emitting devices*". Organic Electronics, **4**, pp. 105, 2003.

[Tomozawa87] Tomozawa, D. Braun, S. Phillips, A.J. Heeger, H. Kroemer, ''*Metal-polymer Schottky barriers on cast films of soluble poly(3-alkylthiophenes)*'', Synth. Met., **22**, pp. 63, 1987.

[Torsi96] L. Torsi, A. Dodabalapur, L.J. Rothberg, A.W.P. Fung, H.E. Katz. ''*Intrinsic transport properties and performance limits of organic-field effect transistors*'', Science, **272**, pp. 1462, 1996.

[Tsang06] S.W. Tsang, S.K. So, J.B. Xu. "*Application of admittance spectroscopy to evaluate carrier mobility in organic transport materials*". J. Appl. Phys., **99**, pp. 013706-1, 2006.

[Tuladhar05] M. Tuladhar, S.M.; Poplavskyy, D. Choulis, S. A.;Durrant, J.R. Bradley, D.D.C. Nelson. "*Ambipolar charge transport in films of Methanofullerene and Poly (phenylenevinylene) / Methanofullerene blends*". J. Adv. Funct. Mater., **15**, pp. 1171, 2005.

[universaldisplay] www.universaldisplay.com

[U.S. Department of Energy] http://www.netl.doe.gov/ssl

[U.S. Department of Energy01] U.S. Department of Energy, "*National lighting inventory and energy consumption estimate*", U.S. Government Printing Office, Washington D.C., pp. xii, 2001.

[U.S. Department of Energy03] U.S. Department of Energy, "*Illuminating the challenges: solid state lighting program planning workshop report*", U.S. Government Printing Office, Washington D.C., 2003.

[Vijila07] C. Vijila , A. Pivrikas , H. Chun, C. Zhikuan, R. Österbacka, C. S. Jin, "*A study of charge transport in a novel electroluminescent poly(phenylene vinylene-co-fluorenylene vinylene)based p-conjugated polymer* ", Organic Electronics, **8**, pp. 8, 2007.

[Weaver02] M.S. Weaver, L.A. Michalski, K. Rajan, M.A. Rothman, J.A. Silvernail, J.J. Brown, P.E. Burrows, G.L. Graff, M.E. Gross, P. M. Martin, M. Hall, E. Mast, C. Bonham, W. Bennett, and M. Xumhoff, "*Organic light-emitting devices with extended operating lifetimes on plastic substrates*", Appl. Phys. Lett., **81**, pp. 2929, 2002.

[Wilson01] J.S. Wilson, A.S. Dhoot, A. J.A.B. Seeley, M.S. Khan, A. Köhler, and R. H. Friend, "*Spin-dependent exciton formation in pi –conjugated compounds"*, Nature, **413**, pp. 828, 2001.

[Wohlgenannt02] M. Wohlgenannt, X.M. Jiang, Z.V. Vardeny, R.A.J. Janssen. "*Conjugation-length dependence of spin-dependent exciton formation in pi-conjugated oligomers and polymers*", Phys. Rev. Lett., **88**, pp. 197401, 2002.

[Wolf85] E.L. Wolf, "*Principles of electron tunnelling spectroscopy*". Oxford University Press, 1985.

[Woudenberg01] T. van Woudenberg, P.W. Blom, M.C.J.M. Vissenberg, J.N. Huiberts, "*Temperature dependence of the charge injection in poly-dialkoxy-p-phenilene vinylene*", Appl. Phys. Lett., **79**, pp. 1697, 2001.

[Woudenberg04] T. van Woudenberg, P.W.M. Blom, J. J. A. M. Bastiaansen, B. M. W. Langeveld_voss, "*Electron-Enhanced hole injection in blue polyfluorene-based polymer light-emitting diodes*", Adv. Funct. Mater., **14**, pp. 677, 2004.

[Xiao03] S. Xiao, M. Nguyen, X, Gong, Y. Cao, H. B. Wu, D. Moses, A. J. Heeger, "*Stabilization of semiconducting polymers with silsesquioxane*", Adv. Funct. Mater., **13**, pp. 25, 2003.

[Yoshida01] A. Yoshida, A. Sugimoto, T. Miyadera, and S. Miyaguchi, "*Organic light emitting devices in polymer substrates*", J. Photopolymer Sci. Technol., **14**, pp. 327, 2001.

[You07] B-H. You, J-H Lee, M-K Han, *"Polarity balance driving scheme to suppress the degradation of Vth in a-Si:H TFT due to the positive gate bias stress for AMOLED*", J. of Display Technology, **3**, pp. 40, 2007.

[Young05] B. Young, "*Will OLEDs replace small TFT-LCDs?*", Inform. Display, **21**, pp. 22, 2005.

[Yu95] Yu, J. Gao, J.C. Hummelen, F. Wudl, A.J. Heeger. *''Polymer photovoltaic cells: Enhanced efficiencies via a network of internal donor-acceptor*", Science, **270**, pp. 1789, 1995.

[Zhou05] T.X. Zhou, Tan-Ngo, J.J. Brown, M. Shtein, S.R. Forrest, "*Stable and efficient electrophosphorescent organic light-emitting devices grown by organic vapour phase deposition*", Appl. Phys. Lett., **86**, pp. 21107-1, 2005.

[Zhu02] Zhu ZT, Mason JT, Dieckmann R, Malliaras GG. "*Humidity sensors based on pentacene thin-film transistors*". Appl. Phys. Lett., **81**, pp. 4643, 2002.

APPENDIX I

I APPENDIX I: Analytical solutions for F_0

Obtaining the analytical solutions for F_0 from equation [4.30] required complex computational algebra. These calculations were carried out with the software "*Mathematica*" achieving the following rather complicated expressions:

$$F_{01} = \frac{V}{L}\left(\frac{1}{4} + \frac{1}{4\sqrt{3}}\sqrt{f_7} + \frac{1}{2}\sqrt{\frac{1}{2} - \frac{f_4}{3} - \frac{f_5}{3} - \frac{f_6}{3\cdot 2^{2/3}} + \frac{\sqrt{3}\cdot(1-f_4)}{2\sqrt{f_7}}}\right) \quad [I.1]$$

$$F_{02} = \frac{V}{L}\left(\frac{1}{4} + \frac{1}{4\sqrt{3}}\sqrt{f_7} - \frac{1}{2}\sqrt{\frac{1}{2} - \frac{f_4}{3} - \frac{f_5}{3} - \frac{f_6}{3\cdot 2^{2/3}} + \frac{\sqrt{3}\cdot(1-f_4)}{2\sqrt{f_7}}}\right) \quad [I.2]$$

$$F_{03} = \frac{V}{L}\left(\frac{1}{4} - \frac{1}{4\sqrt{3}}\sqrt{f_7} + \frac{1}{2}\sqrt{\frac{1}{2} - \frac{f_4}{3} - \frac{f_5}{3} - \frac{f_6}{3\cdot 2^{2/3}} - \frac{\sqrt{3}\cdot(1-f_4)}{2\sqrt{f_7}}}\right) \quad [I.3]$$

$$F_{04} = \frac{V}{L}\left(\frac{1}{4} - \frac{1}{4\sqrt{3}}\sqrt{f_7} - \frac{1}{2}\sqrt{\frac{1}{2} - \frac{f_4}{3} - \frac{f_5}{3} - \frac{f_6}{3\cdot 2^{2/3}} - \frac{\sqrt{3}\cdot(1-f_4)}{2\sqrt{f_7}}}\right) \quad [I.4]$$

where the f_1, f_2, f_3, f_4, f_5, f_6 and f_7 are given by,

$$f_1 = \left(-81BV^{10}L^3 + 504B^2V^8L^6 - 352B^3V^6L^9 + \sqrt{B^2V^{12}L^6\left(9V^2 - 8BL^3\right)\left(9V^2 + 8BL^3\right)^3}\right)^{\frac{1}{3}}$$

$$f_2 = 2\cdot 2^{\frac{2}{3}} BL^3\left(-9V^2 + 10BL^3\right)$$

$$f_3 = V^4,\ f_4 = \frac{8BL^3}{V^2},\ f_5 = \frac{f_2}{f_1},\ f_6 = \frac{f_1}{f_3}$$

$$f_7 = 3 - 2f_4 + 4f_5 + 2 \cdot 2^{\frac{1}{3}} f_6$$

$B = \frac{J}{\mu\varepsilon_r\varepsilon_0\Phi}$, where $\Phi = \frac{p_n}{p}$, given by equation [4.24].

APPENDIX II

II APPENDIX II: Algorithms to simulate and fit the J-V characteristic using the complete model

II.1 Algorithm to simulate the J-V characteristic using the complete model

Figure II.1 shows the algorithm employed to generate the theoretical J-V curves using the complete model presented in chapter 4. First, both the injection and bulk currents are evaluated for a certain set of parameters (mobility, injection barrier…), an initial voltage value and an initial electric field at the interface, F_0. Next, these currents are equated at the metal-polymer interface to obtain a solution for F_0. This solution is used to obtain the current density along the device, J_{BULK}. This is performed for a set of voltage values to obtain a J-V characteristic. Simultaneously, for every value of F_0, J_{BULK} and V, the distribution of carrier density $p_0(x)$ and the space charge field, $F_{SC}(x)$ are obtained along the active layer.

The complete model was implemented in *FORTRAN 90*. The calculus of the injection current was performed using the subroutine DQ2DAG for the integrals computation with double precision. The continuity equation at the interface was solved using the DZREAL subroutine, which looks for the zeros of a given function.

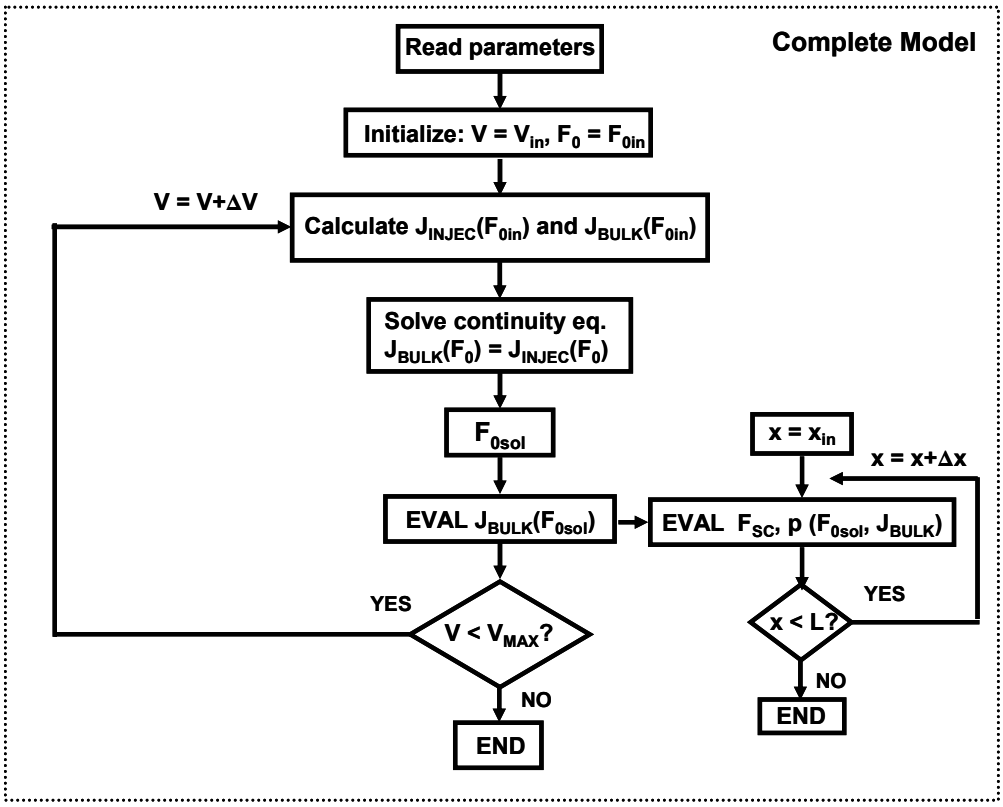

Figure II.1 – Flowchart of the complete model

II.2 Algorithm to fit the J-V complete model to the experimental characteristic

II.2.1 Introduction to genetic algorithms

Genetic algorithms (GAs) are designed to simulate processes in natural systems resembling those of evolution first postulated by Charles Darwin. They are based on natural selection, meaning that the fittest individual will survive within a population of finite resources. These types of algorithms produce adaptive heuristic searches based on the evolutionary ideas of natural selection and genetics.

GAs were first introduced by John Holland and his colleagues in the 60s and 70s. They studied the phenomenon of adaptation as it occurs in nature and developed ways in which the

mechanisms of natural adaptation might be imported into computer systems [Hollands75]. Namely, by means of a method based on natural selection together with the genetics−inspired operators of crossover, mutation, and inversion, to move from one population of "chromosomes" (e.g., strings of ones and zeros, or "bits") to a new population. Each chromosome consists of "genes" (e.g., bits), each gene being an instance of a particular "allele" (e.g., 0 or 1). The selection operator chooses those chromosomes in the population that will be allowed to reproduce, and on average the fitter chromosomes produce more offspring than the less fit ones. Genes from good individuals propagate throughout the population so that two good parents will sometimes produce offspring that are better than either parent. Each successive generation will become more suited to their environment.

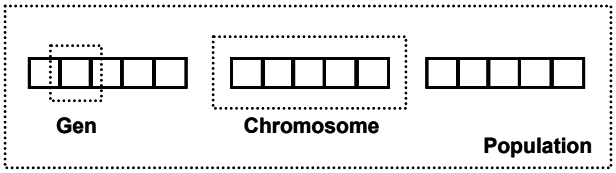

Figure II.2 – Genetics inspired terminology

The mechanisms of evolution seem to be well suited for some of the most pressing computational problems in many fields. Many computational problems require searching through a huge number of possibilities for solutions. In this sense, GAs are more robust and reliable than conventional deterministic algorithms.

Figure II.3 shows the basic diagram of a GA. For a given computational problem, a GA searches the possible solutions among a population of individuals. Each individual is coded in binary as a finite length vector of variables. In genetic terminology, these individuals are equivalent to chromosomes and the variables are analogous to genes. Thus, a chromosome (solution) is composed of several genes (variables). A fitness score is assigned to each solution representing the abilities of an individual to compete. The individual with the optimal fitness score is sought. Parents are selected to mate, on the basis of their fitness, producing offspring. Highly fit solutions are given more opportunities to reproduce, so that offspring inherit characteristics from each parent. As parents mate and produce offspring, room must be made for the new arrivals since the population is kept at a static size. Least fitted individuals in the population die and are replaced by the new, more fitted solutions. Eventually, once the population has converged and is not producing offspring noticeably different from those in

previous generations, the algorithm itself is said to have converged to a set of solutions to the problem at hand. A deeper insight into AG can be found in [Mitchell99].

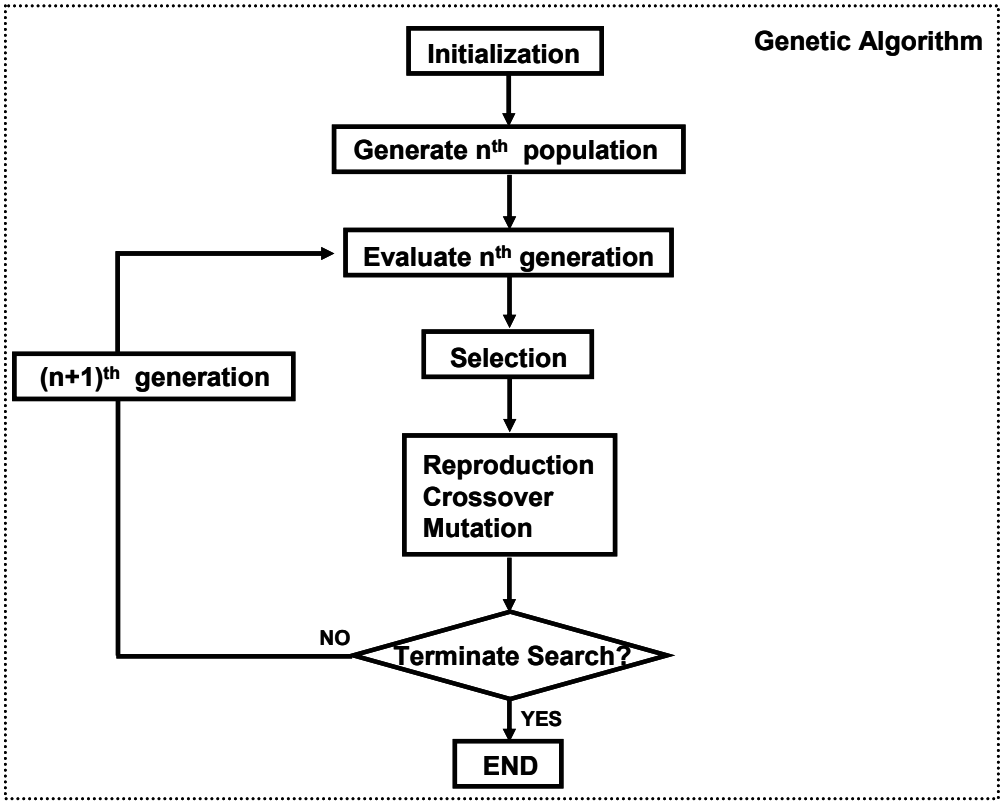

Figure II.3 – Genetic algorithm structure.

II.2.2 Genetic algorithm adapted to fit J-V characteristics

Our specific problem requires a set of parameters whose resulting theoretical J_{theor} obtained with the complete model presented in chapter 4 best fits to a given experimental J_{exp}. The solution to the problem would consist of a subset of microscopic parameters that minimize the error function J_{theor} - J_{exp}. Using genetic terminology: the total population is composed of the set of possible solutions, each solution corresponds to a certain individual with a characteristic chromosome (parameter subset), and every individual's chromosome is composed of a set of genes, each of them equivalent to a parameter (injection barrier, mobility…).

Figure II.4 shows the structure of the genetic algorithm adapted to our fitting problem.

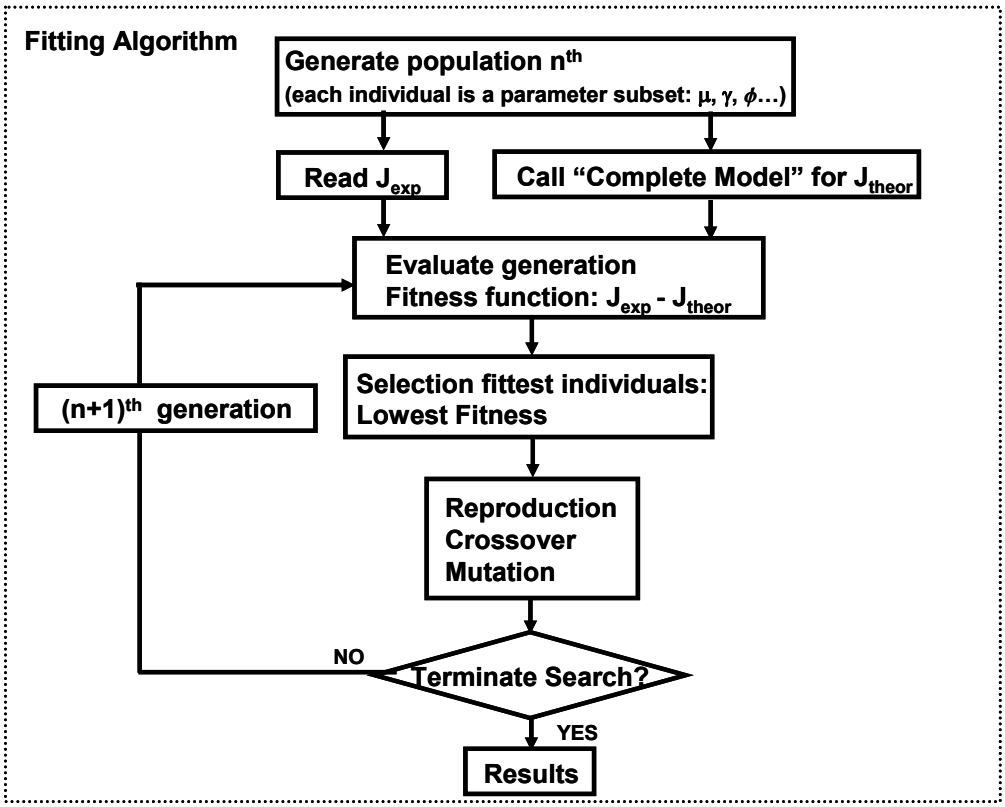

Figure II.4 – Block diagram of the fitting program

RESUMEN

Antecedentes

La posibilidad de compatibilizar los compuestos orgánicos con la electrónica se hizo posible a principios de los 70 gracias al desarrollo de ciertos polímeros conjugados con carácter conductor eléctrico (poliacetileno y otros varios). Dichos polímeros se denominan conjugados por permitir cierta deslocacalización electrónica vía una estructura repetitiva de enlace doble-simple entre carbonos de la cadena. Durante las dos últimas décadas se han producido grandes avances en la investigación de dispositivos microelectrónicos y optoelectrónicos basados en materiales moleculares orgánicos y polímeros semiconductores. En este sentido se han fabricado dispositivos de diferente índole como son diodos, [Tang87], [Tomozawa87], [Saricifti94], diodos emisores de luz [Burroughs90], [Friend99], fotodiodos [Halls95], [Someya05], transistores de efecto campo [Torsi96], [Katz02], [Muccini06], [Kitamura03], celdas electroquímicas emisoras de luz (LECs) [Pei95], biosensores [Zhu02], [Crone02], células fotovoltaicas [Yu95], dispositivos optoelectrónicos integrados [Sirringhaus98], [Huitema02], [Kitamura03], celdas de memoria no volátil [Scott07], etc.

En 1987 Eastman Kodak fabricó los primeros diodos emisores de luz orgánicos (OLEDs, del inglés *Organic LEDs*), basados en bicapas moleculares. En este caso, la capa activa era una molécula orgánica, tris-(8-hidroxiquinolina) (Alq3) con propiedades conductoras y luminiscentes [Tang87]. Los voltajes de operación eran inferiores a 10 V, aunque con eficiencias muy pobres, del orden del 1%. Poco después, en 1990, un grupo de investigación en Cambridge sintetizó por primera vez polímeros semiconductores fluorescentes y los usaron como capa activa en OLEDs, duplicando la eficiencia [Burroughs90].

Al contrario que en los LEDs basados en semiconductores inorgánicos como GaAs y GaN, la física subyacente en los diodos orgánicos no se basa directamente en el concepto de unión p-n con contactos óhmicos, sino en un sándwich de un material orgánico electroluminiscente entre dos metales distintos que actúan como ánodo y cátodo. Por ello, es común interpretar el comportamiento eléctrico de los OLEDs en términos de dos mecanismos diferentes que participan en la conducción: inyección de portadores desde los electrodos a las capas orgánicas y transporte de portadores a lo largo del material orgánico.

Respecto a los modelos que explican el mecanismo de inyección, actualmente existen dos enfoques principales. En primer lugar, los mecanismos clásicos, que se basan en el efecto termoiónico y necesitan definir una magnitud similar a la constante de Richardson [Scott99], [Davids97]. En segundo lugar. el mecanismo más aceptado es de carácter microscópico y se basa en la conducción por saltos entre el metal y el material orgánico que presenta desorden espacial y energético [Arkhipov98].

Por otra parte, el transporte de carga en las capas activas de los OLEDs se aproxima más al que tiene lugar en materiales aislantes que al basado en teoría de bandas de semiconductores inorgánicos [Coropcenau07]. En diodos orgánicos con contactos cuasi-óhmicos la corriente está determinada por una acumulación de carga espacial en el dispositivo, y la característica J-V viene dada por la expresión de Mott-Gurney [Mott48]. En este tipo de materiales la movilidad está afectada por una barrera energética que el portador debe superar para saltar de un estado localizado a otro. Por tanto, la movilidad no es constante, presentando una dependencia con el voltaje aplicado al dispositivo y con la densidad de carga inyectada [Pasveer05].

En diodos orgánicos con una gran barrera de inyección (diferencia de energía entre la función de trabajo del metal y el nivel de conducción – LUMO u HOMO - del material orgánico) la corriente está limitada también por la inyección de portadores. En la práctica la limitación de corriente no suele ser consecuencia de un único mecanismo (inyección o transporte). Por el contrario, en diodos con una barrera de inyección moderada, ambos mecanismos suelen ser responsables de la limitación de corriente. Los modelos actuales que simulan regímenes intermedios son complejos y requieren tiempos de computación elevados [Arkhipov03].

En esta tesis se fabrican, caracterizan y modelan eléctricamente diodos orgánicos basados en derivados de polifluorenos (PF). La unidad fluoreno es un compuesto aromático que recibe su nombre por su intensa fluorescencia en el violeta. Los PFs son solubles en disolventes orgánicos estándar como cloroformo, tolueno, tetrahidrofurano etc, aunque el grado de solubilidad depende de su peso molecular, siendo éste variable de un lote a otro. Estos materiales presentan cierta diversidad según sean homopolímeros o copolímeros. Los primeros consisten en unidades de fluoreno unidas entre sí, mientras que en los copolímeros se introducen otras unidades aromáticas entre los anillos de fluoreno.

Los PFs han despertado gran interés gracias a sus propiedades como emisores de luz azul. Además poseen eficiencias de emisión elevadas, valores elevados de la movilidad (dentro del

rango de movilidades de materiales orgánicos) y excelentes valores de estabilidad térmica y química en atmósfera inerte [Lang04].

A pesar de las excelentes propiedades que presentan los PFs, la mayoría de los polímeros sintetizados hasta la fecha presentan en su espectro de emisión una variedad de bandas no deseadas a menores energías, atribuidas a diversos efectos. La más estudiada es la centrada en 530 nm, que aparece tanto durante el calentamiento del material como durante la operación eléctrica del dispositivo, y se atribuye a diversos procesos de degradación como consecuencia de las reacciones químicas del material con agentes externos (oxigeno y humedad). Estas reacciones provocan la presencia de defectos "fluorenona" (dobles enlaces C=O) en la cadena de polímero [List02]-[Gaal03]-[Romaner03]. Otras bandas, como la centrada en 480 nm, o más hacia el rojo, en la zona de 550-650 nm son aún objeto de estudio.

Dentro del ámbito tecnológico, el paso más complicado en la fabricación de pantallas basadas en material orgánico radica en el diseño del cátodo. Debido a que el cátodo se deposita encima de las capas orgánicas, su diseño requiere técnicas que no dañen estos materiales. La técnica más usada para la fabricación de pantallas basadas en disoluciones poliméricas es la impresión por chorro (*jet printing*). Dicha técnica se aprovecha de que muchos de los compuestos orgánicos empleados en la fabricación pueden ser procesados en disolución y por tanto pueden ser depositados de la misma forma que la tinta de una impresora [cambridgedisplay]. La principal ventaja radica en que permite diseñar un patrón directamente gracias a la capacidad de depositar los tres colores RGB dentro de un mismo píxel. Además, esta técnica es escalable a sustratos de área grande, reduce pasos de fabricación y es controlable por PC mediante un programa CAD, lo que facilita la implementación de diseños variados. Las principales desventajas de esta técnica son los grandes costes de los equipos necesarios para su implementación y la limitación de su resolución a decenas de micras. Por tanto, la técnica de *jet printing* está orientada a la fabricación de *displays* de tamaño medio-grande (monitores de PC, TV…).

Por otro lado, la técnica fotolitográfica, muy utilizada en el ámbito de la microelectrónica, no es adecuada para realizar patrones sobre el cátodo de pantallas basadas en material orgánico ya que requiere el uso de productos químicos que puede degradar las propiedades ópticas de las capas orgánicas (ácidos, reveladores…).

Objetivos

a) El primer objetivo de esta tesis es fabricar y caracterizar óptica y eléctricamente diodos orgánicos electroluminiscentes basados en un derivado del polyfluoreno fenilideno con emisión azul.

El nuevo material utilizado para la fabricación de matrices pasivas de diodos orgánicos es un derivado del polyfluoreno fenilideno (PFP) con emisión en el azul sintetizado en el IBMC-UMH (Instituto de Biología Molecular y Celular, Universidad Miguel Hernández) [Mallavia05]. En primer lugar se fabricarán estructuras en las que intervenga un solo portador (huecos) y se medirán las curvas corriente-voltaje e impedancia-frecuencia con el objetivo de comprobar el comportamiento como diodo. Se propondrán estrategias para adaptar técnicas convencionales de fabricación tales como depósito de capas delgadas por centrifugado (*spin-coating*), fotolitografía, evaporación por efecto Joule, etc., para obtener estructuras de varias capas (al menos dos) que ayuden a la inyección de portadores (se incluirá una capa transportadora de huecos).

Por otro lado, se desarrollarán técnicas de encapsulado en atmósfera inerte (N_2) con el objetivo de aislar el dispositivo de agentes externos tales como oxigeno y humedad responsables de la degradación de los materiales orgánicos disminuyendo su tiempo de vida. En segundo lugar, se caracterizarán las propiedades emisivas de los OLEDs basados en PFP. En el caso de emisión azul, la gran diferencia energética entre los niveles HOMO y LUMO suele significar también un fuerte desnivel respecto a los niveles metálicos. En consecuencia, las barreras para la inyección de portadores son elevadas lo que supone tensiones de operación elevadas, que aceleran el proceso de degradación. En este contexto, se estudiará la evolución del espectro de emisión durante largos periodos de operación con el objetivo de hacer un seguimiento de los mecanismos de degradación.

b) El segundo objetivo de esta tesis es proponer un modelo completo para la conducción en OLEDs que incluya los mecanismos de inyección y de transporte simultáneamente. Este modelo se verificará con curvas experimentales densidad de corriente-voltaje (J-V).

El segundo objetivo de este trabajo abarca un estudio exhaustivo de las propiedades intrínsecas del material así como las propiedades de conducción de la estructura de capas. Para ello son necesarias, por un lado, la utilización de dos técnicas de caracterización

eléctrica (espectroscopia de impedancias y característica corriente-voltaje), y por otro, la elaboración de un modelo para la conducción en estos dispositivos.

Hasta la fecha, los modelos propuestos de carga espacial están orientados a describir estructuras en que la inyección de portadores se produce a través de contactos óhmicos [Arkhipov03]-[Mott48]. La principal aportación de esta tesis en este punto consiste en la incorporación de un nuevo término al modelo clásico de Mott-Gurney para transporte de portadores en régimen de carga espacial (*space charge)*. Dicho término incluye el campo eléctrico en la intercara, que equivale a tener en cuenta una barrera de potencial no despreciable en la misma. Combinando esta nueva expresión junto con el modelo para la inyección [Arkhipov98] se pretende obtener un modelo completo para la conducción en dispositivos orgánicos. Este modelo se validará comparándolo con curvas experimentales de diodos orgánicos con distintos espesores de la capa activa. Asimismo se realiza un estudio de la impedancia en pequeña señal (Z) de estos dispositivos en el dominio de la frecuencia. Para ello nos basaremos en los modelos de pequeña señal propuestos por [Martens99] y [Tsang06] modificándolos y adaptándolos a nuestro nuevo modelo de conducción. Con este nuevo modelo, se realizarán ajustes a las curvas experimentales Z-f y J-V de los que se obtendrán los valores de los parámetros que describen el comportamiento del material y la estructura del diodo.

c) El tercer objetivo de esta tesis consiste en la fabricación de una matriz pasiva de 7x5 píxeles utilizando una nueva técnica de ablación mecánica.

Se fabricará un prototipo de *display* alfanumérico con emisión en el azul de 7x5 píxeles direccionados por filas y columnas, utilizando una combinación novedosa de técnicas de fotolitografía en el ánodo y ablación mecánica en el cátodo. Los píxeles quedarán definidos en los puntos de intersección de las filas que actúan de ánodo y las columnas que actúan de cátodo.

Con esta técnica propuesta para el diseño del cátodo se pretende una reducción del número de procesos intermedios y por tanto un ahorro en el tiempo y los costes de fabricación. Además, es una técnica que no requiere la utilización de productos químicos tales como disolventes, fotorresinas, etc., evitando así la posible degradación de los materiales orgánicos. La aplicación y validación de esta técnica es una de las aportaciones originales de esta tesis.

Metodología

La metodología seguida en este trabajo ha seguido la siguiente línea tradicional:

- Fabricar dispositivos para verificar y depurar nuestras técnicas de procesado. Proponer estrategias novedosas.
- Poner a punto las técnicas de caracterización.
- Proponer hipótesis de comportamiento físico que derivan en modelo matemáticos.
- Definir y fabricar estructuras test para probar el modelo.
- Caracterizar dichas estructuras para obtener parámetros microscópicos e información estructural a partir del modelo.

En concreto esta trayectoria se puede sintetizar en tres tareas principales:

a) Fabricación y caracterización de diodos electroluminiscentes con emisión azul basados en un nuevo material derivado del polyfluoreno fenilideno.

Se han fabricado matrices pasivas de diodos electroluminiscentes orgánicos basados tanto en materiales comerciales como en un nuevo derivado del polyfluoreno. Se han utilizado sustratos de vidrio de 25x30mm recubiertos con ITO y técnicas estándar de fotolitografía, "*spin-coating*" y evaporación de metales. Las matrices de diodos tienen configuración de cátodo común, con estructura ITO/PEDOT:PSS/material activo/Al.

Los dispositivos han sido encapsulados en atmósfera inerte haciendo uso de un *"Epoxy"* y una cubierta de vidrio.

Se ha medido y comprobado una mejora en el tiempo de vida del dispositivo, con evidencias de la disminución de la degradación eléctrica del mismo.

Se ha medido la respuesta característica corriente-tensión. Se ha realizado un estudio de la respuesta eléctrica en función del espesor de la capa activa y con diferentes materiales. Se ha comprobado que el tiempo de vida eléctrico de los dispositivos encapsulados mejora considerablemente.

Las medidas J-V han servido para validar el modelo de conducción propuesto. De los ajustes de este modelo a las curvas experimentales se han extraído los parámetros de la estructura y la información relativa al semiconductor orgánico.

Además, se han realizado medidas de la respuesta capacidad-frecuencia de las que se ha obtenido un modelo equivalente de pequeña señal así como la movilidad y los parámetros microscópicos que describen el grado de desorden del material.

Finalmente se han llevado a cabo las medidas de la emisión óptica. Se han medido los espectros de fotoluminiscencia, electroluminiscencia y luminancia de los diodos para distintos voltajes aplicados y durante intervalos de tiempo prolongados. Analizando las bandas obtenidas, y comparando con los espectros de fotoluminiscencia se ha obtenido información de los mecanismos de degradación.

b) Desarrollo de un modelo para el comportamiento eléctrico de diodos orgánicos.

Se ha desarrollado un modelo teórico para la simulación del comportamiento eléctrico de los OLEDs. La aportación del nuevo modelo consiste en la inclusión de un nuevo término en la expresión de Mott-Gurney para la corriente debida a la carga espacial, concretamente el campo en la intercara debido a la existencia de una barrera para la inyección de portadores.

Haciendo uso de la nueva expresión y utilizando el modelo de inyección de portadores propuesto por Arkhipov et al. [Arkhipov98], se formula un modelo completo que incorpora la contribuciones de inyección y de transporte al cálculo de la corriente total.

Se ha validado el modelo utilizando diodos con capas activas de espesor variable y se han realizado ajustes utilizando el modelo propuesto a las curvas experimentales corriente-voltaje de los diodos fabricados. A través de estos ajustes se han extraído los parámetros más relevantes del material y de la estructura (barrera de inyección, movilidad, etc.).

Se ha desarrollado un modelo del comportamiento del dispositivo en el dominio de la frecuencia para diodos con contactos no óhmicos, incorporando un término que da cuenta del campo eléctrico en la intercara. Se han realizado ajustes a las curvas experimentales Z-f y se han extraído la movilidad de los huevos del material y los parámetros que dan cuenta del desorden en el material orgánico.

c) Diseño e implementación de una nueva técnica para realizar patrones en el cátodo de pantallas orgánicas.

Se ha diseñado y desarrollado una nueva técnica para realizar patrones en el cátodo de una pantalla basada en material orgánico basada en ablación mecánica. Para ello se ha utilizado como base un equipo comercial que consta de un posicionador XY controlado por ordenador

y se le ha adaptado una punta de prueba metálica. La técnica consiste en arrastrar la punta por la superficie del cátodo siguiendo un trazado previamente diseñado por una aplicación vectorial. La punta levanta las zonas correspondientes del metal obteniendo una resolución entre pistas del orden de pocas centenas de micras.

Se ha utilizado la técnica de ablación mecánica del cátodo para fabricar una pantalla de 5x7 píxeles basada en polímero comercial MDMO:PPV (área del píxel 1 mm^2). Se han usado técnicas convencionales de fotolitografía para diseñar el ánodo y *spin-coating* para depositar los polímeros.

Conclusiones

Las principales contribuciones de esta tesis pueden enmarcarse dentro de tres niveles principales:

En primer lugar, se han fabricado y caracterizado matrices pasivas de diodos electroluminiscentes orgánicos (OLEDs) adaptando técnicas de fabricación estándar tales como fotolitografía, depósito por giro, evaporación. Los dispositivos fabricados se basan en un material nuevo derivado del polyfluoreno fenilideno, PFP:$(CN)_2$, cuya emisión está centrada en el azul (420 nm).

La caracterización eléctrica de estos dispositivos revela un comportamiento eléctrico similar en términos de voltaje umbral a dispositivos basados en polyfluorenos comerciales (PFC_6). Es bien sabido que los materiales electroluminiscentes orgánicos se degradan en presencia de oxigeno y humedad. En este sentido, se ha llevado a cabo un estudio comparativo con diodos similares, unos encapsulados en atmósfera inerte (N_2) y otros con los contactos al aire. Los diodos no encapsulados presentan “zonas negras” al cabo de pocas horas de funcionamiento eléctrico. Estas zonas se identifican con áreas no conductivas como consecuencia de las reacciones químicas del material con el oxigeno, disminuyendo considerablemente el tiempo de vida eléctrico del dispositivo.

Por otro lado, la caracterización óptica para los diodos basados en PFP:$(CN)_2$ presenta un pico de emisión principal en 420 nm y un pico vibrónico asociado, en 450 nm como consecuencia de las transiciones óptica asistidas por fonón. Estos dispositivos han alcanzado luminancias de 500 cd/m^2. La caracterización espectral también revela otras dos características centradas en 480 y 530 nm, ya mencionadas en la literatura. Estos picos se atribuyen a distintos mecanismos de degradación en el polímero. El primero se propone como consecuencia de un exceso de electrones en el material, que cambia la morfología al

provocar nuevos enlaces C=C en la cadena principal. El segundo es el resultado de los defectos "keto" o fluorenonas, doble enlaces C=O que se generan como consecuencia de la interacción con oxígeno.

En segundo lugar, se ha llevado a cabo una reformulación del comportamiento eléctrico de diodos orgánicos emisores de luz. La conducción en este tipo de dispositivos viene limitada por el régimen de carga espacial ("*space charge*"). En este contexto, se ha desarrollado una expresión para la corriente máxima que atraviesa el dispositivo que tiene en cuenta un contacto no óhmico en los electrodos, es decir, una barrera de inyección no despreciable. Se propone la existencia de un campo eléctrico en la intercara metal-orgánico como consecuencia de dicha barrera de inyección. Además, se ha propuesto un modelo completo para la conducción en OLEDs que tiene en cuenta tanto la corriente de inyección como la corriente a través del "*bulk*". Para ello, se ha usado la expresión mencionada anteriormente y un modelo de inyección basado en teoría probabilística de conducción por saltos en materiales desordenados espacial y energéticamente [Arkhipov98].

El modelo completo se ha ajustado a curvas experimentales de diodos con diferentes espesores de la capa activa confirmando la validez del modelo. De los ajustes se han obtenido la movilidad, la barrera de inyección y otros parámetros microscópicos del los materiales empleado como capa activa. La movilidad obtenida para el PFP:$(CN)_2$ están en el orden de 10^{-10} cm^2/Vs.

Por otro lado, se ha definido una función analítica, β, como el cociente entre la corriente debida al régimen de carga espacial teniendo en cuenta el campo eléctrico en la intercara y la corriente debida al régimen de carga espacial puro para el dispositivo con contactos óhmicos. Esta función cuantifica en qué grado la conducción en el dispositivo está limitada por el mecanismo de inyección o el de transporte.

Finalmente, dentro del plano del estudio teórico, se ha reformulado un modelo de pequeña señal para la admitancia del OLED en la que se incluye la contribución del campo eléctrico en la intercara. El ajuste de las curvas experimentales C-f a este modelo ha servido para obtener la movilidad y los parámetros de dispersión que dan cuenta del grado de desorden del material.

En tercer lugar, se ha desarrollado una nueva técnica para diseñar el cátodo de una pantalla de material orgánico basado en ablación mecánica que levanta el metal. Este procedimiento no hace uso del proceso fotolitográfico, evitando así el contacto entre los productos químicos

y el material orgánico, lo que podría degradar las propiedades electroluminiscentes. Además, no se requieren costosos equipos de producción como baños húmedos y lámparas UV.

El sistema experimental consta de un posicionador electromecánico con capacidad de desplazamiento en dos dimensiones (plano horizontal, XY) y con una resolución de al menos 100 micras, controlado por un ordenador, así como de un cabezal de material metálico duro, que es el que realiza la ablación sobre el cátodo. La punta del cabezal que realiza la ablación tiene una forma de cono, con un ángulo que puede llegar a alcanzar los 120 grados, y dispone de un sistema de amortiguación asistido por muelle que le permite absorber las irregularidades de la capa metálica. El dispositivo posicionador del cabezal dispone de un sistema de aspiración que absorbe las virutas que se desprenden del proceso de ablación, para evitar que provoquen cortocircuitos entre las diferentes pistas metálicas. Utilizando esta técnica se han fabricado prototipos de matrices pasivas de OLED (PMOLED) de 7x5 píxeles, obteniendo buenas definiciones del píxel.

LIST OF PUBLICATIONS

Publications in JCR

- R. Mallavia., F. Montilla, I. Pastor, P. Velasquez, **B. Arredondo**, A. L. Alvarez, C. R. Mateo. *"Characterization and Side Chain Manipulation in Violet-Blue Poly-[(9,9-dialkylfluoren-2,7-diyl)–alt-co-(benzen-1,4-diyl)]Backbones*", Macromolecules, 38, pp. 3188, 2005. ISSN 0024-9297.
- A. L. Álvarez, **B. Arredondo**, B. Romero, X. Quintana, A. Gutiérrez-Llorente, R. Mallavia, J. M. Otón, "*Analytical evaluation of the ratio between injection and space-charge limited currents in single carrier organic diodes*", IEEE Transactions on Electron Devices, **55**, 2008. Accepted for publication (in press). ISSN 0018-9383.

Proceedings in international conferences

- **B. Arredondo**, C. Coya, B. Romero, A. L. Álvarez, X. Quintana, R. Molina, R. Mallavia, P. Velásquez, J.M Otón, "*Comparison between electroluminescent organic diodes based on new poly(2,7-fluorene phenylidene) derivatives and commercial polymers"*, SPIE, Microtechnologies for the New Millenium, Seville, 2005. ISBN 0-8194-5849-X.
- A. L. Álvarez , **B. Arredondo**, B. Romero, X. Quintana, A. Gutiérrez-Llorente, R. Mallavia, J. M. Otón, "*Analytical expression for the electric field at the metal-organic interface in single carrier organic diodes under space-charge conduction*", European Materials Research Society (E-MRS) Spring Meeting, Strasbourg, 2007.
- **B. Arredondo**, B. Romero, A. L. Alvarez, A. Gutiérrez-Llorente, X. Quintana, R. Mallavia, R. Vergaz, F. Montilla, J. M. Sánchez-Pena, J. M Otón, "*Determination of hole mobilities in new blue emitting organic diodes by means of impedance spectroscopy*", Society for the Information Display (SID), Long Beach Ca., 2007. ISSN 0007-966X.

Proceedings in national conferences

- **B. Arredondo**, X. Quintana, A. L. Álvarez, B. Romero, C. Coya, R. Mallavia, P. Velásquez, J. Arias, R. Molina, M. Ramos, J. M. Otón, "*Organic light emitting diode passive matrix based on a new blue fluorescent polymer*", 5ª Conferencia de Dispositivos Electrónicos, Tarragona, 2005. ISBN 0-7803-8810-0.

- B. Romero, **B. Arredondo**, C. Coya, X. Quintana, A. L. Álvarez, R. Mallavia, P. Velásquez, J. Arias, R. Molina, M. Ramos, y J. M. Otón, "*Fabricación y caracterización de matrices pasivas de diodos electroluminiscentes basados en material orgánico"*, 4ª Reunión Española de Optoelectrónica, Elche, 2005. ISBN 84-609-6139-7.
- **B. Arredondo**, B. Romero, X. Quintana, A. Gutiérrez-Llorente, A. L. Alvarez, R. Mallavia, J. M. Otón, "*Novel lithographic technology for OLED-based display manufacturing*", 6ª Conferencia de Dispositivos Electrónico-s, El Escorial, 2007. ISBN 1-4244-0869-5.

Poster contributions

- **B. Arredondo**, R. Molina, C. Coya, B. Romero, A.L. Alvarez, X. Quintana a, R. Mallavia b, P. Velásquez c, J.M. Otón, "*Organic diode passive matrices based in new fluorescent poly(2,7-fluorene phenylidene) derivatives*", 8th European Conference of Molecular Electronics., Bologna, 2005.
- A. L. Álvarez, R. Mallavia, X. Quintana, B. Romero, C. Coya, F. Montilla, **B. Arredondo**, R. Molina, M. Ramos, P. Velásquez, J. Arias, J. M. Otón, "*Development of organic light emitting diode passive matrix based in new poly-[(9,9-dialkylfluoren-2,7-diyl)-alt-co-(benzen-1,4-diyl) derivatives*", Conferencia Invitada. 1ª Primera Reunión sobre Dispositivos Orgánicos Fotovoltaicos, Electro-Ópticos y Electrónicos, Benicasim, 2005.
- A. L. Álvarez, **B. Arredondo**, B. Romero, A. Gutiérrez-Llorente, R. Mallavia, X. Quintana, J. M. Otón, "*A Complete Model for Electrical Conduction in Organic Diodes*", International Conference on Organic Electronics, Eindhoven, 2007.

PATENTS

- **B. Arredondo**, X. Quintana, B. Romero, A. L. Álvarez, J. M Otón, "*Nuevo procedimiento de fabricación de cátodos para diodos luminiscentes*". Application number P200703237.